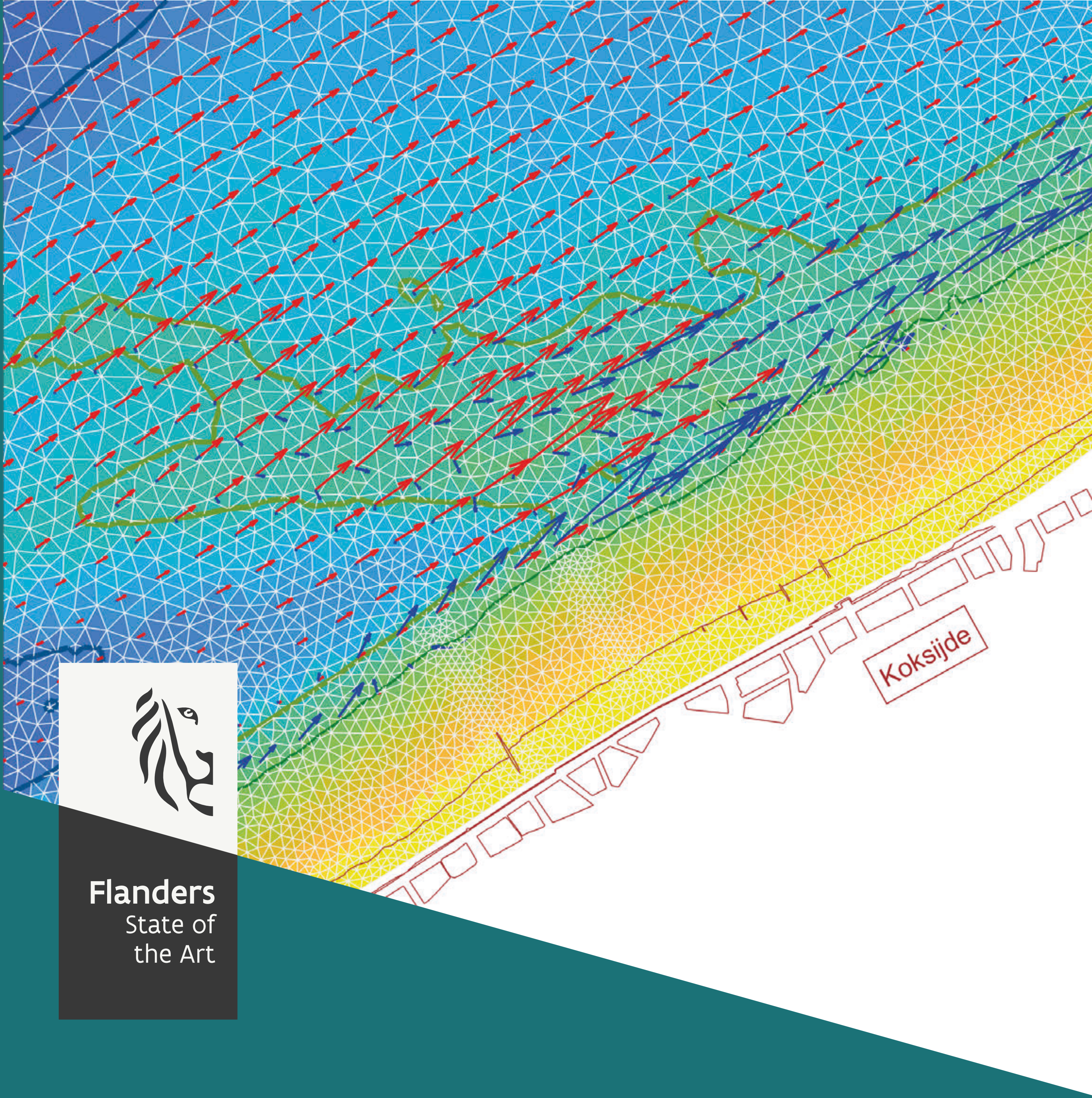

Flanders
State of
the Art

20_079_2
FH reports

MOZES – Research on the Morphological Interaction between the Sea bottom and the Belgian Coastline

Working year 2

DEPARTMENT
MOBILITY &
PUBLIC
WORKS

www.flandershydraulics.be

MOZES – Research on the Morphological Interaction between the Sea bottom and the Belgian Coastline

Working year 2

Dujardin, A.; Houthuys, R.; Nnafie, A.; Röbke, B.; van der Werf, J.; de Swart, H.E.; Biernaux, V.;
De Maerschalck, B.; Dan, S.; Verwaest, T.

Flanders Hydraulics
Flanders
State of the Art

Cover figure © The Government of Flanders, Department of Mobility and Public Works, Flanders Hydraulics

Legal notice

Copyright and citation

D/2024/3241/072

This publication should be cited as follows:

Dujardin, A.; Houthuys, R.; Nnafie, A.; Röbke, B.; van der Werf, J.; de Swart, H.E.; Biernaux, V.; De Maerschalck, B.; Dan, S.; Verwaest, T. (2024). MOZES – Research on the Morphological Interaction between the Sea bottom and the Belgian Coastline: Working year 2. Version 4.0. FH Reports, 20_079_2. Flanders Hydraulics: Antwerp

Document identification

Customer:	Flanders Hydraulics / Coastal Division	Ref.:	WL2024R20_079_2
Keywords (3-5):	Coastal Morphology, Sediment Transport		
Knowledge domains:	Hydraulics and Sediment > Morphology > Erosion / Sedimentation > Literature and desktop study Hydraulics and Sediment > Morphology > Erosion / Sedimentation > Numerical modelling		
Text (p.):	132	Appendices (p.):	30
Confidential:	☒ No	☒ Available online	

Author(s):	Dujardin, A.; Houthuys, R.; Nnafie, A.; Röbke, B.

Control

	Name	Signature
Reviser(s):	De Maerschalck, B. Dan, S.	Getekend door:Bart De Maerschalck (Sig Getekend op:2024-04-04 10:02:47 +02:00 Reden:Ik keur dit document goed De Maerschalck Bart Vlaamse overheid Getekend door:Sebastian Dan (Signature Getekend op:2024-04-07 08:30:05 +02:00 Reden:Ik keur dit document goed Dan Sebastian Vlaamse overheid
Project leader:	Verwaest, T.	Getekend door:Toon Verwaest (Signatur Getekend op:2024-04-04 10:24:38 +02:0 Reden:Ik keur dit document goed Verwaest Toon Vlaamse overheid

Approval

Head of Division:	Bellafkih, K.	Getekend door:Abdelkarim Bellafkih (Sig Getekend op:2024-04-04 12:10:55 +02:0 Reden:Ik keur dit document goed Bellafkih Abdelkarim Vlaamse overheid

Abstract

The MOZES-project (**MO**rfolgische interactie kustnabije **ZE**ebodem en **S**trand) investigates the morphodynamic interaction between the Belgian offshore seabed (inner shelf + nearshore) and adjacent shoreline across varying time scales (months to centuries). The project aims to enhance the understanding of the region's morphodynamics for effective coastal management.

This report outlines progress in four Work Packages (WP1, WP2, WP3 and WP4) during the second project year. WP1 addressed analysis of field data, WP2 involved the further development of the idealized models established in the first year, WP3 delved into investigating the hypothesis of natural beach feeding through sediment transport over shoreface-connected sand ridges using the complex numerical models FlemCo and Scaldis-Coast. Finally, using the latter two models, WP4 examined the effects of the observed deepening of nearshore channels on beach erosion.

WP1: Further digitization of bathymetric and beach topographic data and the collection of bed sediment data. The depth uncertainty of bathymetric surveys was analyzed; yielding an empirical uncertainty of ± 0.15 m. The produced data confirm that over the last four decades, the base of the shoreface suffers structural erosion. In a case study of Pas van Stroombank, the routinely reported "Bagger Informatie Systeem" (BIS) parameter "reduced volume" correlates well with the surveyed volume differences. Longitudinal transport over Stroombank was estimated in 2014 to be about 100 m^3/m. In Kleine Rede, sediment transport was in 2010 about 4 times higher.

WP2: Efforts were concentrated on further developing 1) the morphodynamic shelf model and 2) the coupled morphostatic (i.e., bottom does not change) shelf-shoreline model established in the first year. The development of the morphodynamic shelf model marked an important step forward, enabling the simulation of self-developing shoreface-connected sand ridges by incorporating (for the first time!) wave-topography feedbacks. The simulated ridges resemble those observed on the Belgian shelf, although some differences are noted. Significant improvements were made to the coupled shelf-shoreline model, enabling the reproduction of observed shoreline progradation (erosion) adjacent to the ridge crest (channel) and the steeper bathymetry profile in the breaker zone near the channel compared to that near the crest. Simulations with this model indicate that the observed onshore movement of ridges on the Belgian shelf is likely to intensify shoreline retreat near the channels and progradation near the ridge crests. Finally, a new analytical tide model showed that wave-induced sediment transport dominates in the breaker zone, while tide-induced transport becomes significant further offshore. These findings qualitatively align with results from FlemCo and Scaldis-coast models.

WP3: Primary focus was to understand the observed differences between simulated longshore sediment transport and sediment pathways over ridges by the Scaldis-Coast and FlemCo models. Results from sensitivity runs revealed that these differences primarily stem from a larger wave-induced longshore sediment transport in Scaldis-Coast compared to FlemCo. As was found by the idealized model (WP2), these results confirm that wave-induced sediment transport dominates in the breaker zone, while tide-induced transport becomes significant further offshore. Finally, these results do not indicate an onshore-directed component of the residual sediment transport towards the beaches. However, no firm conclusion regarding the process of natural feeding is possible from this as these models do not include cross-shore processes in a validated way.

WP4: Model results from sensitivity runs using different synthetic bathymetries in the Knokke-Heist region (shallower Appelzak channel and a deeper Paardenmarkt ridge, situation of 1986) provide no clear evidence that a deeper Appelzak channel or a steeper shoreface leads to more erosion on the beaches of Knokke-Heist. As emphasized in WP3, given the absence of 3D cross-shore processes in the Scaldis-Coast and Flemco models, it is crucial to interpret these results with caution. Therefore one cannot conclude about the effect of channel deepening on beach erosion yet.

Contents

List of tables

List of figures

1 Introduction

The MOZES-project (**MO**rfolgische interactie kustnabije **ZE**ebodem en **S**trand) studies the morphodynamic interaction between the Belgian offshore seabed (inner shelf + nearshore) and the adjacent shoreline across various time scales, ranging from months to centuries. The project primary objective is to advance the understanding of the morphodynamics of this region to facilitate effective coastal management.

The MOZES-project is established by Flanders Hydraulics (FH, Antwerp) in close collaboration with Antea Group (an international consultant in Antwerp), Utrecht University (Netherlands), and the research institute Deltares (Netherlands). Commencing in 2022, the project was initially granted for one year, with the possibility of three extensions, allowing a maximum duration of four years.

This report provides an overview of progress made in four Work Packages (WP1, WP2, WP3, and WP4) during the second project year. WP1 focuses on the collection and analysis of field data, WP2 involves the further development of idealized models to study shelf-shoreline coupled morphodynamics, WP3 investigates the hypothesis of natural beach feeding through sediment transport over shoreface-connected sand ridges (sfcr) using the complex numerical models FlemCo and Scaldis-Coast. Finally, utilizing these two models, WP4 examines the effects of the observed deepening of nearshore tidal channels on beach erosion.

1.1 WP1: Data acquisition and analysis

WP1 is dedicated to acquiring extensive data crucial for addressing the research questions within the MOZES-project. The primary focus is on collecting historical bathymetric and topographic data, as well as sediment data, not yet available in vectorized formats. These data will be utilized to create Digital Elevation Models (DEMs) covering the entire area of interest at specific time points, such as 1866 (pre-construction of coastal harbours) and the late 1980s (after the Zeebrugge extension). These datasets serve as inputs for numerical models, contributing to research on the morphological evolution of nearshore channels and shoreface-connected sand ridges on decadal time scales.

In the first year of MOZES, it was observed that the overall depth change in the overlap area of the 1984/7 and the 2022 DEM is a depth increase of 0.32 m (Dujardin et al., 2023). This contrasts with an average 0.02 m depth decrease between 1866 and 1984/7. The depth increase over the last approximately 35 years would represent a very big loss of sediment of about 0.32 m x 746 Mm² = 239 Mm³. This is a huge amount of sediment erosion for which neither a straightforward explanation nor a clearly related destination area can be found. In the past decades, substantial dredging has made the harbour entrance channels deeper and wider. However, if the dredging areas and the disposal areas are left out of consideration, the overall depth change is still 0.27 m. So, the influence of these works is limited and can only explain 16% of the change. This raises questions about uncertainties in bathymetric data.

In year 2 of MOZES, the specific subtasks within WP1 include:

- Subtask 1: Vectorizing maps of the beach, shoreface, and inner shelf, with emphasis on the second half of the 20th-century maps. These maps cover the inner shelf through surveys in the 1960s and 1990s, the nearshore survey of Spring 1992, and topographic mapping of the beach and outer dunes in Spring 1992.
- Subtask 2: Investigating the depth uncertainty of bathymetric surveys over the past decades.
- Subtask 3: Providing a review of bed sediment parameters in the inner shelf and nearshore zone, particularly in relation to dredging activities.
- Subtask 4: Analyzing the evolution of the Belgian coast, with a focus on areas of progradation and erosion, also considering effects of human activities on this evolution.
- Subtask 5: Analyzing the morphological evolution in relation to dredging works in the zone around the access channel to Oostende.

1.2 Numerical modelling

WP2

In year 1 of the MOZES project, a new morphodynamic shelf model was developed, which successfully reproduced ridges with characteristics (heights, orientation, length, width, alongshore spacings) resembling those of observed sfcr on the Long-Island shelf (USA). This model underwent validation using the Long-Island shelf data (Dujardin *et al.,* 2023). Additionally, in year 1, an existing coupled shelf-shoreline model was applied to the Belgian coast, where a field of morphostatic (i.e., the bottom does not evolve during the simulation) synthetic ridges was introduced on the shelf, acting as a forcing template for the morphodynamic development of the shoreline. Preliminary results suggested that an onshore movement of sfcr could lead to shoreline retreat in some areas and progradation in others. However, due to several simplifications in the model (non-representative background bathymetry for the Belgian shelf, absence of tides, simplified waves), no definitive statements could be made regarding the potential impact of onshore migrating sfcr on the evolution of the Belgian shoreline.

The results of year 1 motivated the specific objectives of year 2, which are divided among two activities:

- Activity 1: Further development of the morphodynamic shelf model by 1) using a shelf bathymetry that is based on that of the Belgian shelf; and by 2) solving wave propagation on the shelf using SWAN.
- Activity 2: Further improvement of the coupled shelf-shoreline model by 1) using a field of synthetic ridges with a geometry (length, width and orientation) similar to those of the Belgian shelf; by 2) implementing a more realistic wave climate; and by 3) considering tides in the Q2Dmorfo shoreline model.

WP3

In the first year of the MOZES-project, both the Scaldis-Coast and the FlemCo models were applied in order to investigate the longshore sediment transport along the Flemish coast and the sediment pathways in the area of the shoreface-connected sand ridges. The comparison between the two models revealed the following significant differences in both the simulated longshore sediment transport and the sediment pathways (Dujardin *et al.,* 2023):

- The Scaldis-Coast model predicted significantly larger longshore transport compared to the FlemCo model.
- While the FlemCo model depicted distinct cross-shore sediment pathways in the sand ridge area, suggesting natural feeding of beaches in those regions, the Scaldis-Coast model indicated pathways predominantly parallel to the coast.

Another aspect that was raised in the first year is to what extent are the tides significant in the breaker zone relative to waves.

The findings in the first year motivated the objectives in the second year, which encompass:

- Examining the reasons behind observed differences between the two models, with a specific focus on longshore sediment transport, wave characteristics, and flow dynamics.
- Quantifying the relative importance of tides compared to waves in the breaker zone.
- Investigating the hypothesis of natural feeding of the coast, coming from the adjacent shoreface-connected sand ridges.

WP4

The goal of WP4 is to assess the impact of the gradual deepening of nearshore channels along the Belgian coast on beach erosion and the necessary intensity of beach nourishments to preserve the shoreline. The hypothesis is that a deeper and wider channel leads to increased erosion of adjacent beaches, requiring larger nourishment volumes.

This objective is investigated using the Appelzak channel off the coast of Knokke-Heist, situated between Zeebrugge harbour and the Dutch border, as an illustrative example. Following the extension of Zeebrugge harbour in 1986, a substantial deepening of the Appelzak channel occurred, while the Paardenmarkt ridge (located seaward of Appelzak) experienced noticeable sedimentation. The morphological changes in the Appelzak channel are likely linked to the harbour extension, observed erosion along the harbour breakwaters, and sedimentation on the Paardenmarkt ridge. Additionally, intensive beach nourishments and the presence of groynes at Knokke-Heist slow down or even prevent the landward migration of the Appelzak channel.

Detailed results from each of the Work Packages are presented in the following chapters.

2 Data Acquisition and Analysis

2.1 Vectorising pre-2000 maps of beach, shoreface and inner shelf

2.1.1 Outsourcing of vectorization of 2nd half 20th century beach, shoreface and inner shelf maps

This task continues the work started in the first working year. Table 1 provides an overview of the work progress and was updated for the parts in working year 1 that were finished after the report. In the second working years, budgets allow outsourcing to Sparks bvba, 1601 Sint-Pieters-Leeuw, the work to vectorize the maps of "deelopdracht" 6 to 9.

Table 1 – Progress of the outsourced vectorisation work. Text in blue is added for Year 2.

Work package	Sheets	Date commissioned	Date of delivery	Date of acceptance
Selection stage	A typical beach map: SIT_1985_1_OOST10.jpg (1 sheet) A typical nearshore map: VO_1986_1_8616.jpg (1 sheet) A typical inner shelf map: wie-sch1986.jpg (1 sheet)	16/06/2022	8/07/2022	12/07/2022
Deelopdracht 1	SIT_1985_1_OOST05 – 09, OOST11; SIT_1983_1_OOST05 – 08 (10 sheets) and ZUYWE_1987 en west-dh1984 (2 sheets)	20/07/2022	22/08/2022	29/08/2022
Deelopdracht 2	SIT_1983_1_OOST09 – 11; OOST03 – 04; MIWE28 – 32 (10 sheets)	5/09/2022	10/10/2022	11/10/2022
Deelopdracht 3	SIT_1983_1_MIWE01 – 09; VO_1987_2_87130	14/10/2022	14/11/2022	16/11/2022
Deelopdracht 4	SIT_1983_1_MIWE10 – 20	21/11/2022	4/01/2023	5/01/2023
Deelopdracht 5	SIT_1983_1_MIWE21 – 27	9/01/2023	3/02/2023	7/02/2023
Deelopdracht 6	ZuyWe1967.jpg (locally the first survey) wie-sch1962.jpg (the 1968 sheet was originally selected, but it covers only a small part of the inner shelf. Priority was given to a complete coverage of the inner shelf, for which 1962 was the closest in time)	27/03/2023	25/04/2023	27/04/2023

	WestDH1969.jpg (locally the first survey) ZuyWe1991.jpg WestDH1993.jpg WieSch1992.jpg			
Deelopdracht 7	8 nearshore plans of the Spring 1992 survey which was the first to cover the complete Belgian coast	5/05/2023	12/06/2023	15/06/2023
Deelopdracht 8	SIT_1983_1_MIWE21-30	23/06/2023	31/07/2023	2/08/2023
Deelopdracht 9	SIT_1983_1_OOST05-11	2/08/2023	26/09/2023	29/09/2023
Deelopdracht 10	SIT_1983_1_OOST01-04	2/10/2023	24/10/2023	26/10/2023
Deelopdracht 11	SIT_1983_1_MIWE01-09	27/10/2023	ongoing	

Preparation of each part involves georeferencing of the map images in Lambert 72 using all coordinate marks in the map area and using a spline transformation.

Each delivery is controlled using the acceptance criteria of the terms of reference.

Georeferenced plan packages, vectorisation work deliveries and the control reports can be found here: P:\20_079_MorfoInteract\3_Uitvoering\Deeltaak1_DataAcquisition\OudeKaarten\VectorisatieKustplannen in subfolders "plannen" (georeferenced plan packages sent out) and "lev" (delivery and report). The control and acceptance of each delivery of the vectorisation work is done according to section 5 of the work specifications (see Appendix 1 in Dujardin et al., 2023).

Processing of deliveries after Year 1: part 4 and 5 were processed into 2 x 2 m DEM rasters and part 3 (nearshore map) and 6 were processed into 10 x 10 m DEM rasters using the methodology of section 1.1.9 in Dujardin et al. (2023).

The following DEMs (Table 2) have been made and are available on P:\20_079_MorfoInteract\3_Uitvoering\Deeltaak1_DataAcquisition\DEMs. The rasters are in ESRI raster format. They are referenced in Lambert72 and, while the source maps are either in Z MOW or GLLWS, they have been converted to TAW before making the DEMs. For the datum conversion GLLWS to TAW, use has been made of *gllws_to_taw_vlaamsebanken_l72.tif*, a conversion raster borrowed from aMT available at FH on G:\Masterarchief\cnv.

Table 2 – DEMs made of vectorised data. Names in blue added after Year 1.

Topic	Source of data	DEM	Area
Beach and dune foot maps (cell size 2 m)	SIT_1983_1_MIWE01-09.jpg	G_1983_1A	De Panne to Nieuwpoort
	SIT_1983_1_MIWE10-20.jpg	G_1983_1B	Nieuwprt to Oostende
	SIT_1983_1_MIWE21-31.jpg	G_1983_1C	Oostende to Wenduine

	SIT_1983_1_MIWE31-OOST04.jpg	G_1983_1D	Blankenberge to Zeebr.
	SIT_1983_1_OOST05-11.jpg	G_1983_1E	From Heist to Zwin
	SIT_1985_1_OOST05-11.jpg	G_1985_1E	From Heist to Zwin
Nearshore maps (cell size 10 m)	VO_1986_1_8616.jpg	G_vo1986_1_Knok	From Heist to Zwin
	VO_1987_2_87130	G_vo1987_2_Kks	De Panne to Oostduinkerke
	VO_1992_1 (8 sheets)	G_vo1992_1	Complete coast
Inner shelf maps (cell size 10 m)	ZuyWe1967.pdf	G_ZW1967_taw	Inner shelf eastern part
	WestDH1969.pdf	G_WD1969_taw	Inner shelf central part
	wie-sch1962.pdf	G_WS1962_taw	Inner shelf western part
	Mosaic 1962-1969	G_BS62_69_taw	Complete inner shelf
	Wie-sch1986.pdf	G_WS1986_TAW	Inner shelf eastern part
	West-dh1984.pdf	G_WD1984_TAW	Inner shelf central part
	ZUYWE_1987.pdf	G_ZW1987_TAW	Inner shelf western part
	Mosaic 1984-1987	G_BS84_87_TAW	Complete inner shelf
	ZuyWe1991.pdf	G_ZW1991_taw	Inner shelf eastern part
	WestDH1993.pdf	G_WD1993_taw	Inner shelf central part
	WieSch1992.pdf	G_WS1992_taw	Inner shelf western part
	Mosaic 1991-1993	G_BS91_93_taw	Complete inner shelf

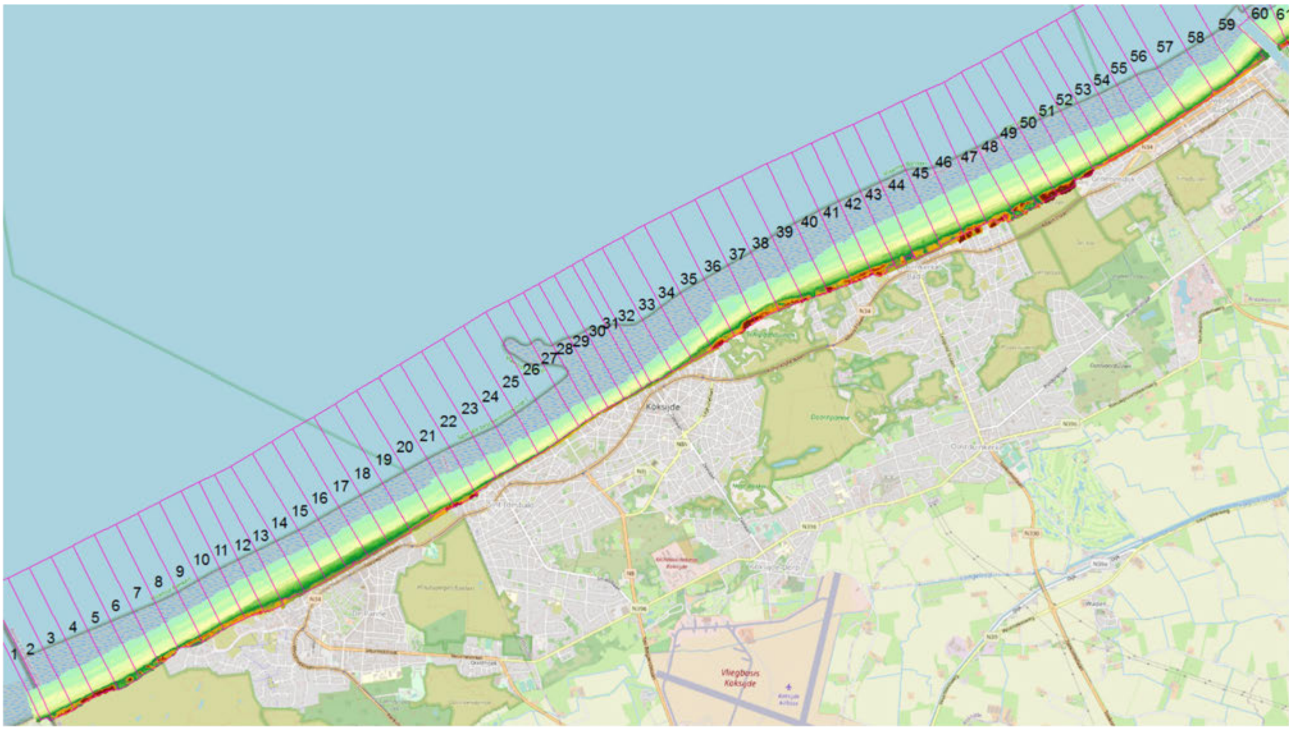

Figure 1 – 2 m-DEM of vectorised survey Spring 1983 between French border and Nieuwpoort. Land area is latest Openstreetmap.

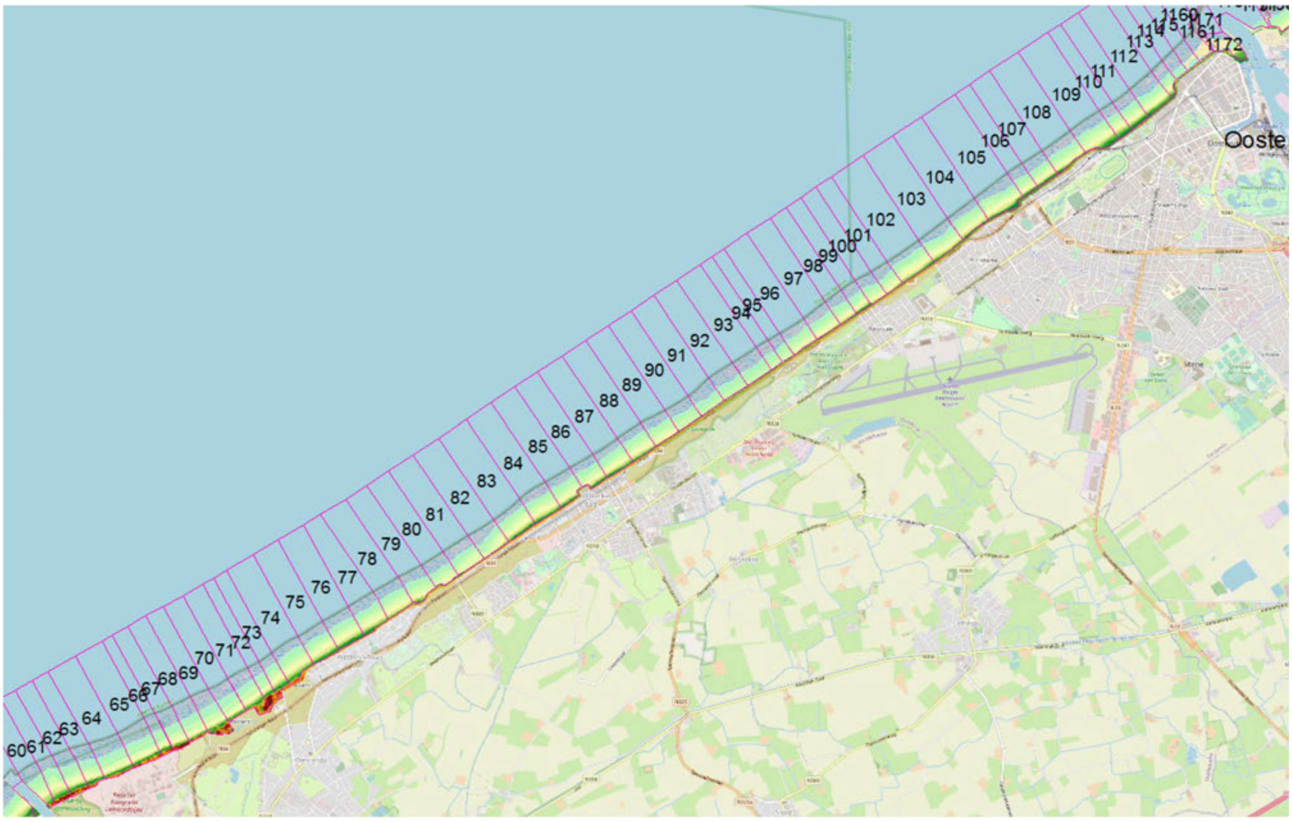

Figure 2 – 2 m-DEM of vectorised survey Spring 1983 between Nieuwpoort and Oostende.

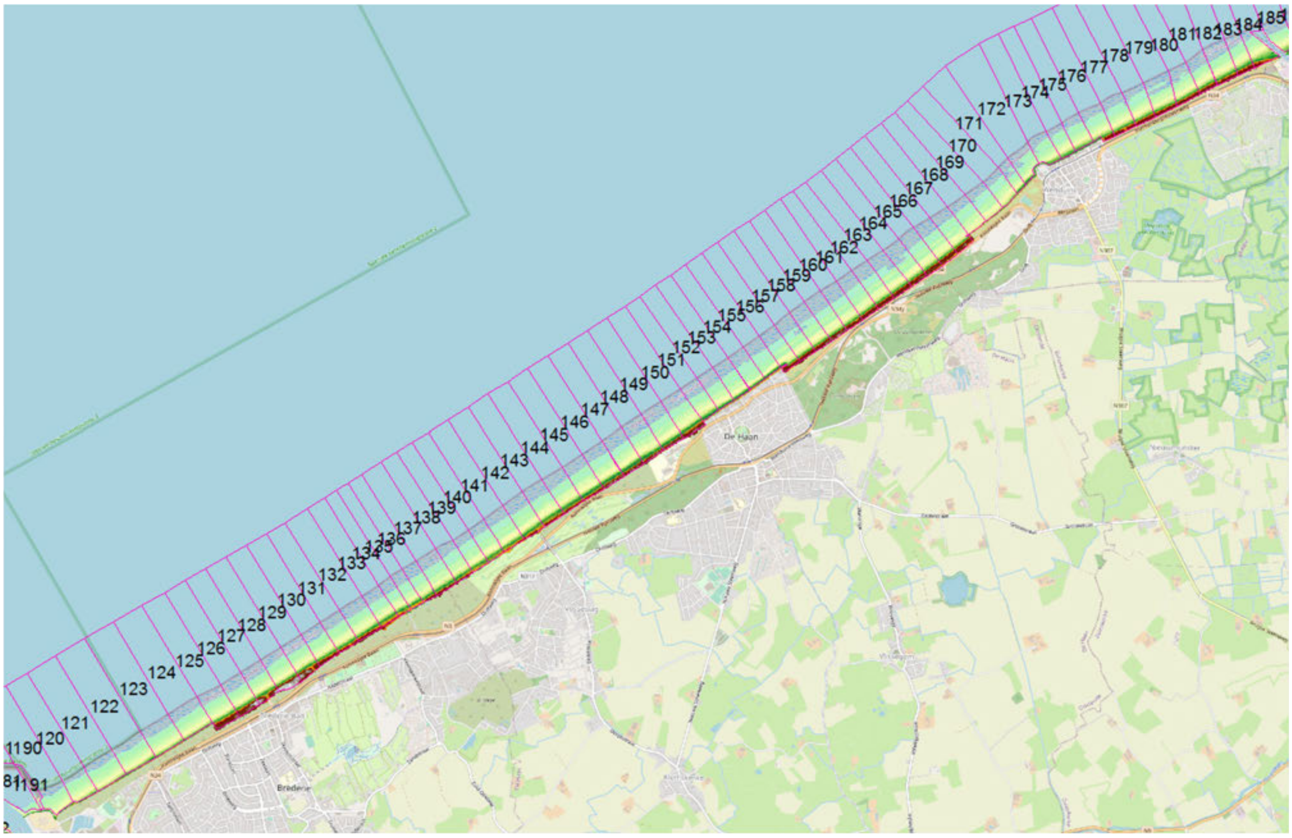

Figure 3 – 2 m-DEM of vectorised survey Spring 1983 between Oostende and Blankenberge.

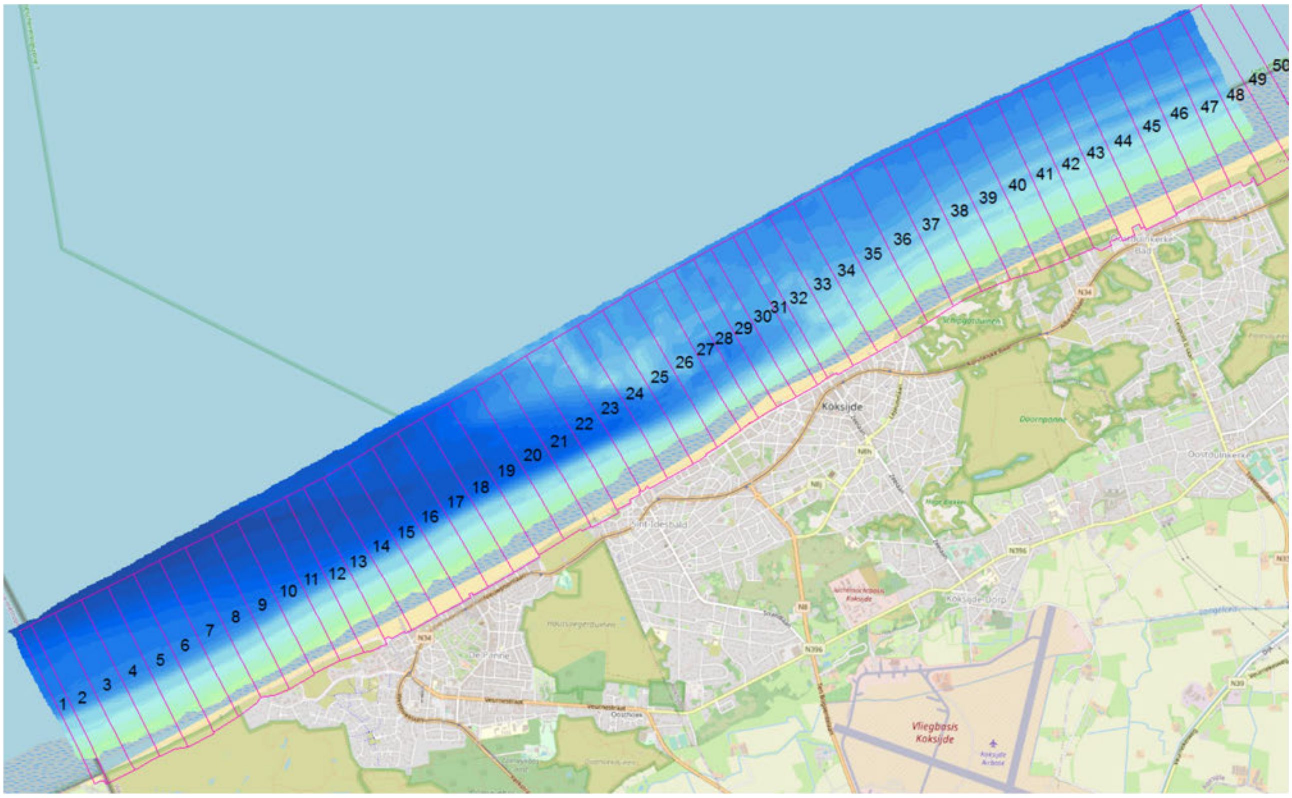

Figure 4 – 10 m-DEM of autumn 1987 nearshore survey between French border and Oostduinkerke. Elevations range from about -8 to +1 m TAW.

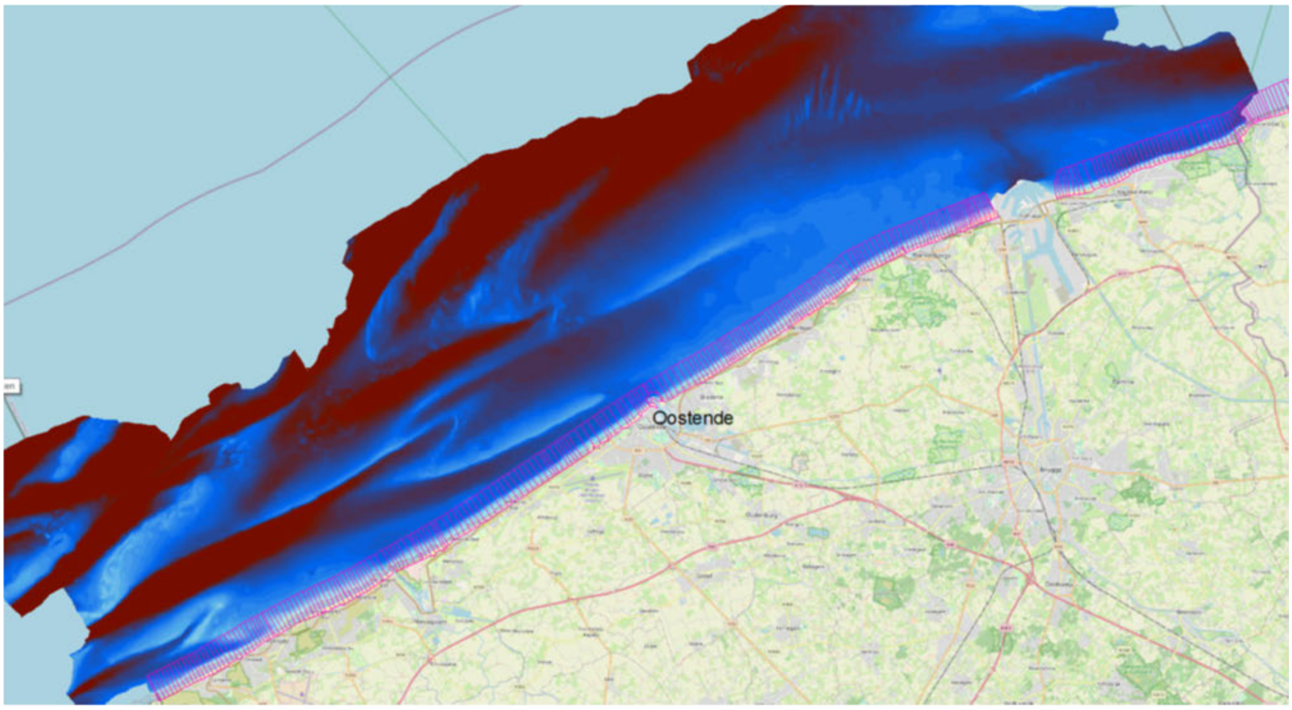

Figure 5 – Mosaic 10 m-DEM of 1967, 1969 and 1962 inner shelf surveys. Sections in thin pink lines. Elevations range from about -15to 0 m TAW. The DEM shown already incorporates the additional structural lines shown in Figure 6.

Note for the inner shelf 1962-1969 charts: they contain insufficient depth points to adequately model the major bedforms but show in addition to the depth points manually interpreted depth contours. They were probably based on previous editions and more points than those shown in the map. The depth contours have been digitized (Figure 6). In order to avoid interpolations through crest and trough areas, crest and trough lines have also been added. The contour lines and crest and trough lines have been added to the 1962-1969 inner shelf DEMs as hard structure lines.

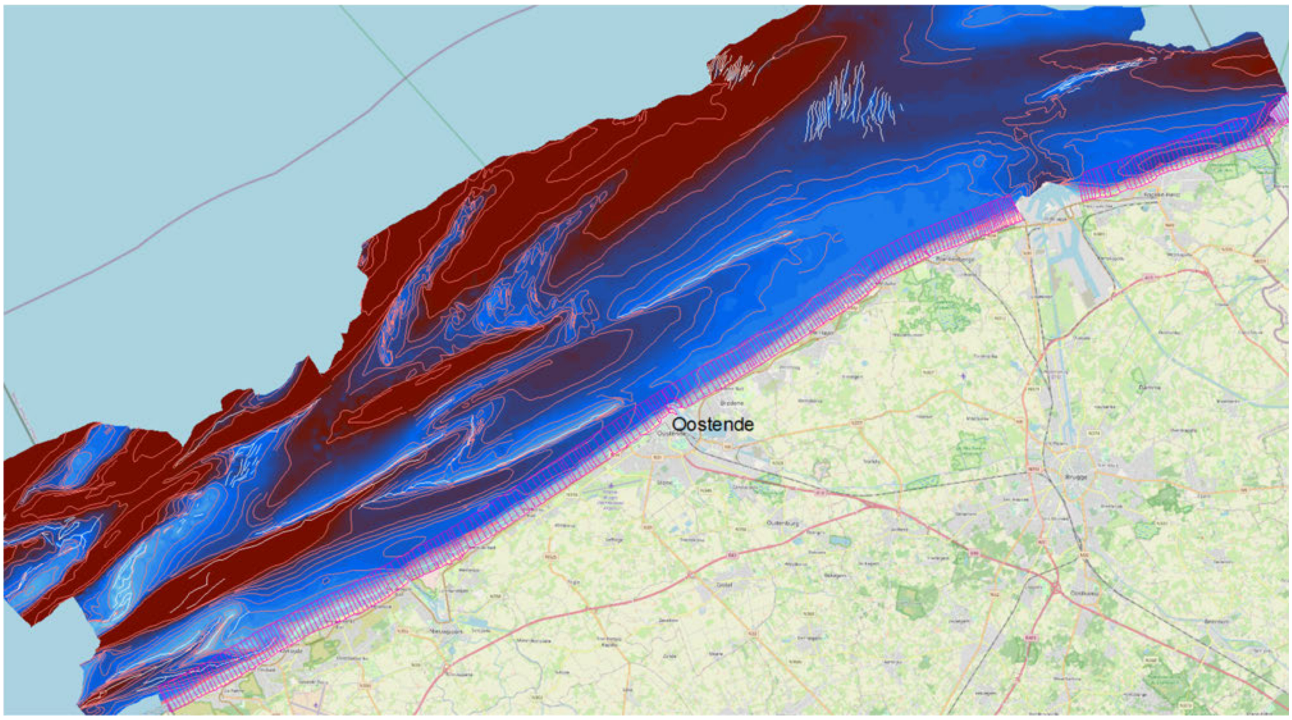

Figure 6 – Depth contours added from the 1967, 1969 and 1962 charts (red lines), and interpreted crest and trough lines (white).

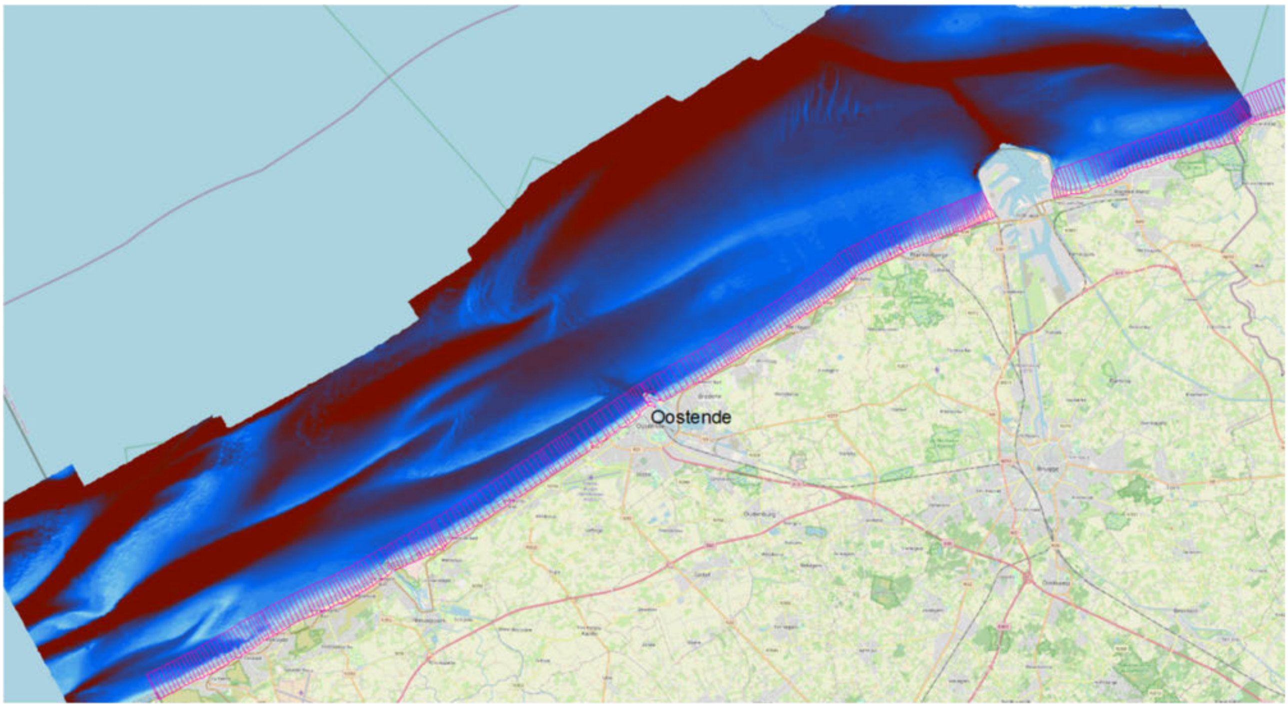

Figure 7 – Mosaic 10 m-DEM of 1991, 1993 and 1992 inner shelf surveys. Sections in thin pink lines. Elevations range from about -15 to 0 m TAW.

Figure 8 – 10 m-DEM of spring 1992 nearshore survey between French border and Oostende. Elevations range from about -8 to +1 m TAW.

Figure 9 – 10 m-DEM of spring 1992 nearshore survey between Oostende and Cadzand. Elevations range from about -8 to +1 m TAW.

2.2 Investigation of bathymetric uncertainty

2.2.1 Introduction

In Mozes Year 1, it was observed that the overall depth change in the overlap area of the 1984/7 and the 2022 DEM is a depth increase of 0.32 m (Dujardin et al., 2023). This contrasts with an average 0.02 m depth decrease between 1866 and 1984/7. The depth increase over the last approximately 35 years would represent a very big loss of sediment of about 0.32 m x 746 Mm² = 239 Mm³. This is a huge amount of sediment erosion for which neither a straightforward explanation nor a clearly related destination area can be found.

In the past decades, substantial dredging has made the harbour entrance channels deeper and wider. However, if the dredging areas and disposal areas are left out of consideration, the overall depth change is still 0.27 m. So, the influence of these works is limited and can only explain 16% of the change.

It is examined here whether a systematic bias in depth for the 1984/87 may have occurred.

First, an overview of possible depth bias components in function of morphological analysis is presented. Their contribution to uncertainty is then evaluated especially applied for morphological change studies.

2.2.2 Overview and estimation of possible depth bias components

Introduction on error in bathymetric charts

The IHO (2020) describes total propagated uncertainty (TPU) by two components: total horizontal uncertainty (THU) and total vertical uncertainty (TVU). The TVU and THU values must be understood as an interval of ± the stated value.

A statistical method, combining all uncertainty sources for determining both the horizontal and the vertical positioning uncertainty is adopted to obtain THU and TVU respectively. The uncertainties at the 95% confidence level must be recorded with the survey data.

The ability of the survey system should be demonstrated by a priori uncertainty calculations (THU and TVU). These calculations are predictive and must be calculated for the survey system as a whole, including all instrument, measurement, and environmental uncertainty sources. This estimation should be updated during the survey to reflect changes from environmental conditions such as wind, waves, etc. in order to make appropriate changes to survey parameters.

Final uncertainty values for the survey may consist of an a priori and a posteriori calculation, explicitly empirical values (e.g. based on standard deviation of vertical depths alone), or some combination of the aforementioned values. The metadata should include the uncertainty achieved for both horizontal and vertical uncertainty components (TVU and THU).

On the gently submarine slopes of the inner shelf, THU has a minor impact, at least since RTK positioning was implemented since around 2000. THU and TVU are rigorously determined by Flemish Hydrography for each survey. It adopts the level "IHO Special Order" that specifies for areas where underkeel clearance is critical THU is maximally 2 m and the maximum accepted TVU is $\sqrt{(0.25\ m)^2 + (0.0075 \cdot D)^2}$ where D is the depth. Before operation a TVU verification must be performed in a controlled setting (entrance of sluice) where TVU should maximally be 0.1 m.

THU and TVU related to each survey are determined a posteriori. The values are determined for each measuring point of the survey and are derived from the uncertainties of all sensors involved in the measurement. One component is depth related. Other components of TVU are the measured acoustic propagation velocity, margins on positioning and the applied heave/roll/pitch compensation. The average TVU over the survey points should be lower than the maximum accepted TVU.

For "historic" surveys, the THU and TVU have not been systematically reported. A practical approach using observed average depth change (per specific area) over time allows to estimate the uncertainty margins to use in morphological bed change studies.

Contribution of measurement errors

Though echosounding provides very precise measurements of depth with respect to the survey vessel, a large contribution to bathymetric uncertainty used to arise in the 1950s to 1980s from the conversion of echosounder-measured depths to the height datum, the so-called tidal reduction. The uncertainty (standard deviation) was estimated at 0.2 – 0.3 m for SB echosounding before Real Time Kinematic RTK positioning was used. The possible influence of location-related bias due to the use of different tidal reduction maps is discussed in the following paragraph.

Echosounding used radiopositioning in the 2nd half of the 20th century. Positioning precision improved from the order of 10 m in the 1950s to 1970s to the order of 1 m in the 1980s to 1990s. Positioning errors are therefore a small contribution to depth uncertainty, especially as gradients of the seabed are commonly small.

Since the early 2000s, RTK positioning was systematically used by the survey vessels. The positioning makes use of the Flepos service. Depending on the wavelengths used, precision in all directions on the order of a few mm can be achieved. Many issues, including the movements of the water surface and the ship, reduce the actual accuracy. The vertical tolerance for a survey delivery used today by Flemish Hydrography is 0.15 m.

Contribution of the tidal reduction

The Flemish Hydrographic Service used manual tidal reduction to convert measured depths to a height datum, usually the MLLWS surface, also named H surface. The method used reduction charts that related the tidal M2 phase and amplitude to standard stations at the shore.

The method was gradually automated; one program in use in the 1980s and 1990s was "TIJDUC". The legends of bathymetric charts mention a 1972, 1987 and 1994 reduction chart version. For the 1987 inner shelf chart (West Coast), the 1987 reduction chart had been used. The 1984 chart (Middle Coast) and the 1986 chart (East Coast) had been reduced using the 1972 reduction chart.

The 1987 reduction chart couldn't be retrieved by the Hydrographic Service, which did provide a scanned copy of the 1972 and the 1994 reduction chart. These charts were overlaid and visually compared (Figure 10). The reduction lines on the map connect the locations with the same M2 tidal amplitude as, or with a small constant difference in M2 tidal amplitude from, a coastal tide gauge. The reduction zones indicate which coastal gauge to use. It is observed:

- the 5 cm-contour lines determined from the reduction raster "gllws_to_taw_vlaamsebanken_l72.tif" are capricious in shape, hinting at a strong influence of interpolation and raster building. However, on the scale of the inner shelf, they coincide well with the 1994 tidal reduction lines.
- the reduction lines of the 1972 and 1994 reduction chart differ strongly in the inner shelf zone at the West Coast. Differences vary from over 10 cm (with the 1972 chart resulting in shallower depths) near the coast to about zero at about 12 km offshore. A similar, but smaller difference characterizes the Middle Coast, from about 5 cm near the coast to about zero at about 12 km offshore. The difference decreases further east of De Haan and could be approximated by zero at the East Coast.

The use of successively better tidal reduction charts thus may have caused elevation bias of around 10 cm on the West inner shelf at the coast, and diminishing offshore, 5 cm on the Middle inner shelf at the coast and diminishing offshore, and less than 5 cm on the East inner shelf.

The 1984/87 inner shelf bathymetry mosaic contains a western part based on the 1987 reduction chart, which we couldn't evaluate. However, the 2022 – 1984/87 elevation difference map indicates that a 10 cm depth bias for the West inner shelf is possible. Likewise, a 5 cm depth bias for the Middle inner shelf is possible. The difference map shows large bed depth changes at the East inner shelf. They are mostly negative, but also include strong accretion areas. As here, there have been extensive navigational works, the change is probably a real morphological change.

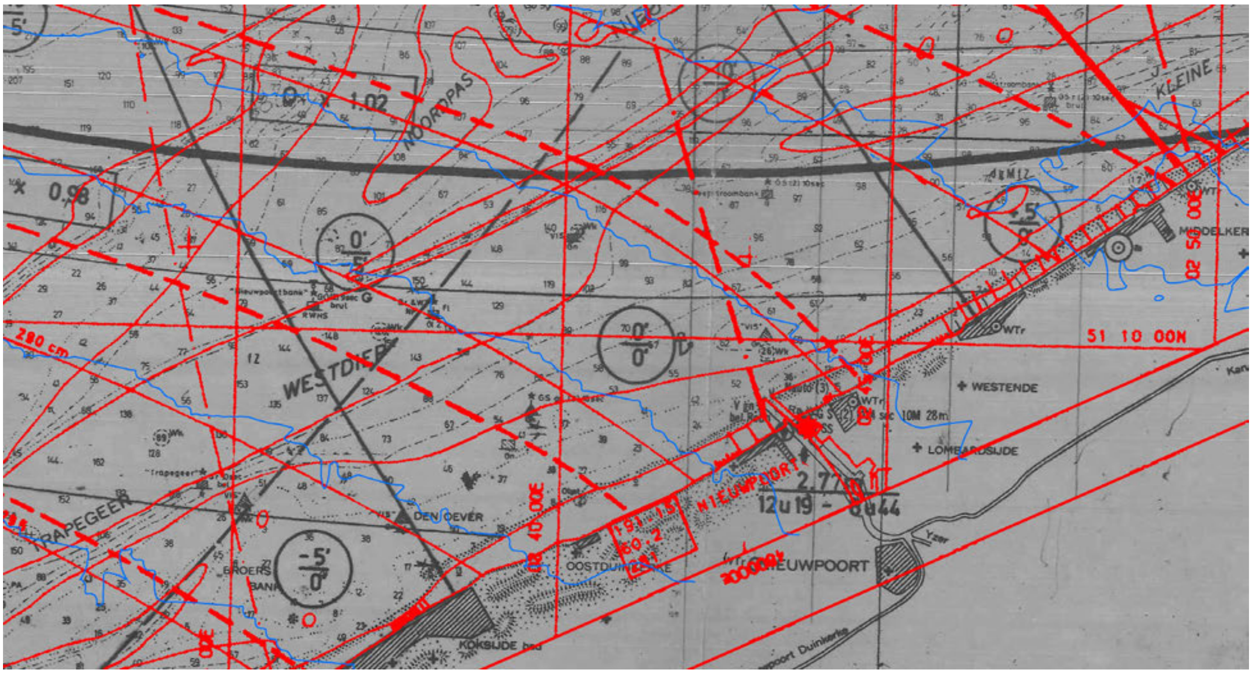

Figure 10 – Overlay of the 1972 (gray background with black lines), 1994 (red lines) and currently used (blue lines) reduction maps.

Extract near Nieuwpoort, from Koksijde-Bad left to Middelkerke-Bad right. Note the strongly different pattern of the reduction lines (full lines) especially in the nearshore zone, between 1972 on the one hand and 1994 and the currently used map on the other hand.

Contribution of the selection method

Spatially covering maps are produced by interpolating a surface between observation points.

An additional source of error is the selection method of depth points. Until the late 20th century, measurements were reported on printed or plotted charts, usually at scale 1/20,000. This allowed to report only one point every 40 to 50 m in the echosounding track. As a rule, the shallowest point in this length window was selected and plotted at its real location, so as to provide safe navigation charts.

The selection bias that arises from this method, was estimated for a small area situated on Wenduinebank.

A simulation of a SB survey was made from a dense, recent (2019) MB point cloud dataset. Two SB survey tracks were simulated, one crossing the Wenduinebank from NW to SE, the other following the top area from SW to NE.

Due to the selection method of shallowest points per selection window, the simulated SB profiles "hover" above the full-resolution profile. The average depth underestimation of the selection method was determined using the difference between the distance-integrated average depth of the full-resolution and the selected profiles: 0.063 m for the NW-SE profile and 0.099 m for the SW-NE profile. The latter profile has a slightly larger selection bias due to the slightly more irregular morphology.

It is clear that the uncertainty generated by point selection depends on the actual and spatially varying roughness of the surveyed area. The selection bias found would be significantly larger in areas with many subaqueous dunes. In the case of the test site on Wenduinebank, most of the area is smooth, and the overall selection bias can be estimated at 0.1 m.

This effect should be similar in all maps derived from SB surveys where points were reported on charts. The example elaborated here for a chart scale of 1/20,000 is presented here just to raise awareness of the magnitude of the effect. It is no longer present from the time, around 2000, when all measured depth points (often several points per metre inside the navigation tracks) are made available in digital point files.

As the depth bias is systematically towards "bed too shallow", it should be considered to correct the overall 1984/87 depth model by 5 to 10 cm, say 7.5 cm. This correction should then be applied to all maps established from vectorized paper charts.

Effect of gridding

Gridding is the interpolation of depth values on a regular grid of points. The selection bias of shallow points in early SB surveys will be incorporated in the grid. But even when from around 2000, there is no longer a selection bias, the gridding of SB depth points will cause some bias due to the fact that point density is high inside the navigation tracks and absent between the navigation tracks, that are typically 100 m or 200 m apart. Especially in areas where the bed has a general concave or convex profile, systematic errors due to interpolation will arise. But this effect is always the same from survey to survey, and therefore, even though a biased surface is produced for each survey, comparing it through time will cause no bias.

For classical navigation maps, MB point clouds are gridded using the minimum depth per grid cell. In large-scale maps based on MB, there is no effect as these maps have 1m-cells. The mosaic raster on the bathymetric portal can be downloaded using a number of gridding methods; in this analysis, it was downloaded on a 10 m cell resolution, and the real depth nearest to the cell centre was used. In our morphological study at the scale of the inner shelf, it can be concluded there is no bias due to gridding from MB data.

Comparing 10 m cell grids from SB data with 1 or 10 m cell grids from MB data will introduce a gridding bias. In general, morphological concavities will be gridded from SB data as a tangent surface that will contain sections above the real surface, while morphological convexities will be gridded as a tangent surface that will contain sections below the real surface. There is no simple method to compensate for this effect. **When interpreting differences, this effect must be kept in mind.**

Contribution of daily surveying and processing

It was noted that SB surveys performed on several, even successive, days may result in outspoken straight edges inside the depth model constructed from such mosaicked surveys. At the edge, elevations may differ 1 to 2 dm, but in exceptional cases even as much as 5 dm.

The edges are aligned according to the SB survey tracks. The effect was examined in detail for a small test site near the Wenduinebank. Conspicuous straight edges were noted inside a SB dataset acquired in 2011-2012.

The time stamp of the individual survey points of both the 2011 and 2012 datasets is preserved in the archives of Flemish Hydrography. This information allowed plotting the survey dates of the individual depth points (Figure 11). The straight edges in the corresponding DEM are all related to changes in survey date.

It is impossible to correct for this day-to-day effect as the true reasons of the differences in depth from day to day are unknown. It must be taken into consideration as a factor of general uncertainty of the seabed depth, and can be estimated at 0.2 m. **As this is about the range of the error due to tidal reduction, it may be largely due to tidal reduction and doesn't need to be accounted for separately on top of the error due to tidal reduction.**

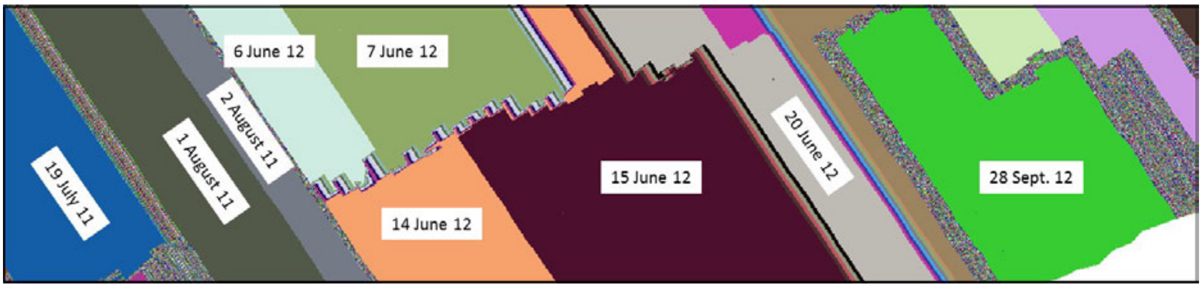

Figure 11 – Survey dates of the 2011/2012 SB cover of the test area. Coloured areas are areas surveyed on the same day. Stippled areas are transitions between neighbouring survey date areas. The wide stippled area near the right edge is an area with interlocking single SB tracks surveyed on different dates.

Depth measurement is more accurate since RTK and attitude logging systems were used. Such accurate systems are a prerequisite in MB surveys. But even for them, the resulting bathymetric maps are not entirely morphologically coherent. Due to the shallow water depths, several survey days are needed to cover a given area. Conditions and settings may be different from day to day, and bed change may have occurred when survey dates are several days or weeks apart. It was noted in an offshore study (Trouw & Houthuys, 2024) relying on spatially extensive MB maps, using elevation difference areas characterized by straight outlines, and therefore associated to the processing of survey strips, that elevation uncertainties of around 0.2-0.3 m for MB surveys performed around 2000 and still about 0.1 m for present-day MB surveys must be taken into account.

Present-day SB surveys are still subject to this important source of uncertainty. Figure 12 shows the elevation difference map of the Spring/Summer 2023 – Spring/Summer 2022 SB nearshore surveys. These surveys are conducted each year over the same tracks, perpendicular to the shoreline and spaced 100 m. The nearshore in this area is relatively stable. The elevation difference maps show two clear, straight "joint lines", indicated by the blue arrows in Figure 12. These joints are interpreted to be due to survey-day related bathymetric errors. It is not known whether they occurred in the 2022 or 2023 survey (or both). The elevation difference over the joint line is on average between 0.15 and 0.25 m.

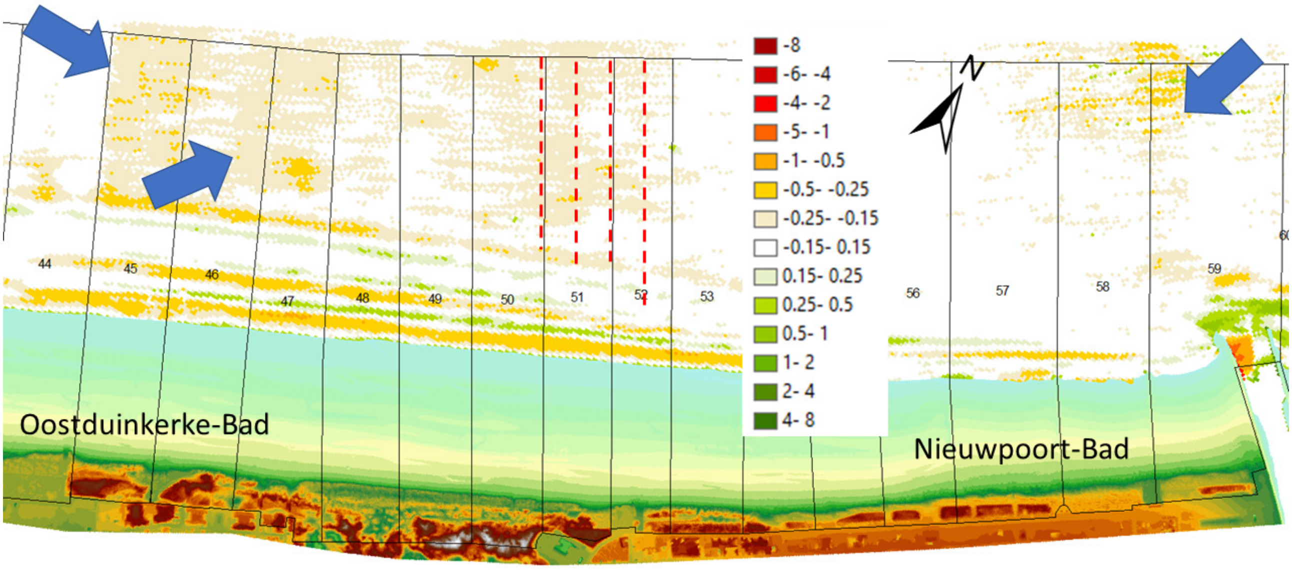

Figure 12 – Height difference map of Spring/Summer 2023 – Spring/Summer 2022 nearshore surveys. Lower part of map with contiguous cover is beach elevation survey Spring 2023. Elevation differences in m (see legend in middle of map). The blue arrows indicate joints interpreted to be due to survey-day related bathymetric errors. Red dashed lines indicate SB track lines and thus zones with alternating elevation differences.

In sections 2.5.4 and 2.5.5, a SB survey is compared with a MB survey in Pas van Stroombank, both conducted on the same day, 2/04/2014. Systematic depth differences between both surveys are of the order of 0.1 m.

The zigzag effect

Zigzags in interpolated depth contours arise when SB tracks are not perpendicular to the main slope of the seabed. Due to "blind" interpolation, the elevation model shows "stairs" in the area and interpolation of depth contours on such surfaces results in zigzag lines.

However, it was often noted that also on flat or smoothly sloping surfaces, zigzag depth contours indicate alternating shallower and deeper bed profiles in neighbouring sounding tracks. The effect occurs in SB models from the 1970’s up to now. The effect is easily recognized by the zigzag pattern of the depth contours on smooth surfaces, and also on elevation difference maps, where stripes of alternating more and less elevation difference alternate according to (one or both of) the echosounding navigation tracks. It can also be recognized by alternating elevation difference strips on elevation difference maps, aligned with the SB tracks (see in coastal sections 51 and 52 in Figure 12).

As the depth shows differences following neighbouring survey lines, they must be explained by navigation direction, supposing that the survey vessel sailed up and down the area.

The reason of this difference is not yet found.

It can be put forward that the amount of uncertainty on depth caused by the zigzag effect is equal to the difference in depth at the summits and bottoms of the zigzags. Most probably, the true depth is the average depth.

Summary of possible systematic corrections

For all bathymetric surveys based on SB, a general uncertainty of about 0.25 m must be taken into account. It is mainly caused by the reduction of instantaneous depth measurement to a height datum. It appears to heavily impact on partial surveys performed on successive survey days. Also in MB surveys, such an effect was noted. It can be estimated at about 0.25 m for the "early days" of MB surveying, around 2000, gradually decreasing to about 0.1 m today. No correction is possible without numerous and independent reference data. The uncertainties specified here must always be allowed for when interpreting morphological change based on bathymetric surveys.

It may be taken into consideration to compensate older SB surveys for a change in the reduction chart of the Belgian shelf by applying a location-dependent correction at the West coast and the western part of the Middle coast, such as specified above.

2.2.3 Is a compensation in the 1984/1987 dataset needed?

In order to investigate if a compensation on systematic depth bias should be carried out, the "problematic" 1984/4987 survey was compared to earlier and later surveys and evaluated for long-term consistency in morphological change.

Comparison of 1986 inner shelf map with 1986 nearshore map

A small part of the 1986 inner shelf map overlaps with the 1986 nearshore map (area from Heist to Zwin). Both charts are derived from surveys performed in the same period but using different survey vessels.

A difference map (inner shelf minus nearshore) was made of the corresponding DEMs in this area. It appears that the inner shelf area (converted to TAW) in this area is on average 4 cm shallower than the corresponding nearshore area. The standard deviation on the elevation difference is 16 cm. Areas of shallower inner shelf are scattered among areas of deeper inner shelf. It can be concluded that the correspondence between both surveys is good and well below accepted differences on the order of 10 – 15 cm.

Check of consistency of large-scale morphodynamic evolution over time

A series of bathymetric maps of 1866, 1962/69, 1984/87, 1991/93, and 2022 was compared using the same scale, bathymetric legend and cut-out. Systematic movements of the large-scale morphology could be detected, such as the systematic migration of nearshore sandbank to the east. In this, the 1984/87 DEM represents no interruption. This time series will be completed by more time steps, and this will be used to describe in more detail the observed large-scale morphological change on the inner shelf.

It is concluded that the 1984/87 survey represents no outlier in the large-scale morphological evolution.

Check of elevation evolution at selected points

A set of 48 points was created at locations scattered over the inner shelf. Locations of erosion, resp. accretion or no change between the 1980s and 2022 were picked at inshore as well as more offshore sites (Figure 13).

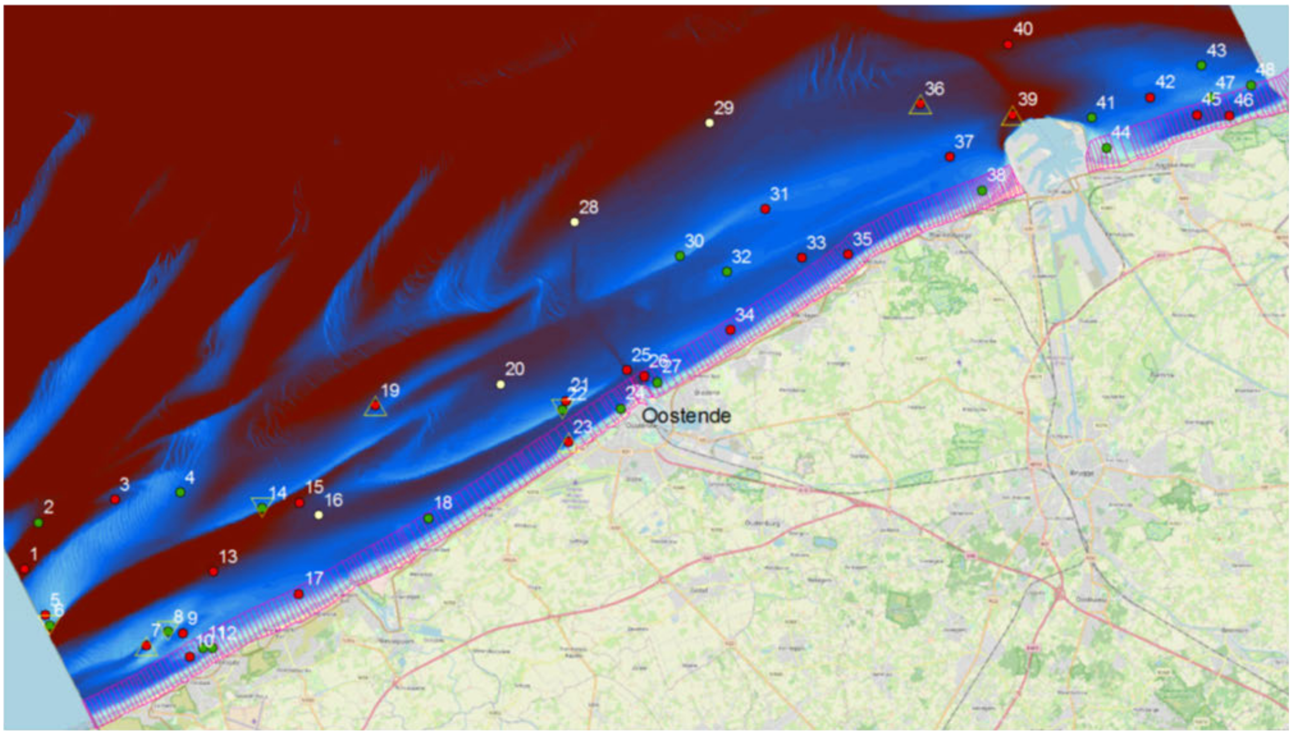

Figure 13 – Locations at which the depth is plotted vs. time in Figure 14 to Figure 16.

Location dot red at sites where erosion was observed between 1984/87 and 2022, green where accretion was observed, and white at locations of no depth change. Triangles around dots show outliers in the time graph; top points upwards: outlier is shallower; top points downwards: outlier is deeper.

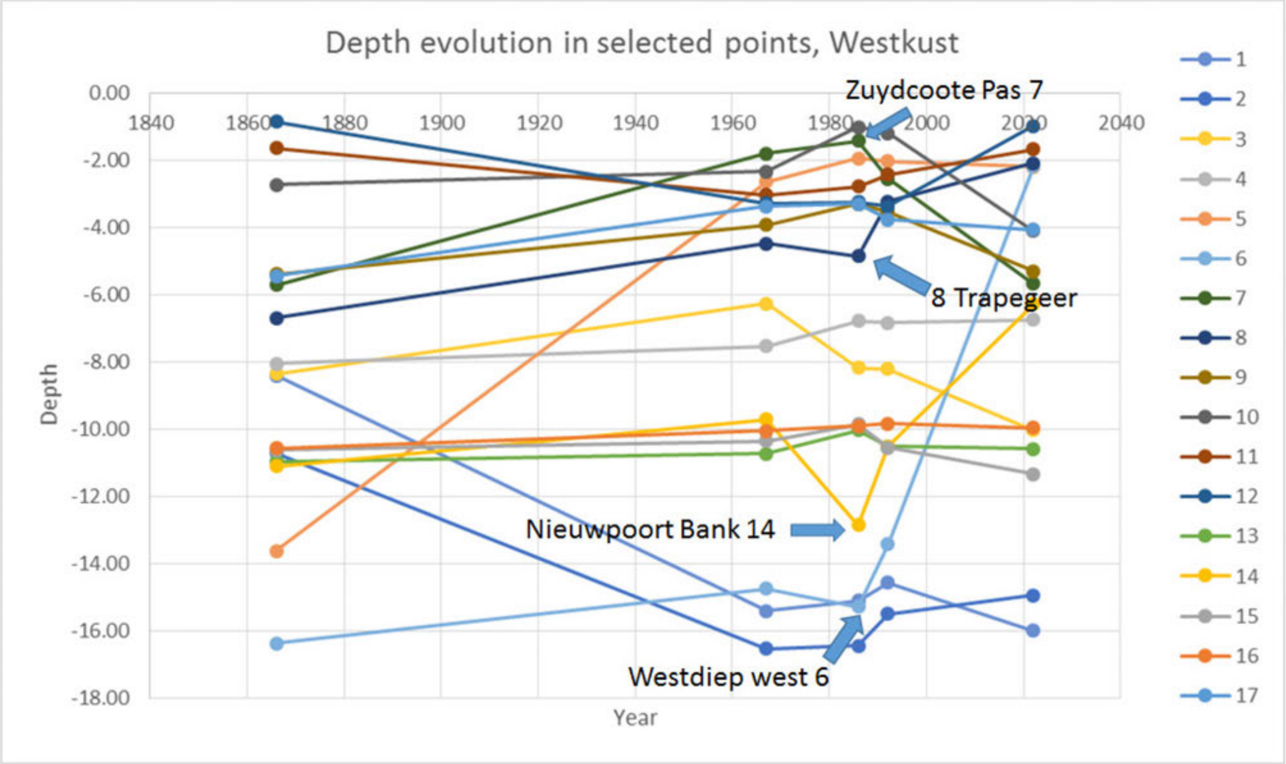

Figure 14 – Depth evolution (in TAW) at locations 1-17 of Figure 13. Blue arrows indicate outliers for 1984/87 in the time series.

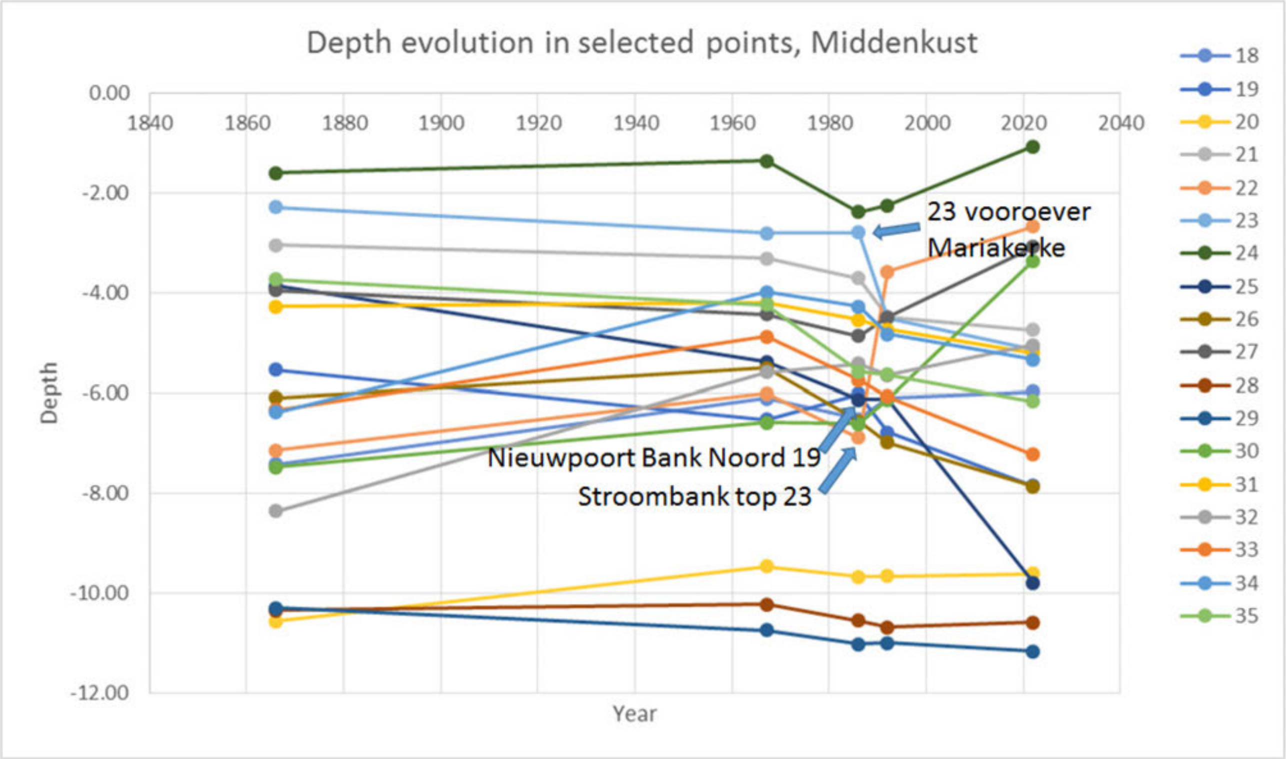

Figure 15 – Depth evolution (in TAW) at locations 18-35 of Figure 13. Blue arrows indicate outliers for 1984/87 in the time series.

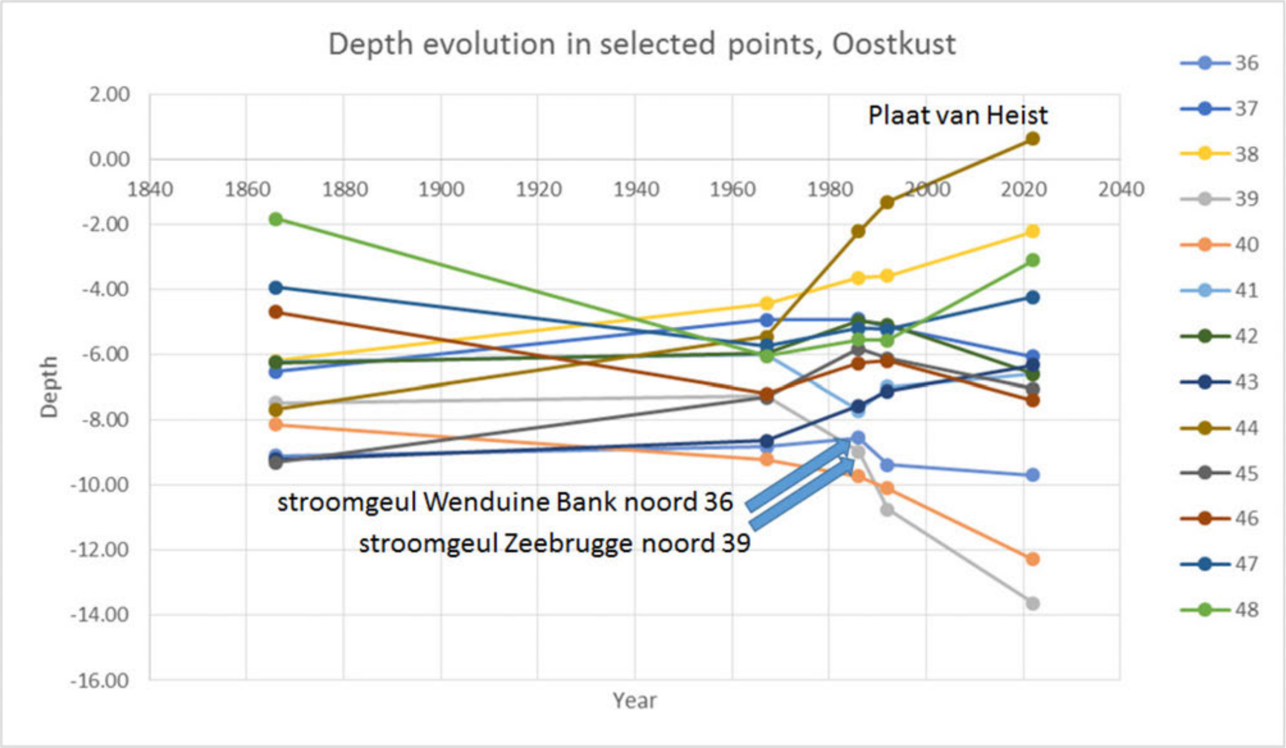

Figure 16 – Depth evolution (in TAW) at locations 36-48 of Figure 13. Blue arrows indicate outliers for 1984/87 in the time series.

Most of the 1984/87 depth values represent no break in the time graphs of Figure 14 to Figure 16. The outliers are indicated by thick blue arrows. It appears that all outliers can be explained by their specific location: they were picked near effectively migrating banks and channels, where the migration movement can give rise to a trend change. Moreover, there are about as many upwards (5) as downwards (4) outliers, suggesting the 1984/87 depth values are not biased.

Check of mean elevation evolution over large areas

A final check involved the overall depth in three large areas, that correspond more or less to the separate 1/20,000 inner shelf map sheets. Care was taken to outline areas so that they were fully bathymetrically covered in all surveys from 1866 to 2022 (Figure 17).

The variation inside each box, illustrated by the standard deviation of depths at each survey, shows no exception for the 1984/87 survey. However, the average depth value of 1984/87 makes a small outlier, especially at the West Coast (Figure 17). There, it can be estimated as 0.15 m "too shallow". A correction by 0.15 m downwards for the 1984/87 dot in the Mid and East Coast would also result in smoother graphs. **This observation is in agreement with the analysis of the change in tidal reduction chart above.**

It is remarked that 0.15 m is inside the error margin for depth adopted for SB bathymetric surveys. It remains striking that the error would occur in 1984/87 in the same (upward) direction for all three areas.

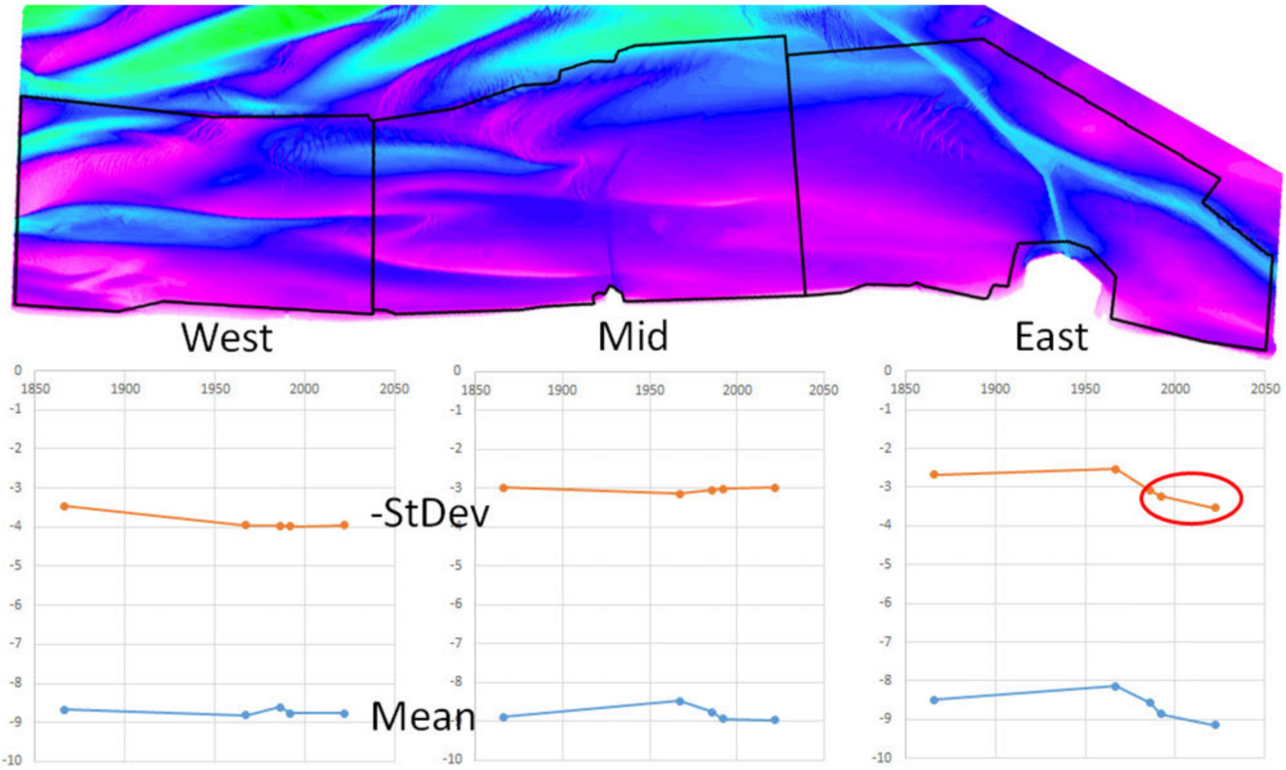

Figure 17 – Time evolution of the average value (blue graph) and the standard deviation (of which here the negative value is shown; orange graph) of the depth inside three areas labelled West, Mid and East on the bathymetric map above.

Conclusion

At this point, an overall depth bias of about 15 cm shallower is possibly present in the 1984-1987 inner shelf charts. However, in some areas and points the 1984-1987 depth model agrees with the longer-term trend. Therefore, applying an overall correction is not justified at this stage. It is suggested to await the digitization of more depth charts from both before and after the 1980s, which will provide a better resolution of the time evolution. If needed, a location-dependent compensation can then be applied for the West Coast and western part of the Middle Coast, as specified above in the section about the tidal reduction.

This analysis also made clear that even using today's bathymetric surveys, an **uncertainty margin on absolute depth of ± 0.15 m** (standard deviation) is to be taken into account in all analyses, regardless of whether they are based on SB or MB surveys. This uncertainty will often emerge on mosaic edges of surveys conducted over several days. Inside the area surveyed on one day, the morphological coherence is better than over the survey day edge. But when the survey is compared to a survey of the same area on a different date, the same uncertainty applies.

In time series of bathymetric surveys, "outlier" surveys can be identified, where the overall average depth deviates from the longer-term trend. Sometimes, the outlier survey can be corrected for this (see section 2.5.4 for the 7/01/2015 survey of Pas van Stroombank).

The longer-term trend at any place emerging from multiple successive surveys is generally a reliable standard to evaluate individual survey bias. Morphological change on the seabed is often slow and continuous. Inside each depth difference map, individual areas occur where depth change exceeds the uncertainty. These depth change patches are reliable indications of real bed change. Also there geographical evolution over time gives reliable indications of morphological change.

2.3 Review of sedimentological data along the Belgian Coast

2.3.1 Survey for the Living Lab Raversijde project

Nine Van Veen grab samples were taken by MUMM in the framework of the SUSANA campaign with RV Simon Stevin for the Living Lab Raversijde project in March 2023. The location of the samples as well as the D50 grain size is shown in Figure 18. The sorting was calculated as half the difference between D10 and D90, both expressed in Krumbein phi. It appears that both the seaward slope and the crest area of the Stroombank contain fine to medium sand. Note that the grain size at the crest of Stroombank is slightly coarser than at its seaward flank. The sand at the crest is much better sorted than at the seaward flank: the average sorting of the three crest samples is 0.56 and of the three seaward slope samples 1.74. These results can be interpreted as a sorting effect indirectly indicating net sand transport from the seaward slope to the crest area. The good sorting at the crest, combined with the overall smooth morphology there, also indicate wave reworking.

The three samples from the Kleine Rede flow channel contain muddy sediment. The poor sorting averaging at 4.01 for the three samples indicates a sedimentary area receiving mostly sediment from suspension (mud) but also from current transport (D90 in all three samples is same sand size as D50 of Stroombank).

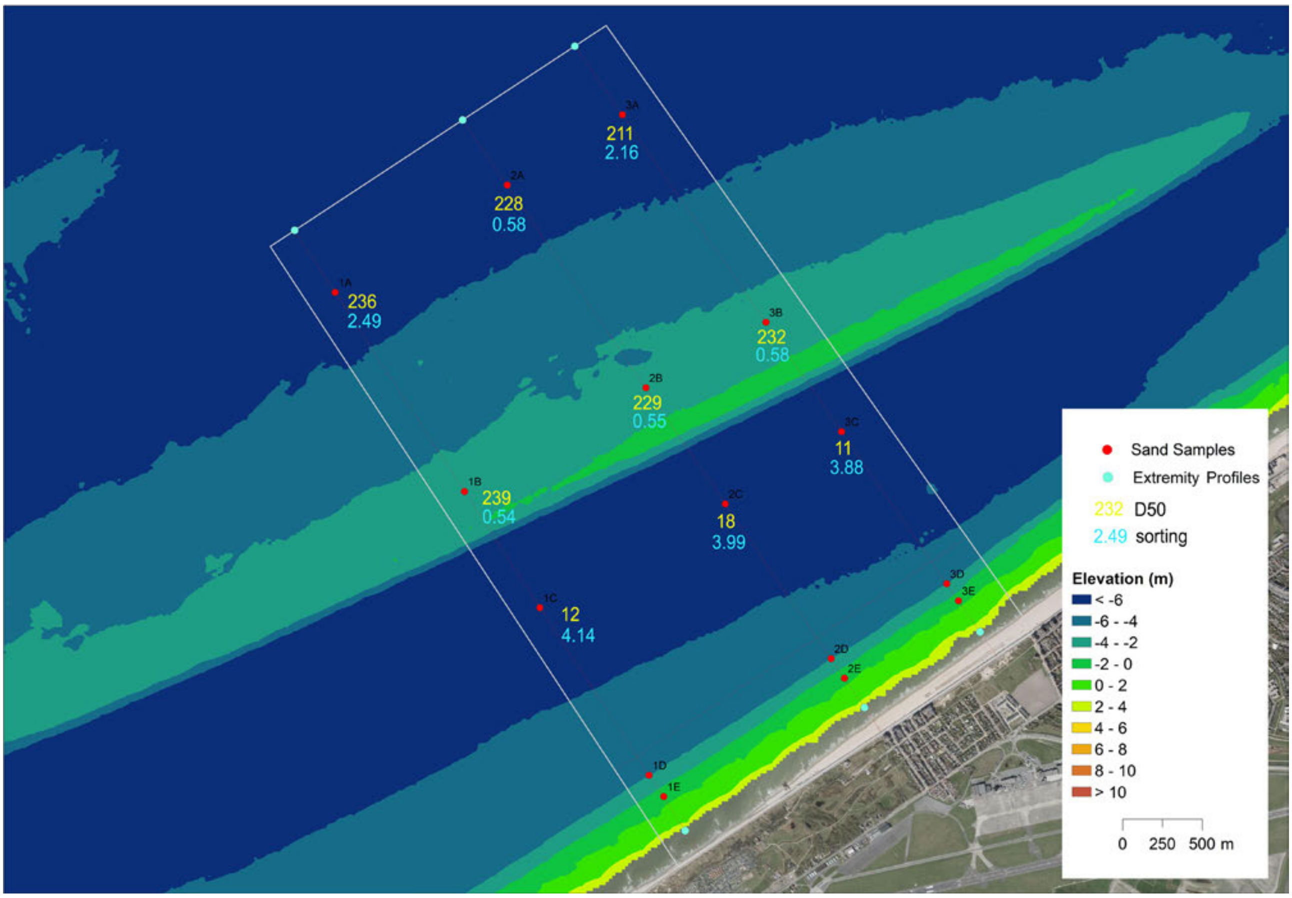

Figure 18 – Location of grab samples (rod dots) and median grains size D50 (yellow figures) in µm. Background is simplified bathymetry; Stroombank traverses the image while the coast near Raversijde is in the lower right corner.

2.3.2 Bed sediment taken in relation to dredging operations near Oostende

Maritime Access provided results of a sampling campaign in 2018 of bed samples near Pas van Stroombank, the navigation access channel of Oostende harbour. From the analysis results, the Total Organic Matter content, grain size D50 and grain size sorting were plotted in Figure 19.

The bed sediment inside the harbour dams is definitely muddy. The sample in Kleine Rede is fine sand. The very poor sorting reflects the important admixture of fine particles. The two samples on Stroombank are fine to medium sand, and well sorted, thus containing no mud. Going more seawards, the sand becomes finer and probably again muddier.

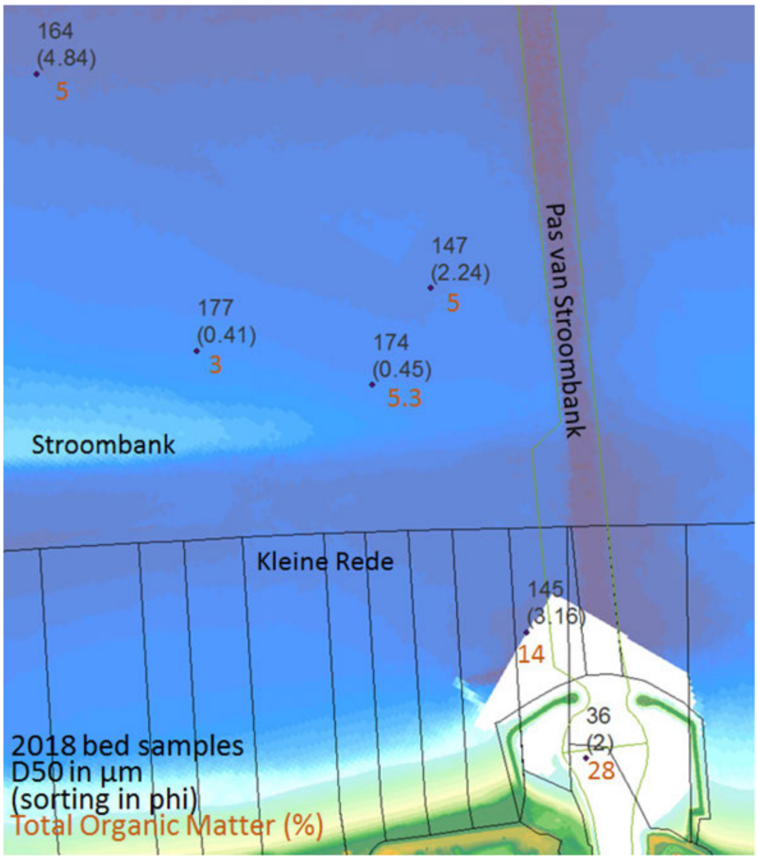

Figure 19 – Results of bed samples taken in 2018 near Pas van Stroombank.

2.3.3 Seabed sediment maps of the inner shelf

The latest seabed substrate map of the Belgian Part of the North Sea was published by MUMM in August 2023, on a 125 m pixel resolution (available at https://metadata.naturalsciences.be/bmdc.be:dataset:2762). A proxy of the surficial sediment type was mapped using automated seafloor classification using derivates of very-high resolution multibeam bathymetry from Flemish Hydrography (a mosaic at 1 m resolution composed of MB surveys performed from 2015 to 2022), informed by sediment dynamics and geological processes. The mapping was steered towards a Folk classification (Folk, 1954) representing a maximum of fifteen major textural groups defined on ratios of silt-clay (< 63 µm), sand (63 µm to 2 mm) and gravel (> 2 mm) percentages. The original classification (15 classes) was merged into 6 classes and 4 classes, the latter to align with the requirements of Europe’s Marine Strategy Framework Directive. The map classifies bedforms and bed roughness into habitat bed sediment classes. The classification was trained in areas where gravel substrate is of large ecological importance, and where this substrate is frequently covered by migrating large and small sandy dunes. An additional classification method used bed roughness. Training was further supported by sediment analyses from samples. An extract of the map showing the inner shelf is given in Figure 20.

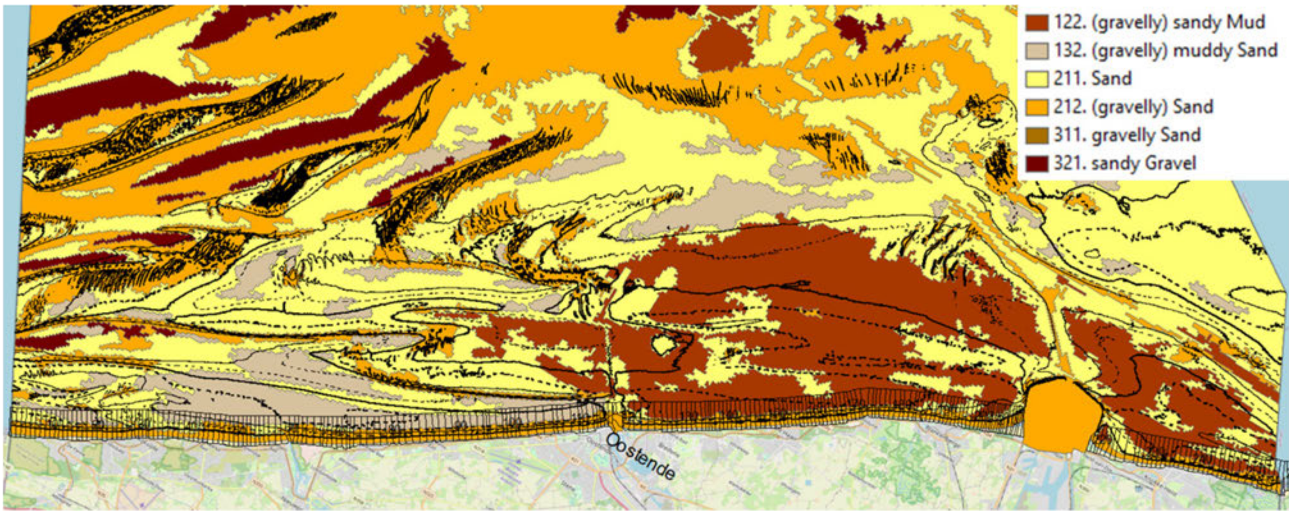

Figure 20 – Seabed substrate map of the inner shelf.

This map must be used taking the classification procedure into account.

Especially in the shallow depths of the inner shelf and the nearshore, MB mosaics consist of narrow strips, often surveyed on separate days. And often here, the bed is rather flat. This results in artificial roughness often more related to survey and mosaic issues rather than real bed variations. Other artefacts may arise from dredging. The navigation channels often show dredging furrows, producing a roughness similar to sandy substrates with dunes. In the inner shelf zone, flat areas with low roughness were trained as muddy sand. Finally, the nearshore and shoreface was not detailed as they were not needed in the habitat map. They have been lumped in one sand class. Around coastal defence structures and in and near harbours the sediment type may differ; in the latter it is mostly mud.

The map provides a rational spatially covering image of the seabed sediment, but it has its shortcomings due to the procedure used to realize it. It is therefore supplemented by a classical grain size map based on samples.

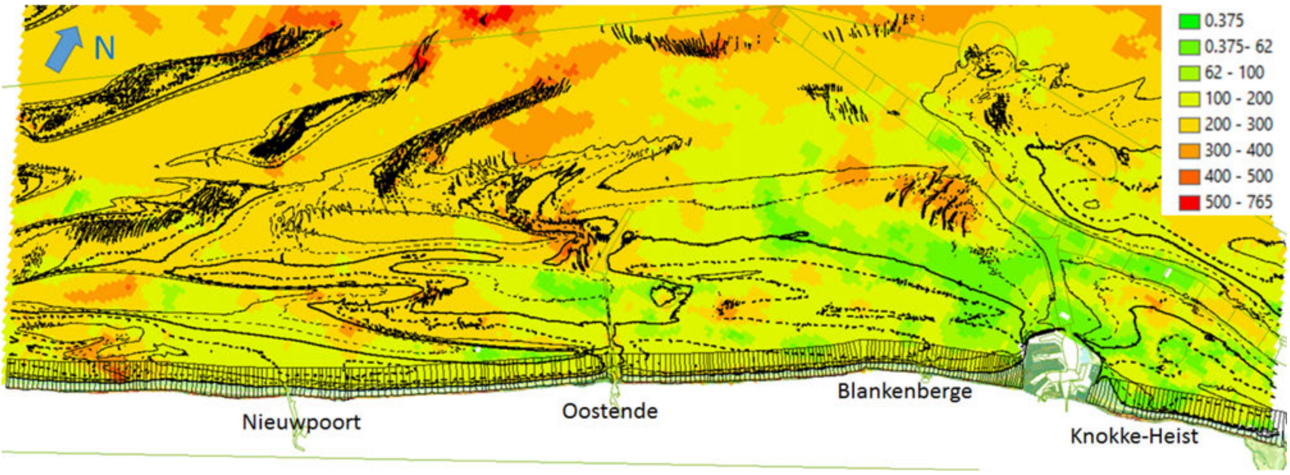

Figure 21 – D50 of seabed. Source: Verfaillie et al. (2006). Colour classes are D50 in µm (see legend).

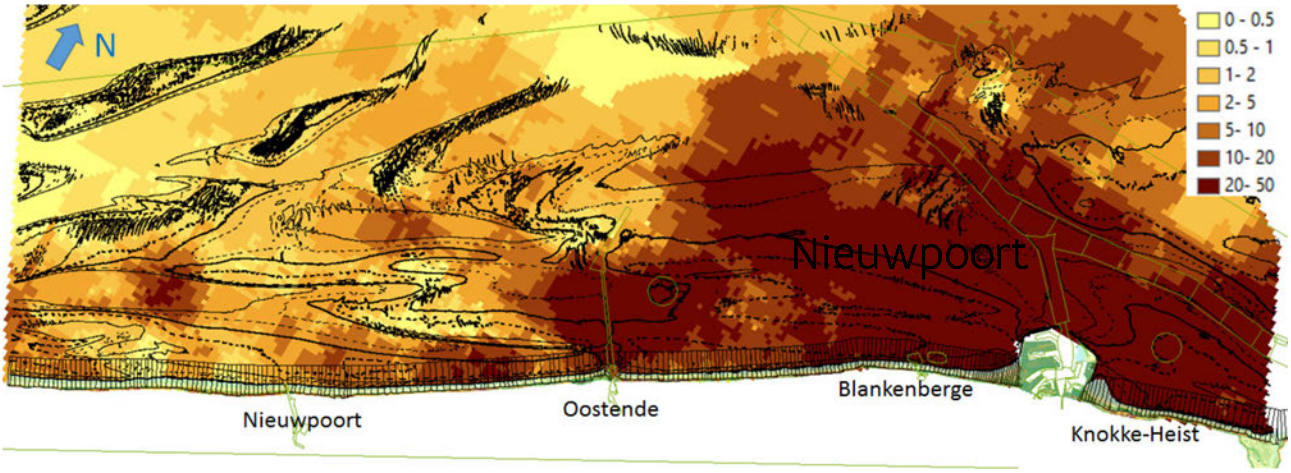

Figure 22 – Silt/clay content of seabed. Source: Verfaillie et al. (2006). Colour classes are mud content in % (see legend).

The maps of Figure 21 and Figure 22 are derived from samples taken over a long time. Some samples may have been taken over a century ago, while the inner shelf is subject to large change due to harbour construction, dredging of navigation channels, etc. The map interpolates the area between the data points. The interpolation was bathymetrically steered. It is remarked however that bathymetry in the inner shelf is often flat and therefore gave poor guidance to the interpolation.

The maps demonstrate the sandy nature of the inner shelf bed. The sandbanks are often coarser grained than the channels between them. Overall, the grain size fines towards the area of Zeebrugge and the Westerschelde Mouth. The mud content increases in the same direction. Mud content is also higher in the channels between the sandbanks. Some sandbanks are shown to have a high mud content on their top where this probably is not the case in reality (e.g. Wenduine Bank, Paardenmarkt). This may be an interpolation effect. MUMM currently prepares an update of the seabed grain-size map.

2.4 Analysis of representative contour lines displacement through time in relation with the evolution of the Belgian coast

When looking at the trends per section or coastal stretch (Houthuys et al., 2022), it appears that about three quarters of the Belgian coast shows erosion, while the remaining quarter accretes. This result is valid for the observed volume time series as well as for the corrected volumes. The image may be biased, as trend periods were typically chosen to start just after a nourishment in areas where beach nourishments take place. Nevertheless, these replenishments are often needed to compensate for erosion, so it is probably correct to state that the Belgian coast is largely erosional. The active zone though expanded nearly gradually over the last 30 years by about 300 m^3/m in the layer above low water and by about 150 m^3/m in the layer below low water, averaged over the entire coast (Houthuys et al., 2022). Calculating with an active profile height of 11 m, this growth corresponds with a generalized seaward progradation of about 40 m.

As this is an averaged result, it is interesting to find out which parts of the Belgian coast experienced most progradation. In this section, a bird's eye view of the major developments at the Belgian coast on a decadal scale is proposed using the geographical shift through time of a set of contour lines thought to be representative of the active zone (i.e., the -5.11 m, -2.11 m, +1.39 m and +6.89 m TAW contour lines).

It would be interesting to add the +4.39 m contour line as well, but this would crowd the represantations at the scale of the current analysis, The position of the selected contour lines was determined for 1983 (1984/87 for the nearshore part – the exact position may still change depending on the choice adopted to correct the 1984/87 depth model) – 1992 (note: beach part is being processed, contour lines will follow in next year's report) – 2000 – 2012 and 2022. Each time, the spring elevation model was used, except for 2000, where we only have the September DEM.

In Figure 23 to Figure 27, the time dimension is shown by colour:

- 1983/1984/1987: blue
- 1992: green
- 2000: orange
- 2012: red
- 2022: black

The representative contour lines are displayed using different line styles:

- -5.11 m: long dashes
- -2.11 m: short dashes
- +1.39 m: full line
- +6.89 m: short dashes

In Figure 23 to Figure 27, the red and green arrows highlight a significant and consistent shift in the location of the representative contour lines. The arrows are red if the shift is associated with erosion and green if it is accompanied by accretion. The figure next to the arrow mentions the approximate amount of contour line shift since the 1980s, in m.

2.4.1 West Coast: French border to Nieuwpoort

Potje and Broers Bank shift NE-wards. The top of Broers Bank builds outwards: it benefits probably from the erosional shift of Potje channel. West of Broers Bank, Potje encroaches on the shoreface. The beach west of De Panne expands seawards. Similarly, shoreface base and intertidal beach build out at Koksijde-Bad. This is the joint effect of two long groynes built in the 1980s and nourishments mainly at Sint-Idesbald. The beach east of Koksijde-Bad accretes. This was interpreted as natural growth where sand supply follows a transport path along Broers Bank. However, the wide shoreface Den Oever recedes gradually.

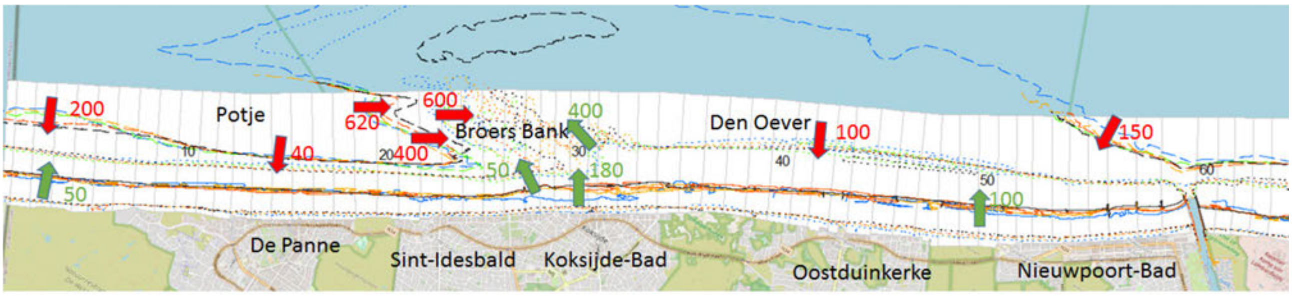

Figure 23 – Decadal shift of representative contour lines at the West Coast.

2.4.2 Middle Coast: Nieuwpoort to Oostende

From Nieuwpoort to Oostende, the beach has expanded while the shoreface base retreated landwards. The amount of retreat is equal over this 16 km coast stretch. The low-water mark remained at the same position between Nieuwpoort and Middelkerke, save at two locations where around 1990 groynes have been expanded seawards. Where nourishments have maintained the beach at Westende and Middelkerke, from east of Middelkerke to Oostende they realized a beach expansion.

The expansion is at a maximum near Oostende Harbour, where the dams constructed in 2009 blocks the littoral drift. Here, also the shoreface has expanded seawards. Apart from the area near the harbour dam, the shoreface has now a considerably smaller footprint meaning it is steeper now than back in the 1980s.

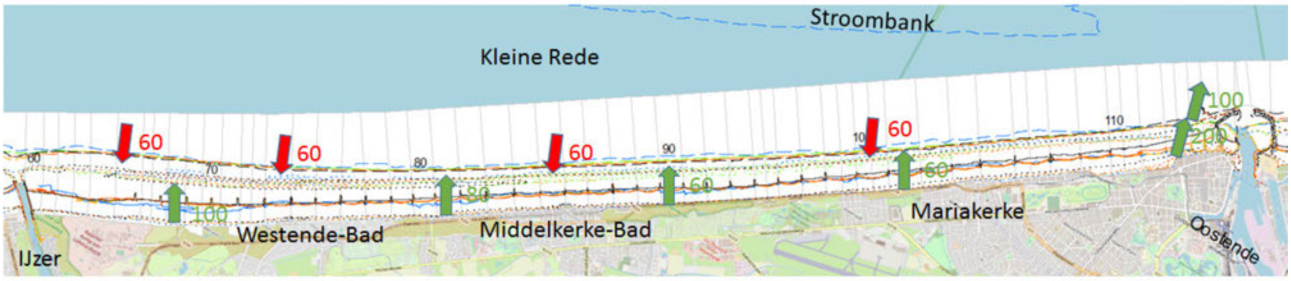

Figure 24 – Decadal shift of representative contour lines at the west part of the Middle Coast.

2.4.3 Middle Coast: Oostende to Blankenberge

Also this 12.5 km long stretch of the coast is characterised by the contrasting evolution of the shoreface base and seabed versus the beach. The channels Kleine Rede and Grote Rede have deepened and the relict of the former connection area of Stroombank to the shoreface east of Bredene is practically gone. Nourishments have kept the low-water mark in place: between Oostende and De Haan, it built 30 m out seawards. The resultant supply due to replenishments at De Haan and between De Haan and Wenduine was larger, resulting in a net seaward shift of the low-water mark by 100 m. The low-water mark at Wenduine is at the same position as nearly 40 years ago, but this status quo required many nourishments. The seaward flank of Stroombank retreated strongly, while the shoreface base east of De Haan also retreated, by about 50 m. Apart from the area near Oostende harbour, the shoreface has now a considerably smaller footprint meaning it is steeper now than back in the 1980s.

Figure 25 – Decadal shift of representative contour lines at the east part of the Middle Coast.

2.4.4 Around Zeebrugge

East of Wenduine, the beach benefited from the nourishments around De Haan. The low-water mark prograded seawards. The progradation at Blankenberge is mainly related to the prolongation of a few groynes. Also, the beach is maintained re-using dredged sand from the local harbour entrance. Disposal of excess dredged sand at 0.5 km seawards of the low-water mark on the seabed explains a westward contour line shift of about 400 m. Seaward of this, in compensation an eastward erosional shift of the -5.11 m contour takes place. The western harbour dam of Zeebrugge blocks the littoral drift and shows a marked accretion of shoreface and beach. The sheltered east of Zeebrugge harbour also attracts sand. This explains the growth of the beach at Heist and the sand shoal off Heist. The seaward shift of the low-water mark just east of Zeebrugge's eastern dam is mainly due to nourishment.

Figure 26 – Decadal shift of representative contour lines around Blankenberge and Zeebrugge.

2.4.5 East Coast

Apart from the accretion off Heist, the seaward shift of the low-water mark at Duinbergen is a recent movement related to the February-March 2021 nourishment there. A landward shift of shoreface and intertidal beach is still apparent at Knokke, in spite of the several maintenance nourishments that have been carried out there. More to the east, between Knokke and Zwin, only the shoreface base has shifted landwards while the beach itself maintained its position. The accretion of beach and shoreface near Cadzand can be related to the recent construction, in 2016, of the marina and dams there. An important and consistent change is the accretion of Paardenmarkt, both landwards and eastwards.

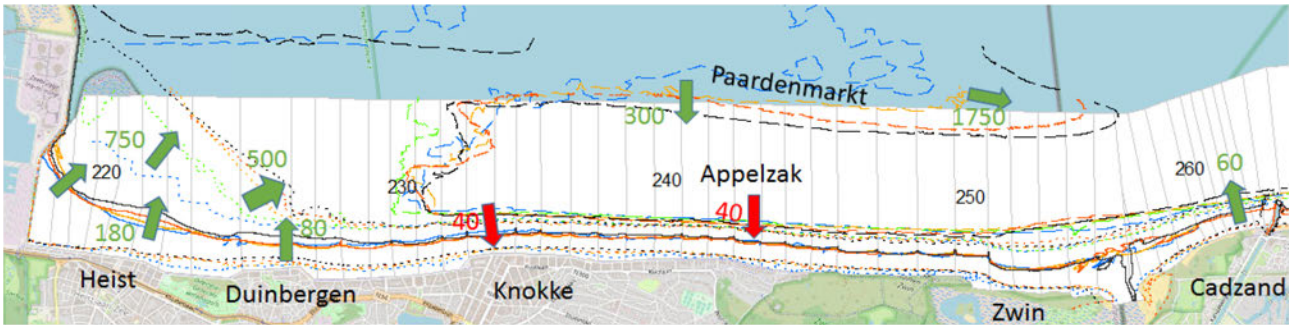

Figure 27 – Decadal shift of representative contour lines east of Zeebrugge.

2.4.6 Steepening of the beach and shoreface profile

Figure 28 shows coast-normal shifts in the location of the representative contour lines (Houthuys *et al.,* 2022): the dune foot (+6.89 m TAW), the low water line (+1.39 m TAW), the lower shoreface (-2.11 m TAW) and the shoreface foot (-5.11 m TAW). For all contour lines derived here above, the intersections with the coast-normal profile locations as defined in the dataset of Bart Roest (2019) were computed. In this way, the representative contour lines are all given a cross-shore distance in respect to the so-called “kilometerpalen lijn”, an old reference for the coastline. The coast-normal shifts are then computed by subtracting the cross-shore location of the representative contour lines in subsequent years. The coast-normal slope (shown in Figure 29) is calculated by dividing the height difference between two consecutive contour lines by their mutual cross-shore distance.

The beach gradient (coast-normal slope) gets steeper from west to east, from about 2% to between 3 and 4% at Knokke. There is no large-scale change in slope trend through time. The upper shoreface has some mildly sloping parts, such as at Koksijde, and around the harbours of Oostende and Zeebrugge. Overall, it displays a characteristic slope of about 1 to 1.5%, that remained constant over the last decades.

The section around Knokke is exceptional, in that the upper shoreface there has a gradient of 3 to 4%, a bit steeper than the 2.5% sloping beach. Also here, there is no large-scale change in gradient through time.

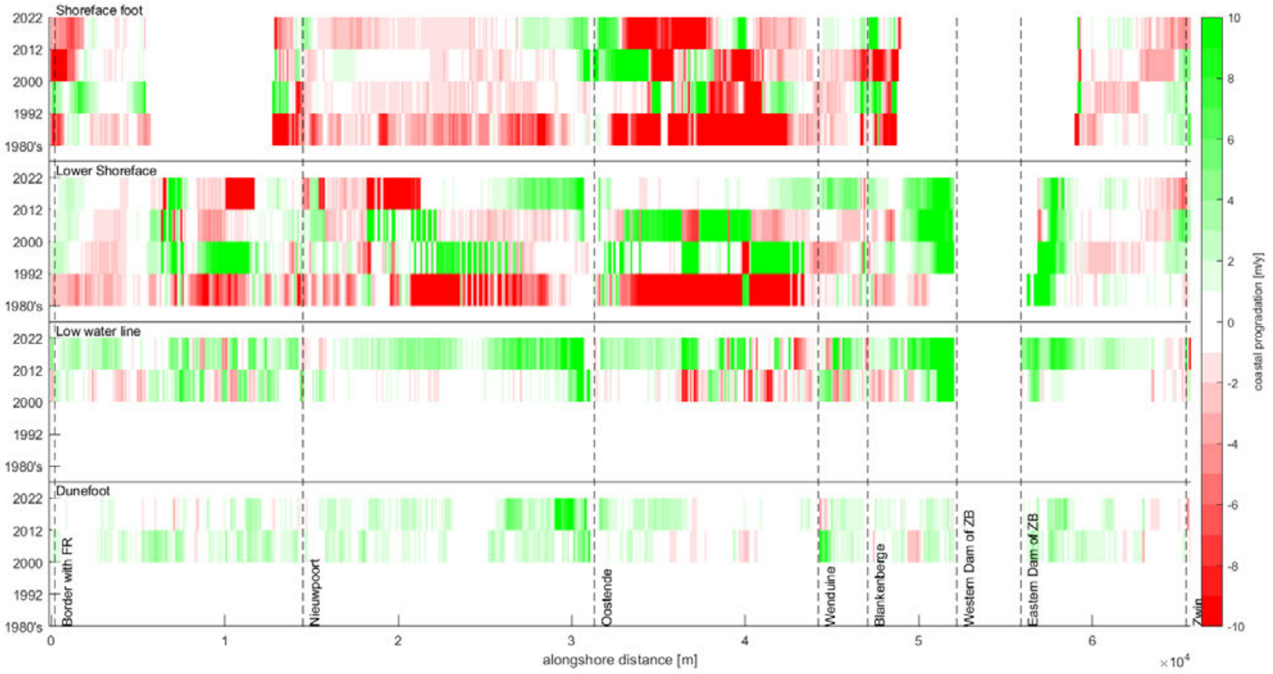

Figure 28 – Progradation of the representative contour lines through time (y-axis). Green: seaward movement (progradation); red: landward movement (erosion).

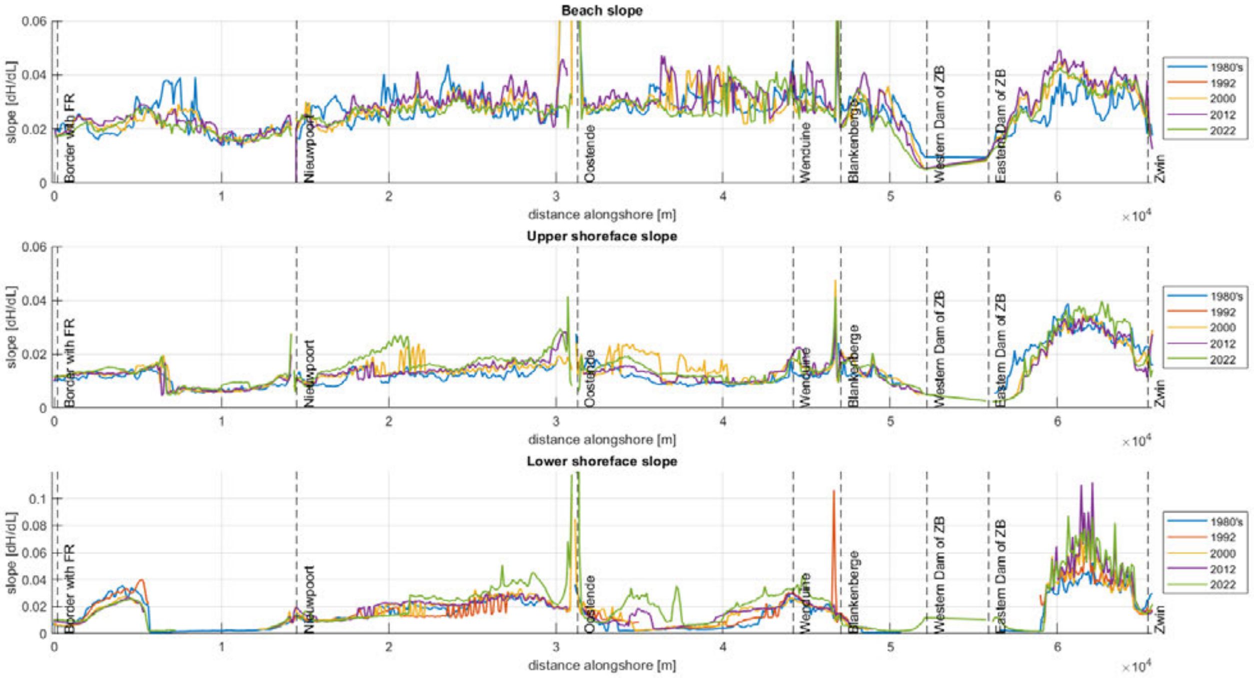

Figure 29 – Slope of the beach (between +6.89 m TAW and +1.39 m TAW), upper shoreface between (+1.39 m TAW and -2.11 m TAW) and lower shoreface (between -2.11 m TAW and -5.11 m TAW).

The most prominent trend is displayed by the lower shoreface. Some zones show a clear trend of steepening over the last decades, most noteworthy between Middelkerke and Oostende, between Bredene and De Haan, and from Wenduine to Blankenberge. The average slope more or less doubled.

At Knokke-Zoute, the lower shoreface has the same steep gradient as the upper shoreface and beach. While the shoreface remained steep over the last decades, the beach slope gradually increased.

2.4.7 Conclusion

The present analysis based on the behaviour of a few representative contour lines complements (in that we have now also 1980s and 1990s geographical coverage) and confirm some of the main conclusions about the coastal evolution (Houthuys et al., 2022).

In one about 7 km long part of the West Coast, between Koksijde-Bad and Nieuwpoort, the beach expands gradually and continuously due to a natural sand supply.

Two strategies of coastal defence had large impacts on the position and evolution of the Belgian coastline: the construction of long groynes and sustained nourishments.

In the 1980s and early 1990s, groynes were constructed or extended seaward at Koksijde-Bad, west of Westende-Bad, between Westende-Bad and Middelkerke-Bad, and at Blankenberge. The morphological response was each time a several tens of metres seaward growth of the beach. The growth occurred in the first years after the groynes' construction, but the effect was durable.

Since the mid-1990s, sand nourishment has been the preferred coastal defence strategy. Almost 20 Mm³ of sand have been borrowed offshore and supplied to the beach. The replenishments invariably suffered erosion, explaining why so much of the Belgian coast shows an erosive trend. The evolution of the representative contour lines shows clearly where this type of intervention stabilizes the coastline, where it caused a net progradation and where erosion keeps encroaching on the coastline. In relation to the west-to-east natural longshore transport, the western sections of nourished beach are always the first to suffer erosion. The eastern sections sustain much longer. The harbour dams of Oostende and Zeebrugge catch much of the eroded sand and cause significant beach progradation in their western lee. At the eastern lee, it is primarily the shoreface that accretes. Looking at the large scale, it can be put forward that most of the nourished sand ultimately remains in the active zone.

Apart from the previous, the sandbank Paardenmarkt off Knokke-Zoute shows landward and eastward accretion.

2.5 Analysis of the morphological evolution in relation to dredging works of the zone around the access channel to Oostende

2.5.1 Introduction

In 2009-2010, a new and deeper navigation channel to Oostende harbour was created by dredging. This "Pas van Stroombank" crosscuts the Stroombank and Kleine Rede channel. Its floor is 1 to 2 m deeper than the Kleine Rede channel floor (Figure 30, Figure 31). It is thought that much of the alongshore sediment transport, both coastal drift and current transport in the tidal channel, is intercepted by the channel. Also, any alongshore transport on Stroombank would be trapped in the channel. The amounts of sedimentation in Pas van Stroombank could therefore provide useful information on the amounts and variations in longshore sand transport.

Since 2009 all dredging activities on the Belgian continental shelf have to report online and continuously during operations to the BIS (Bagger Informatie Systeem) database. This is an electronic navigation and recording system used to plan, monitor and verify dredging operations. It contains three software components: (1) for planning a dredging trip, (2) for on-board recording and (3) for processing and reporting the data. BIS calculates from the on-board measurements the location and depth of the dredging, the disposal location, and the dredged amounts. BIS records about 6 million measurements per ship per week. The data are added to a database. The standard processing generates reports that summarize the dredging operations. The reports contain several maps: track plots of the dredging route and depth, intensity maps that show where and how much was dredged and dredge head soundings showing the final dredged depth. BIS is operated by the Maritime Access administration. Arrangements were made with Maritime Access (Mr. Laurens Hermans) on 4/04/2023 to facilitate consulting BIS output in a form suited for our study.

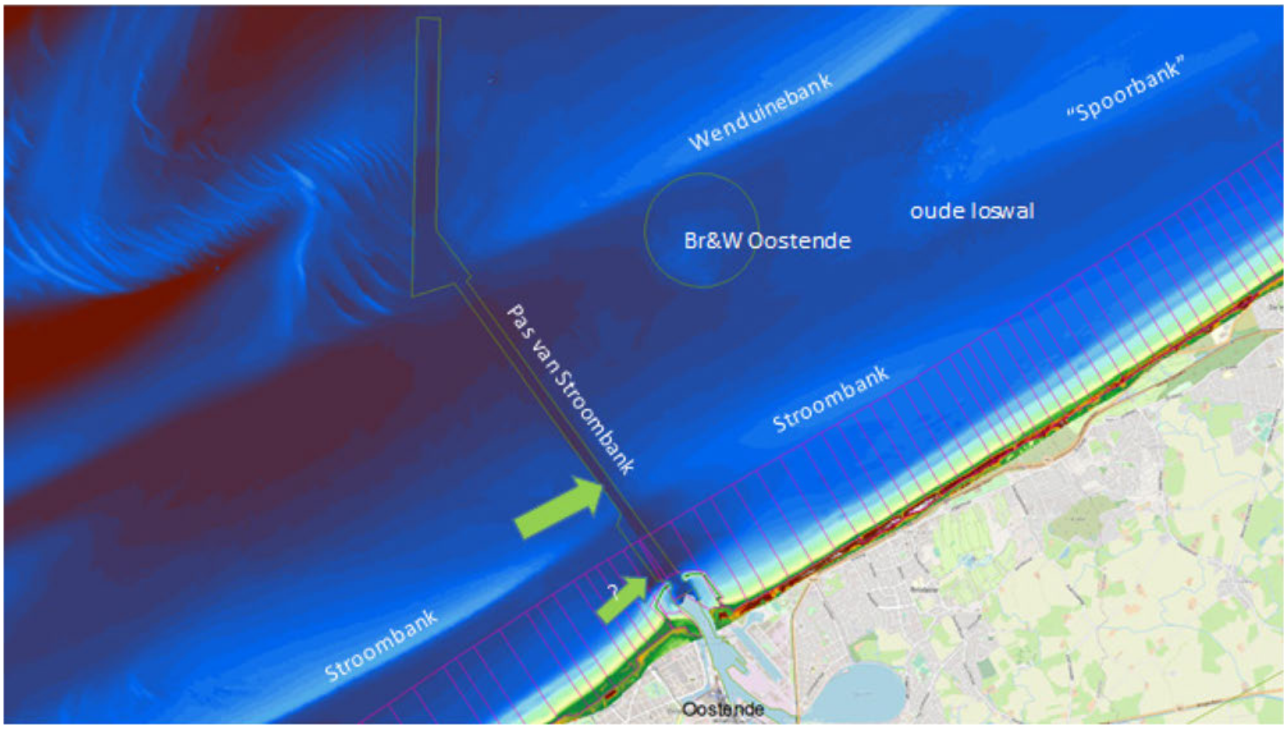

Figure 30 – Locaton of navigation channel Pas van Stroombank, created in 2010. Background is 2022 bathymetry. Green arrows indicated (assumed) sediment transport paths.

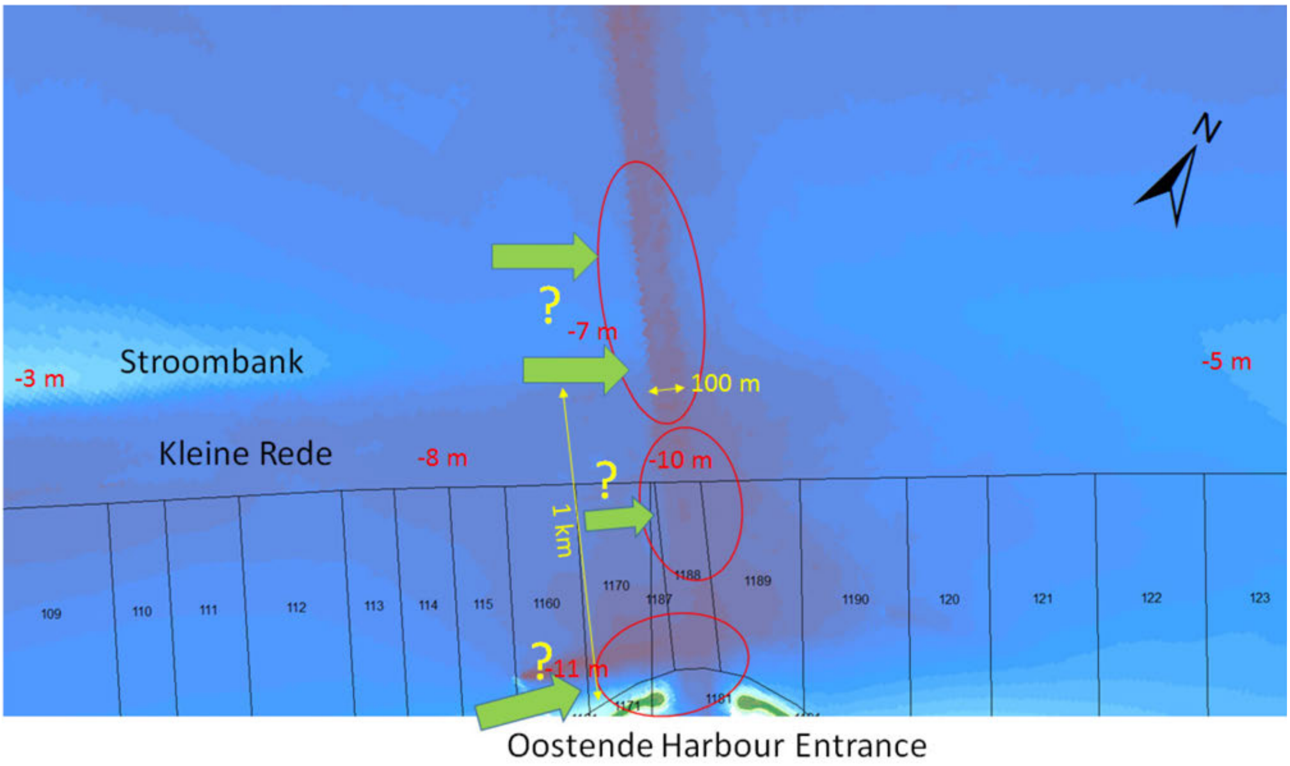

Figure 31 – Zoom on study area.

Green arrows show assumed sediment transport paths possibly feeding the navigation channel. Yellow figures denote distances. Red figures denote depth in m TAW.

As the BIS data density is high, and as a large number of accompanying bathymetric surveys are available, it is hoped that these data can provide quantified insights and geographical differentiation of the natural sediment transport.

Figure 32 illustrates a standard output from the BIS database: a georeferenced raster containing accumulated dredged volumes over a calendar year in 5 x 5 m-cells (here an example for 2022). This map shows larger dredging volumes at the east flank of the channel in the outer harbour, possibly related to works for widening the channel, and also at the western side of the passage through Stroombank.

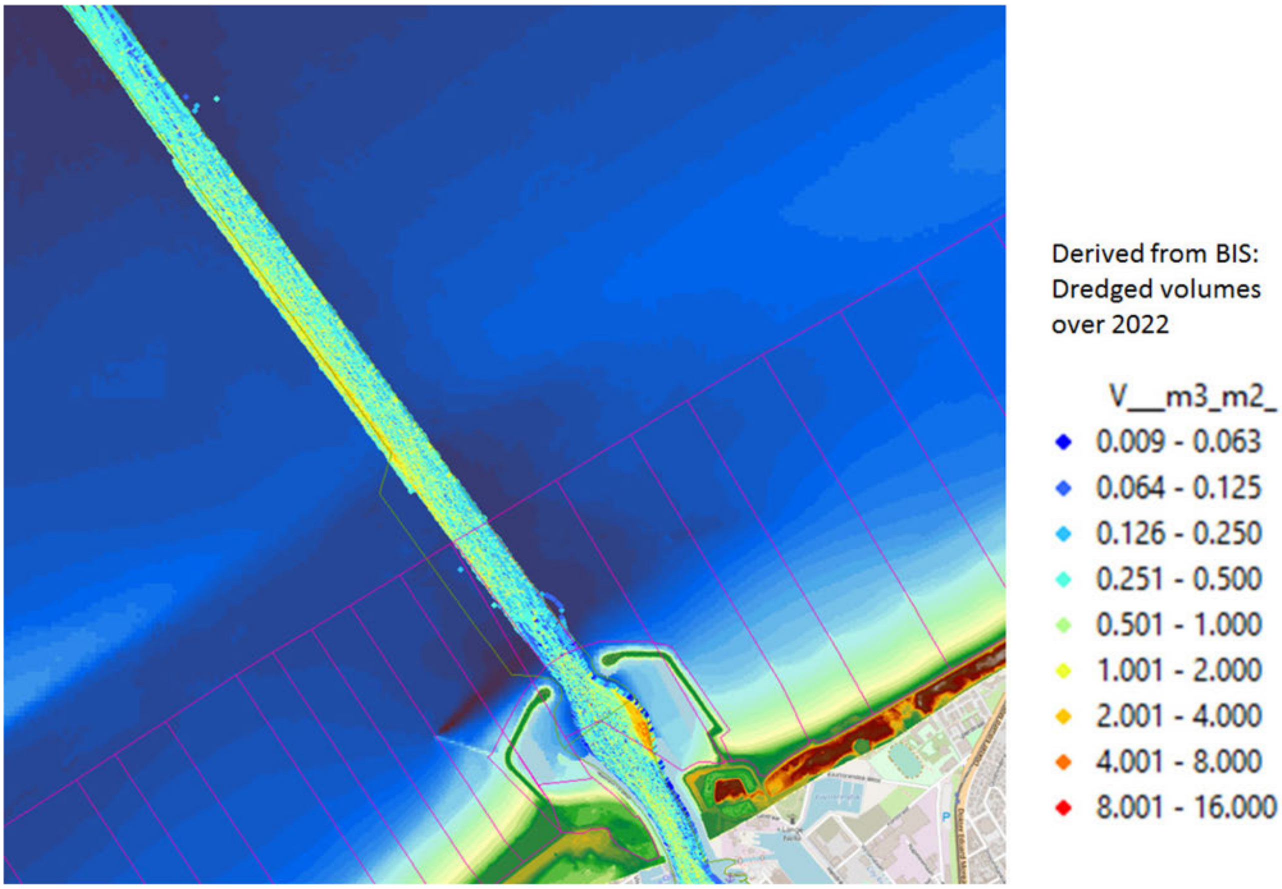

Figure 32 – A standard output of the BIS: dredged volumes accumulated over a year (here 2022) in 5x5 m cells.

2.5.2 Operation of BIS and parameters stored

This description is derived from an internal note from 2008 by Frederik Roose, Maritime Access Division of the Flemish Authorities. To this is added how the BIS parameters are used in this study.

Data acquisition during the dredge trip

A dredging trip has three consecutive actions: dredging, sailing and dumping. At each time, the BIS (Bagger Informatie Systeem) keeps track of the ship's position and its action. During dredging, the pumping speed and concentration of the dredge slurry in the suction pipe is measured. At the end of a dredging trip, the BIS has collected the following relevant information that allows to produce dredging and dumping maps:

- sailed track during dredging
- weight (mass) of the slurry in the ship's hold
- volume of the slurry in the ship's hold
- sailed track during dumping

Weight and volume of the slurry in the ship's hold are measured just before dumping. During this measurement, the ship is halted. The weight of the dredged material in bunker is the difference of the total weight of the vessel (measured by sinkage of the vessel) minus the empty weight of the vessel and the weight of the tanks. The bunker volume is calculated from the acoustic measurement of the clear height above the dredged material.

The 3 parameters below are calculated with the known weight and volume in bunker:

- density of dredged slurry in bunker = weight/volume in bunker
- reduced volume (V' or R) = weight of slurry in bunker – volume of slurry in bunker. The reduced volume V' is defined as the volume of the solid matter V_s when the density of the solid matter (D_s) is equal to 2 t/m³.
- mass of dry matter (TDS) = 2.65 x volume in bunker x [(density in bunker-1.025)/(2.65-1.025)]

Production of dredging and dumping intensity maps

To represent the dredging and dumping data as a grid, the dredging track and dumping site are discretised into 5x5m cells. To create a dredge intensity map, the BIS system distributes the measured quantities (dredge weight, dredge volume, V' and mass of dry matter) among all cells of the dredge track with a distribution coefficient directly proportional to the measured pumping speed and to the concentration of the mixture in the suction pipe. The locations where more dry matter was dredged are proportionally assigned more volume and weight than the locations where less dry matter was dredged. The dredge intensity map obtained in this way is stored. The dump intensity map is obtained by distributing the bunker dredge weight and dredge volume evenly over all cells that make up the dumping location

The weekly dredging and dumping intensity data are obtained by cumulating the intensity data of all trips in that week. The weekly dredging and dumping data are exported from the BIS system.

Format of the BIS exports and derived parameters

The supplied dredging and dumping data are structured in 6 columns. The first two columns are the X and Y coordinate of the respective cell, in the UTM31N ed50 coordinate system. The third and fourth columns contain the weight [kg] and volume [l or dm3] dredged or dumped within the cell in question, respectively. The fifth column contains the reduced volume V' (l or dm3) calculated from the weight and from the volume.

Attention should be paid to this change: up to end 2012, the export parameters from BIS were reported in ton or m³ per 5m x 5m cell. This implies that in order to obtain the weight, volume or reduced volume per m², the value in columns 3 to 5 had to be divided by the area of the cell (5mx5m=25 m²). From 2013 onwards, however, the parameters are reported in ton/m² of m³/m². As a result, in order to obtain cumulated values over several cells, the reported values must by multiplied by the number of cells of the studied area and by the area of the cell, 25 m². The BIS export provided in this project however already incorporated this conversion to grid cell value.

For each 5x5m cell, both the (bulk) density and the mass of dry matter (TDS) can be calculated from the weight and volume. For the density of water, BIS assumes a value of d = 1,025 tons/m³.

The volume of the slurry in the ship's bunker has a lower density then the sediment in-situ, before dredging. It can be assumed that in case of dominantly sandy sediment, that the in-situ density is approximately 2 t/m³. So, the removed volume can be considered equal to the calculated reduced volume V'. In case the sediment before dredging was dominantly fluid mud, the volume V in bunker can be used. To get an idea of the original density, the density of dredged slurry in bunker = weight/volume in bunker is used. Maritime Access uses the following threshold to discriminate between the type of dredged sediment:

- density smaller than 1.4 t/m³: mud;
- density between 1.4 and 1.6 t/m³: difficult settleable sand;
- density more than 1.6 t/m³: sand

2.5.3 Data overview and selection of case study

Selection of case study

In view of the large number of data, a potentially interesting site was selected: the crossing of Pas van Stroombank through the Stroombank sandbank. The research project TESTEREP (https://www.testerep-project.be/nl) collected evidence for a "young" age of Stroombank, meaning it would have developed after 1000 AD. It is also clearly demonstrated that the internal structure of Stroombank consists of large-scale clinoforms dipping eastwards; the dip has both a coast-longitudinal and a coast-normal direction component, implying lateral bank shift towards Zeebrugge and towards the coastline. This is in agreement with the development observed over the last centuries (Houthuys et al., 2021; and the current MOZES project). The "germ" of the sandbank is situated off Nieuwpoort and is partly buried beneath younger sediment. All evidence implies a west to east sand transport path must exist on the seaward flank and crest of the sandbank. The sediment advected via this transport path is assumed to be trapped in the dredged navigation channel Pas van Stroombank. The continuous dredging activities are expected to reflect the ongoing sediment transport.

Also a restriction in time was needed. After internal consultation with the Scaldis-Coast development team, it was chosen to focus on the main calibration time of the Scaldis-Coast model, the years 2014-2016.

Bathymetric surveys

The Flemish Bathymetric Database (TRITON) contains over 800 surveys covering all or part of the Pas van Stroombank and Oostende harbour entrance over the period 2009-2022. From these, a selection was made using the following criteria:

1. the dataset should cover the passage of the navigation channel through Stroombank or the area near the outer harbour dams
2. no disposal site
3. for SB the 210 kHz survey frequency was chosen
4. for MB, points gridded on a 1m-grid were chosen
5. nearshore surveys are already processed and available from coastal morphology projects
6. the study interval was narrowed to 2009-2017.

This reduced the available surveys to 102. A list and naming conventions are given in Appendix 1.

In this project year, the scope was further narrowed to the 2014-2016 period, so as to get a feel with the data and to learn how they can be exploited for morphological research. This further reduced the needed dataset to 26 (see Appendix 1).

A few of bathymetric surveys have been done on the same day, one using SB, the other MB, and partly overlap. In the dataset series used here, one such case was present, i.e. datasets 140402_PVS_SB_210 and 140402_RO_MB_300.

This provided an opportunity to compare them to further document the uncertainty on bathymetric surveying. It appears that depth differences between both simultaneous surveys of 5 to 15 cm occur. The differences are more or less equally spread over the overlapping area, with the SB dataset being on average 0.087 m deeper than the MB data. It is thought that the difference in acoustic frequency doesn't explain the difference in mapped depth. As the average depth difference is within the range adopted for the error on depth measurement, it is treated as such.

Five surveys cover specifically the harbour entrance area. They were processed like the other ones, but were not exploited in this study that focuses on the crossing of Stroombank.

The remaining 20 surveys (taking the two surveys into account that were performed on the same day) define 19 time intervals. These are listed in Table 3.

Survey date	Type	DEM name	DH raster	BIS raster
3/02/2014	MB	g_140200_ro		
2/04/2014	SB	g_140402_pvs	dh140402-0200*	2014_0614
2/04/2014	MB	g_140402_ro	dh140416-0200	
16/04/2014	SB	g_140416_pvs	dh140416-0402**	2014_1416
5/05/2014	SB	g_140505_pvs	dh140505-0416	2014_1719
27/05/2014	SB	g_140527_pvs	dh140527-0505	2014_1921
26/06/2014	SB	g_140626_pvs	dh140626-0527	2014_2226
25/08/2014	SB	g_140825_pvs	dh140825-0626	
15/10/2014	MB	g_141015_ro	dh141015-0825	
7/01/2015	MB	g_150107mb+35	d150107c-1015	2014_2701
20/03/2015	SB	g_150320_pvs	d150320-0107c	2015_0212
23/04/2015	SB	g_150423_pvs	dh150423-0320	2015_1217
30/06/2015	MB	g_150630_ro	dh150630-0423	2015_1827
31/07/2015	SB	g_150731_pvs	dh150731-0630	2015_2731
25/09/2015	MB	g_150925pvsmb	dh150925-0731	2015_3139
22/01/2016	SB	g_160122_pvs	dh160122-0925	2015_4008
10/03/2016	SB	g_160310_pvs	dh160310-0122	2016_0810
9/05/2016	SB	g_160509_pvs	dh160509-0310	2016_1119
22/06/2016	SB	g_160622_pvs	dh160622-0509	2016_1925
4/10/2016	SB	g_161004_pvs	dh161004-0622	2016_2540
15/03/2017	SB	g_170315_pvs	dh170315-1004	2016_4011

Table 3 – List of bathymetric surveys, bathymetric difference (DH) rasters and BIS export rasters used in this study.

There are two surveys on 2/04/2014. *For the bathymetric difference raster with the previous survey, g_140402_ro was used. **For bathymetric difference raster with the next survey g_140402_pvs was used. The names of the BIS rasters contain year and week number (from, to). Per interval, four raster were provided, corresponding to the four export parameters. The raster name was differentiated using the prefix W_ (weight), V_ (volume) and R_ (reduced volume). The TDS parameter was not used in this study. Name of 7/01/2015 raster: the addition "+35" refers to an overall correction made by adding 0.35 m to the depth of this survey (see section 2.5.4). Likewise, the addition of "c" in the name of the DH rasters refers to this correction.

BIS export per survey interval

Spatial grids containing the BIS parameters "gewicht" (Weight), "volume", "TDS" (Ton Droge Stof, Tons Dry Matter) and "gereduceerd volume" (Reduced Volume), in 5x5m-cells, cumulated over the time intervals between the above surveys, were obtained from Maritime Access. The rasters are geoTIFF files, referenced in ETRS89 UTM31N. The number of intervals is 17, as in some intervals no dredging had taken place (Table 3). After evaluating the available BIS parameters, the "TDS" was not used in this study. The raster values express the parameters Weight (Mass) in tons and Volume and Reduced Volume in m^3. They are a sum representing the total value in each grid cell of 5 x 5 m^2.

2.5.4 Methodology of this analysis

In the selected case study, 26 bathymetric survey datasets and 17 BIS export rasters had to be processed (Table 3). This table also lists the intervals between the survey dates, as well as the names of the rasters collected and produced in this study. The research data are available at FH server P:\20_079_MorfoInteract\3_Uitvoering\Deeltaak1_DataAcquisition\CaseStudyPvS.

The bathymetric datasets, for this study converted to Lambert 72 and TAW, were obtained from Hydrography of the Coastal Division. The conversion WGS84 to Lambert 72 was done in the Caris chart system. The conversion LAT to TAW made use of the conversion grid "LATtoTAW_VlaamseBanken_v2".

The point clouds were interpolated on 1 x 1 m^2 cell rasters (DEMs), using TIN interpolation.

Depth difference maps were made for all time intervals using ArcGIS Raster Calculator. For each interval, the initial bathymetric raster was subtracted from the final one. This yields positive depth change values for shallower beds (sedimentation or nourishment/dredge disposal) and negative values for deeper beds (erosion or dredging).

In this study, the value of 0.15 m is used as depth uncertainty on all bathymetric surveys. For depth difference values, this value was multiplied by $\sqrt{2}$ to give an uncertainty of 0.21 m following the rule of error propagation.

The series of depth difference maps showed a remarkable outlier in the 7/01/2015 MB survey of Pas van Stroombank: it is about 0.35 m deeper than both the previous (15/10/2014) and the following survey (20/03/2015). This value is found evenly over the partial areas outside the navigation channel (there the overall change was about 0.25 m, but this channel is subject to strong depth variations due to dredging and subsequent sedimentation). The bias was compensated by adding 0.35 m to the depth value of the 7/01/2015 DEM (this correction is made clear in the DEM name by adding "+35" and in the DH raster names by adding "c", see Table 3. The correction resulted in consistent change, both in the geographic longer-term evolution of the surrounding area and in relation to the BIS reports.

The BIS export rasters relating to the intervals of Table 3 were obtained from Maritime Access.

Possibly due to erroneous on-board measurements, some of the exported rasters contained some cells with negative values, which in areas of dredging should not be the case. They were present in the sets of the parameters "weight", "volume" and "TDS" and should be set to zero. This was done in the sets of the parameters "weight" and "volume" ("TDS" being not used in this study).

In the BIS database, data have been stored per week and can only be exported per week or group of weeks. Due to this restriction, the received export grids of consecutive intervals had often an overlap of 1 week. In order to correct for this (some dredged volumes would in the end balance possibly be counted twice), also the BIS export raster of the separate connection week was obtained. It was evaluated geographically whether this separate week had to be counted with the previous or next time interval. The necessary raster subtractions and/or additions were done so as to obtain non-overlapping grids representing the week intervals listed in Table 3. The export rasters contain NoData cells, where no dredging has taken place in the time interval covered by the raster. In the Raster Calculator operations, NoData is output if one of the input rasters had NoData. Therefore, the NoData cells were first set to 0.

For longer time intervals, it is not known whether dredging was carried out throughout the interval or concentrated in some weeks. It can however be assumed that a control bathymetric survey was carried out soon after dredging, and that consequently the dredging activities probably took place in the last weeks of long intervals.

The grids were made available in ETRS89 UTM31N and had in this project to be projected to Lambert 72.

Most bathymetric surveys cover the navigation channel and about 100 m east and west of it. The study zone was divided in zones of interest, labelled 1 to 14 (Figure 33).

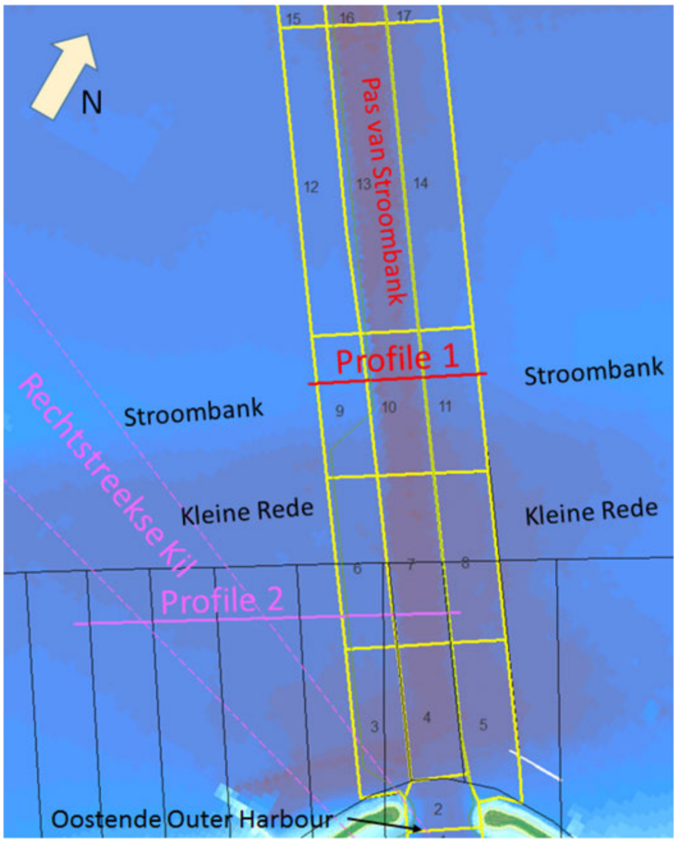

Figure 33 – Subdivision of study area in zones (yellow outlines) and location of the profiles. Thin pink dashed line indicates the former navigation channel Rechtstreekse Kil, abandoned in 2010.

The evolution of bathymetry in the study area and over the study period was visualized geographically using DEMs and Difference of Height (DH) rasters (see Table 3). The successive DH rasters per time interval are gathered in Appendix 2: Analysis results of morphological change and dredged amounts in Pas van Stroombank. The dredging activities per time interval are also displayed geographically using the Reduced Volume values of the BIS export rasters cumulated over the time interval.

To further visualize the morphological change across the Pas van Stroombank, a time series of cross profiles was made on Profile 1 (Figure 33). The evolution is compared with the evolution of the previous navigation channel "Rechtstreekse Kil". This old channel was abandoned in 2010. The evolution of that channel is shown on Profile 2.

Per zone of interest, the sum of DH was obtained using ArcGIS tool "Zonal Statistics as a Table". This sum is the volume difference (DV) between the initial and final survey of each time interval. It is called in this study the "Survey DV".

Per zone of interest and time interval, the sum of the BIS export rasters Weight (W), Volume (V) and Reduced Volume) was made using the same tool.

It was attempted to obtain a measure of dredged sediment density D by calculating D = W / V.

It was remarked that all zones and all intervals in the export rasters provided for this case study yield BIS-densities between 1.2 and 1.3 t/m^3, ranking all dredged sediment as mud. The morphological evolution of the cross section 1 (presented in the next section) implies that at least the area of the Stroombank crossing at the west flank of the navigation channel should consist of sand. But even if inside this area the density is calculated pixelwise in the BIS export rasters, densities of the same range are obtained. Following §2.5.2, all BIS volumes should be taken from the export rasters "volume".

However, "volume" from BIS export yielded values per zone, cumulated per analysis time interval, that were often two to four times greater than the observed volume change from the bathymetric surveys. This inconsistency could not be explained straightforward, even after analysing variations per zone and in function of the interval duration. It is concluded for now that the method adopted to calculate density from BIS weight and volume is, at least over the study area and period, not valid to derive in-situ removed volumes.

It was subsequently observed that "reduced volume" yielded much better agreement with the observed volume change from the bathymetric surveys. Both volumes are of the same order per zone and per time interval.

So, density was neglected and throughout this study, the BIS parameter "reduced volume" is considered as representative of the volumes removed by dredging and thus representative for this morphological study.

2.5.5 Analysis results

Evolution of a cross section of Pas van Stroombank

Figure 34 displays a time series of cross profiles situated on Profile 1 (see location in Figure 33). The profile is located at the intersection of the navigation channel with the shallowest part of Stroombank. Depths are in m TAW and profile distances are in m from the western end of the profile line eastwards. This time series focuses on 2014, featuring more frequent profiles for that year, as it shows the response of the navigation channel morphology on a widening created by dredging the western flank of the channel. The profiles after 7/01/2015 were selected each time before a dredging campaign, so that the morphology is shown in its best state of morphological repair after dredging.

The profiles of 3/02/2014 and 2/04/2014 show the channel before widening. It was about 100 m, had its bottom at about -9.2 m TAW and had a steep (about 7.5%) western flank where the channel crosses Stroombank. The eastern flank is less steep (about 1.1%) except the lower metre which was as steep as the western flank.

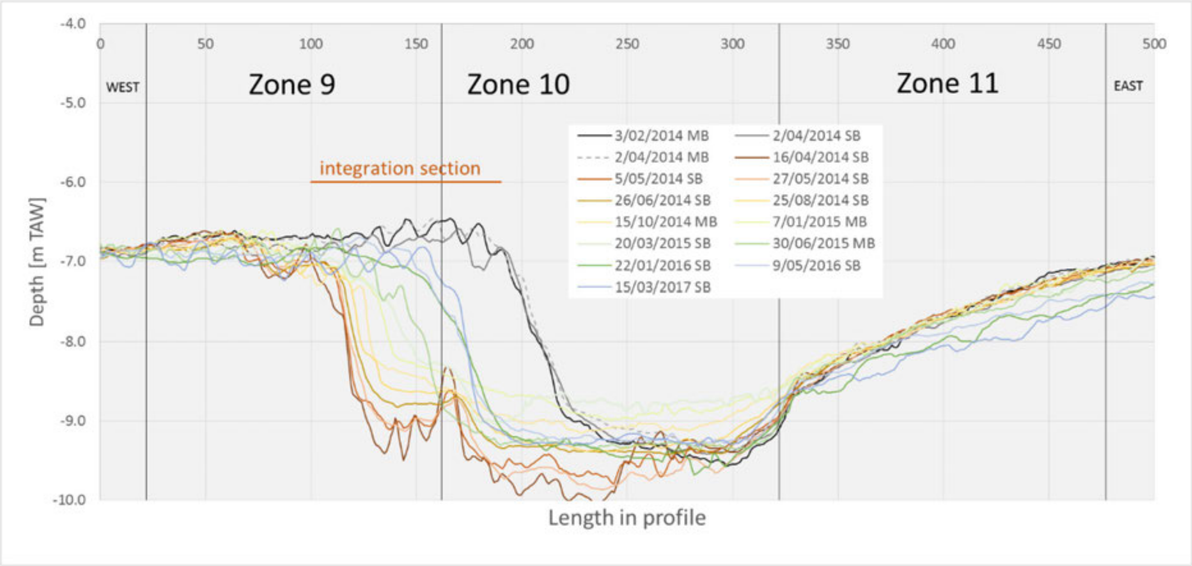

Figure 34 – Time series of profile 1 (see location in Figure 33).

On 2/04/2014, two bathymetric surveys were conducted, one using SB and the other using MB. Profiles derived of both surveys are displayed in Figure 34 to illustrate another time the uncertainty on bathymetric measurement. Overall, the agreement is good (average depth difference over profile is 0.103 m, with MB shallower throughout the profile regardless of the morphology and hence probably of the bed sediment type). Part of the difference may be due to the denser spatial coverage of the MB survey. Part may also be due to the different used acoustic frequency (210 kHz for SB and 300 kHz for MB). Finally, the inherent uncertainty due to different survey settings, conditions and processing discussed earlier remain contributing to the uncertainty.

Between 2/04 and 16/04/2014, the navigation was expanded to the west by 90 m and deepened in the centre to -10 m TAW. This was done by dredging.

Over the following months, the western flank gradually and consistently shifted eastwards while the channel bed filled. The small ridges present on the bed of the widened channel, especially in the surveys short after the dredging campaign, are most probably due to the morphology created by the dredging activity. The rate of eastern displacement of the channel flank was more or less constant between 16/04/2014 and 7/01/2015. The channel bed shallowed quickly after the deepening and reached its shallowest depth of the study period at between -8.8 and -9.0 m TAW. Between 7/01/2015 and 30/06/2015, both the base of the western flank and the channel bed were deepening by dredging. The dredging restored 50 m of the earlier 90 m of widening and replaced the bed at about -9.2 m TAW.

The eastward growth of the western channel flank can only be due to sand transport over the top of Stroombank feeding the western channel flank. During the process of flank shift, its slope remains steeper than the initial 7.5%, even up to 10%. Such slopes can only be maintained in sand.

The fill of the channel bed may consist of deposition of suspended fine sand and of mud, as the bed morphology before each dredging campaign is nearly flat.

The eastern channel flank maintains its slope, but it recedes also eastward. This may be explained by a lack of sandy sediment available to rebuild the isolated part of Stroombank east of the channel. As a result, the east slope deepened by more than 0.5 m over two years.

Dredged and surveyed volumes per zone

Volume differences of the analysis zones were computed for all analysis time intervals from the bathymetric surveys on the one hand, and on the other from the BIS export rasters. For the latter, the parameter "reduced volume" was used.

The computation results are added in Appendix 2. This contains for each bathymetric survey interval a map showing the BIS export raster over the same interval (parameter Reduced Volume), a map showing the bathymetry difference over the interval (most recent minus earlier survey), and a table containing (1) the volume difference (DV) per analysis zone, (2) the area of the part of the zone covered jointly by the survey before and after the interval, (3) the uncertainty of the corresponding volume difference (obtained by multiplying the covered area of the analysis zone by $\sqrt{2} \cdot 0.15$), and (4) the average depth difference over the interval, all (1) to (4) derived from the after minus before bathymetric survey difference map; and (5) the volume and (6) type of dredged matter derived from the BIS export rasters.

The type of dredged matter is in all export rasters in all zones mud, according to the criteria described above and applied on density obtained by dividing weight by volume. This result is considered to be not valid for the study area and study period of this report; it was derived from the morphological evolution on the cross section that at least in some areas and intervals sand has been dredged. The reason for this discrepancy has not further been investigated.

In this section "Survey DV" is short for the volume difference derived from the initial and end survey of each analysis time interval inside each analysis zone. Positive DV means sedimentation, negative is erosion or bed deepening due to dredging. "BIS DV" is the dredged volume, reported by BIS, such as derived from the BIS export raster (parameter "reduced volume") inside each analysis zone.

Figure 35 shows the volume evolution over time of analysis zones 6 to 14, near the Stroombank crossing. On the year scale, the volumes remain constant. They vary especially in zones 7, 10 and 13: the navigation channel. The volume tends to increase and is at irregular times set back by dredging (the end of each dredging campaign is shown by vertical lines).

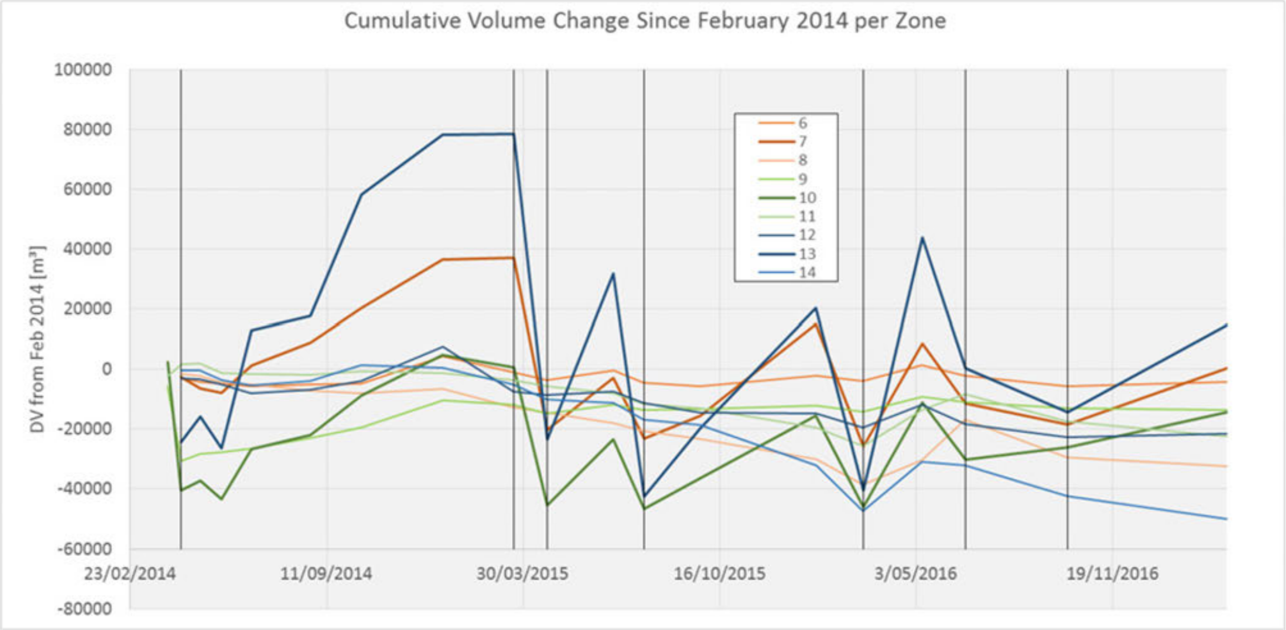

Figure 35 – Cumulative volume change over time per zone. Vertical lines show the end of each dredging campaign affecting the area..

Table 4 summarizes the main dredging campaigns and the sum of dredged volumes and volume change from the bathymetric monitoring over the study period. Dredged volumes total mostly between 30,000 and 90,000 m³ and once exceeded 200,000 m³. There is a close spatial correspondence between dredging locations and bed change (see successive BIS and Survey DV maps in Appendix 2). The agreement in volume change derived from bathymetric surveys ranges from very good to opposite.

Table 4 – Summary of dredging campaigns and related volume change.

Dredging campaign no.	Date of survey before campaign	Date of survey after campaign	Areas affected by dredging	Type of dredging	Total BIS (reduced) volume [m³]	Total before and after survey volume difference [m³]	Agreement in volume change
1	2/04/2014	16/04/2014	9, 10, 13	west flank widening	90 500	-109 300	good
2	7/01/2015	20/03/2015	10, 13	base of west flank	40 500	-3 800	bad
3	20/03/2015	23/04/2015	7, 10, 13	channel bed	208 200	-205 100	very good
4	30/06/2015	31/07/2015	7, 10, 13	channel bed	86 300	-117 800	moderate
5	22/01/2016	10/03/2016	4, 7, 10, 13	W flank and channel bed	86 200	-146 800	moderate
6	9/05/2016	22/06/2016	7, 10, 13	west flank	70 500	-82 400	good
7	22/06/2016	4/10/2016	13	channel bed	31 000	-14 600	moderate
8	4/10/2016	15/03/2017	7, 10, 13	channel bed	34 400	59 600	opposite

Figure 36 details the volume change per time interval for all available surveys in the zones affected by dredging, i.e. zones 4, 7, 9, 10, and 13. The major influence of dredging is in zones 7, 10 and 13 as they were defined in the navigation channel. The magnitude of the volumes depends (among other things) on the area of the zones: 13 is the largest, then comes 7, and finally 4, 9 and 10 with about equal areas.

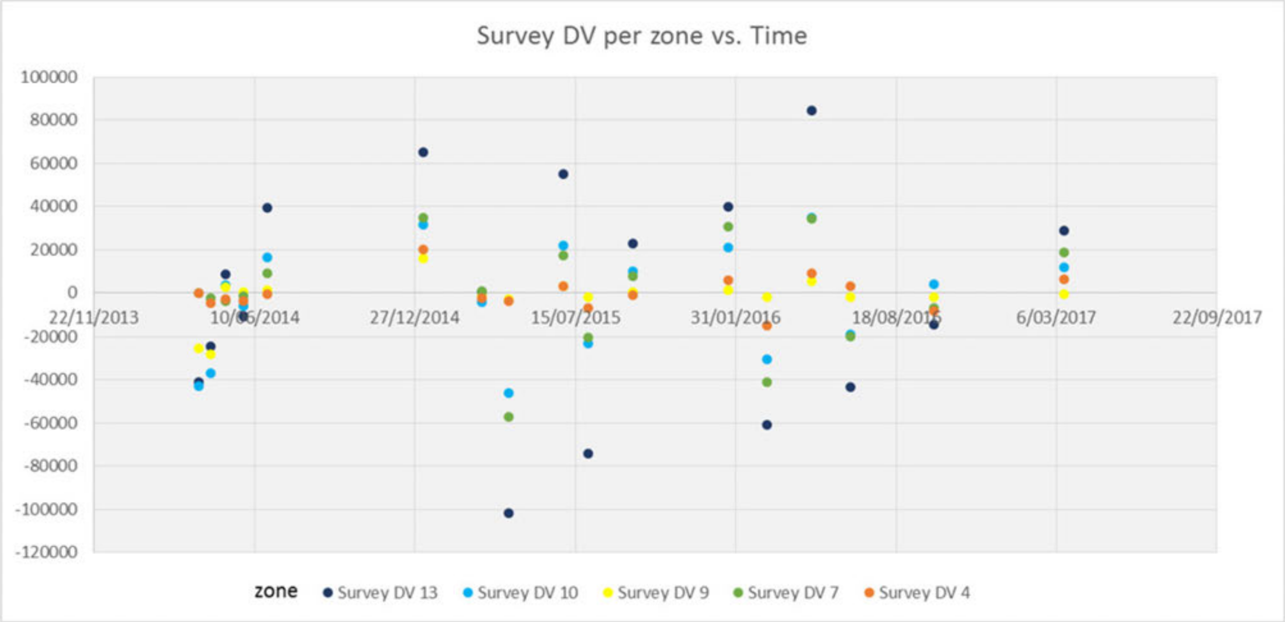

Figure 36 – Volume difference (each time difference with previous survey) per zone, derived from the successive surveys.

Comparing Figure 36 with Figure 37 shows that each setback in volume is due to dredging. Overall, the volumes from BIS and the bathymetric surveys are in good agreement.

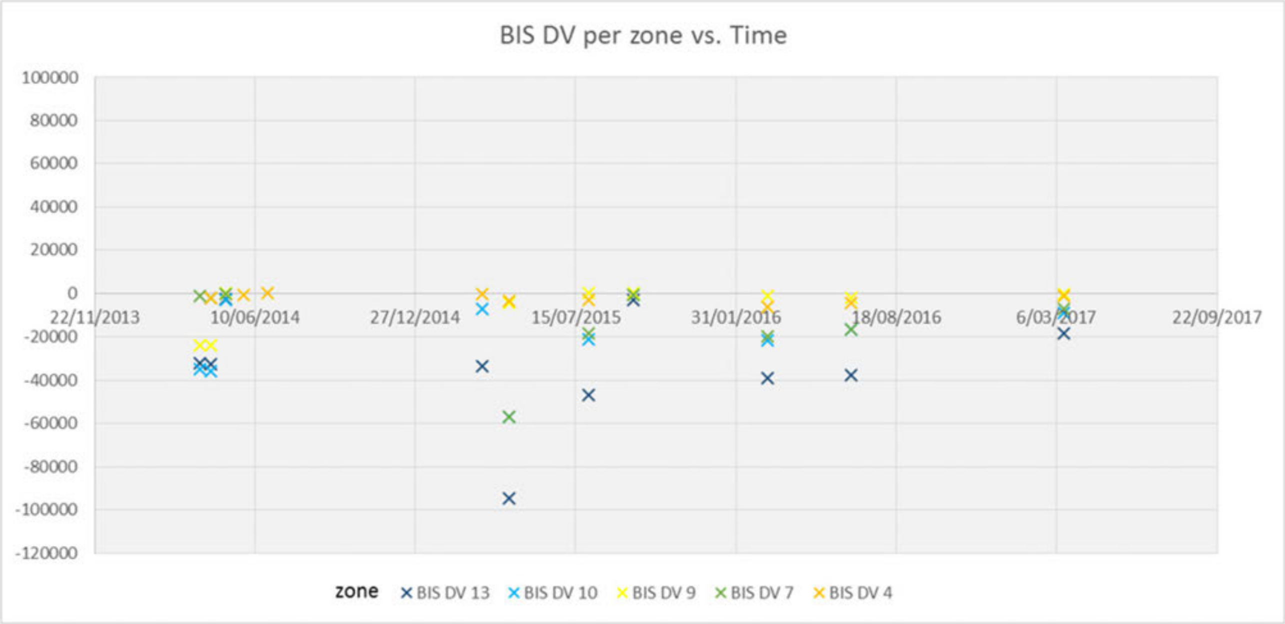

Figure 37 – Dredged volumes reported from BIS, summarized per zone and shown at the and of each dredging campaign..

The volume decrease computed from the bathymetric surveys are generally greater than the reported BIS volumes when they are large (dots in left half of Figure 38). Smaller dredged volumes either match well with the survey volume differences or have bed accretion (dots right of Y axis in Figure 38). This may be explained by the error on bathymetric surveying, whose effect is smaller in zones with a large area, and by sedimentation that occurs before or during dredging. The latter happens in some time intervals, and may even be considerable in short time intervals, probably depending on hydrodynamic conditions.

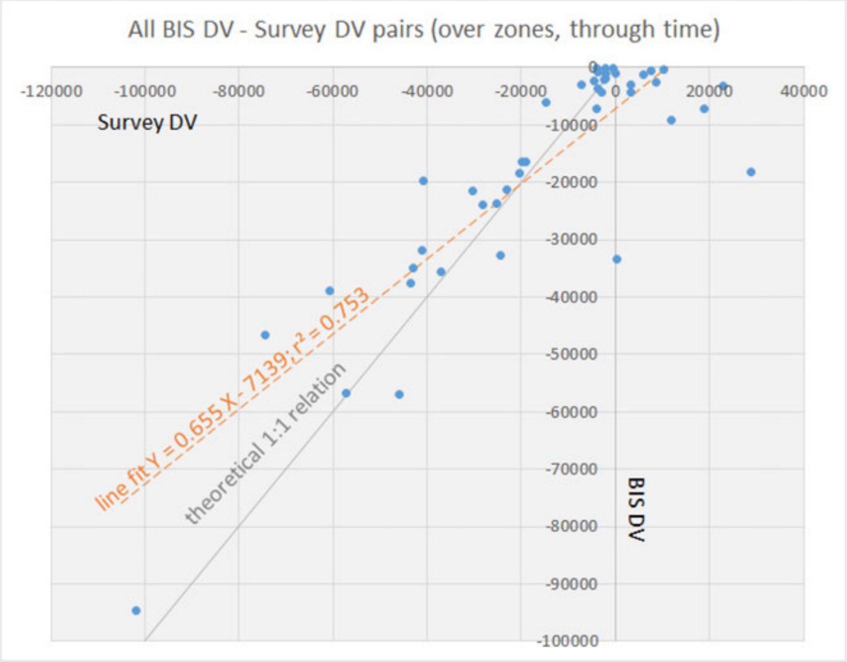

Figure 38 – Scatter plot of all BIS DV – Survey DV pairs available in the study area and period.

The overall good match between Survey DV and BIS DV gives confidence that BIS exports of reduced volume provide good information on amounts and location of bed sediment removed by dredging. The residual between known dredged amounts and observed bed volume change per zone could be further interpreted to provide information on temporary transport phenomena.

From these deviating intervals, and all the intervals where no dredging took place, it is observed in the present case study that two sedimentation regimes appear to be active in the Stroombank crossing channel: one involves western flank sedimentation, the other is spatially expansive sedimentation in almost equal vertical amounts spread across the navigation channel floor. Western flank sedimentation was observed between the surveys of 16/04/2014 and 5/05/2014, 26/06/2014 – 7/01/2015, 31/07/2015 – 25/09/2015, 25/09/2015 – 22/01/2016, 22/06/2016 - 4/10/2016 and 4/10/016 – 15/03/2017. Expansive channel bed sedimentation occurred in the survey intervals 27/05/2014 – 26/06/2014, 26/06/2014 – 7/01/2015, 23/04/2015 – 30/06/2015, 25/09/2015 – 22/01/2016, 10/03/2016 – 9/05/2016 and 4/10/016 – 15/03/2017. Some intervals show both types of sedimentation regime. The spatial distribution pattern and the profile analysis above strongly suggest that western flank sedimentation is sand carried in from the west, over the flank and crest area of Stroombank and trapped at the western slope of the navigation channel. The expansive channel floor sedimentation is probably a combination of fine sand carried in from suspension and fluid mud.

Transport estimated over the cross-section

Here, an estimation is made of the longitudinal bed transport causing the sedimentation at the western flank of Pas van Stroombank from the time series of bathymetric profiles.

The volume between the successive bed profiles of Figure 34 was integrated over the section between distance 100 and 190 m, like indicated in the figure. In this section, the accretion can be interpreted to be natural sedimentation of largely longitudinal bed transport along the crest of Stroombank. When divided by the time interval over which this accretion occurred, it provides a measure for the longitudinal bed transport over Stroombank, per transversal unit metre. The results are listed in Table 5.

Table 5 – Volume change in the integration section of profile 1 across Pas van Stroombank (see Figure 34).

Survey Date	DV [m³]*	Uncertainty on DV [m³]	Cum. DV [m³]	Transport [m³/m/year]	Notes
3/02/2014	0		0		
2/04/2014	-1.2	19	-1.2		
16/04/2014	-192.9	19	-194.1		dredging campaign
5/05/2014	11.5	19	-182.6	*221*	DV < uncertainty
27/05/2014	4.1	19	-178.5	*68*	DV < uncertainty
26/06/2014	16.5	19	-162.0	*201*	DV < uncertainty
25/08/2014	13.9	19	-148.1	*85*	DV < uncertainty
15/10/2014	11.0	19	-137.1	*79*	DV < uncertainty
7/01/2015	20.4	19	-116.7	89	over four months
7/01/2015	77.5	19	-116.7	**106**	sum over grey interval
20/03/2015	3.7	19	-113.0		part of section dredged
30/06/2015	0.6	19	-112.4		part of section dredged
22/01/2016	43.1	19	-69.3	**76**	over half year
9/05/2016	5.0	19	-64.3	*17*	DV < uncertainty
15/03/2017	-3.4	19	-67.6		part of section dredged

*Volume difference (DV) is each time between the survey and the previous one. For the 7/01/2015 survey, an additional DV is added summarizing all accretion of the lines in light grey, between 16/04/2014 and 7/01/2015. The uncertainty on DV is obtained by multiplying the length of the integration section by $\sqrt{2} \cdot 0.15$. Transport intensity over a year is calculated by $DV \cdot (number\ of\ days\ in\ a\ year)/(survey\ interval\ in\ days)$. If DV is smaller than the uncertainty, the corresponding transport is in italics.

The widening and deepening of the channel between 2/04/2014 and 16/04/2014 involved the removel of almost 200 m³/m. This removal of bed material created an accommodation space for the longitudinal bed transport along the crest of Stroombank.

The calculated transport fluctuates largely. The uncertainty on depth measurement and the sometimes short time intervals may partly explain the observed fluctuations. When integrated over the interval 16/04/2014 – 7/01/2014, all partial contributions are added to obtain a significant accreted volume, accumulated during more than half a year in a period without dredging. The transport is ~100 m³/m/year. Another value was obtained over the interval 30/06/2015 – 22/01/2016 and was ~76 m³/m/year.

If dredging would be interrupted in the crossing of Pas van Stroombank, the bank morphology can be expected to be restored in a matter of 5 to 10 years, completely closing the navigation channel. The east side of the navigation channel shows erosion, most likely related to depletion of the longitudinal transport (everything is trapped in the channel and removed by dredging). This depletion would be healed.

In order to validate the obtained transport, use was made of the swift natural filling of the abandoned old navigation channel "Rechtstreekse Kil" in 2010 (Houthuys et al., 2022). This navigation channel was a more westerly approach to Oostende harbour and obliquely intersected Stroombank and Kleine Rede (see approximate location in Figure 33). After the creation of the new access channel Pas van Stroombank, the old channel was just abandoned, i.e. it was not artificially filled but left to fill by natural sedimentation. The fill was very fast: after one year, the channel that initially had its bed 1.5 m deeper than the Kleine Rede, was filled. A profile line was selected parallel to the coast and the assumed direction of the longitudinal transport (see Figure 33). This line crosses the axes of Rechtstreekse Kil obliquely. The profiles are displayed in Figure 39. This figure also shows that the creation of the new Pas van Stroombank started before the Spring 2010 survey and created a crossing with a bed about 2 m deeper than Kleine Rede.

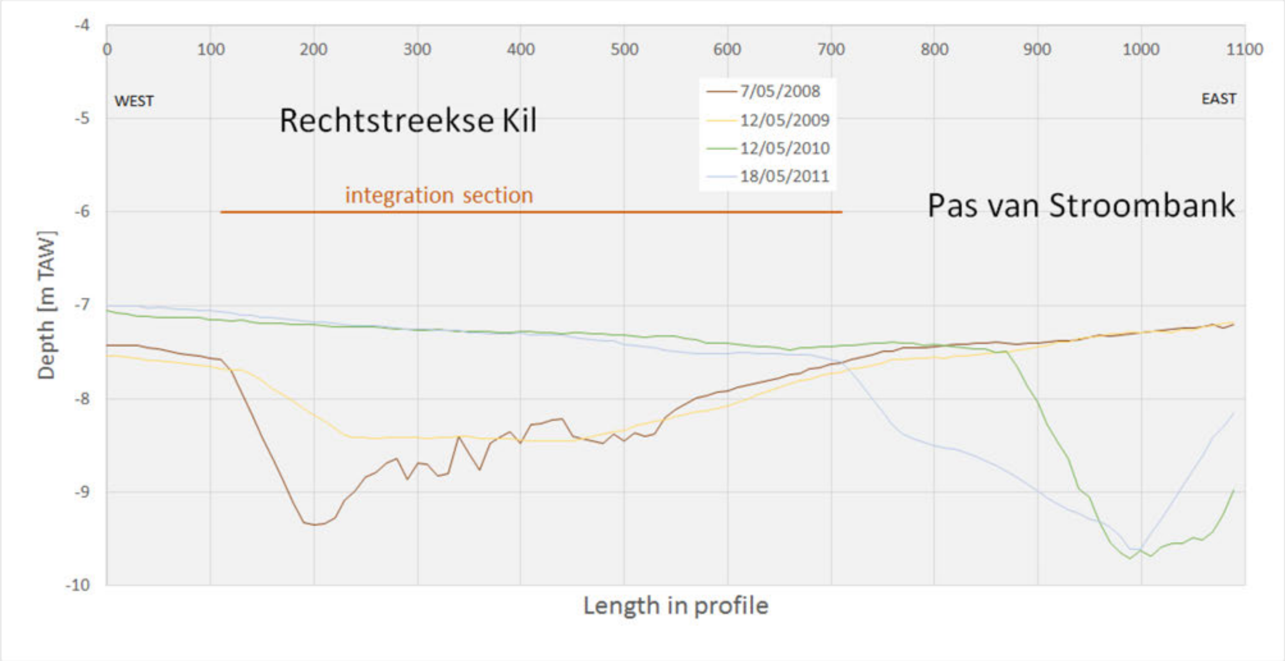

Figure 39 – 2008-2011 time series of profile 2 (see location in Figure 33).

The eastern slope had in 2008 a gradient of about 3% (perpendicular to the axis of the channel) while the eastern flank was about 0.5%. The channel probably incised in sand, but the fill may also have been muddy.

The calculated volumes and transport values are listed in Table 6. The integration section is 600 m long (see Figure 39). The precise time of the fill is less well confined than in the above analysis of Pas van Stroombank, as we only have the Spring Nearshore SB surveys with each time a year interval.

Table 6 – Volume change in the integration section of profile 2 across Rechtstreekse Kil (see Figure 34).

Survey Date	DV [m³]*	Uncert. [m³]	Cum. DV [m³]	Transport [m³/m/year]	Notes
13/05/2008	0		0		
20/04/2009	109.8	126	109.8	*117*	period unknown, probably only part of year
12/05/2010	538.0	126	647.7	**508**	good estimate
23/05/2010	647.7	126	647.7	**325**	good estimate
18/05/2011	-20.8	126	626.9	-20	stability reached

*Volume difference (DV) is each time between the survey and the previous one. For the Spring 2010 survey, an additional DV is added summarizing the accretion of the lines in light grey, from Spring 2008 to Spring 2010. The uncertainty on DV is obtained by multiplying the length of the integration section by $\sqrt{2} \cdot 0.15$. Transport intensity over a year is calculated by $DV \cdot (number\ of\ days\ in\ a\ year)/(survey\ interval\ in\ days)$. If DV is smaller than the uncertainty, the corresponding transport is in italics.

It can be concluded that ~400 m³/m/year is a good estimate of the longitudinal bed transport in the Kleine Rede. This would be about 4 times greater than on Stroombank. It is probably muddy sand or sandy mud, while most of the transport on Stroombank is thought to be sand.

The results agree well with longitudinal transport modelled in Scaldis-Coast and FlemCo (Figure 40). Transport rates at the Stroombank crossing are about 70 to 145 m³/m/year in Scaldis-Coast and 95 m³/m/year in Flemco. Calculations in Kleine Rede are about 120 m³/m/year in Scaldis-Coast and 185 m³/m/year in FlemCo. The agreement raises confidence in the modelling of (mainly tidal) longitudinal transport by the models.

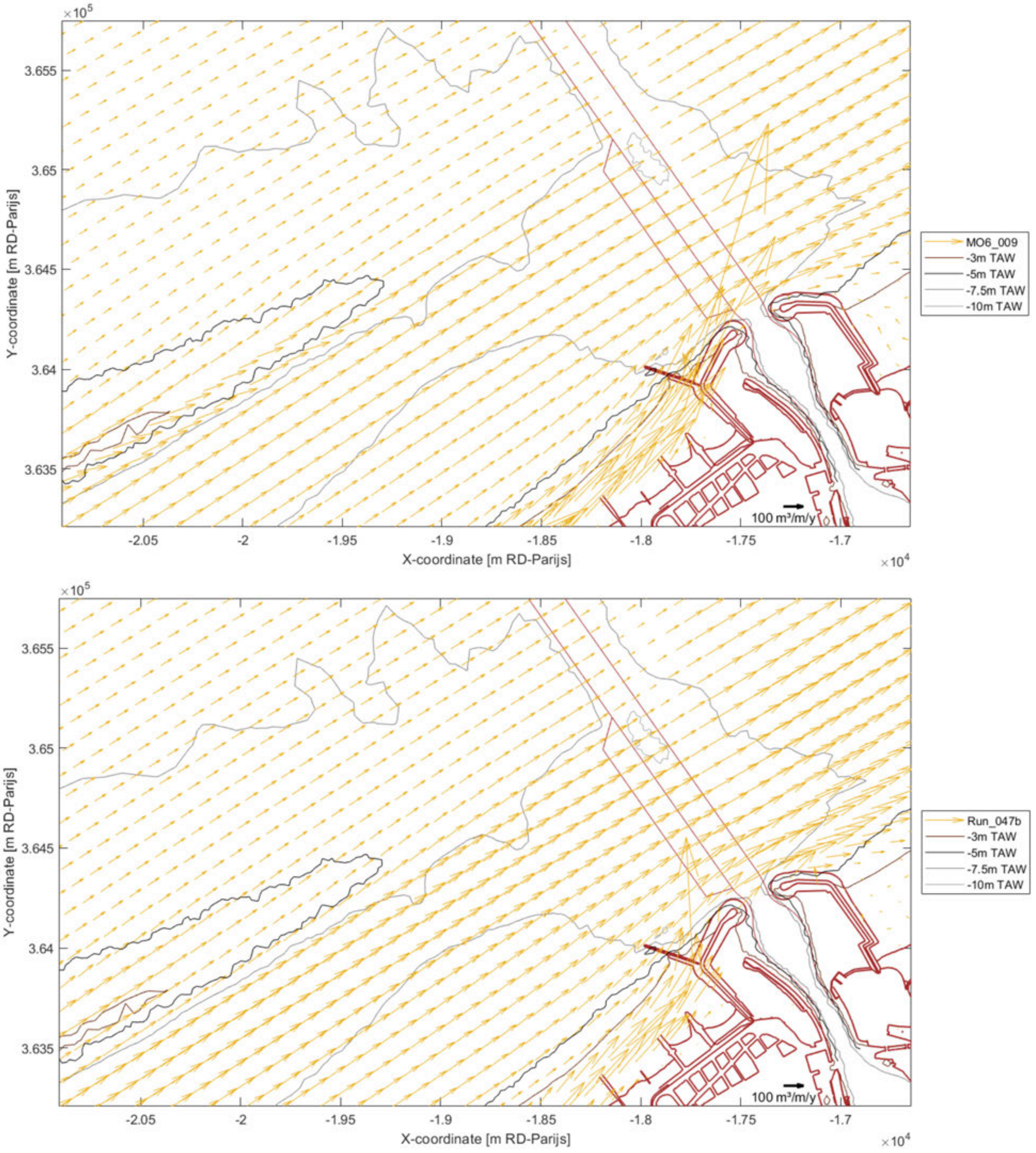

Figure 40 – Modelled annual longshore transport with Scaldis-Coast (top panel) and FlemCo (bottom panel) numerical models: area between Stroombank and Oostende.

2.5.6 Conclusions

The morphological evolution of the dredged navigation channel Pas van Stroombank, created in 2010, was studied in a test case spanning 2014, 2015 and 2016, focused on the navigation channel crossing of Stroombank. On the one hand, a series of 21 SB and MB bathymetric surveys were used to obtain geographic images of bed level change and bed volume differences in a number of zones. On the other hand, 17 BIS export rasters spanning the same time intervals as the bathymetric surveys were obtained. They provide aggregated BIS parameters weight, volume, reduced volume and tons of dry matter over the survey intervals, in 5 x 5 m cells.

From the available BIS export rasters, no reliable information on dredged sediment type could be obtained, as sediment density appeared to be equal across all time intervals and zones. While densities suggested all dredged sediment was mud, the morphological analysis implies that often sand has been dredged.

The BIS parameter "reduced volume" gave the best agreement between dredged amounts per time interval and zone, and volumes calculated from successive bathymetric surveys. The agreement is so good that it can be concluded that this parameter can be used to keep stock of sediment volumes removed by dredging, at least in the study environment of Pas van Stroombank.

In the study period and area (excluding the harbour mouth and outer harbour), yearly dredged volumes range from about 100,000 to over 300,000 m^3.

In the study area, two regimes of sedimentation are active, sometimes simultaneously. One is sandy sedimentation at the western flank of the navigation channel due to trapping of longitudinal bed transport on Stroombank. The other is spatially extensive sedimentation most likely caused by a combination of trapping fine suspended sand and influx of fluid mud.

From successive bathymetric profiles, estimates were obtained of the longitudinal bed transport (from WSW to ENE) over Stroombank and trough Kleine Rede: resp. 100 m^3/m/year versus 400 m^3/m/year. Based on bed sediment data shown above, the bed transport over Stroombank is fine sand, while the one in Kleine Rede is thought to be muddy sand or sandy mud. Possibly, there also fluid mud transport occurs. The sandy mud or fluid mud could contribute to the fast, spatially expansive fill of Pas van Stroombank that repeatedly occurred in 2014-2016. The results agree well with longitudinal transport rates calculated using Scaldis-Coast and Flemco, especially at the Stroombank crossing.

3 Numerical modelling

Besides results from the analysis of field data presented in Chapter 2, this chapter delves into findings from the modelling studies that explore the hydro- and morphodynamic interaction between the sea bottom (including its shoreface-connected sand ridges) and the evolution of the shoreline. These modelling studies serve distinct purposes and are distributed across three different Work Packages: WP2, WP3, and WP4.

In WP2 (Section 3.1), an idealized numerical model set is further developed, capable of simulating the slow morphodynamics (time scales of tens and hundreds of years) of shoreface-connected sand ridges (sfcr). This model set relies on an idealized representation of the Belgian coastal zone, incorporating schematized tide, wind, waves, bottom, shoreline, etc. It is crucial to note that this idealized model primarily aims to enhance our understanding of the system behaviour.

WP3 (Section 3.2) and WP4 (Section 3.3) employ the complex models Scaldis-Coast and FlemCo. The overall objectives of these two work packages are, respectively, 1) to quantify any natural beach feeding by adjacent shoreface-connected sand ridges, and 2) to investigate the effects of the observed gradual deepening of channels on the adjacent shoreline and the necessary beach nourishments.

3.1 Coupled shelf-shoreline model morphodynamics: idealized model study (WP2)

3.1.1 Introduction

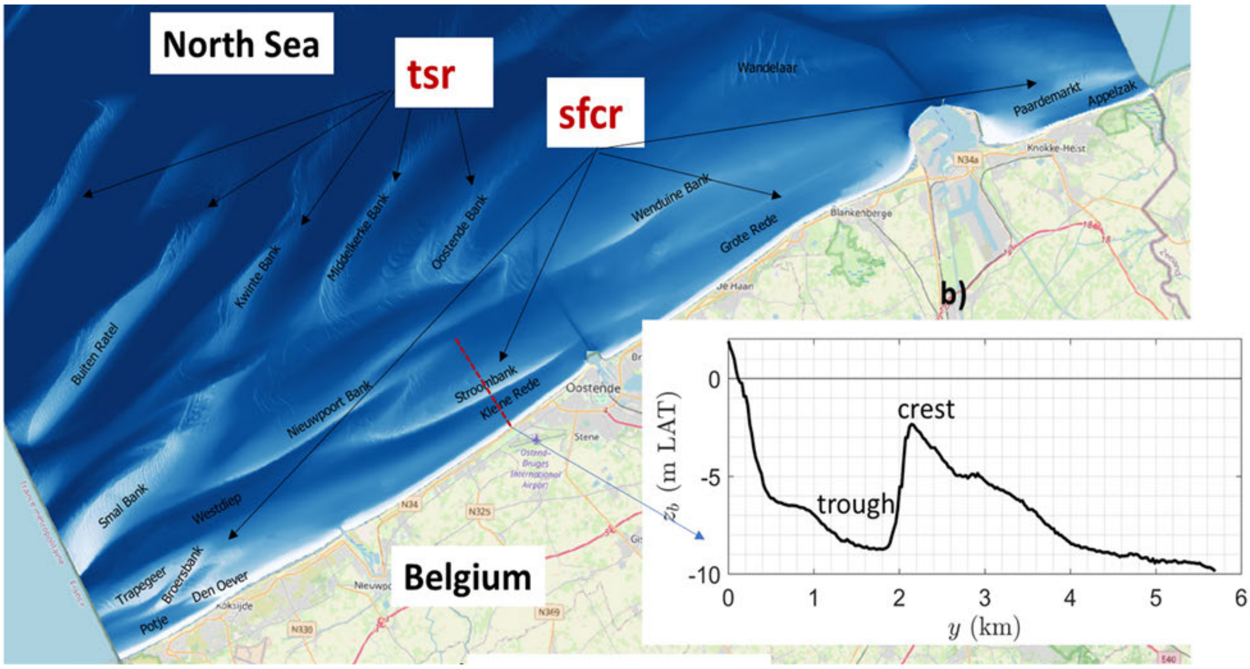

Figure 41 – a) Bathymetric map (LAT, m) of observed fields of shoreface-connected sand ridges (sfcr) and the more offshore located tidal sand ridges (tsr) on the Belgian shelf. b) Bathymetric profile along a transect over the ridge ”Stroombank”.

The Belgian inner shelf is characterized by the presence of a field of rhythmic sand ridges, which are aligned highly oblique with respect to the shoreline, i.e., their seaward ends are shifted several kilometres southwest with respect to their landward ends (Figure 41, panel a, see also Chapter 2). These so-called shoreface-connected sand ridges (sfcr) have alongshore crest-tot crest distances of 10-20 km, are 15-20 km long, 2-3 km wide, up to 6 m high (panel b) and they have an alongshore migration speed of several meters per year in the north-east direction (dominant direction of the storm-driven flow on the Belgian shelf). Such ridges are also observed on other inner sandy shelves where frequent storms occur, such as those of the Dutch coast (Van de Meene et al., 1996), Germany (Antia, 1996), the East Coast of United States (Duane et al., 1972; Swift & Freeland, 1978) and Argentina (Parker et al., 1982). Noticeably, crests of sfcr are oriented persistently up-current with respect to the local storm-driven alongshore current, which, in the case of the Belgian shelf, is directed predominantly to the northeast. Indeed, observations have revealed that sfcr evolve in stormy conditions, during which the joint action of high waves and strong currents causes erosion and transport of sediment at the bottom (Swift et al., 1978; Parker et al., 1982).

The formation of sfcr has been explained by Trowbridge (1995) and the mechanism is visualized in Figure 42 (see also the review by Ribas et al., 2015). The offshore sloping bathymetry of the inner shelf causes the flow to converge. Since sediment transport is assumed to be proportional to the current, convergence of sediment occurs over the ridge as well, resulting in ridge growth. Offshore decreasing wave stirring increases the sediment convergence, thereby enhancing growth (Calvete et al., 2001). A downcurrent oriented ridge will not grow because divergence of sediment would occur over its crest due to onshore flow deflection. This mechanism explains why only up-current oriented ridges are observed in the field. Note that further offshore on the Belgian shelf (Figure 41a), tidal sand ridges (tsr) are present, which have a different orientation compared to that of sfcr and whose formation mechanism is due to tides (Huthnance, 1982; see also the review by Vittori & Blondeaux, 2022).

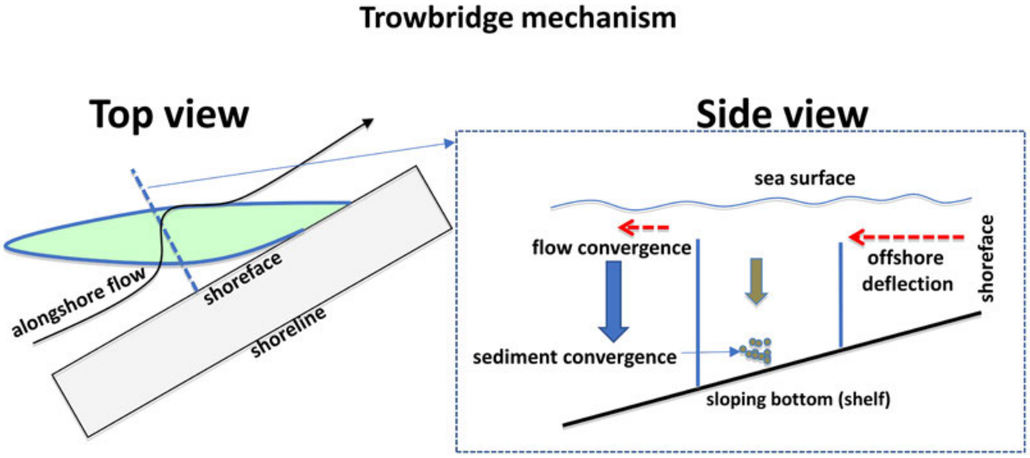

Figure 42 – Schematic view of the Trowbridge (1995) mechanism. A ridge that is up-current aligned with respect to the alongshore storm-driven flow causes an offshore deflection of this flow due to mass conservation. The offshore sloping bottom results in convergence of sediment over the ridge, resulting in ridge growth.

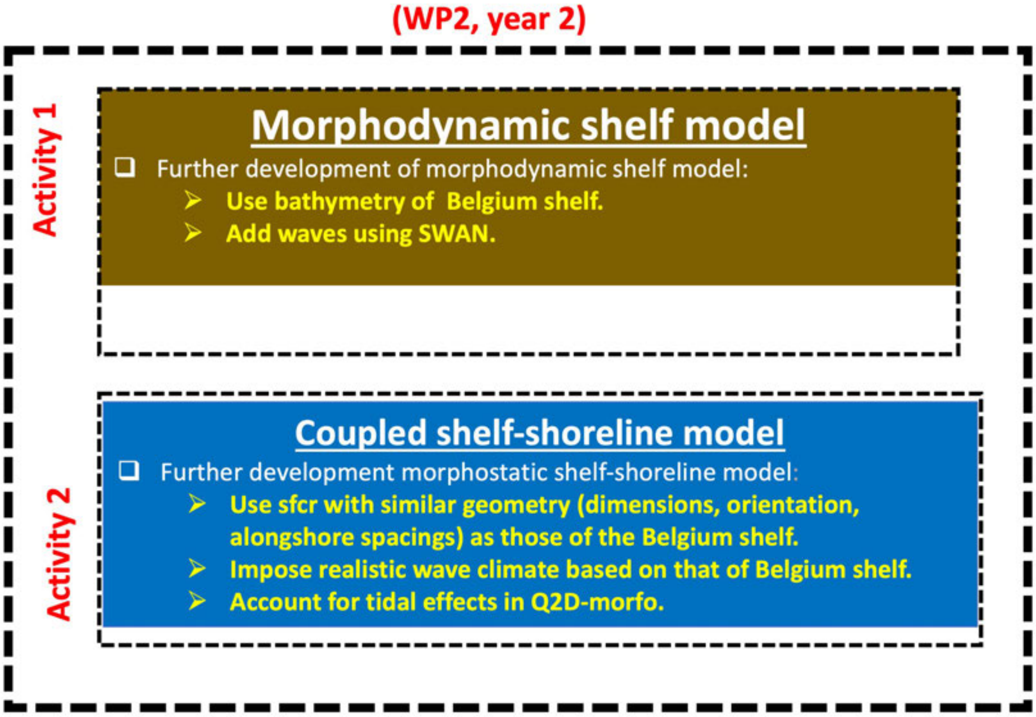

Figure 43 – Block diagram showing the steps toward the improvements of the existing coupled shelf-shoreline morphodynamic model to be used in the Mozes project (indicated by yellow text). The two activities within subtask 2 of Work Package 2 (WP2) in the second year of the Mozes project are also shown.

Besides an alongshore migration, analysis of historical bathymetric data of the Belgian shelf reveals that sfcr migrate also landward, at rates in the order of meters per year (see Chapter 2). As these ridges affect the onshore wave propagation and consequently patterns of wave breaking and refraction in the nearshore, the onshore migration of the sfcr is expected to have significant impacts on the adjacent shoreline. To quantify these impacts, a new model tool is being developed in the MOZES project, which couples a shelf model (Delft3D+SWAN) to a shoreline evolution model (Q2Dmorfo). In year 1 of the MOZES project, a new morphodynamic shelf model was developed, which successfully reproduced ridges with characteristics (heights, orientation, length, width, alongshore spacings) that resembled those of observed sfcr on the Long-Island shelf, which was used to validate this new model. Furthermore, in year 1, an existing coupled shelf-shoreline model was applied to the Belgian coast, where a synthetic field of morphostatic sfcr (i.e., the bottom does not evolve during the simulation) was placed on the shelf, which provided a forcing template for the morphodynamic development of the shoreline. Preliminary results suggested that an onshore movement of sfcr is expected to cause the shoreline to retreat in some areas and to prograde in others. However, due to the many simplifications in the model (background bathymetry not representative for the Belgian shelf, no tides, simplified waves), no statements yet could be made for the Belgian shoreline.

The results of year 1 motivated the specific objectives of year 2, which are divided among activities 1 and 2 (Figure 43). The objectives in **Activity 1** are to further develop the morphodynamic shelf model by 1) using a shelf bathymetry that is based on that of the Belgian shelf; and by 2) solving wave propagation on the shelf using SWAN. It is important to note here that this wave model should be capable of accounting for wave-topography feedbacks, i.e., the evolving bathymetry affects the wave characteristics. The objectives in **Activity 2** are to further improve the coupled shelf-shoreline model by 1) using a field of synthetic ridges with a geometry (length, width and orientation) similar to those of the Belgian shelf; by 2) imposing a more realistic wave climate; and by 3) accounting for tides in the Q2Dmorfo shoreline model.

3.1.2 Schematizing the bathymetry and wave climate

Bathymetry

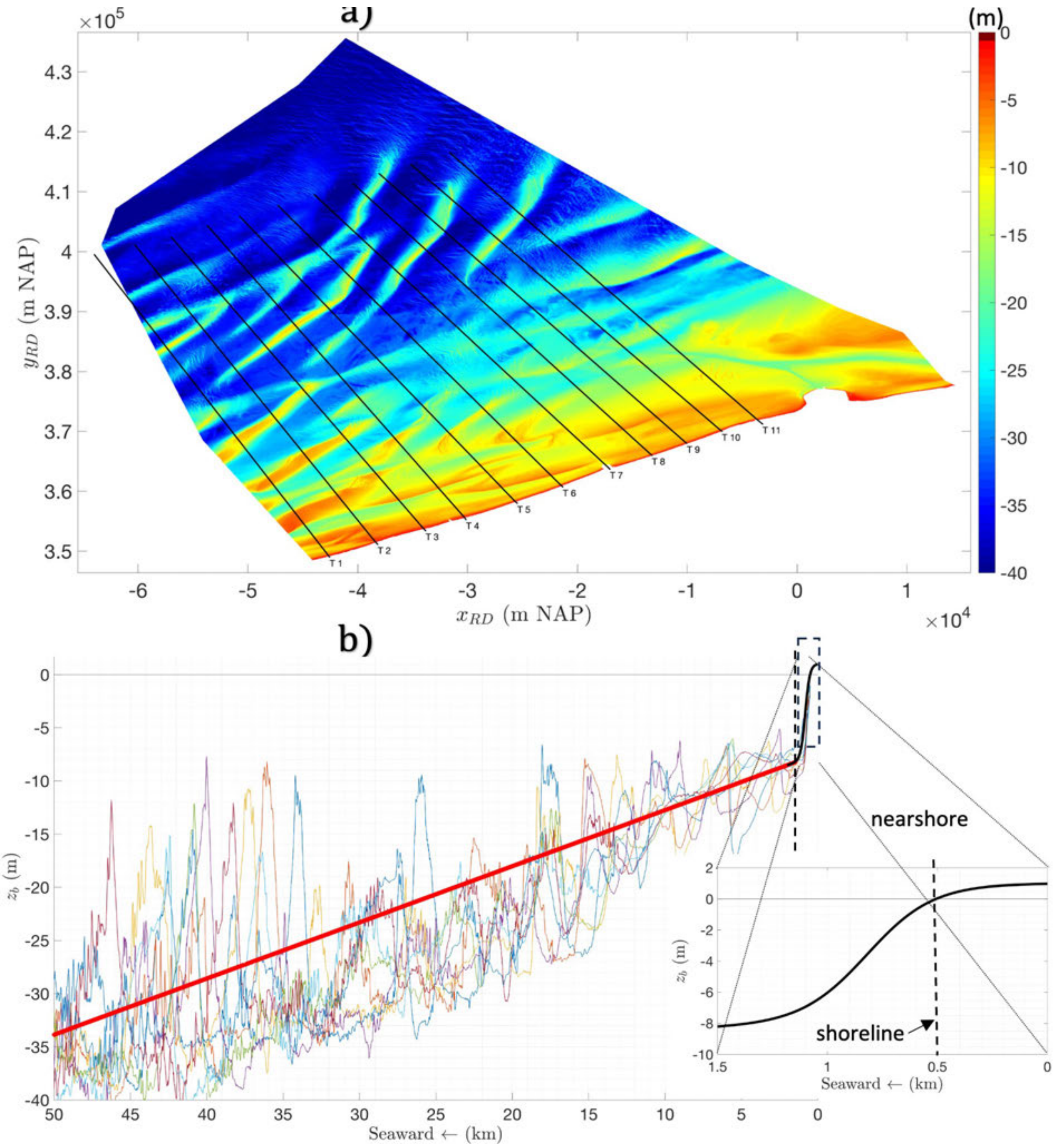

Figure 44 – a) Bathymetric map of the Belgian coastal zone (in m NAP, which is equivalent to mean seal level=MSL). Here, x_{RD} and y_{RD} represent the so-called ”RijksDiehoek” coordinates. b) Bathymetry profiles along the cross-shore transects (T1 − T11) depicted in panel a. The vertical dashed line marks the nearshore-shelf transition, which is set in this study at x = 1.5 km, with x the cross-shore coordinate. The thick black and red lines are approximations of the average bathymetry in the nearshore and shelf regions, respectively, which are obtained by averaging the observed profiles along all the transects. The inset on the bottom right shows a zoom-in on the nearshore area, whose bed level profile is approximated by a modified hyperbolic tangent (Eq. 1). The bed level profile of the shelf area is approximated by a linear profile, which decreases from H_c = 8.2 m at x = 1.5 km to 34 m at x = 50 km (Eq. 2). The vertical dashed line in this inset denotes the position of the shoreline (x = 0.5 km), which divides the dry beach (with an onshore increasing height to 1 m) and the wet beach.

The bathymetric map depicted in Figure 44 (panel a) serves as the basis for establishing a representative bathymetry within the model. Within the nearshore region (defined here within interval $0 \leq x \leq 1.5$ km, where x represents the cross-shore coordinate), characterized by a steeper bathymetry compared to the shelf ($x \geq 1.5$ km), the observed bathymetry profiles along cross-shore transects $T1$-$T11$ are approximated using a modified hyperbolic tangent function (thick black line in Figure 44b, see also the zoomed-in profile in the bottom right inset):

$$z_b = -H_c \left[\frac{\exp(\tilde{x}) - \frac{b}{H_c}\exp(-\tilde{x})}{\exp(\tilde{x}) + \exp(-\tilde{x})} \right], \qquad \tilde{x} = \frac{x - x_{s0}}{w}. \quad . \quad (1)$$

Here, x_{s0} represents the shoreline position, H_c is the depth at the transition between the nearshore and shelf areas ($x = 1.5$ km) and w is a fitting parameter. The vertical dashed line in the inset in panel b denotes the position of the shoreline (set to $x = 0.5$ km), which divides the dry beach ($x \leq 0.5$ km, with an onshore increasing height b to 1 m) and the wet beach ($0.5 < x \leq 1.5$ km). In the shelf region, a representative background bathymetry (excluding the variability due to the presence of the ridges) is derived by initially fitting a linear profile to each of the transects $T1$-$T11$ and subsequently averaging over the number of profiles. The resulting final bathymetry is as follows:

$$z_b = \alpha x - H_c \ . \qquad (2)$$

The optimal parameter values are determined to be $H_c = 8.2$ m, $w = 300$ m and $\alpha = -5.23 \times 10^{-4}$.

Wave climate

To derive a representative wave climate to force the model, time series of significant wave height (H_s, in m), wave direction (θ, in degrees with respect to geographic north) and peak wave period (T_p, in s) collected at different wave buoys (”Westhinder”, ”Akkaert Southwest”, ”Bol van Heist” and ”Ostend”, Figure 45) between 1990 and 2019 are used. The corresponding wave roses for these buoys are shown in Figure 45. This figure reveals that in offshore areas, wave conditions are predominantly from the south-south-west (SSW) and north-north-east (NNE) directions. Upon approaching the shore, refraction leads to prevailing wave directions from west-west-north (WWN) and north-north-west (NNW). Notably, the WWN waves are anticipated to induce a net longshore sediment transport towards the northeast.

Utilizing these time series, synthetic wave time series of H_s, T_p and θ were constructed following the methodology outlined in the study by Nnafie et al. (2021). First, the probability of occurrence (in %) of wave events belonging to distinct classes of wave heights H_s and wave angles θ was computed. This wave climate classification (Table 7) was then employed to create a 100-year-long time series of randomly occurring wave events. Specifically, the probabilities of occurrence for various wave classes determined the number of days each class of wave events would occur within the 100-year simulation period (maximum duration of the experiments). The assumption made here was that each wave event lasts for one day. Each wave event was assigned the mean values of its corresponding wave class, namely $\langle H_s \rangle$, $\langle T_p \rangle$, and $\langle \theta_0 \rangle$. To mimic the stochastic nature of a realistic wave climate, all the wave events (100 × 365 = 36500 in total) were randomly distributed across the 100-year interval, assuming no correlation between individual wave events. The resulting synthetic time series is presented in Figure 46. The wave events in these time series follow a specific sequence of appearance, signifying that this synthetic wave forcing represents just one possible realization among numerous potential scenarios in a realistic wave climate. Ideally, this process should be repeated for a significant number of different realizations (i.e., distinct orderings of wave events), followed by averaging the results across these realizations. Currently, simulations are restricted to a single realization, but future studies will explore multiple realizations.

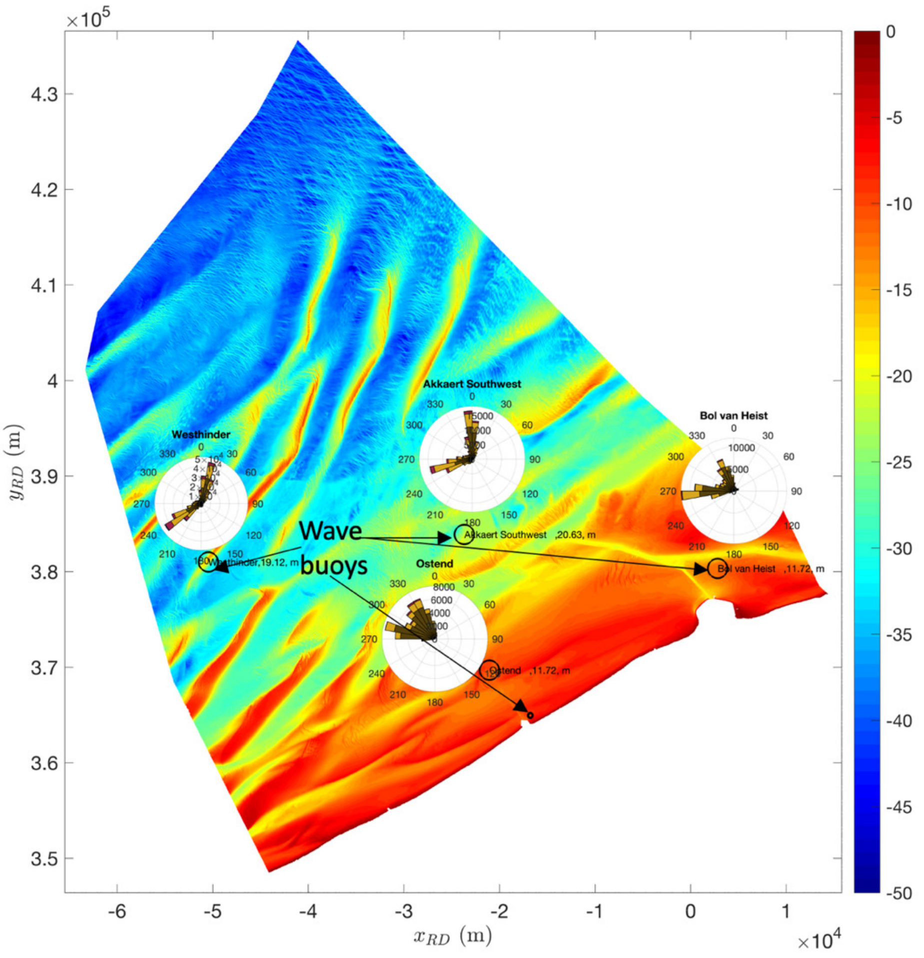

Figure 45 – Wave climate in the Belgian coastal zone, showing wave roses at four different wave buoys (”Westhinder”, ”Akkaert Southwest”, ”Bol van Heist” and ”Ostend”). The parameters Hm0: significant wave height and “REM”: direction of maximal wave energy are used to build the wave roses. Arrows denote the locations of the wave buoys. Water depths at which these buoys are situated are also shown.

Table 7 – Overview of probability of occurrence (in %) per wave height/direction class at Ostend station. Significant wave height (H_s) and wave direction (θ, in degrees with respect to geographical north) are sorted in 5 and 8 classes, respectively.

H_s (m)	θ (^{o}) 0-45	θ (^{o}) 45-90	θ (^{o}) 90-135	θ (^{o}) 135-180	θ (^{o}) 180-225	θ (^{o}) 225-270	θ (^{o}) 270-315	θ (^{o}) 315-360	Total (%)
0-1	6.74	0.64	0.00	0.03	0.01	4.38	37.13	34.74	83.68
1-2	0.46	0.01	0.00	0.00	0.00	0.14	7.25	6.64	14.50
2-3	0.00	0.0	0.00	0.00	0.00	0.00	0.59	1.09	1.68
3-4	0.00	0.0	0.00	0.00	0.00	0.00	0.01	0.12	0.13
> 4	0.00	0.0	0.00	0.00	0.00	0.00	0.00	0.00	0.00
Total (%)	7.21	0.65	0.00	0.03	0.01	4.52	44.98	42.60	100

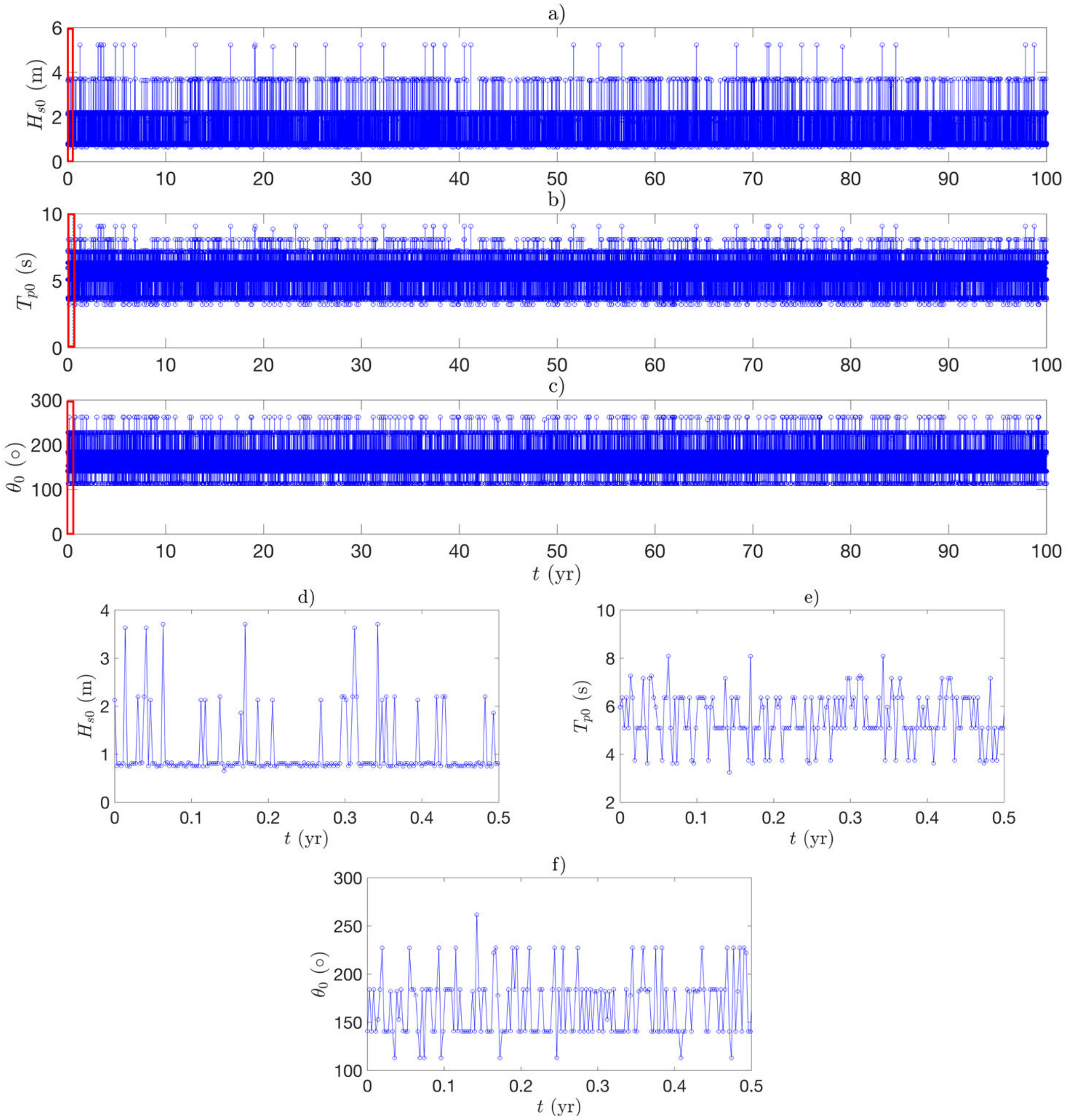

Figure 46 – Synthetic wave time series used as a forcing in the model, which was constructed based on wave time series collected at different wave buoys offshore the Belgian coast. a) Synthetic time series of a) H_{s0} (m), (b) peak period T_{p0} (s) and wave angle of incidence θ_0, (degrees with respect to geographical north) which are prescribed at the seaward boundaries in the shelf model. Zoom-ins on the first 6 months are displayed in, respectively, panels d, e and f.Note that, due to the difference in the shoreline orientation in the model (S-N) compared to that of the Belgian shoreline (NE-SW), the wave angle of incidence in the model was rotated 60° counter-clockwise.

3.1.3 Morphodynamic shelf model

Model description

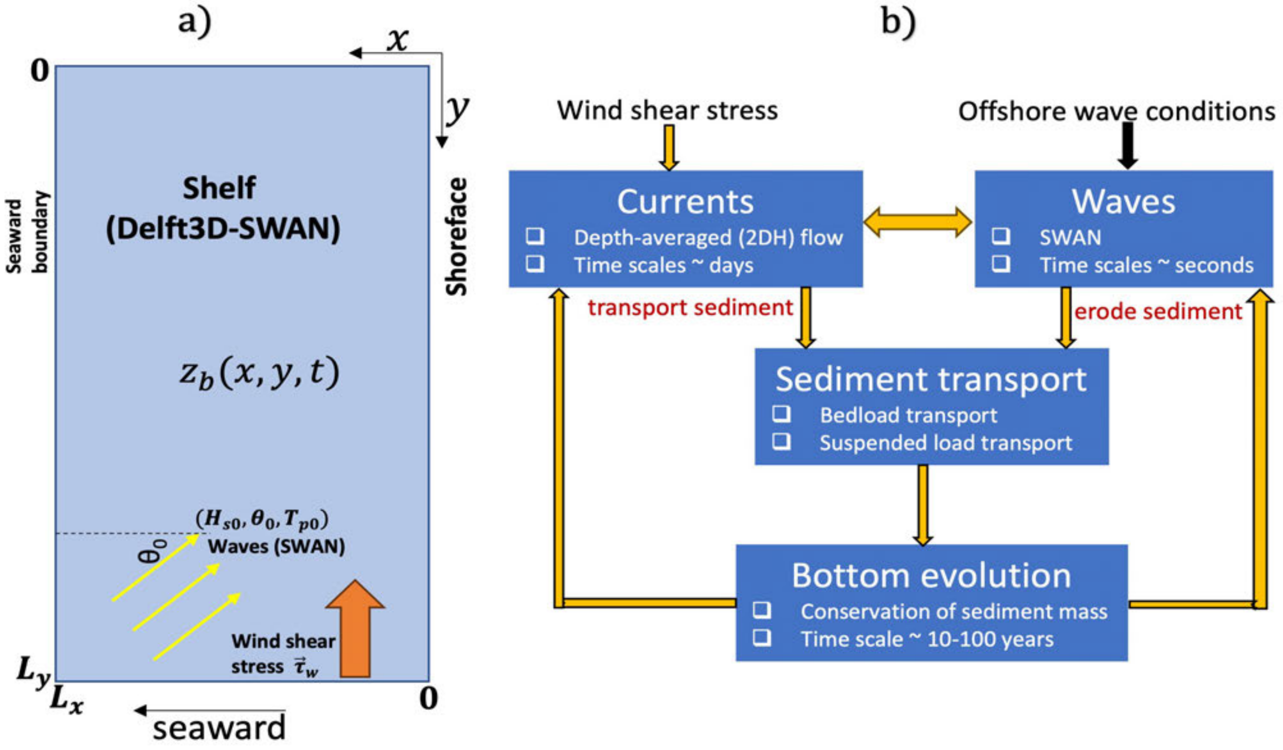

Figure 47 – a)Top view of the rectangular model domain, with dimensions $L_x \times L_y$ and with x- y pointing in the cross- and alongshore directions, respectively. The model is forced with obliquely incoming (time-invariant) waves and a constant wind stress $\vec{\tau}_w$ pointing in the negative y-direction. The waves, which are computed by SWAN, are characterized by a significant wave height H_{s0}, angle of wave incidence θ_0 (with respect to the negative x-axis, positive counter-clockwise) and peak period T_{p0}. These waves are assumed to have a JONSWAP shape. b) Structure of the morphodynamic shelf model: Waves erode sediment from the bottom, which is transported by the wind-induced currents.The divergence or convergence of sediment transport cause bottom changes, which influence the current and the waves. Waves affects also the currents and vice versa.

Delft3D (depth-averaged, 2DH) and the SWAN wave model are used for the development of the morphodynamic shelf model. The shelf model assumes a rectangular shelf with dimensions $L_x \times L_y$, where *x*- *y* pointing in the cross- and alongshore directions, respectively (Figure 47a). Coordinate *z* denotes a vertical position, while $z_b(x,y,t)$ marks the position of the bed level, positive downward. Perturbations in bed level $z_b(x,y,t)$ with respect to its initial value ($z_b(x,y,0)$) are represented by *h* (positive upward), i.e., $h(x,y,t) = z_b(x,y,t) - z_b(x,y,0)$. The following bed-shear stress formulation is used, which is derived by assuming stormy conditions (Calvete et al., 2001):

$$\vec{\tau}_b = \rho r_0 u_{rms} \vec{v}, \qquad (3)$$

with ρ the density of water, r_0 a drag coefficient, u_{rms} the root-mean-square (rms) amplitude of the wave orbital velocity at the bottom and $\vec{v}$ the velocity vector with *x*-*y* components (*u*,*v*). Rms amplitude u_{rms} is computed by SWAN, which accounts for the feedbacks between the changing depth and u_{rms} (wave-topography feedbacks) As for sediment transport, the transport formulations of Bailard (1981) are used, which account for bedload ($\vec{q}_b$) and suspended load transport ($\vec{q}_s$):

$$\vec{q}_{tot} = \vec{q}_b + \vec{q}_s = \left[\nu_b u_{rms}^2 + \frac{\delta D}{\hat{u}^3} u_{rms}^3\right]\vec{v} - \left[\nu_b \lambda_b u_{rms}^3 + \lambda_s u_{rms}^5\right]\vec{\nabla} h. \qquad (4)$$

Here,

- ν_b is a coefficient of the bedload transport,
- λ_b and λ_s are bedslope parameters for bedload and suspended load transport, respectively,
- D is the total water depth, $\hat{u}$ is a calibration velocity and δ is the (scaled) layer thickness of the suspended sediment in the water column. A view of the structure of the new morphodynamic shelf model is depicted in Figure 47b.

Waves exert a shear stress at the bottom, thereby eroding sediments from this bottom. Subsequently, these sediments are transported by current $\vec{v}$, which is induced by a wind-shear stress $\vec{\tau}_w$ representative for stormy conditions. The divergence or convergence of sediment transport $\vec{q}_{tot}$ determines changes in bed-level z_b, which influence the current and the waves. Waves affects also the currents and vice versa. At the offshore boundary, obliquely incoming waves (constant in time) and a constant wind stress $\vec{\tau}_w$ pointing in the negative *y*-direction are prescribed. The waves are characterized by a significant wave height H_{s0}, angle of wave incidence θ_0 (with respect to the negative *x*-axis, positive counterclockwise) and peak period T_{p0}. These waves are assumed to have a JONSWAP shape. To avoid the formation of shadow zones caused by the oblique incident waves, periodic boundary conditions for the wave forcing is applied at the lateral boundaries (northern and southern boundaries). Note that the default SWAN version of Delft3D does not support periodic boundary conditions for the waves. Instead, the standalone SWAN model, which does support this type of boundary conditions, is used for wave computation.

Methodology

The rectangular model domain has dimensions 50×10 km. Eq. (**2**) is used to generate an alongshore uniform bed-level profile to start the model simulations, which is visualized in Figure 48a (t = 0 yr). At the shoreface side (x = 0 km), depth is 8 m, and it increases linearly in the seaward direction to 13.2 m at the seaward boundary (*x*-direction). The model is forced with 1) a wind stress $\vec{\tau}_w$ that acts along the coast (in the negative *y*-direction, value is -0.2 Nm^{-2}) and 2) constant waves with H_{s0} = 3 m, $\theta_0 = -70^o$ and $T_{p0} = 11$ s . These forcings are assumed to represent average stormy conditions on the Belgian shelf. Note that the model is run for these continuous conditions, which are assumed to occur during a time fraction of 5%. Model results are corrected for this fraction. Furthermore, at the lateral boundary conditions, Neumann conditions (in both the water level and sediment transport) are imposed, while at the offshore boundary a water level of 0 m is prescribed. As for the numerical parameters, mesh sizes of the computational grid are 200 m in both the cross-shore and alongshore directions, while time step is 0.1 minutes.

The simulations start from small-scale random bottom perturbations (with a root mean square height of 10 cm) superimposed on the bathymetry. The idea here is these perturbations contain all kinds of bottom patterns with different length scales. The mechanism of Trowbridge (1995) will subsequently cause the bottom pattern that initially has the fastest growth rates to dominate after some time. After that stage, when ridges have attained considerable height, they will nonlinearly interact with each other and typically attain a finite height (see e.g. Nnafie et al., 2014). To reduce computation time, a morphological amplification factor of 100 is used. This is justified because the morphodynamic timescale is much longer (order of years) than the hydrodynamic timescale (order of hours to days). The experiment was run for a maximum period of 1000 years. The characteristics of the simulated bedforms are analyzed in terms of their average height H_{av} (crest-to-trough distance), global migration speed V_m and their longshore dominant spacing λ. Migration V_m and spacing λ are defined as follows Vis-Star et al. (2008):

$$V_m = -\frac{1}{\overline{(\partial h/\partial y)^2}}\overline{\frac{\partial h}{\partial y}\frac{\partial h}{\partial t}}. \qquad (5)$$

In these expressions, the overbar indicates averaging over the entire model domain, i.e., $\frac{1}{L_x L_y}\int_0^{L_y}\int_0^{L_x}\cdot\, dxdy$. The discrete Fourier transform was used to retrieve the periods of the harmonic signals that might arise in the time response of the bar height and migration speed to the imposed sinusoidally time-varying wave angle.

The longshore dominant spacing of the sand ridges (λ_d) is computed using the discrete Fourier transform of the bottom perturbations h at the longshore section x = 2.2 km. This dominant spacing is defined as the longshore spacing between ridges for which the modulus of the Fourier coefficients is maximum (Garnier et al., 2006):

$$F(x_t, k_l, t) = \sum_{j=1}^{N_y} h(x_t, y_j) e^{-i\frac{2\pi}{N_y}(j-1)(l-1)}, k_l = \frac{2\pi(l-1)}{L_y}, \quad l = 1 : N_y, \quad y_j = j\Delta y. \qquad (6)$$

Here, $F(x_t,k_l,t)$ is the Fourier coefficient that corresponds to the topographic wavenumber k_l and N_y is the number of grid points in the longshore direction (y). The wavenumber for which the modulus of the Fourier coefficient ($|F(x_t,k_l,t)|$) is maximum for a given time t and longshore position x_t defines the dominant mode, which is used to compute the longshore dominant spacing λ_d.

Results and discussion

Snapshots of the simulated bed level z_b at different points in times are displayed in Figure 48 (panel a). These snapshots illustrate the evolution of randomly imposed bottom perturbations on the initial bathymetry over a centennial time scale, eventually forming large-scale elongated ridges on the shelf. Initially, mode scale selection occurs, wherein bottom modes lacking the most-preferred topographic wavelength (alongshore spacing) decay over time, leaving only the mode with this preferred wavelength. Subsequently, coast-oblique ridges manifest on the shelf, maintaining a connection to the shoreface. These shoreface-connected sand ridges (sfcr) originate close to the shoreface and progressively extend offshore. The offshore segment of the sfcr aligns nearly parallel to the coast, while the onshore portion is less oblique (panel b). The ridges exhibit widths of approximately 5 km, with lengths spanning between 15 and 20 km (panel c). In Figure 49, it is seen that over time, 1) mature ridges attain heights of about 5-6 m (panel a, see also Figure 48c), 2) they migrate downstream (negative y direction) at rates V_m of roughly -15 myr^{-1}, as a result of the storm-driven currents (Figure 49, panel b), and 3) they maintain alongshore spacings of approximately ~ 5 km (panel c). Initially, ridge height experiences exponential growth over time, eventually tending to saturation towards the end of the simulation period. A fully saturated stage is not reached due to the effects of the northern boundary on the evolution of the migrating ridges, which over time collide against this boundary (Figure 48a). This collision can be mitigated by incorporating periodic boundary conditions at the lateral boundaries, an aspect currently under consideration for code improvements.

The characteristics of the simulated ridges described above bear a good resemblance to those observed on the Belgian shelf. However, a notable distinction is apparent in the less oblique nature of the simulated sfcr on their onshore segment when compared to observations (refer to Figure 41). Another difference is evident in the model tendency to underestimate the alongshore spacing, which, in reality, is larger, ranging between 10−15 km. These differences in ridge characteristics between the simulation and observation could stem from factors such as the absence of tides in the model, the simplified nature of the applied wave forcing, and the exclusion of sea level rise (SLR). Tides, time-varying wave forcing and SLR are important topics for the third and fourth year of the MOZES project.

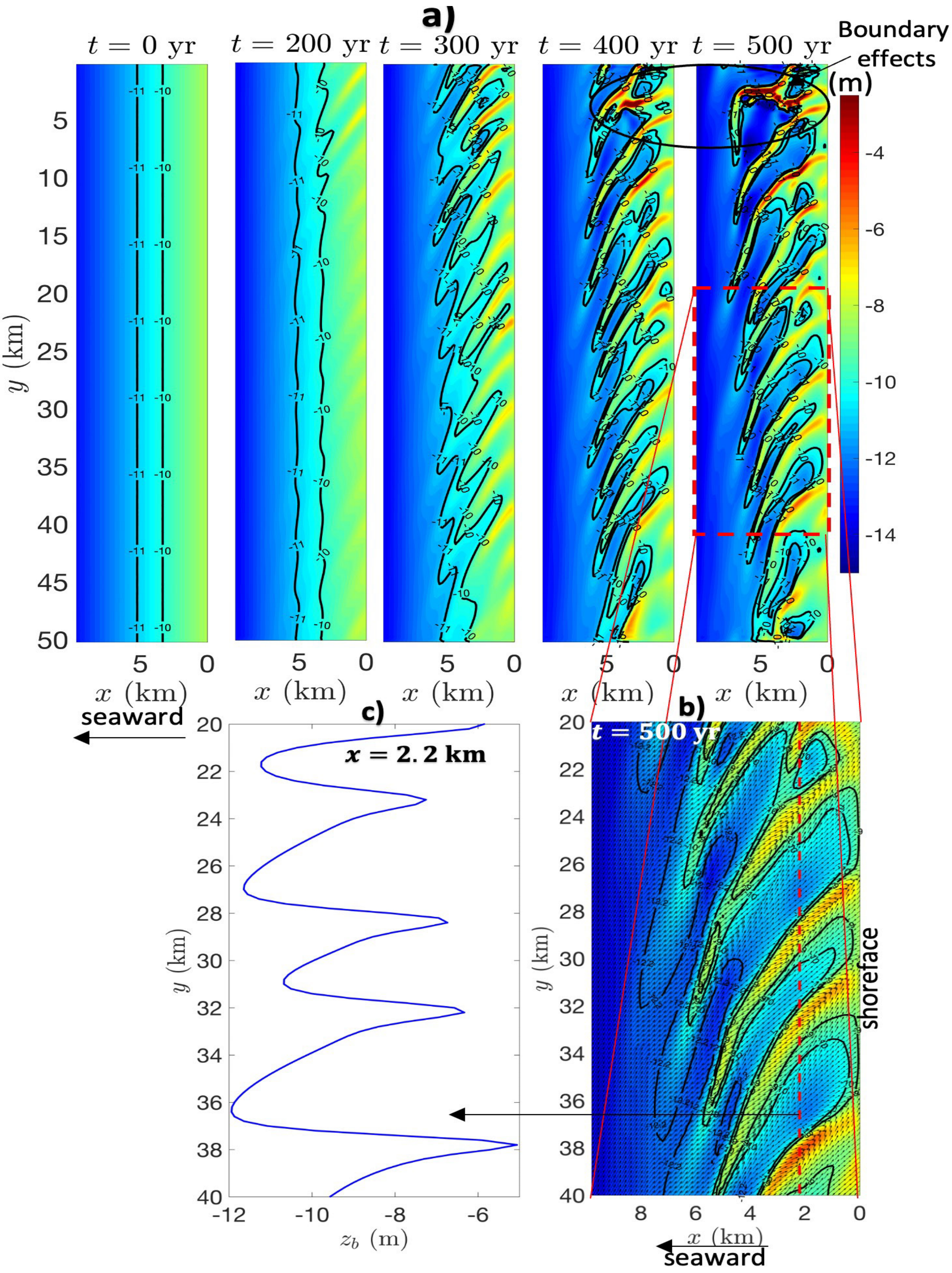

Figure 48 – a) Snapshots of the simulated bed level z_b at times t = 0 yr, t = 200 yr, t = 300 yr, t = 400 yr and t = 500 yr. A zoom-in at t = 500 yr is displayed in panel b, while panel c shows the bed level profile along the alongshore transect depicted in panel b (dashed red line).

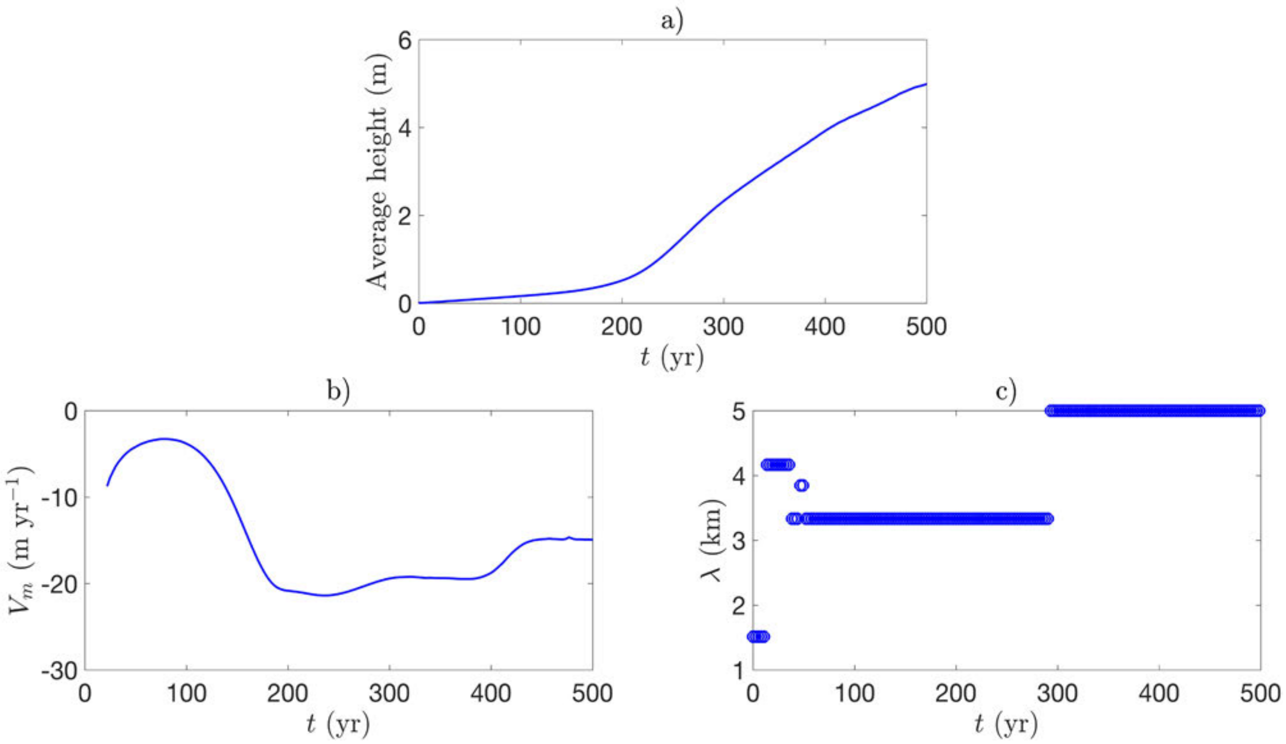

Figure 49 – Average height of the ridges H_{av} (a), their migration speed V_m (b) and their dominant longshore spacings λ_b versus time.

3.1.4 Coupled shelf-shoreline model

Model description

The coupled model distinguishes between processes on the shelf ($x_1 \leq x \leq x_L$, $0 \leq y \leq y_L$) and in the nearshore zone ($0 \leq x \leq x_1$, $0 \leq y \leq y_L$) (see Figure 50). On the shelf, the depth-averaged currents, waves and their interactions are computed with Delft3D (D3D) and SWAN models.

As the shelf model is morphostatic (i.e., bed level does not change in time), the used D3D model configuration consists only of the FLOW module. Sediment and morphology modules (SED and MOR) are switched off. Module FLOW computes the water level and currents on the shelf, which are described by the non-linear depth-averaged shallow water equations. This module is forced with sea-level variations at the seaward ($x = x_L$) and lateral ($y = 0$, y_L) boundaries, which mimic a tidal wave that propagates in the negative *y*-direction (Figure 50). For wave computation on the shelf, the standalone SWAN model is used, which solves the spectral wave action balance. To avoid the formation of shadow zones caused by the obliquely incident waves, periodic boundary conditions for the wave forcing is applied at the lateral boundaries (northern and southern boundaries). Furthermore, JONSWAP spectra of incoming waves are imposed at the seaward boundary. The synthetic wave time series derived in Section 3.1.2, which was constructed based on wave time series collected at different wave buoys offshore the Belgian coast, are prescribed at the seaward boundaries in the shelf model. Note that, due to the difference in the shoreline orientation in the model (S-N) compared to that of the Belgian shoreline (NE-SW), the wave angle of incidence in the model was rotated 60° counter-clockwise. The bathymetry constructed in Section 3.1.2, with superimposed a synthetic ridge (see next section), is used as a bathymetry in the shelf model.

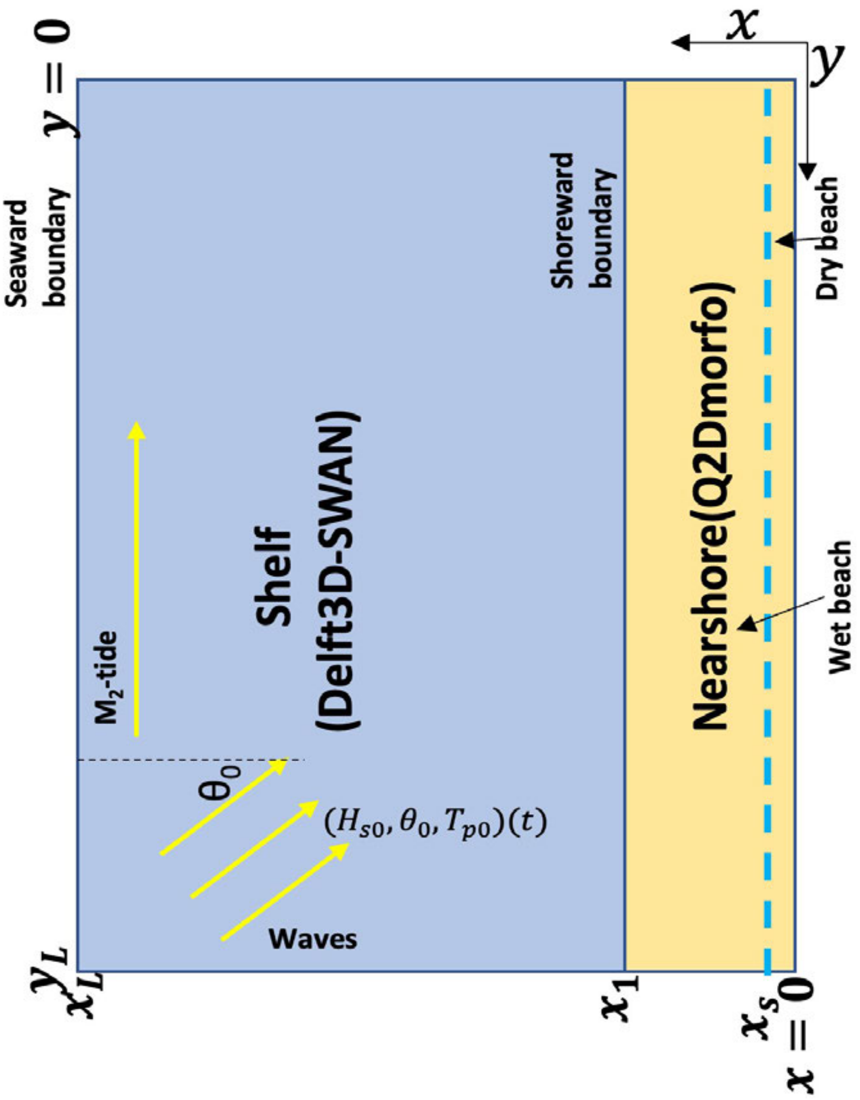

Figure 50 – Domains of the shelf ($x_1 \leq x \leq x_L$, $0 \leq y \leq y_L$) and shoreline models ($0 \leq x \leq x_1$, $0 \leq y \leq y_L$), with $x - y$ pointing in, respectively, the cross-shore and alongshore directions. Shoreline position $x_s(y,t)$ marks the border between the dry ($z_b > 0$) and wet beaches ($z_b \leq 0$). Tidal forcing is imposed at the seaward boundary of the shelf (x_L) as an M_2 wave that propagates from south to north along the coast. Furthermore, a time-varying wave forcing with a significant wave height $H_{s0}(t)$, peak period $T_{p0}(t)$ and wave direction $\theta_0(t)$ (relative to the shore-normal, positive counter-clockwise) is prescribed at the seaward boundary. New wave parameters $H_{s1}(t)$, $T_{p1}(t)$, θ_1 (t), computed by the shelf model at the shoreward boundary (x_1), are subsequently used as a wave forcing for the shoreline model.

In the nearshore region, the non-linear shoreline model known as Q2Dmorfo (Arriaga et al., 2017) is employed to simulate the morphodynamic changes in the nearshore and the position of its shoreline $x_s(y,t)$. This model, which does not explicitly resolve the current field, utilizes empirical formulations to calculate sediment transport directly from the wave field. The model comprises three modules: WAVES, TRANSP, and BED. In the WAVES module, waves (H_{s1},T_{p1},θ_1) at the seaward boundary ($x = x_1$, Figure 50) are computed based on the geometrical optics approximation. This involves the linear dispersion relation, irrotationality of the wave vector (also known as the generalized Snell law) and conservation of wave energy to simulate the wave propagation within the domain. The boundary condition at the up-waves lateral boundary (i.e., the lateral boundary at which wave rays enter) involves extending the bathymetry uniformly alongshore for a specified distance. Wave transformation occurs in this extended bathymetry, and the transformed waves are assumed to enter through the lateral boundary.

The TRANSP module computes wave-driven alongshore sediment transport and considers cross-shore transport in a simplified manner. Alongshore transport is evaluated using a parametrized cross-shore distribution based on the CERC formula, with a coefficient μ controlling the magnitude of this transport. Cross-shore transport is proportional to the departure of the local bed slope from the slope of a prescribed equilibrium profile. The equilibrium profile is based on the modified tangent hyperbolic profile derived in Section 3.1.2 (Eq. 1, Figure 44). The proportionality factor between the actual and equilibrium profiles is computed based on wave energy dissipation. In the TRANSP module, seaward ($x = x_1$) and lateral boundaries ($y = 0$, y_L) are open, allowing sediment to enter or exit through these boundaries. At the shoreward boundary ($x = 0$), the cross-shore sediment component vanishes. The BED module calculates the evolution of the nearshore bed level as a result of spatial gradients in sediment transport. The dry beach is considered part of the computational domain of the shoreline model, undergoing erosion/accretion during the simulation. The shoreline position $x_s(y,t)$ is determined using linear interpolation between the cross-shore locations of the last dry cell and the first wet cell in the nearshore domain. For more details, the reader is referred to Arriaga et al. (2017).

Methodology

Model parameters: Dimensions of the coupled model domain, bathymetry, tides and waves are based on observations on the Belgian coast (see also Section 3.1.2). Other parameter values are adopted from the work by Nnafie et al. (2021) and Arriaga et al. (2017). A list of all the values of model parameters is provided in the Appendix (Table 15). The dimensions of the coupled model domain are $x_L \times y_L = 51.5 \times 75$ km. The dry beach has a width of 0.5 km (i.e., $x_{s0} = 0.5$ km) and its height b is 1 m (Figure 44). The bed level profiles of Eqs. 1-2 (Section 3.1.2) are used to generate the bed levels of the nearshore and shelf areas, respectively. In the (wet) nearshore area ($0.5 \leq x \leq 1.5$ km), the depth is governed by a (modified) hyperbolic tangent, while further offshore, the depth increases linearly from ~ 8.2 m at $x_1 = 1.5$ km to ~ 34 m at the seaward boundary ($x_L = 51.5$ km). The M_2-tidal forcing at the seaward boundary ($x = x_L$) has amplitude $\hat{\zeta}_2 = 1.8$ m and phase difference of 31.5^o between the lateral boundaries, $y = 0, y_L$. This tidal forcing represents a propagating M_2-tidal wave in the negative y-direction.

Furthermore, as the model is forced with wave time series, coefficient μ, which controls the magnitude of the alongshore sediment transport in the shoreline model, is set to 0.06. This yields total average transports (i.e., integrated over the cross-shore direction and averaged over 10 years) of about 1×10^5 m^3/yr, which are consistent with model outcomes of the complex models Scaldis and FlemCo (Chapter 3.4).

Numerical aspects: To be able to couple the standalone SWAN model, which supports periodic boundaries conditions for wave computation, to the D3D-Flow model, code adjustments have been carried out. The used computation grids (for both wave and flow computations) have sizes of 250 m in the cross- and alongshore direction. The hydrodynamic time step is set at 2 minutes. The alongshore grid size in the shoreline model matches that of the shelf model. However, to capture surf zone processes, the cross-shore grid size is significantly smaller at 15 meters, with a time step of 0.005 days.

To transfer wave data computed by the shelf model to the shoreline model, a coupling time of 10 days is used, meaning data exchange between the models occurs every ten days. While a coupling time of 1 day would be more precise for one wave event, the simulations in this case last several months. Results of test runs using different coupling times (1, 5 and 10 days) between the shelf and shoreline models show that using a coupling time of 10 days does not significantly change model results, while maintaining reasonable computation durations.

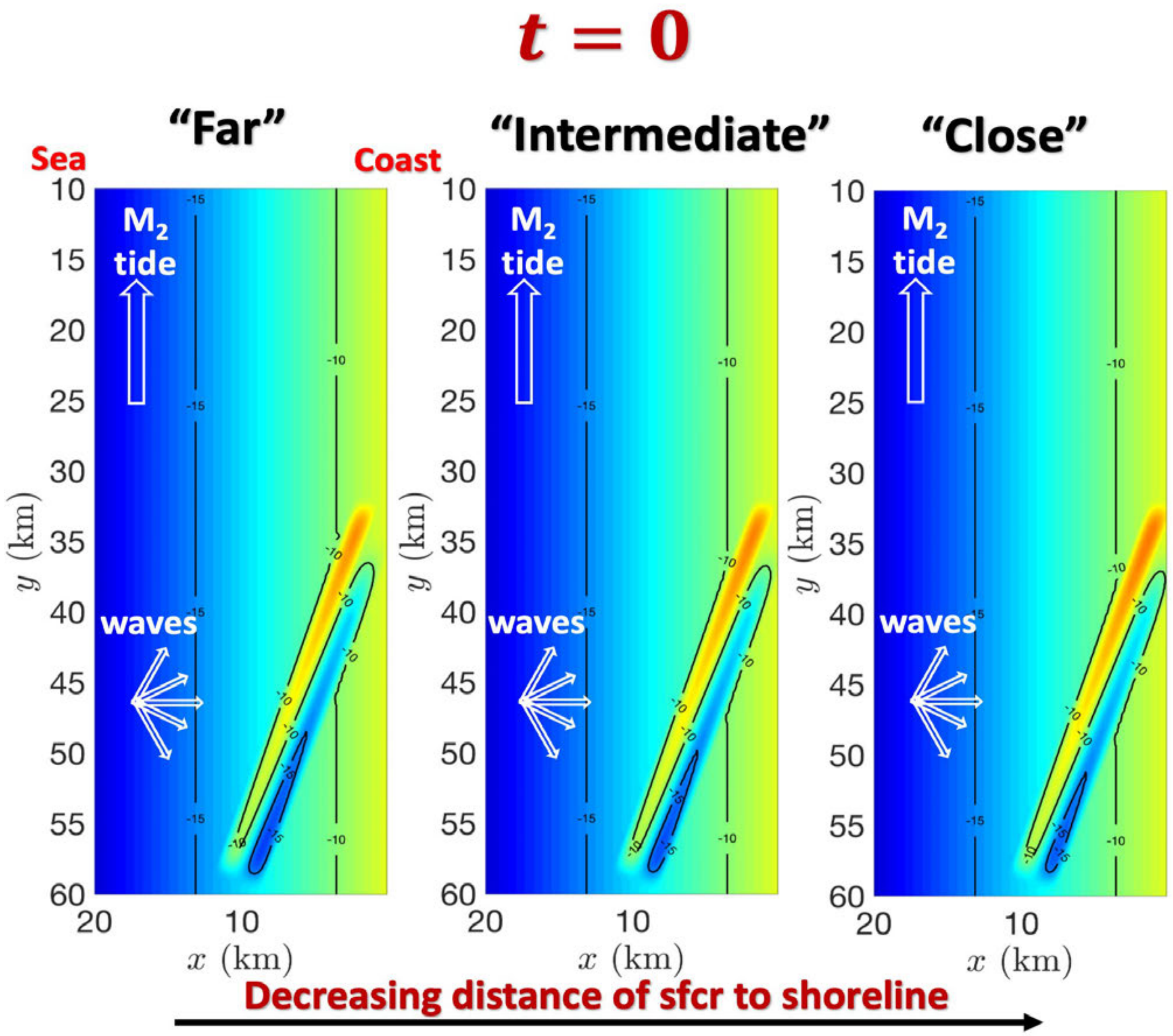

Figure 51 – Initial bathymetry with superimposed a synthetic ridge that is placed at decreasing distance (from left to right) with respect to the shoreline, with spatial intervals between them of 500 m. Ridge dimension (width, length and orientation) are based on those of the ”Stroombank” ridge (Figure 41). Arrows indicate the forcings prescribed at the offshore boundaries (M_2 tidal water level and the wave time series of Figure 46).

Experiments: Utilizing the synthetic wave time series depicted in Figure 46, an experiment spanning 100 years is conducted. In this simulation, a synthetic ridge is overlaid on the initial bathymetry, having heights (crest-to-trough distance), dimensions (width and length) and orientation similar to those of the ”Stroombank” ridge (Figure 41). The shoreline is initially straight and is situated at x_s = 500 m (Figure 50).

A set of runs with 100 years simulation time is carried out, which investigates the potential effects of onshore-migrating ridges on the morphodynamic evolution of the nearby nearshore area and its shoreline. In this context, three experiments, namely ”Close,” ”Intermediate” and ”Far,” are executed using the coupled model. These runs involve the placement of synthetic ridges at progressively decreasing distances from the shoreline, with spatial intervals between them covering a span of 500 meters (Figure 51). The used coupling time is 10 days. One simulation of 100 years lasts about 16 days on an intel Xeon 2.80 GHz Linux computer.

The assessment of the influence of the presence of the ridge on the decadal evolution of the nearshore and shoreline involves: 1) identifying potential erosion and accumulation hotspots along the shoreline, 2) evaluating the strength of these hotspots, and 3) examining changes in the bathymetric profile of the nearshore.

The identification of potential erosion and accumulation hotspots along the shoreline includes assessing their relative positions in relation to the adjacent crest-channel system of the ridge. The strength of these hotspots is quantified by the root-mean-square (rms) amplitude $\sigma'_{x_s}$of shoreline undulations x'_s, defined as $x'_s = x_s - \langle x_s \rangle$ (where brackets ⟨ ⟩ represent alongshore averaging). The mathematical expression is

$$\sigma_{x'_s} = \sqrt{\frac{1}{N}\sum_{j=1}^{N}(x'_s)^2}, \qquad (7)$$

with N = 300 the number of grid points in the y-direction.

The examination of changes in the nearshore bathymetric profiles concentrates on the slope of these profiles ($\partial z_b/\partial x$) in proximity to the ridge and channel. The outcomes from runs ”Close,” ”Intermediate” are compared with those from run “Far”, which serves as a reference case.

Results and discussion

From Figure 52 (panel a), displaying snapshots of shelf and nearshore bed levels along with longshore profiles of shoreline positions (x_s) after 50 years and 100 years of morphodynamic evolution, it is evident that the presence of the ridge on the shelf induces the development of undulations along the adjacent shoreline. Clearly, this ridge serves as a forcing template for shoreline evolution. Shoreline progradation, resulting from sediment convergence, occurs at a rate of 0.2 m/yr toward the ridge crest. In contrast, shoreline retreat at a rate of about 0.5 m/yr, associated with sediment divergence, is noticeable adjacent to the channel and to the north of the ridge. Figure 52b, plotting the cross-shore rms amplitude of shoreline undulations σ'_{x_s} (normalised by its value at t = 100 yr, $\sigma'_{x_s}|_{t=100\mathrm{yr}}$ =16 m), seems to indicate that these undulations do not reach a saturation point in the first 100 years. Instead, they continue to increase with time. Results further demonstrate (panel c) that the slope $z_b/\partial x$ of the landward section of the bathymetry profile adjacent to the ridge crest is smaller compared to that adjacent to the channel. In the seaward section, the opposite effect occurs, with the slope adjacent to the crest being larger than that near the channel.

Results from the experiments in the cases of decreasing distances of the shoreface-connected sand ridge to the shoreline (cases ”Intermediate” and ”Close”) are presented in Figure 53a. This figure compares the longshore shoreline profiles after 100 years of morphodynamic evolution in the two cases with that of the reference case. Clearly, as the ridge is displaced more onshore, shoreline progradation and retreat near, respectively, the ridge crest and channel become more pronounced. Figure 53b shows the temporal evolution of the normalised amplitude $\sigma'_{x_s}/\sigma'_{x_{s0}}$multiplied by the ratio d_i/d_0, with d_0 the distance of the ridge to the shoreline in the reference case (d_0 = 2 km) and d_i the distance of the ridges in the ”Intermediate” case (d_1 = 1.5 km) and ”Close” case (d_2 = 1 km). It is evident from this figure that the obtained profiles closely align with each other. This indicates that the strength of shoreline undulation scales approximately linearly with the inverse of the distance of the ridge to the shoreline. Similar to the ”Far” case, in the ”Intermediate” and ”Close” cases, the slope $\partial z_b/\ \partial x$ of the landward section of the nearshore bathymetry profile adjacent to the ridge crest is smaller compared to that adjacent to the channel (panel c). In the seaward section, the opposite effect occurs. The closer the ridge is located to the shoreline, the more pronounced the differences in the bottom slopes near the ridge crest and channel become. These results imply that the observed onshore movement of sfcr on the Belgian shelf is likely to prompt shoreline retreat adjacent to the channel and progradation adjacent to the ridge crest. Finally, note that, unlike the ”Far” case and to a lesser extent the ”Intermediate” case, in the ”Close” case, the amplitude of shoreline undulations exhibits a weak tendency towards saturation in the 100 years simulation. In fact, the ”Close” run was extended for an additional 100 years (results not shown), revealing that the rms amplitude of the shoreline undulations have almost reached a saturation value, estimated to be $\sigma'_{x_s} \sim$ 45 m.

These morphological changes in shoreline position result from wave refraction over the crest-channel system of the ridge, creating zones of high and low wave energy along the shoreline. This, in turn, generates alongshore gradients in sediment transport, leading to shoreline undulations. The closer the ridge is to the shore, the more pronounced these gradients become, amplifying shoreline undulations accordingly.

These findings appear to align with observations in the Belgian coastal zone (Figure 54):

1. Extensive dune areas have developed along the coast adjacent to the sfcr, indicating shoreline progradation has taken place at this location (panel a).
2. In the "Den Oever" ridge area, the bathymetry profile in the breaker zone is less steep adjacent to the ridge crest compared to that adjacent to the channel (panel b).

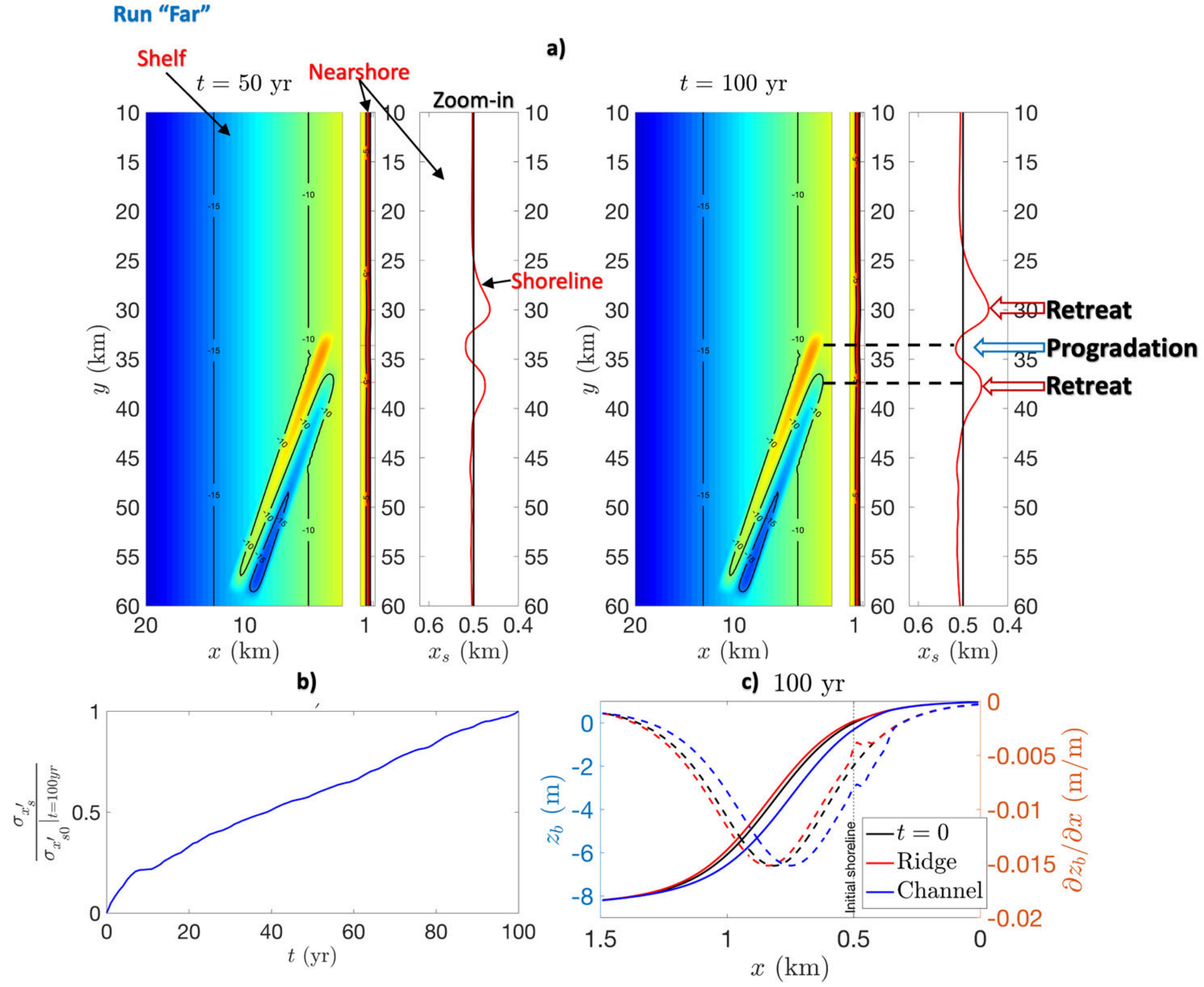

Figure 52 – a) Snapshots of the shelf/nearshore bed levels and shoreline positions x_s (red lines in the zoom-in panels) at t = 50 yr (left panels) and t = 100 yr (right panels). In each panel, the coast is located on the right. The black line denotes the initial shoreline position (t = 0 yr). Areas of shoreline progradation and erosion are also indicated. b) Cross-shore rms amplitude of shoreline undulations σ'_{x_s} (normalised by its value at t = 100 yr, $\sigma'_{x_{s0}}|_{t=100yr}$ =16 m) versus time. c) Cross-shore bed level profiles (solid lines, left axis) and their corresponding slopes $\partial z_b/\partial x$ (dashed lines, right axis) adjacent to the ridge crest (red lines) and adjacent to the channel (blue lines) at t=100 yr. The initial situation is depicted in black. The transects used for the nearshore bed level profiles are indicated by the two thick black dashed lines in panel a at t = 100 yr.

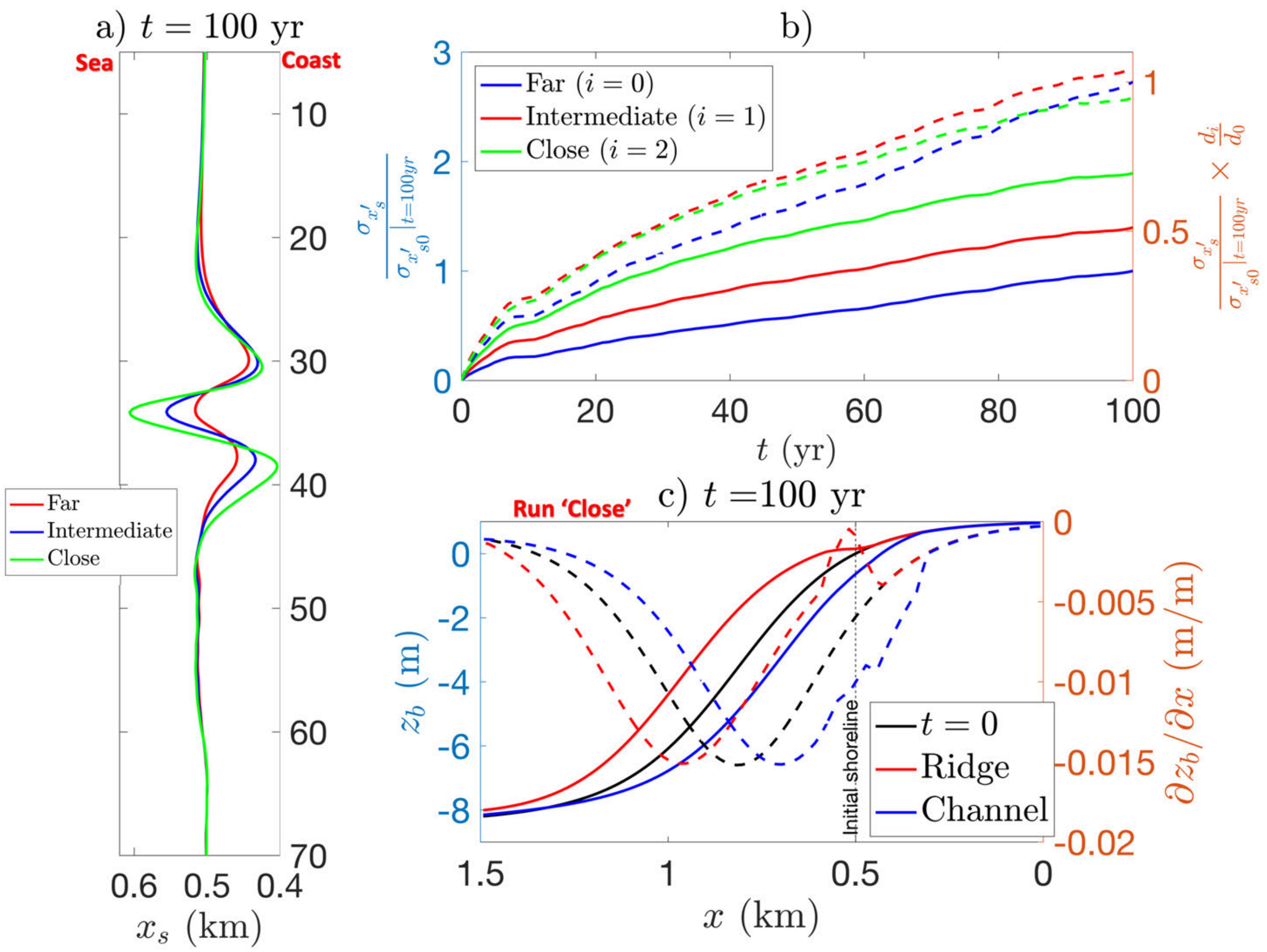

Figure 53 – a) Simulated shoreline profiles in the cases "Far" (red line), "Intermediate" (blue line) and "Close" (green line) at t = 100 yr. b) Left axis (solid lines): Rms amplitudes σ'_{x_s} (normalised by the value at t = 100 yr in the reference case, $\sigma'_{x_{s0}}$ = 16 m) of shoreline undulations in the three cases versus time. Right axis (dashed lines): Similar to the left axis, but multiplying the normalised amplitude $\sigma'_{x_s}/\sigma'_{x_{s0}}$ by the ratio d_i/d_0, with d_0 the distance of the ridge to the shoreline in the reference case (d_0 = 2 km) and d_i the distance of the ridges in the "Intermediate" case (d_1 = 1.5 km) and "Close" case (d_2 = 1 km). c) Cross-shore bed level profiles (solid lines, left axis) and their corresponding slopes $\partial z_b/\partial x$ (dashed lines, right axis) adjacent to the ridge crest (red) and adjacent to the channel (blue) at t = 100 yr in the "Close" case. The initial situation is depicted in black.

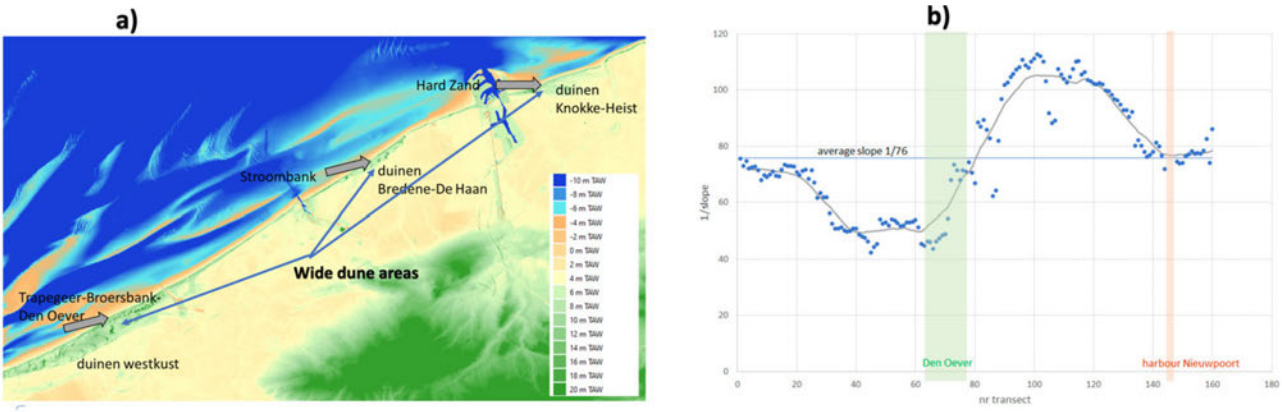

Figure 54 – a) Bathymetric map of the Belgian coastal zone, showing the formation of wide dune areas in the vicinity of three offshore located ridges. The presence of these dune areas indicates that shoreline progradation took place at these locations. b) The inverse of the slope of bathymetry profile of the breaker zone along the Belgian shoreline near the "Den Oever" ridge system.

3.1.5 Role of tides in the nearshore zone

The sediment transport in the Q2Dmorfo shoreline model is computed directly through bulk transport formulas based on the wave field, bypassing the explicit calculation of the flow field. Notably, tidal effects are not considered in this calculation. Tides may exert a significant influence on sediment transport in the nearshore, particularly in macro-tidal coastal environments like the Belgian coastal zone, potentially impacting shoreline evolution. Nevertheless, integrating tides into the bulk transport formulas of Q2Dmorfo proves challenging. This study undertakes an initial step toward creating a new tide model for incorporation into the Q2Dmorfo shoreline model. The primary objective is to quantify the relative contributions of tides and waves to the total longshore sediment transport. The approach, inspired by Longuet-Higgins (1970) and Southgate (1989), involves deriving expressions for wave-induced alongshore velocity ($v_w(x)$) and tidal velocity ($v_t(x,t)$). Subsequently, the relative contributions to the total sediment transport (averaged over waves and tides) are calculated. The summarized equations are provided below, with additional details available in Appendix 3: Development of an idealized coupled shelf-shoreline model

Wave- and tide-induced sediment transport

The total sediment transport (q_{tot}) is assumed to consist of a part due to waves (q_w) and a part due to tides (q_t):

$$q_{tot} = q_w + q_t. \qquad (8)$$

The non-linear interaction between tides and waves, as well as the additional stirring of sediment by tides are neglected. Wave-induced transport q_w (averaged over a wave period) is computed using Bailard (1981) formulae (see Appendix 3),

$$\begin{aligned} q_w(x) &= K_w\overline{V_w^3} = \frac{3}{2}K_w\hat{u}_w^2 v_w \\ V_w(x,t) &= v_w(x) + \hat{u}_w\cos(\omega t), \\ \hat{u}_w &= \frac{\omega H_{rms}}{2\sinh(\kappa H)}. \end{aligned} \qquad (9)$$

Here, $\hat{u}_w$ is the amplitude of the near-bed wave orbital velocity, K_w is a constant, the overline denote wave-averaging and v_w is the wave-induced current, which is given by the following system of equations:

$$\begin{aligned} v_w(x) &= \begin{cases} C_2 v_{w,b}\cdot(\frac{x}{x_b})^{p_1} + C_1 v_{w,b}\cdot(\frac{x}{x_b})^{1/3} & 0 < x < x_b, \\ C_3 v_{w,b}\cdot(\frac{x}{x_b})^{p_2} & x_b < x < \infty. \end{cases} \\ v_{w,b} &= \frac{5\pi}{12}\frac{\alpha}{c_f} g s^2 x_b^{1/3}\frac{\sin\theta_b}{\sqrt{gH_{rms,b}}}, \\ P &= \frac{\pi s N}{2\alpha c_f x_b^{1/3}}, \\ p_1 &= -\frac{2}{3} + \sqrt{\frac{4}{9} + \frac{1}{P}}, \\ p_2 &= -\frac{2}{3} - \sqrt{\frac{4}{9} + \frac{1}{P}}, \\ C_1 &= \frac{1}{1 - \frac{5}{9}P}, \\ C_2 &= \frac{p_2 - \frac{1}{3}}{p_1 - p_2} C_1, \\ C_3 &= \frac{p_1 - \frac{1}{3}}{p_1 - p_2} C_1. \end{aligned} \qquad (10)$$

Furthermore, ω is the wave angular frequency, κ is the wavenumber, H_{rms} is the root-mean-square averaged (rms) wave height, $v_{w,b}$ is the wave-induced current at the breaker line (x_b), H is the water depth, $H_{rms,b}$ and θ_b are, respectively, the rms wave height and wave angle at breaking, $s = \partial H/\partial x$ is the bottom slope, g is the gravity acceleration, ρ is the density, c_f is a friction coefficient, α is a breaking index, θ is the wave angle and N is a dimensionless constant. Values of all the parameters are provided in Table 14.

Tide-induced sediment transport q_t (averaged over M_2 tidal period) is computed as follows (see Appendix 3):

$$q_t(x,t) = K_t\langle v_t^3\rangle = \frac{3}{4}K_t\hat{v}_2^2\hat{v}_4\cos(2\phi_2 - \phi_4). \tag{11}$$

Here, brackets indicate averaging over one tidal period, K_t is constant, $\hat{v}_2$, $\hat{v}_4$ are the amplitudes of the M_2 and M_4 tidal components, respectively, ϕ_2,ϕ_4 are their corresponding phases. The above equation indicates that the phase difference between M_2 and M_4 tidal components ($2\phi_2 - \phi_4$) strongly determines the magnitude of the tide-induced sediment transport. If $2\phi_2 - \phi_4 = 90^\circ$, the transport vanishes, while it is maximum if the phase difference is 0°.

Results

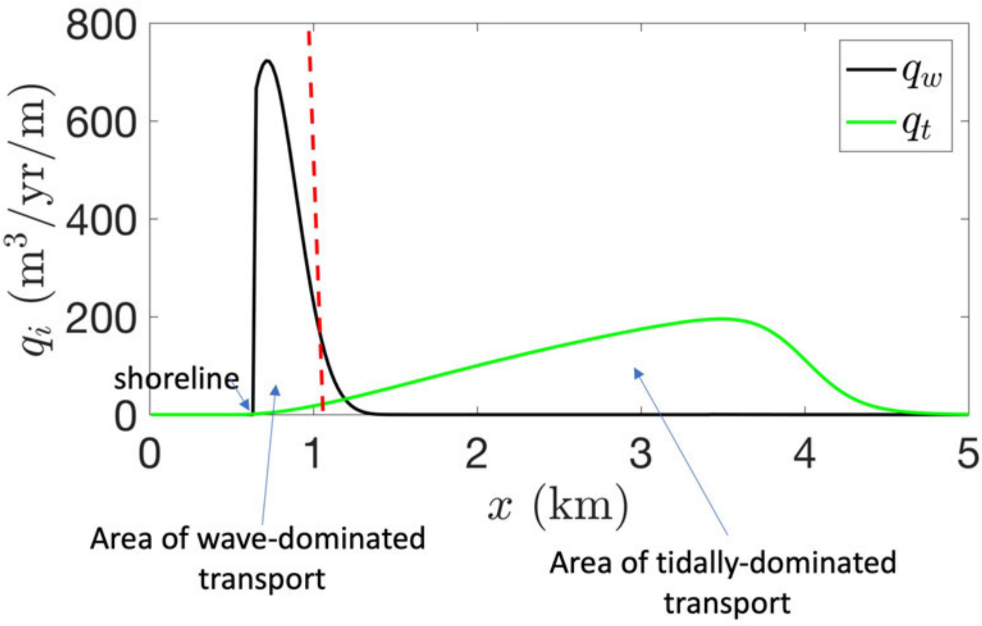

Figure 55 – Cross-shore profiles of wave- and tide-induced sediment transport.

Results of the wave and tide models are shown in Figure 55, which displays the cross-shore profiles of wave- and tide-induced sediment transports. This figure indicates that wave-induced sediment transport is the dominant transport in the breaker zone, while tide-induced transport becomes significant further offshore. These results are in qualitative agreement with those from the two complex models Flemco and Scaldis. Further improvements of these two models comprise further tuning by comparing the results with those simulated by Flemco and Scaldis models. These improvements are subject of future research.

3.1.6 Summary, conclusions and outlook

The primary objective of Work Package 2 (WP2) within the MOZES project was to quantify the impact of onshore migrating shoreface-connected sand ridges on the evolution of the adjacent shoreline. During the second year of the MOZES project, consisting of two main activities (Activity 1 and 2), efforts were concentrated on advancing the morphodynamic shelf model and the coupled shelf-shoreline model established in the first year. The specific goals were:

1. **Activity 1:** Further improve the morphodynamic shelf model (shelf bottom changes in time) by 1) incorporating a shelf bathymetry based on that of the Belgian shelf, and by 2) computing wave propagation on the shelf using the original SWAN model. In this model, the shelf bottom does change during the simulation.
2. **Activity 2:** Further refine the coupled shelf-shoreline model (morphostatic shelf and morphodynamic shoreline) by 1) using a synthetic ridge with geometry (length, width and orientation) similar to those of the Belgian shelf, 2) implementing a more realistic wave forcing, and 3) considering tides in the Q2Dmorfo shoreline model.

In the second year, the following four milestones were achieved:

1. A more realistic wave climate and representative background topography were established based on the bathymetric data and data from wave buoys offshore the Belgian coast.
2. The development of a morphodynamic shelf model marked an important step forward, enabling the simulation of self-developing shoreface-connected sand ridges (sfcr) by incorporating (for the first time!) wave-topography feedbacks. The simulated ridges closely resembled those observed on the Belgian shelf, although distinctions were noted, such as the less oblique nature of the simulated sfcr on their onshore segment and a tendency to underestimate alongshore spacing. These distinctions could be attributed to factors like the absence of tides in the model, the simplified wave forcing, and the exclusion of sea level rise (SLR).

31. Significant improvements were made to the coupled shelf-shoreline model, enabling the reproduction of observed shoreline progradation (erosion) adjacent to the ridge crest (channel) and the steeper bathymetry profile in the breaker zone near the channel compared to that near the ridge crest. Simulations with this model indicate that the observed onshore movement of sfcr on the Belgian shelf is likely to intensify shoreline retreat near the channel and progradation near the ridge crest.
32. Implementation of a new analytical tide model in the shoreline evolution model (Q2Dmorfo) revealed that wave-induced sediment transport dominates in the breaker zone, while tidae-induced transport becomes significant further offshore. These findings qualitatively align with results from the complex models Flemco and Scaldis.

The following list outlines the key enhancements planned for the morphodynamic shelf model and the coupled shelf-shoreline model in the third and fourth year of the MOZES project:

Morphodynamic Shelf Model:

- Application of periodic boundary conditions at the lateral boundaries.
- Inclusion of tides.
- Utilization of wave time series to drive the model.
- Consideration of sea level rise (SLR).

Coupled Shelf-Shoreline Model:

- Implementation of a dynamic onshore movement of the synthetic ridge, replacing the manual replacement of the ridge across the shelf.
- Incorporation of observed sea level rise and increased tidal amplitudes in the Belgian coastal zone.
- Enhancement of the tide model in Q2Dmodel through the introduction of additional sediment stirring by tides.

Ultimately, upon the successful simulations of the key features (orientation, dimension, alongshore spacing) of observed shoreface-connected sand ridges on the Belgian inner shelf by the morphodynamic shelf model, it will be coupled to the shoreline evolution model. This newly formed fully morphodynamic coupled shelf-shoreline model will facilitate the exploration of the impact of human interventions (e.g., harbour construction, nourishments) and sea level rise on the evolution of sfcr and the shoreline.

3.2 Research on natural feeding of the beach over shoreface connected ridges (WP3)

3.2.1 Introduction

In the first year of the MOZES-project, both the Scaldis-Coast and the FlemCo models were applied in order to investigate the longshore sediment transport along the Flemish coast and the sediment pathways in the area of the shoreface-connected sand ridges (sfcr). With regard to both the simulated longshore sediment transport and the sediment pathways, significant differences between the two models were found. The main differences between the model results can be summarized as follows (for more details see Dujardin *et al.,* 2023):

- The predicted longshore transport was significantly larger in the Scaldis-Coast compared to the FlemCo model.
- While the predicted sediment pathways showed a distinct cross-shore component in the area of the sand ridges (indicating a natural feeding of the beaches in these areas) in the FlemCo model, the pathways were mainly parallel to the coast according to the Scaldis-Coast model.

One of the main objectives of the second project year was therefore to investigate the reasons for the observed discrepancies between both models, with a focus on longshore sediment transport, wave and flow characteristics. To this end, we

- applied both models based on the original model settings (see Table 16 in Appendix 4: FlemCo and Scaldis-Coast parameter settings) and realistic wave and wind boundary conditions (i.e. measured time series at Westhinder station) with various model forcing combinations (tide, waves and wind) and compared the simulated
    i) longshore sediment transport,
    ii) its cross-shore distribution,
    iii) wave heights and directions and
    iv) tide- and wave-induced longshore currents (Section 3.2.2).
- applied both models based on identical wave model settings and non-realistic constant wave and wind boundary conditions with the full model forcing (i.e. tidal forcing together with wave and wind forcing) and compared the simulated
    i) longshore sediment transport and
    ii) wave heights and directions (Section3.2.3).

3.2.2 Scaldis-Coast and FlemCo compared; using realistic wave and wind boundary conditions

Introduction

As a first step, both models were run for the representative period from 14 March 2014 to 13 May 2014, which was used in the FlemCo model in earlier studies by Grasmeijer et al. (2020) and Dujardin et al. (2023). As a wave forcing, realistic wave and wind boundary conditions based on the measured times series at Westhinder station were used. In the Scaldis-Coast model, the representative period results in very similar longshore transport rates compared to the previous Scaldis-Coast model runs, which were based on time period from November 2015 to November 2016 (Dujardin et al., 2023). This means that the use of different simulation periods by FlemCo and Scaldis-Coast in the study by Dujardin et al. (2023) does not or hardly hold responsible for the observed discrepancy in the predicted longshore sediment transport by the two models. In order to find out whether a specific model forcing (tide, waves or wind) or which combination of forcings causes differences in the predicted longshore transport, all forcings were switched on stepwise in both models (see Table 8). Specifically, the two models were run with:

- only tidal forcing,
- tidal forcing together with wind forcing,
- only wave forcing,
- wave forcing together with wind forcing,
- tidal forcing together with wave forcing,
- tidal forcing together with wave and wind forcing.

In all simulations, both the flow and the wave module of the models were coupled. In the case of the FlemCo model, all simulations shown in Table 8.

were performed based on a maximum flow and wave grid resolution in the nearshore zone (between the coastline and ca. 2 km offshore) of ca. 46 m x 46 m (as was used earlier in Dujardin *et al.*, 2023) and of ca. 23 m x 23 m, the latter being comparable to the resolution in the Scaldis-Coast model (up to 20 m at the beaches). The numerical and physical model settings are the same for both models as applied earlier by Dujardin *et al.* (2023) (see Table 16 in Appendix 4: FlemCo and Scaldis-Coast parameter settings).

Table 8 – Overview of the Scaldis-Coast and FlemCo sensitivity runs based on realistic wave and wind boundary conditions.

Scaldis-Coast Run ID	FlemCo Run ID	Tidal forcing	Wave forcing	Wind forcing	Max. FlemCo resolution
MO6_004	**049a**	On	Off	Off	46 m x 46 m
	049b	On	Off	Off	23 m x 23 m
MO6_008	**050a**	On	Off	On	46 m x 46 m
	050b	On	Off	On	23 m x 23 m
MO6_005	**051a**	Off	On	Off	46 m x 46 m
	051b	Off	On	Off	23 m x 23 m
MO6_007	**052a**	Off	On	On	46 m x 46 m
	052b	Off	On	On	23 m x 23 m
MO6_003	**048a**	On	On	Off	46 m x 46 m
	048b	On	On	Off	23 m x 23 m
MO6_009	**047a**	On	On	On	46 m x 46 m
	047b	On	On	On	23 m x 23 m

Longshore sediment transport

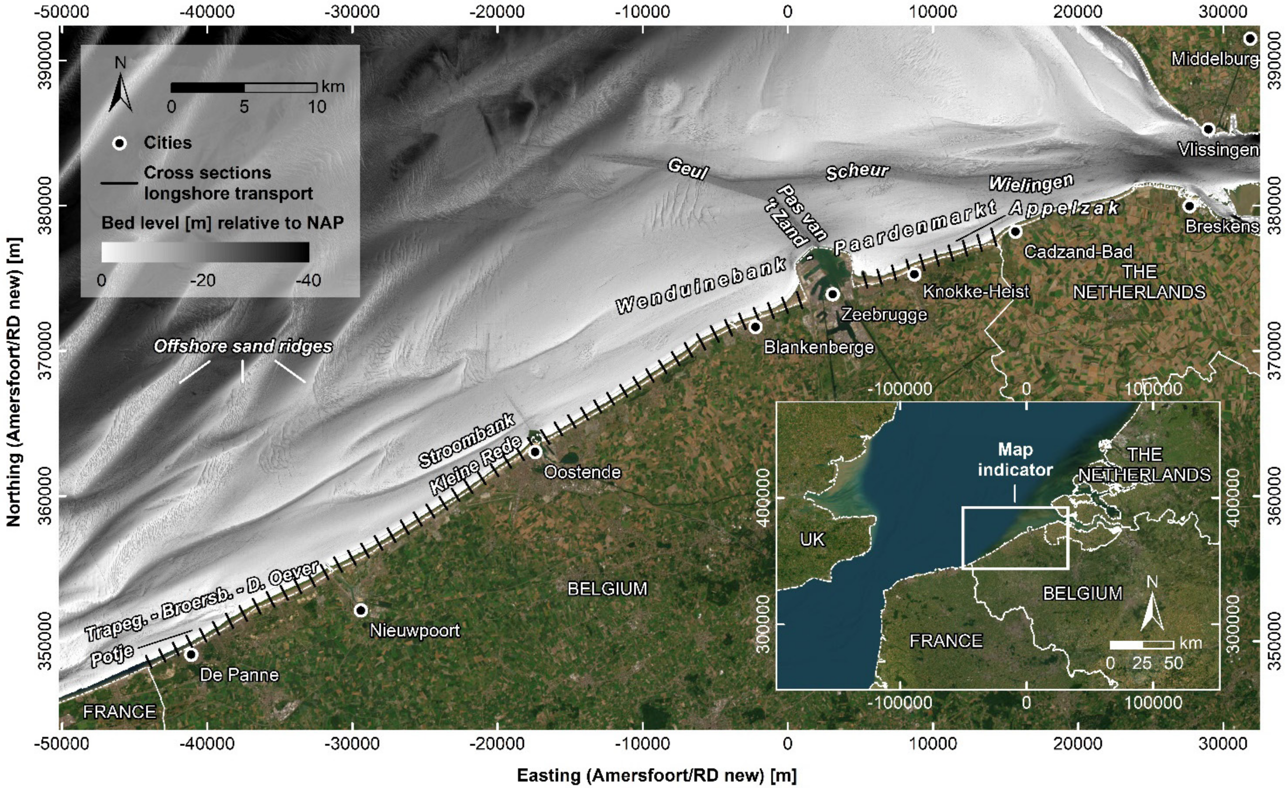

Figure 56 – Satellite image (Esri 2022) and bathymetry of the Belgian (Flemish) coast and the Western Scheldt mouth including the main navigation channel Geul-Scheur-Wielingen and the connecting channel Pas van ’t Zand to Zeebrugge harbour as well as the sand ridges in the western part of the study area. The coastal bathymetry is derived from several sources of data according to Dujardin et al. (2023) . The black lines indicate cross sections based on which the longshore sediment transport along the Belgian coast was simulated. The coordinates are given in km according to Amersfoort/RD New.

The longshore sediment transport in the Scaldis-Coast and FlemCo models was determined based on the simulated cumulative suspended and bedload sediment transport in the ca. 750 m nearshore zone (between the beach and approximately the -5 m TAW/-7.33 m NAP contour) of the Belgian coast. This zone is indicated by the black cross-sections in Figure 56 and is believed to be a good approximation of the wave breaker (surf) zone at the Belgian coast (cf. Dujardin *et al.*, 2023).

Figure 57 shows that the predicted longshore sediment transport is sensitive to the grid resolution applied in the FlemCo model. A higher grid resolution results in slightly larger longshore transport, especially in those areas along the Flemish coast where wave related longshore transport is more dominant. Utilizing a finer grid resolution improves the representation of the currents in the breaker zone, resulting in stronger wave-induced currents and consequently in larger wave-induced sediment transport. Since (i) the predicted longshore transport is sensitive to the grid resolution and (ii) a maximum resolution of 23 m x 23 m in the FlemCo model better coincides with the maximum resolution of the Scaldis-Coast model, all following FlemCo simulations are executed using the 23 m x 23 m resolution.

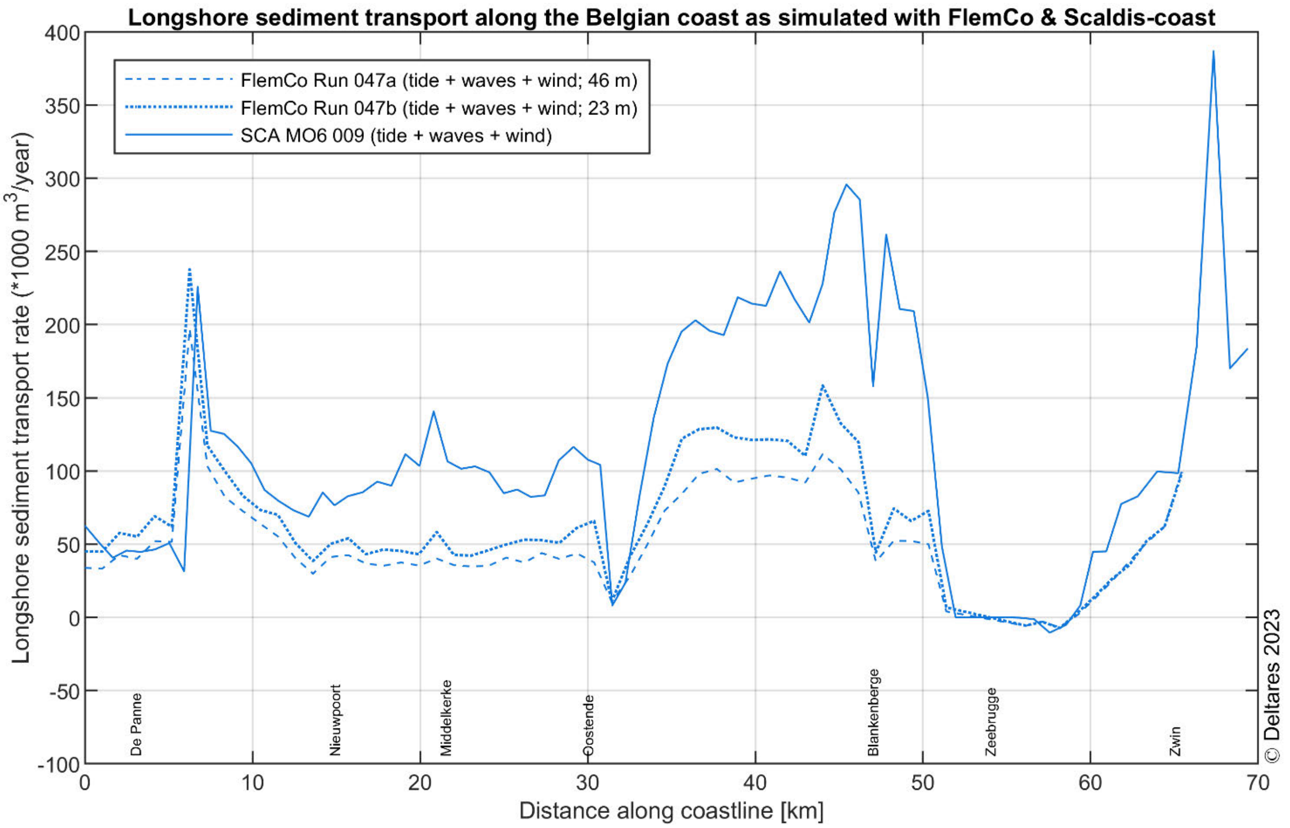

Figure 57 – Longshore sediment transport as simulated with the FlemCo model based on the complete model forcing (i.e. tide, wind and wave) and the two different maximum flow and wave grid resolutions of 46 m x 46 m and of ca. 23 m x 23 m. The model was run for the period from 14 March to 13 May 2014. For comparison, the longshore sediment transport according to the corresponding Scaldis-Coast model run is illustrated.

Figure 58 illustrates the longshore transport as predicted by the Scaldis-Coast and FlemCo model with tide only as well as tide and wind forcing. Generally, the predicted longshore transport agrees well between both models for both types of forcing, although the transport is higher according to FlemCo compared to Scaldis-Coast, especially around the peak at the Broersbank (ca. 7 km east of the French border). When adding wind to the tide, the predicted longshore transport slightly increases in the FlemCo model and to an even smaller degree in the Scaldis-Coast model. This means that wind has a minor effect on the tide-induced transport.

This conclusion however should be treated with care. The Scaldis-Coast results shown here, were produced with an older code-base of openTelemac (v7p2_cookie), which uses a constant wind shear stress coefficient. This coefficient was set rather low, for simulating fair weather conditions. More recent code-bases of the openTelemac modelling suite use by default a shear stress coefficient which varies with the wind speed, as is the case in dFlow-FM. Simulations of the Ciara storm (7 – 9 February 2020) conducted with the Scaldis-Coast model and openTelemac version v8p4 show a better fit of the current magnitude and directions during stormy conditions when the varying wind stress coefficient is applied (personal communication ir. Bart De Maerschalck, December 2023 – January 2024). Also the resulting annual residual alongshore sediment transport increases considerably when this new setting is applied (Figure 59).

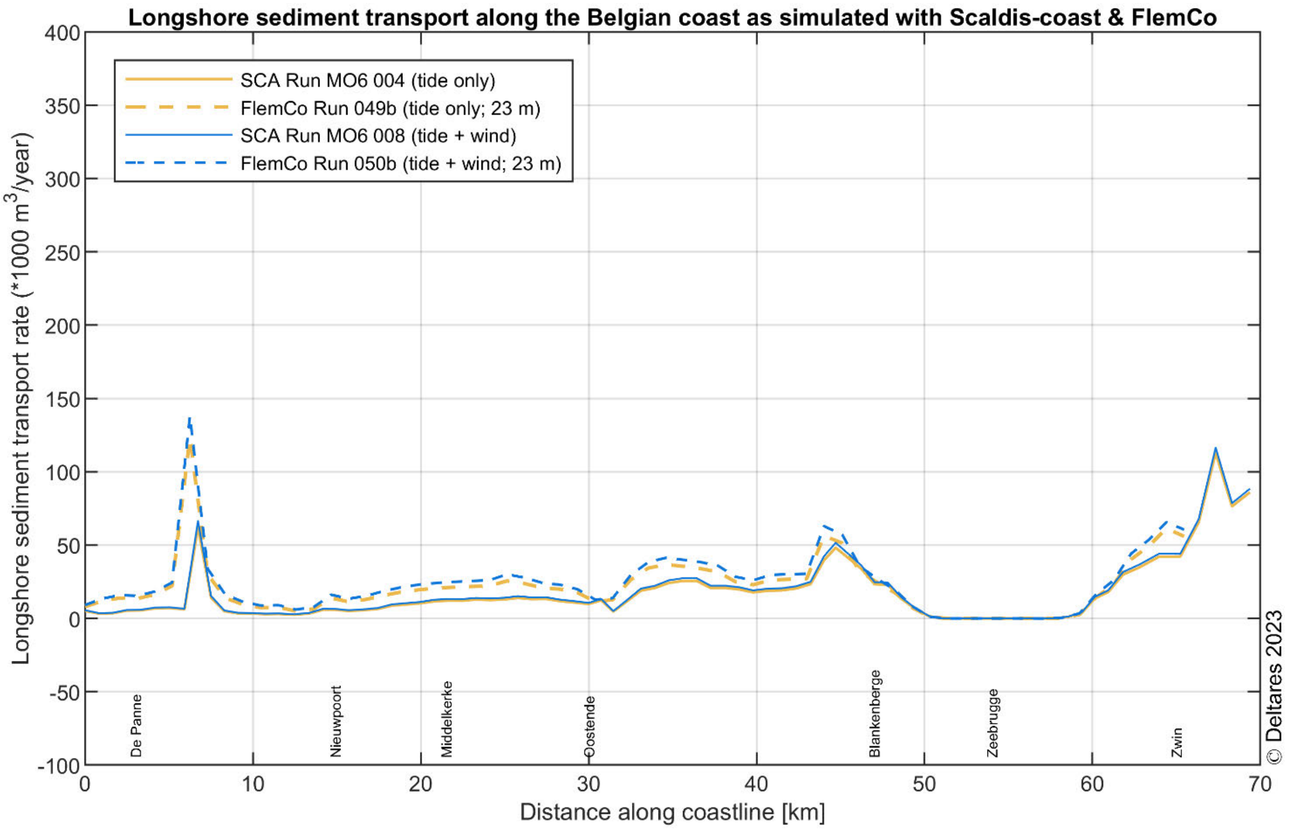

Figure 58 – Longshore sediment transport as simulated with the Scaldis-Coast and FlemCo model based on tide only (yellow lines) and tide + wind (blue lines) forcing. Both models were run for the period from 14 March to 13 May 2014.

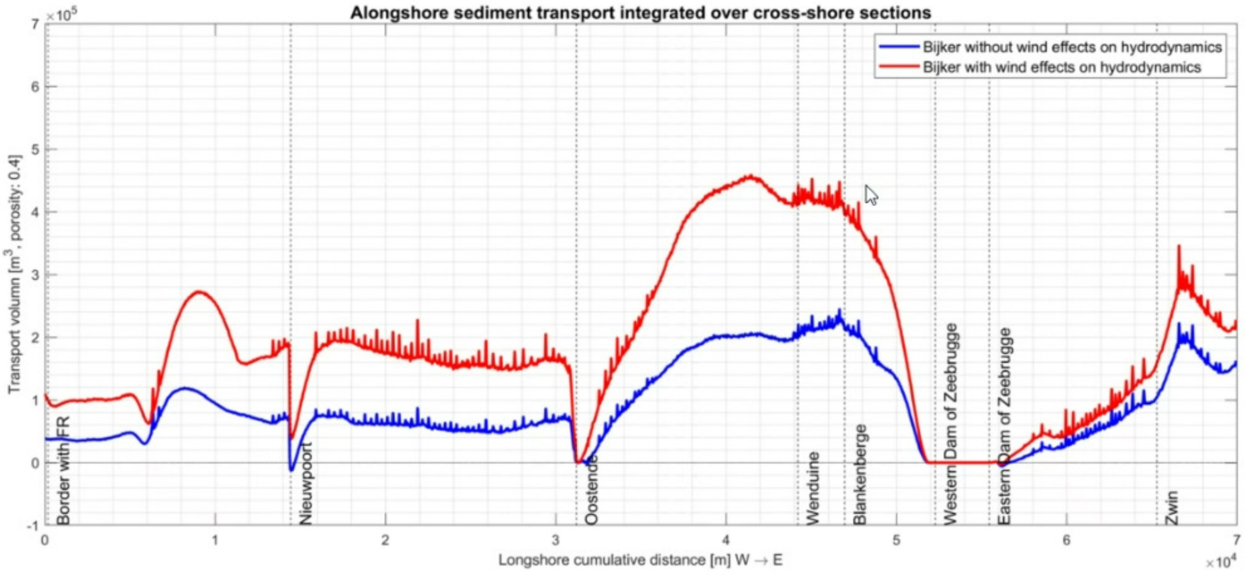

Figure 59 – Longshore sediment transport as simulated with Scaldis-Coast (openTelemac v8p4) with constant and varying wind stress coefficient in the hydrodynamic TELEMAC2D module. The wave module TOMAWAC takes into account wind in both runs. The half year period from 7 November 2013 to 7 May 2014 was simulated. Please note that the results shown here are from morphodynamic runs (thus with bed update), where all other results shown in this section are morphostatic (without bed update).

Based on the waves only forcing, the longshore transport becomes slightly negative (i.e. orientated towards the west) in the FlemCo model and clearly negative in the Scaldis-Coast model (Figure 60). The westward orientated transport is associated with the transport due to waves from the northern to north-eastern sector which – in the case of wave only forcing – seem to be dominant compared to the transport caused by waves from the south-western to north-western sector. Wind together with wind forcing results in clearly higher longshore (eastward) transport compared to the wave only forcing in both models, although the increase in transport is significantly larger in the Scaldis-Coast than in the FlemCo model, particularly between Oostende and Zeebrugge harbour as well as east of Zeebrugge harbour.

Tide and wave forcing (i.e. without wind) result in similar longshore transport in both models (Figure 61). When adding wind (causing wave growth and wind-induced currents), however, the transport increases by up to factor four in the FlemCo model but up to factor ten in the Scaldis-Coast model, resulting in a much larger longshore transport in the Scaldis-Coast model based on the full model forcing (for the comparison with earlier studies see Figure 62). The significant increase in longshore transport when adding wind to the model was also observed in the simulations with waves without tide (cf. Figure 60 but not in the simulations with tide without waves (cf. Figure 58). This means that it is the effect of the wind on the waves and not on the tide that causes a substantial increase of the longshore transport when wind is added to the models (for this version of the modelling suites, see above).

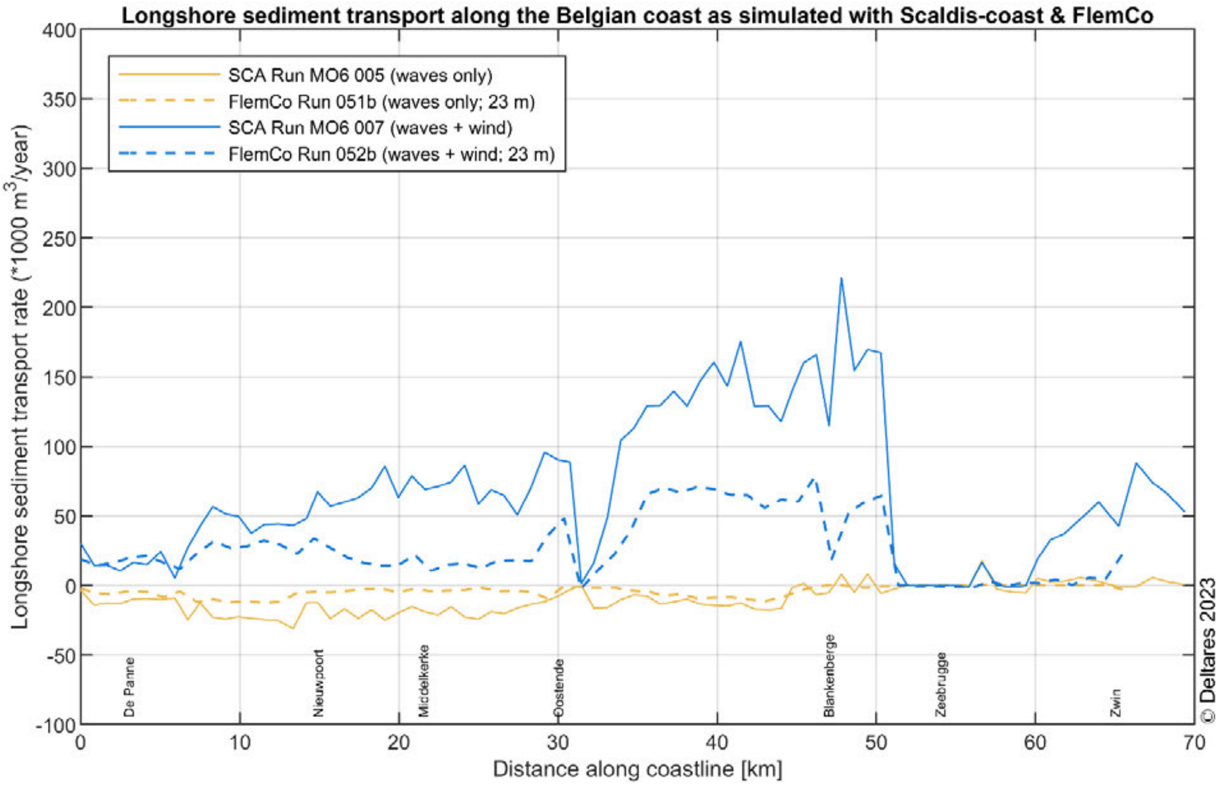

Figure 60 – Longshore sediment transport as simulated with the Scaldis-Coast and FlemCo model based on wave only (yellow lines) and wave + wind (blue lines) forcing. Both models were run for the period from 14 March to 13 May 2014.

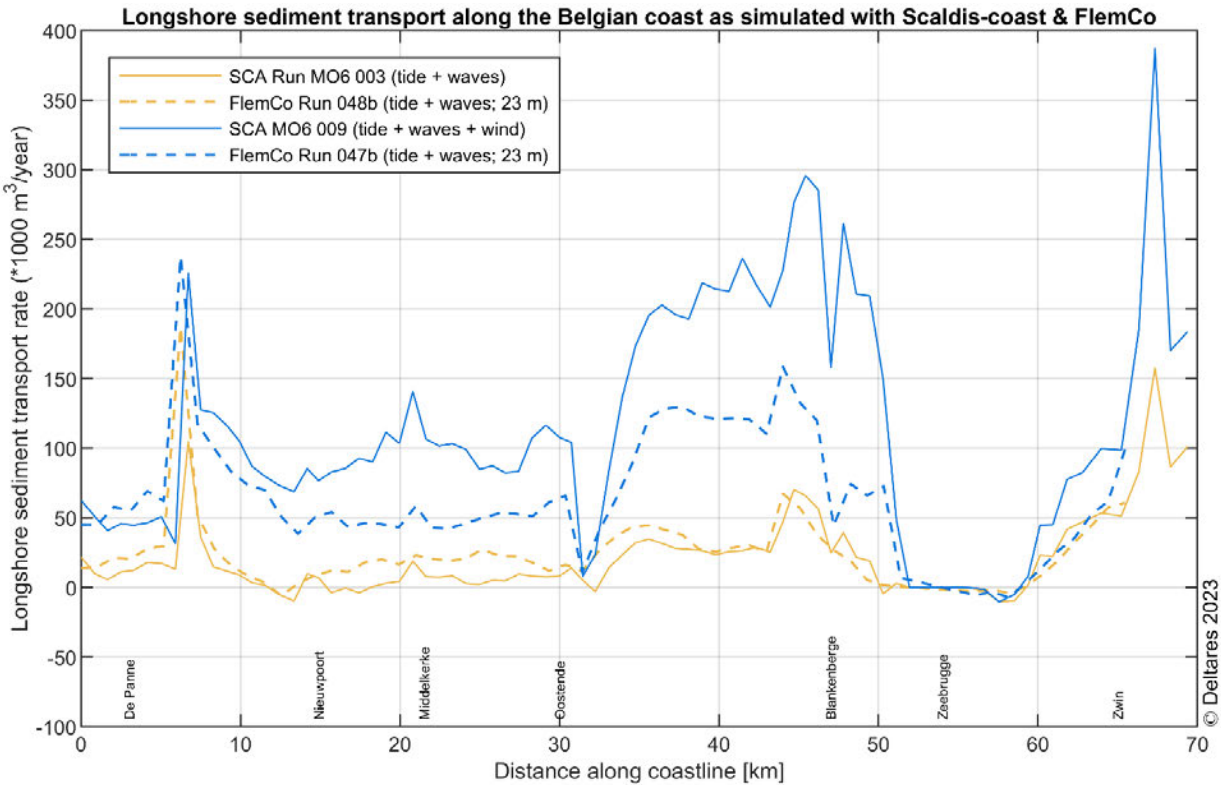

Figure 61 – Longshore sediment transport simulated with the Scaldis-Coast and FlemCo model based on tide + wave (yellow lines) and tide + wave + wind (blue lines) forcing. Both models were run for the period from 14 March to 13 May 2014.

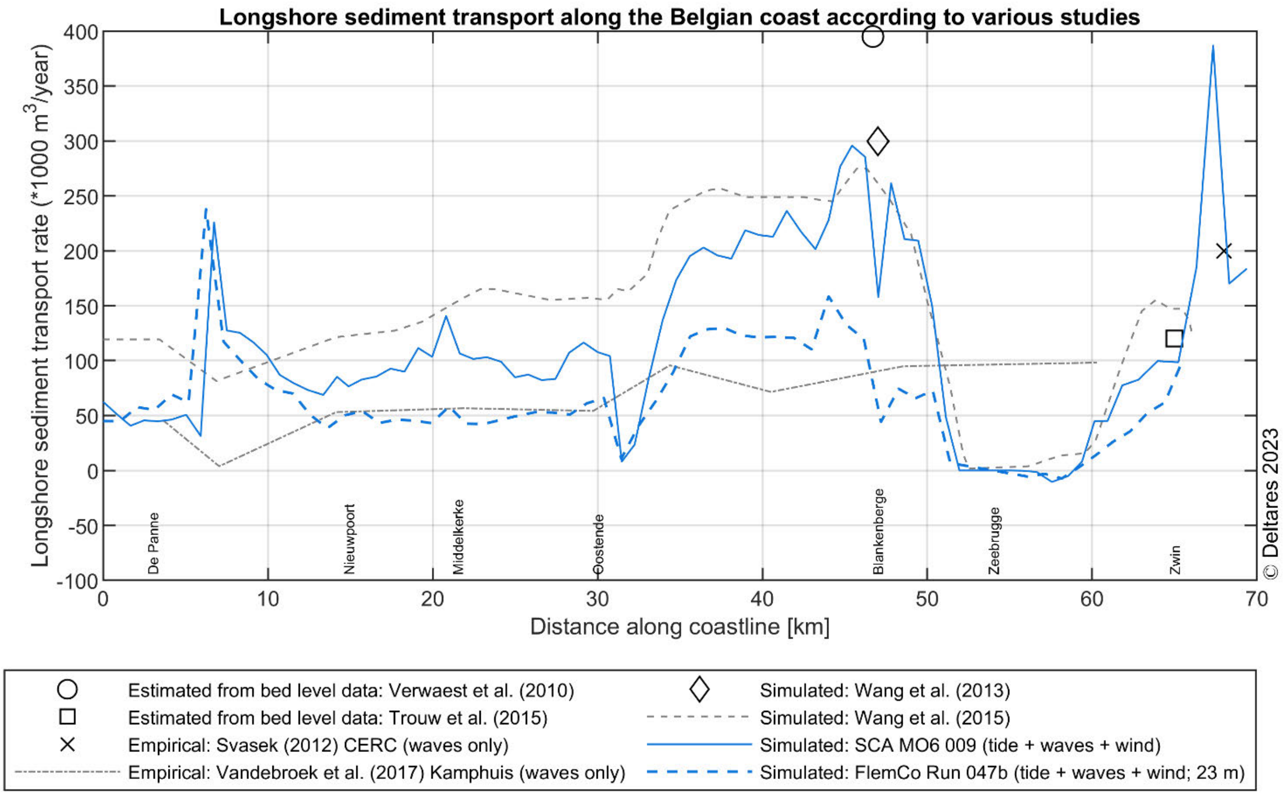

Figure 62 – Longshore sediment transport simulated with the Scaldis-Coast and FlemCo model based on tide + wave + wind (blue lines) forcing and comparison with the longshore sediment transport according to earlier studies. Both models were run for the period from 14 March to 13 May 2014.

Cross-shore distribution of the longshore sediment transport

The previous section showed the variations in longshore sediment transport along the Belgian coast in the ca. 750 m nearshore zone (between the beach and approximately the -5 m TAW/-7.33 m NAP contour) as calculated by the Scaldis-Coast and FlemCo models for different types of hydrodynamic forcing (Table 8).

In this section, the cross-shore distribution of the simulated yearly residual longshore sediment transport is analysed. Figure 63 shows a transect perpendicular to the coast, ca. 5 km west of Oostende. The transects starts at the sea dike between the coastal towns of Mariakerke and Raversijde, and goes over the Kleine Rede gully and the Stroombank sand ridge. The FlemCo model predicts slightly higher alongshore sediment transport than the Scaldis-Coast model in the case of tide + wind forcing (red lines). The tide driven sediment transport gradually increases from the shore till the deepest part of the gully. Seawards of the sand ridge the tide driven sediment transport is almost constant. For the simulations forced by waves + wind (blue lines), the Scaldis-Coast model clearly predicts higher alongshore sediment transport. Both models predict a peak in wave driven sediment transport on the intertidal beach, although this peak is higher and broader in the Scaldis-Coast model. A secondary peak can be observed on the crest of the sand ridge; again with higher values in the Scaldis-Coast model. Please note how the modelled (wave driven) alongshore transport in the breaker zone is in good agreement with the idealised model results shown in §3.1.5, Figure 55.

When comparing the full forcing (tides + waves + wind; yellow lines), the peak in wave driven alongshore sediment transport is broadened even more in the Scaldis-Coast model. This can be attributed to the changing water levels when the tide is added to the model. This effect can also be seen in the FlemCo model, but is not as pronounced. On the seaward flank of the sand ridge, the interaction between tides and waves also increases the sediment transport.

The same general patterns as described above, can be observed in Figure 64, showing a transect from the shoreline at Koksijde over the Potje gully, Broersbank and Trapegeer sand ridges into the Westdiep gully. Mainly wave driven alongshore sediment transport occurs on the intertidal beach (with a broadened peak under influence of the tides' water level variations). The tidally driven alongshore sediment transport increases from the shore till the crest of the Broersbank, and decreases again further offshore in deeper water. For the whole shallow area between the Trapegeer sand ridge (at the 3 km mark) and the Potje gully the wave action increases the alongshore sediment transport, when compared to the solely tidally driven transport. Again, the predicted tidally driven alongshore sediment transport is higher in FlemCo than in Scaldis-Coast. However, for this transect, the tidally driven sediment transport in the FlemCo model does not reach a constant value further offshore, but it increases again in the Westdiep gully.

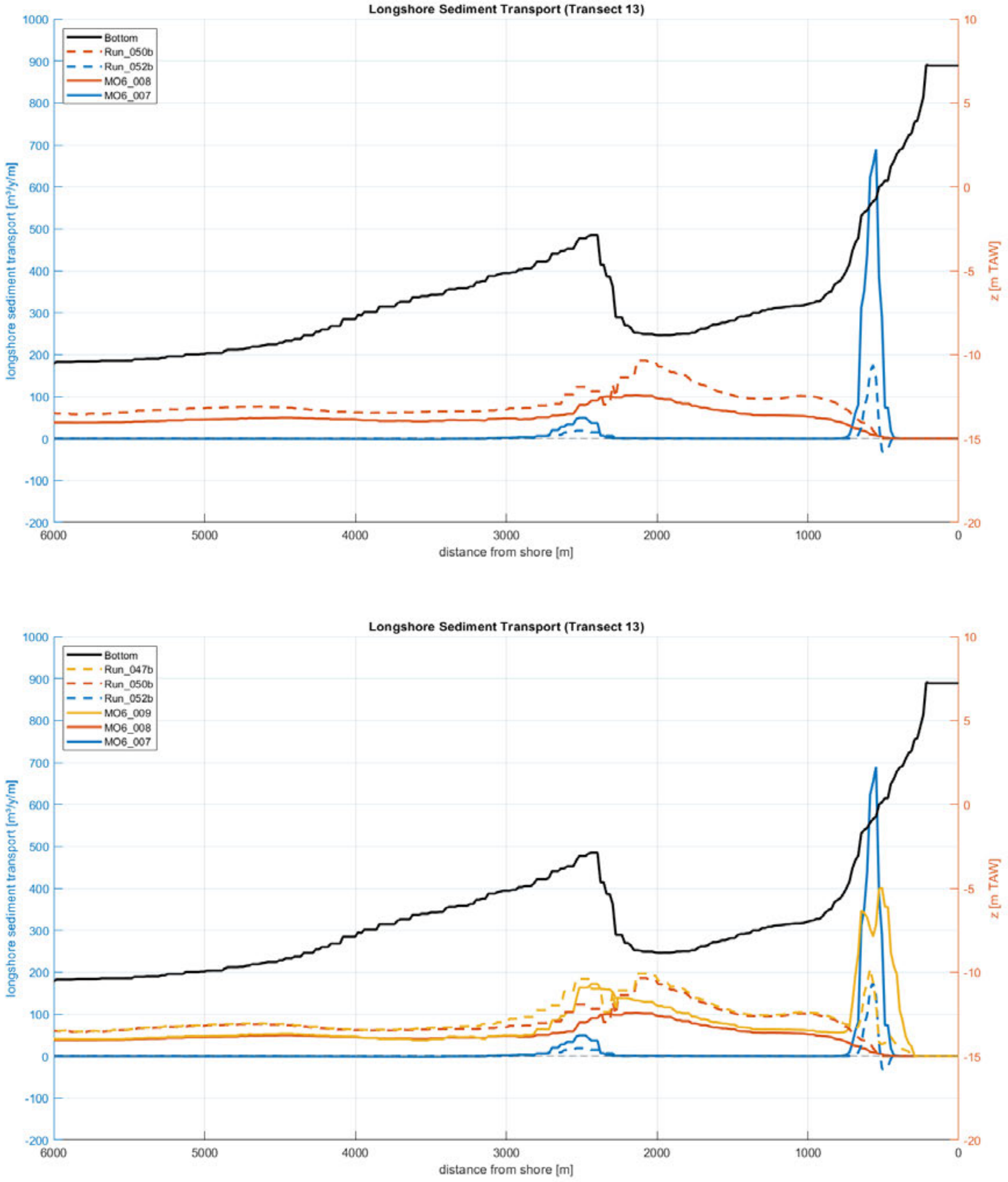

Figure 63 – Cross-shore distribution of the longshore sediment transport simulated with the Scaldis-Coast and FlemCo models; transect over the Stroombank and Kleine Rede, ca. 5 km west of Oostende. Full lines show Scaldis-Coast results; dashed lines show FlemCo results. Top panel: based on tide + wind (red lines) and waves + wind (blue lines) forcing. Bottom panel: as top panel, with tides + waves + wind forcing added (yellow lines). Both models were run for the period from 14 March to 13 May 2014.

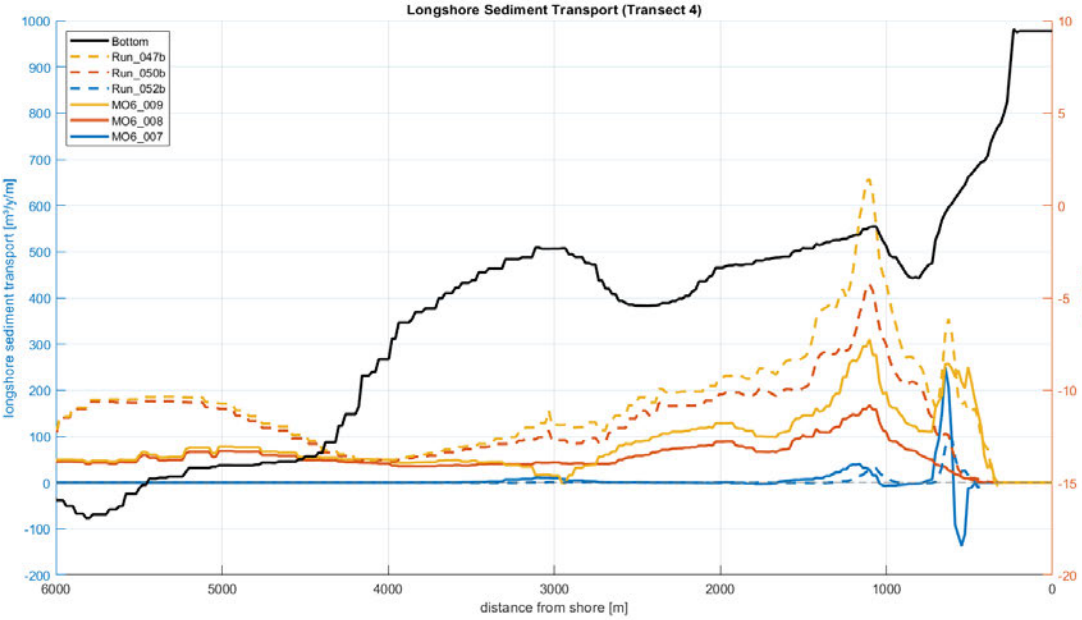

Figure 64 – Cross-shore distribution of the longshore sediment transport simulated with the Scaldis-Coast and FlemCo models; transect over the Trapegeer, Broersbank and Potje gully at Koksijde. Full lines show Scaldis-Coast results; dashed lines show FlemCo results. Blue lines: waves + wind forcing; red lines: tide + wind forcing; yellow lines: tides + waves + wind forcing. Both models were run for the period from 14 March to 13 May 2014.

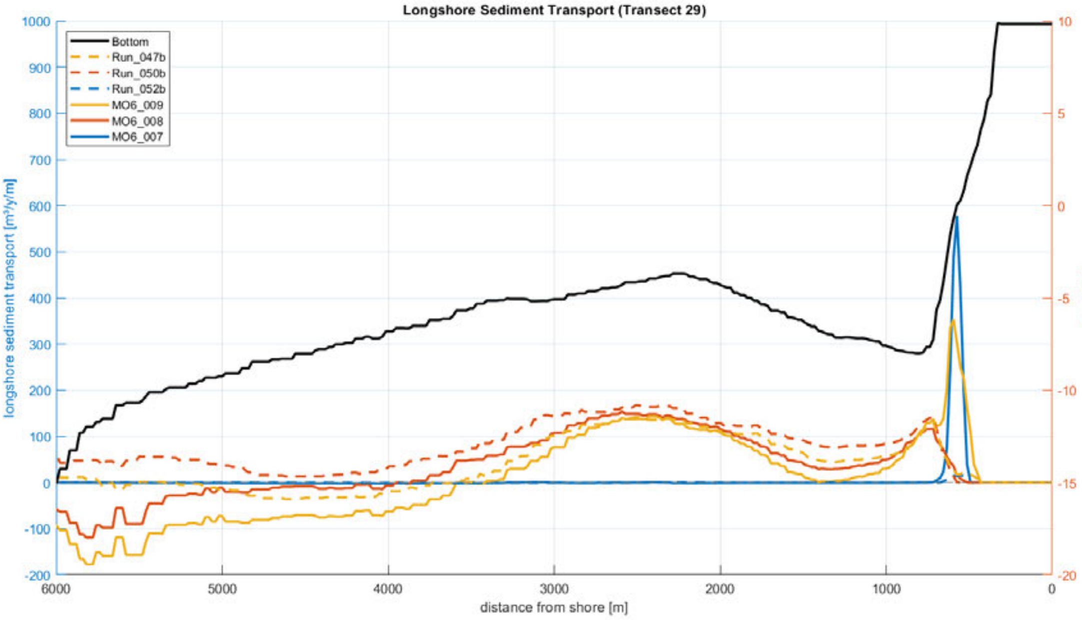

Figure 65 – Cross-shore distribution of the longshore sediment transport simulated with the Scaldis-Coast and FlemCo models; transect over the Paardenmarkt sand ridge and Appelzak gully at Knokke-Zoute. Full lines show Scaldis-Coast results; dashed lines show FlemCo results. Blue lines: waves + wind forcing; red lines: tide + wind forcing; yellow lines: tides + waves + wind forcing. Both models were run for the period from 14 March to 13 May 2014.

Figure 65 shows a transect at Knokke-Zoute, from the sea dike over the Appelzak gully and the Paardenmarkt sand ridge into the Wielingen channel. Remarkably is the absence of a wave driven transport peak on the intertidal beach in the FlemCo model. This seems to be caused by the groyn fields present in this area (Figure 68). The implementation of the groyn fields in the models, and its impact on the simulation results is discussed in §3.2.3. The Scaldis-Coast model simulates a tidally driven residual longshore sediment transport to the Southwest (ebb direction) on the seaward flank of the Paardenmarkt sand ridge. This residual transport to the Southwest is further enhanced by the interaction with the waves. The FlemCo model shows a small residual transport in the flood direction (red dashed line), which is counteracted by the interaction with the waves (yellow dashed line lies lower than the red dashed line).

Figure 66 and Figure 67 show the yearly residual transport for wave + wind forcing (top panels) and tide + wind forcing (bottom panels) for the Scaldis-Coast and FlemCo model respectively. The Scaldis-Coast model shows more intense yearly residual sediment transport under wave forcing (Figure 66, top panel) than the FlemCo model (Figure 67, top panel). The large vectors originating from the Zeebrugge breakwaters in the Scaldis-Coast model should be ignored, as they are numerical artifacts, probably due to the models wetting/drying scheme and the setting of the minimum water depth, kept at its default value of 0 cm. Tidally driven transport is a bit more intense in the FlemCo model (compare bottom panels of Figure 66 and Figure 67).

What is immediately noticeable in these figures, is how the wind-driven residual transport mainly occurs in a narrow zone on the shoreface and beaches (above the -5 m TAW isobath), and to a lesser extent on the shallow crests of the sand ridges (Smalbank, Stroombank, Wenduine bank, Vlakte van de Raan). The tide-driven residual transport is most pronounced in the tidal gullies (Westdiep, Potje, Kleine Rede, Grote Rede, Wielingen, Appelzak), in front of the Zeebrugge harbour breakwaters and over the top of the shoreface connected sand ridge Den Oever. For the names and locations of sand ridges and tidal gullies the reader is kindly referred to Figure 41.

However, the combined effect of tidally driven and wave driven residual alongshore sediment transport is not a simple addition of these components. Rather, non-linear interactions between the two components occur. This can be observed in the plan view of the model results shown in Figure 68 and Figure 69: both models show little to no residual transport in the shallow area connecting Baai van Heist to the Paardenmarkt sand ridge for the runs with only waves or tide forcing. However, when both forcings are applied, in this area a residual transport to the Northwest occurs in both models.

Figure 70 and Figure 71 zoom in on the shoreface connected sand ridge Den Oever, where an increase of the modelled wave-and tide-driven residual sediment transport could be observed for the Scaldis-Coast and FlemCo models (Figure 66 and Figure 67). On the nearshore part of the Den Oever sand ridge the wave-induced residual transport (indicated by blue arrows) is clearly directed towards the coast in both models. However, when reaching the upper shoreface and beach, the transport vectors are scattered, mostly directed along- and even a bit offshore. In the plots for the full forcing (tide + wave + wind) no more coastwards directed vectors for residual transport (indicated by golden arrows) can be observed in the model results.

It seems these models are not able to capture/parametrize the complex 3D currents in the breaker zone – which are assumed to be responsible for the process of natural feeding of the coast – with their current 2DH (depth averaged) setup. To test the assumption of natural feeding further, we think the setup of a 3D version (of a subdomain) of the models will be needed in order to resolve the 3D flow patterns in the breaker zone.

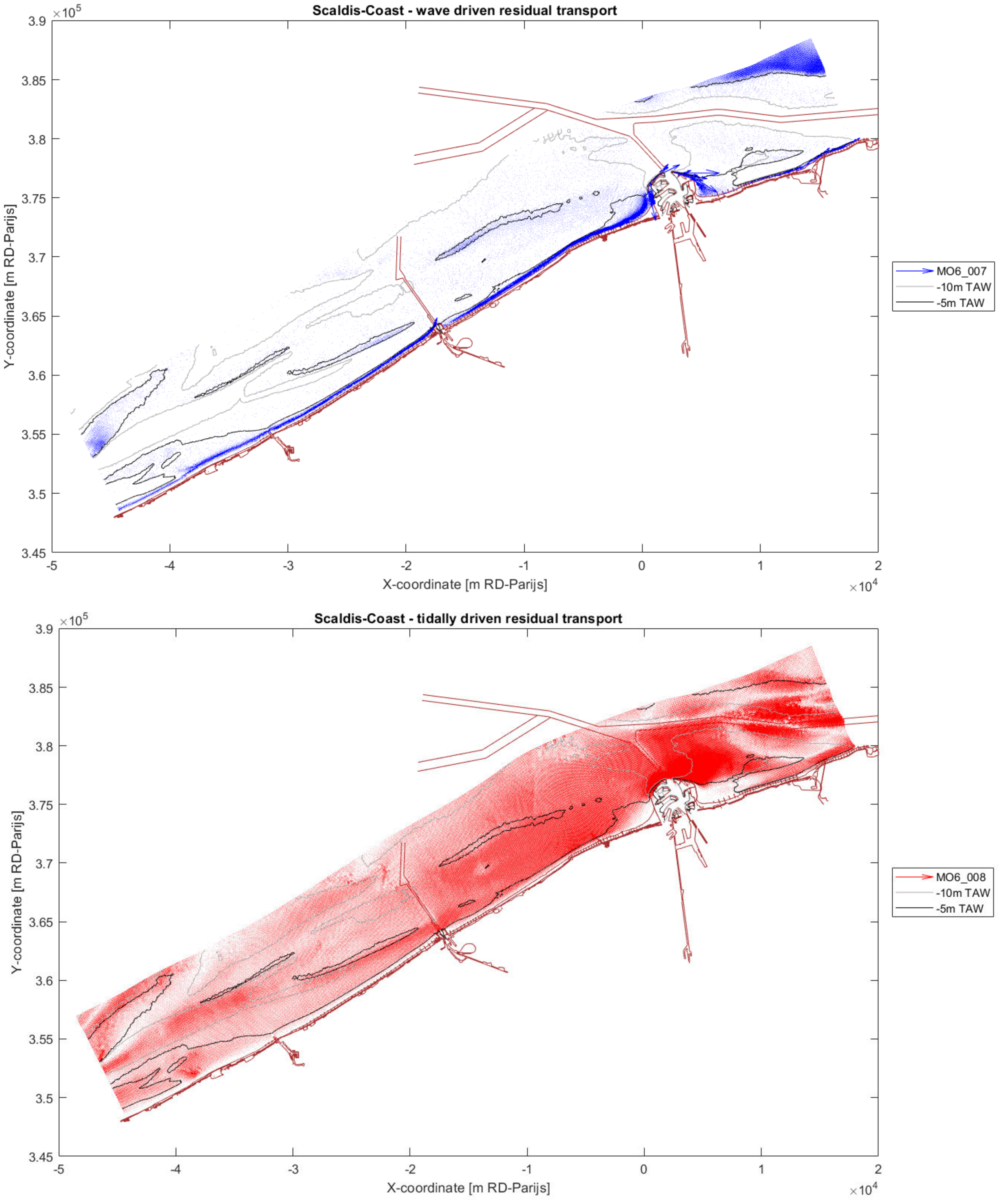

Figure 66 – Yearly residual sediment transport along the Belgian coast as simulated by Scaldis-Coast model for wave + wind forcing (blue) and tide + wind forcing (red). The large blue vectors originating from the Zeebrugge breakwaters should be ignored, as they are numerical artifacts, probably due to the models wetting/drying scheme.

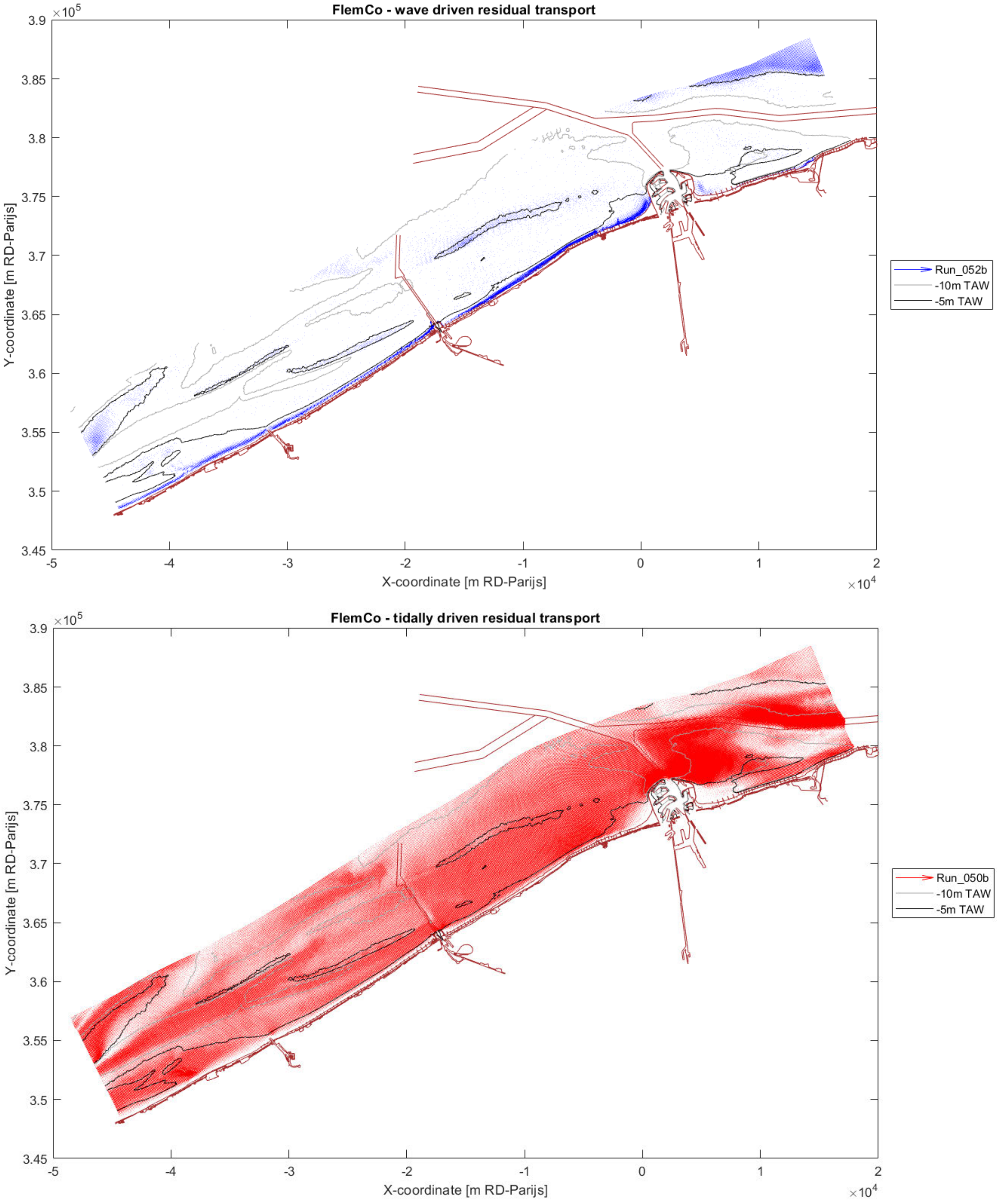

Figure 67 – Yearly residual sediment transport along the Belgian coast as simulated by FlemCo model for wave + wind forcing (blue) and tide + wind forcing (red).

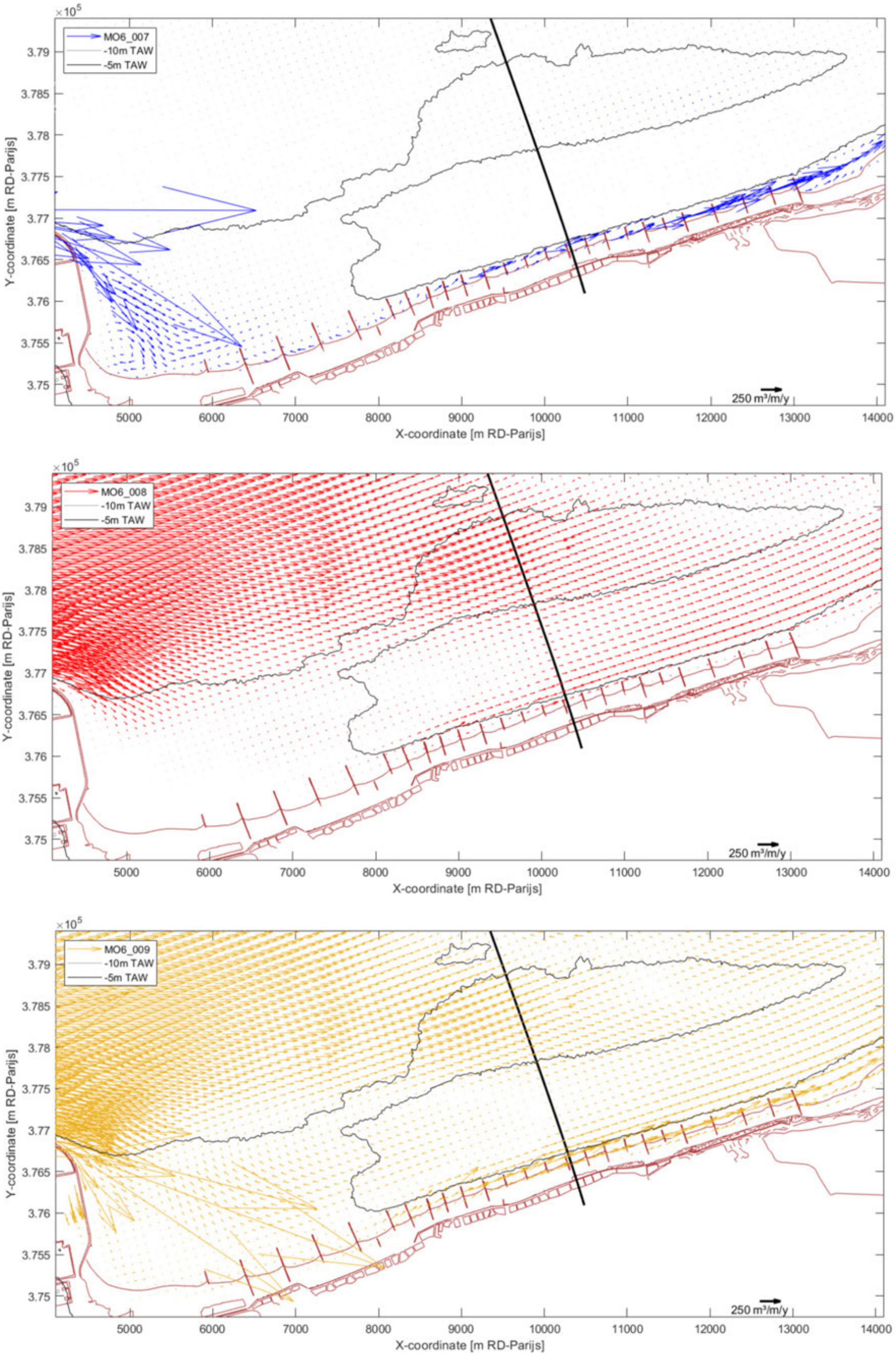

Figure 68 – Yearly residual sediment transport in the area east of Zeebrugge as modelled by Scaldis-Coast: wave forcing (blue arrows, top row), tide forcing (red arrows, middle row) and full hydrodynamic forcing (golden arrows, bottem row). The black line indicates the transect shown in Figure 65.

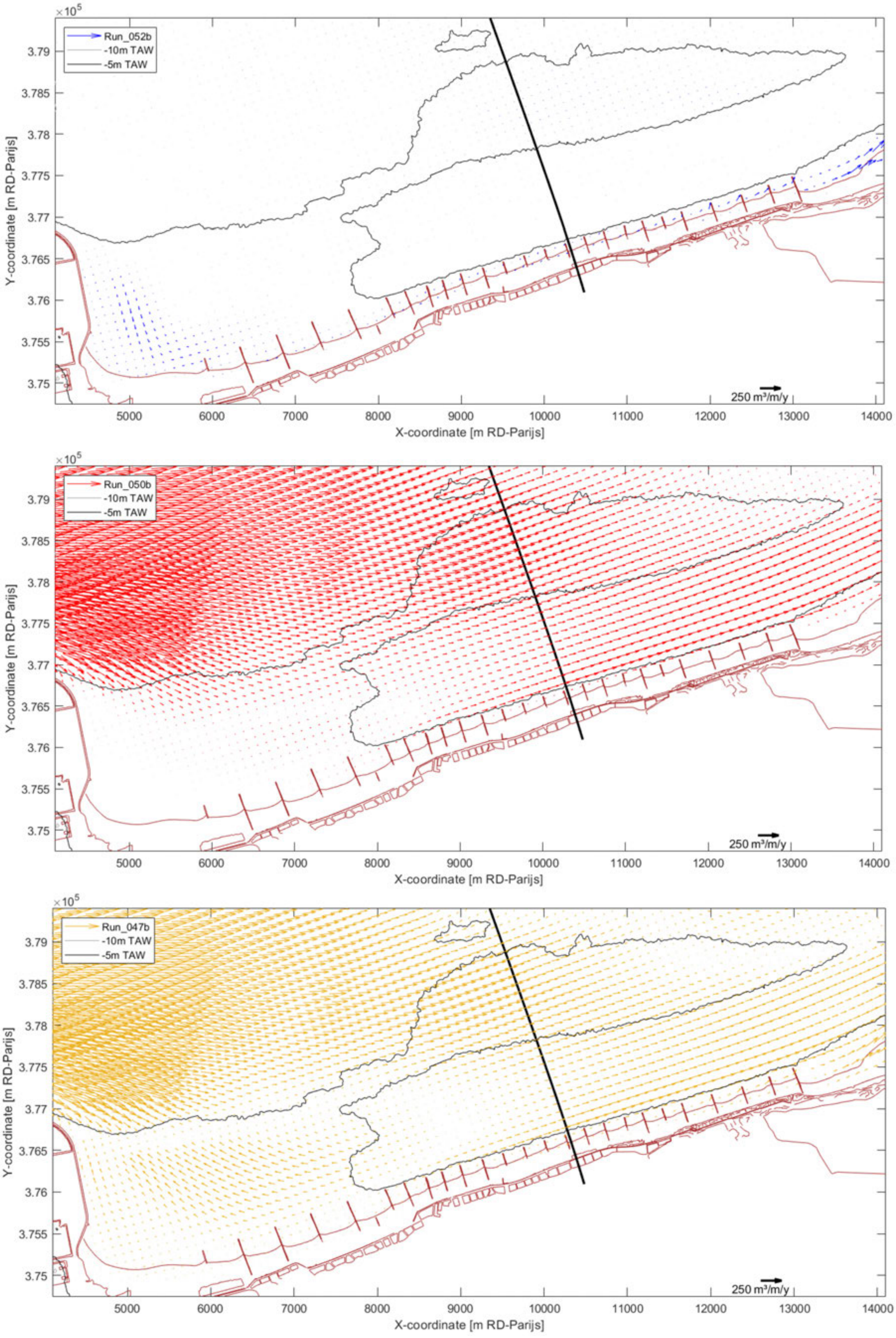

Figure 69 – Yearly residual sediment transport in the area east of Zeebrugge as modelled by FlemCo: wave forcing (blue arrows, top row), tide forcing (red arrows, middle row) and full hydrodynamic forcing (golden arrows, bottom row). The black line indicates the transect shown in Figure 65.

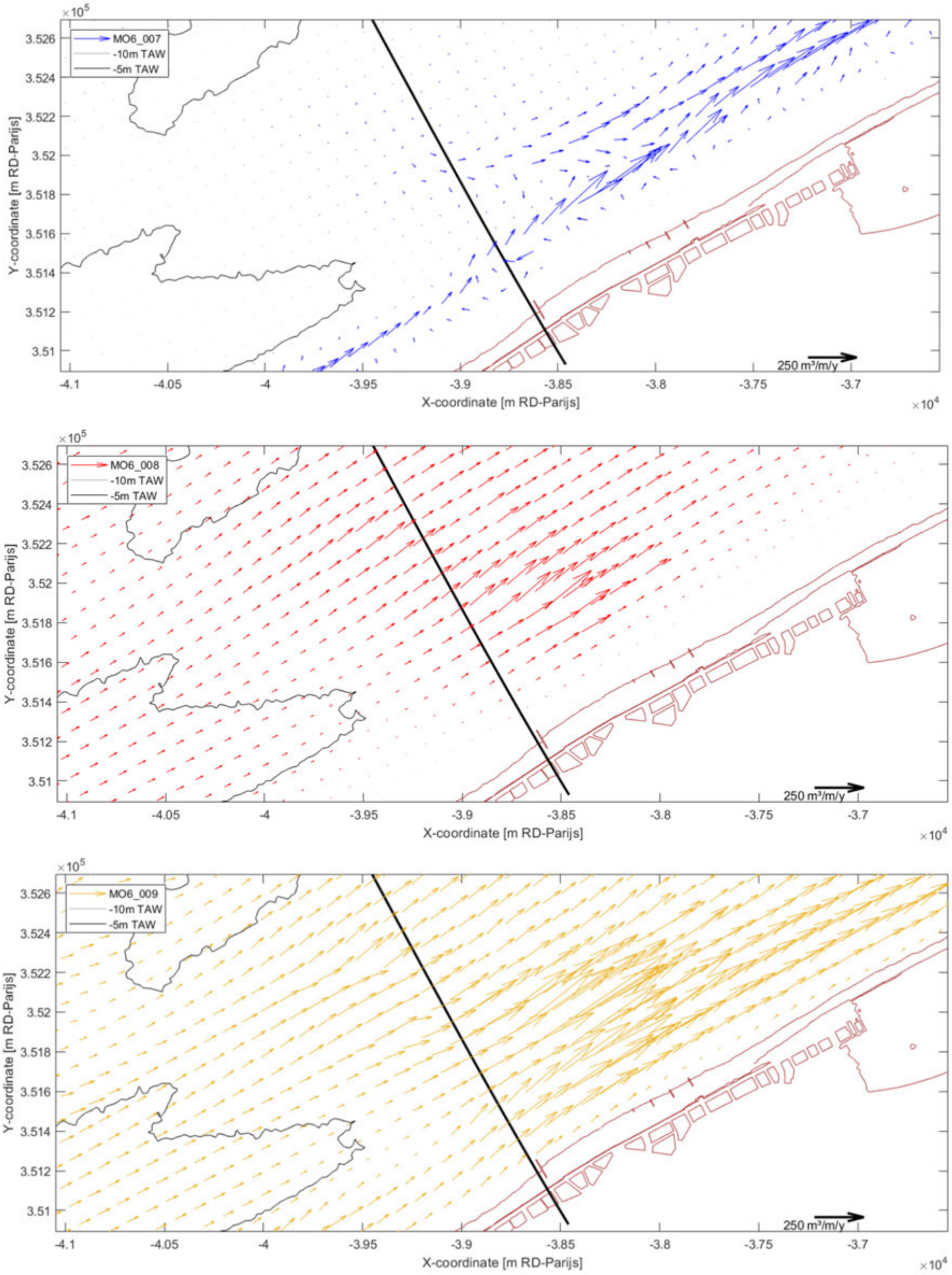

Figure 70 – Yearly residual sediment transport at Den Oever as modelled by Scaldis-Coast: wave forcing (blue arrows, top row), tide forcing (red arrows, middle row) and full hydrodynamic forcing (golden arrows, bottom row). The black line indicates the transect shown in Figure 64.

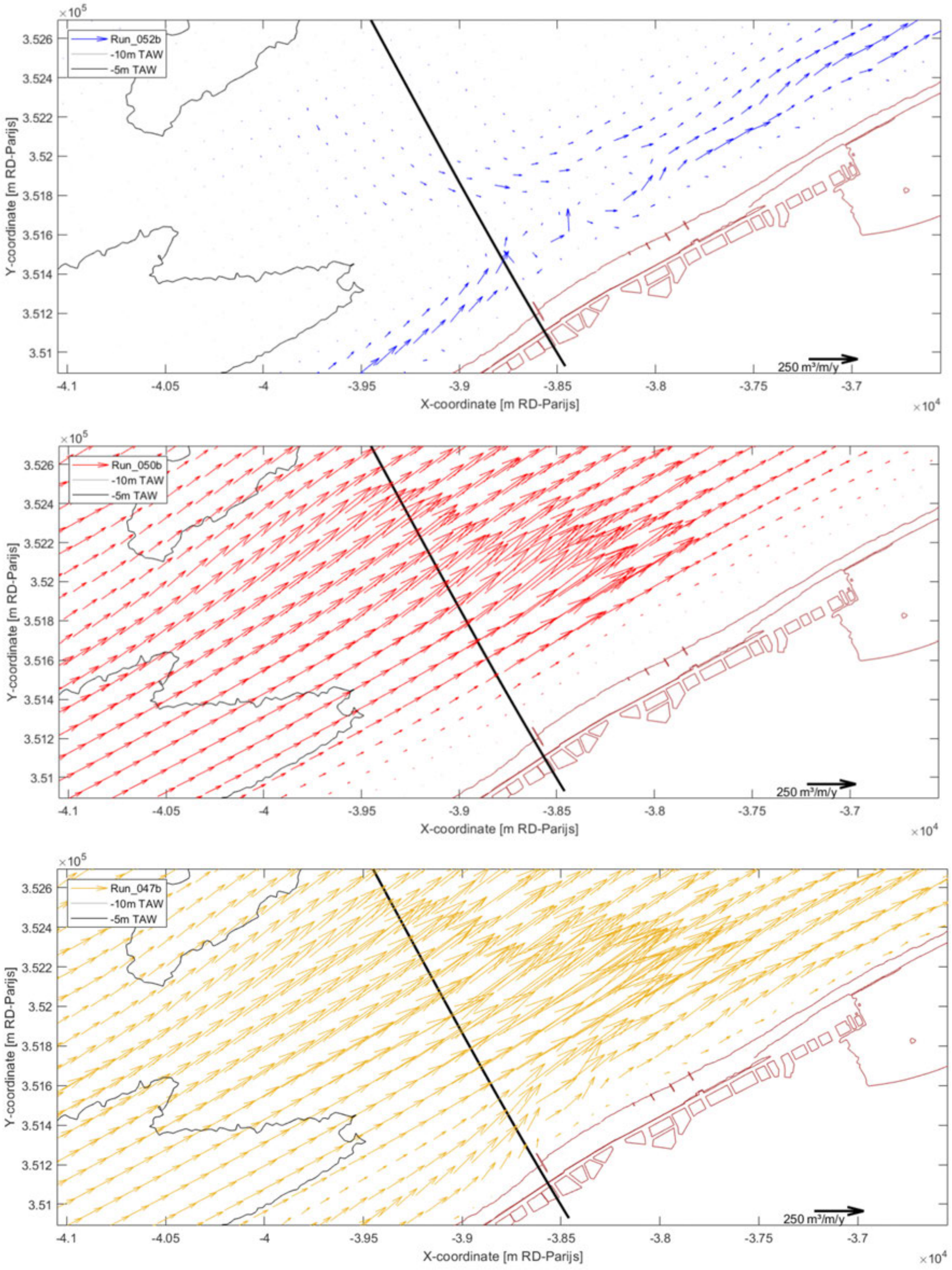

Figure 71 – Yearly residual sediment transport at Den Oever as modelled by FlemCo: wave forcing (blue arrows, top row), tide forcing (red arrows, middle row) and full hydrodynamic forcing (golden arrows, bottem row). The black line indicates the transect shown in Figure 64.

Tide and wave-induced longshore currents

In order to further investigate the reasons for the discrepancies in the predicted longshore sediment transport and its cross-shore distribution between the Scaldis-Coast and FlemCo models, a closer look was taken at the predicted tide and wave-induced longshore currents in both models.

Figure 72 to Figure 74 show the cross-shore distribution of the alongshore current for the same transects along the Belgian coast as for the residual sediment transport above. Tidal longshore velocities are shown in red; wave-induced velocities – with wind growth – are shown in blue. The curves show the mean, or residual, longshore current during the whole simulation period, while the shaded area indicates the mean flood (positive) and ebb (negative) directed wave-induced velocities for Scaldis-Coast. For the FlemCo model mean flood- (positive) and ebb- (negative) directed wave-induced velocities are indicated with thin dashed lines.

The tidal residual current is generally directed in the flood direction, as should be expected due to the tidal asymmetry along the Belgian coast (Appendix 5: Tidal asymmetry, Figure 109). Only in the Wielingen and Appelzak channels the residual tidal current is directed ebb wards. These figures show that the FlemCo model simulates higher tidal current velocities, while the Scaldis-Coast model simulates higher wave driven current velocities in the breaker zone.

Figure 75 to Figure 77 show the vectors of the (yearly) residual tide- and wave-induced currents. While the tidal currents in both models align well in general, but differ in magnitude; the residual wave-induced currents differ strongly both in magnitude as in direction, especially in the breaker zone (above the -5 m TAW isobath).

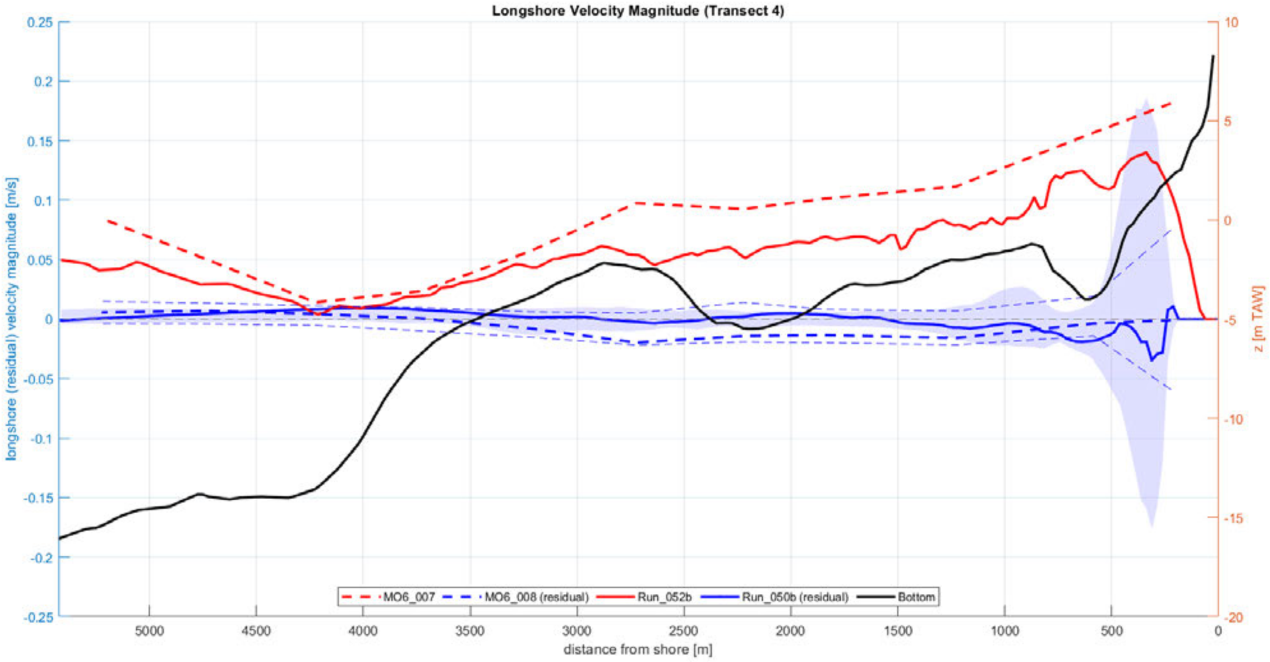

Figure 72 – Cross-shore profile at Broersbank – Den Oever, showing residual alongshore current due to tides (red), and waves with wind growth (blue) as modelled in Scaldis-Coast (full lines) and FlemCo (dashed lines). Shades show the mean flood and ebb-directed wave-induced currents for Scaldis-Coast; thin dashed lines show the mean flood and ebb-directed wave-induced currents for FlemCo.

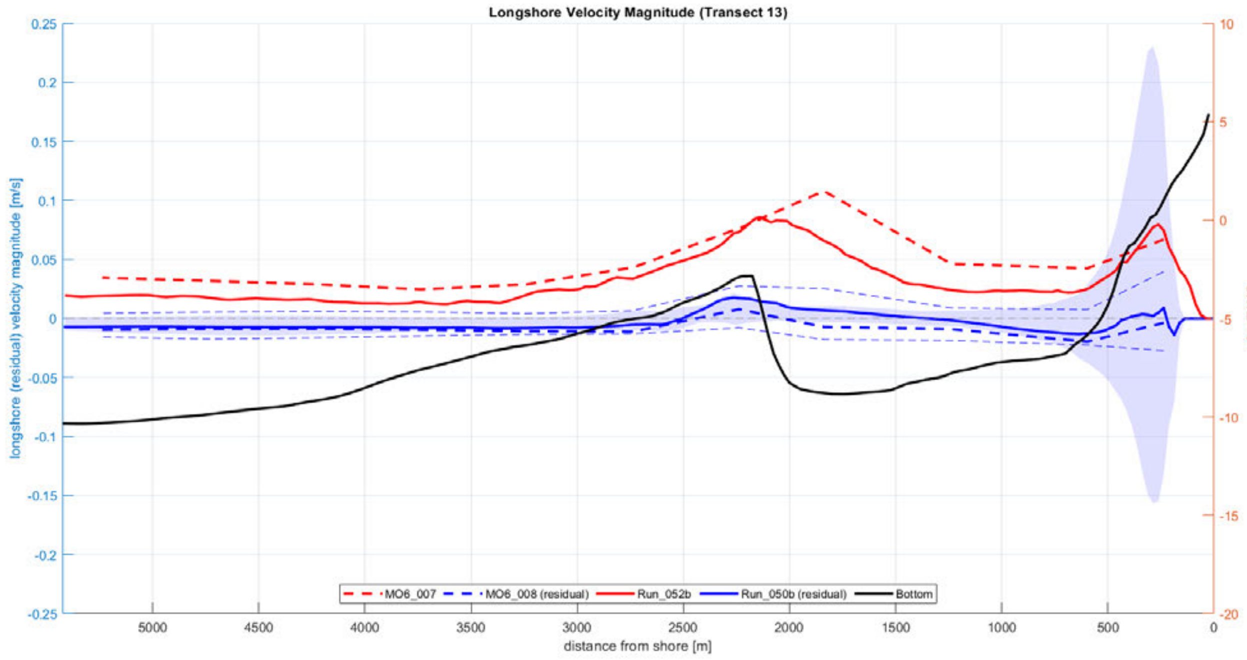

Figure 73 – Cross-shore profile over Grote Rede – Stroombank – Kleine Rede near Oostende, showing residual alongshore current due to tides (red), and waves with wind growth (blue) as modelled in Scaldis-Coast (full lines) and FlemCo (dashed lines). Shades show the mean flood and ebb-directed wave-induced currents for Scaldis-Coast; thin dashed lines show the mean flood and ebb-directed wave-induced currents for FlemCo.

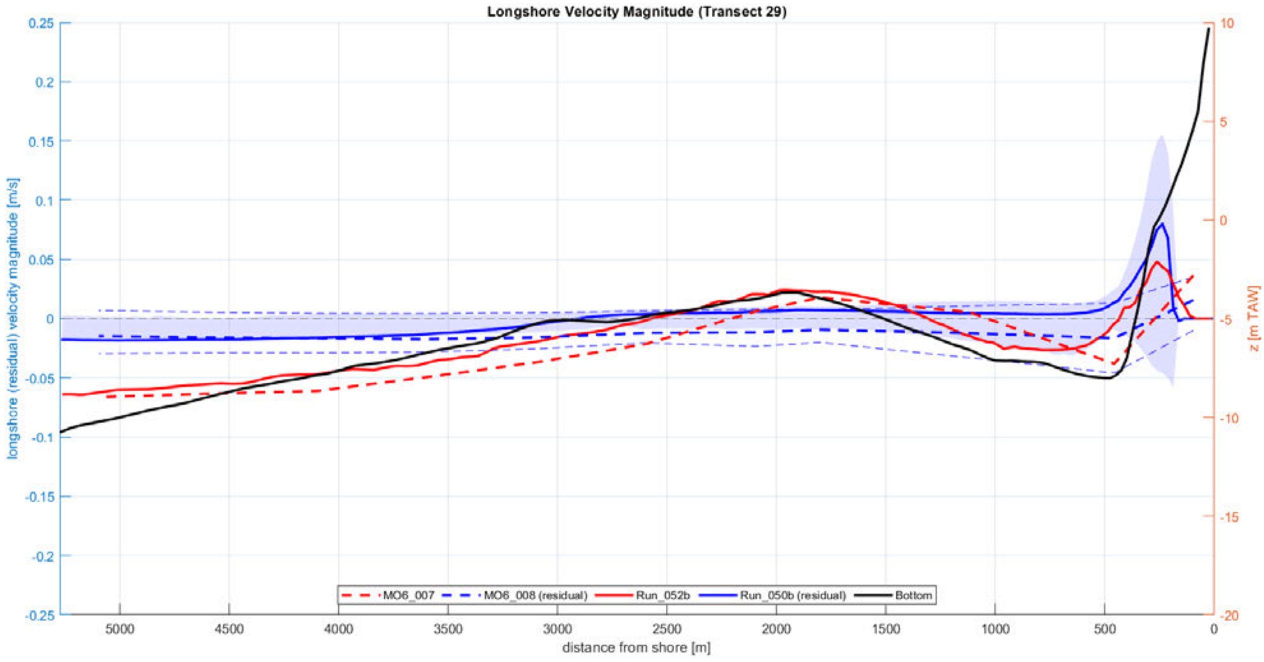

Figure 74 – Cross-shore profile over Wielingen – Paardenmarkt – Appelzak, showing residual alongshore current due to tides (red), and waves with wind growth (blue) as modelled in Scaldis-Coast (full lines) and FlemCo (dashed lines). Shades show the mean flood and ebb-directed wave-induced currents for Scaldis-Coast; thin dashed lines show the mean flood and ebb-directed wave-induced currents for FlemCo.

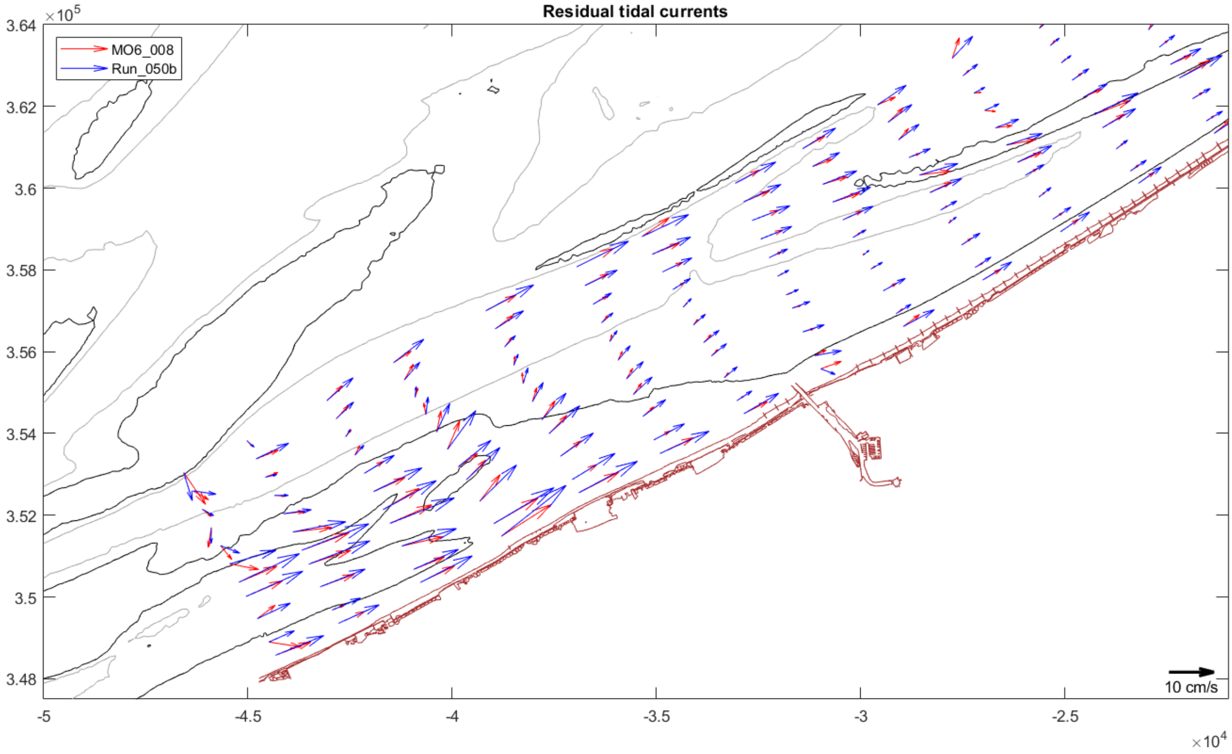

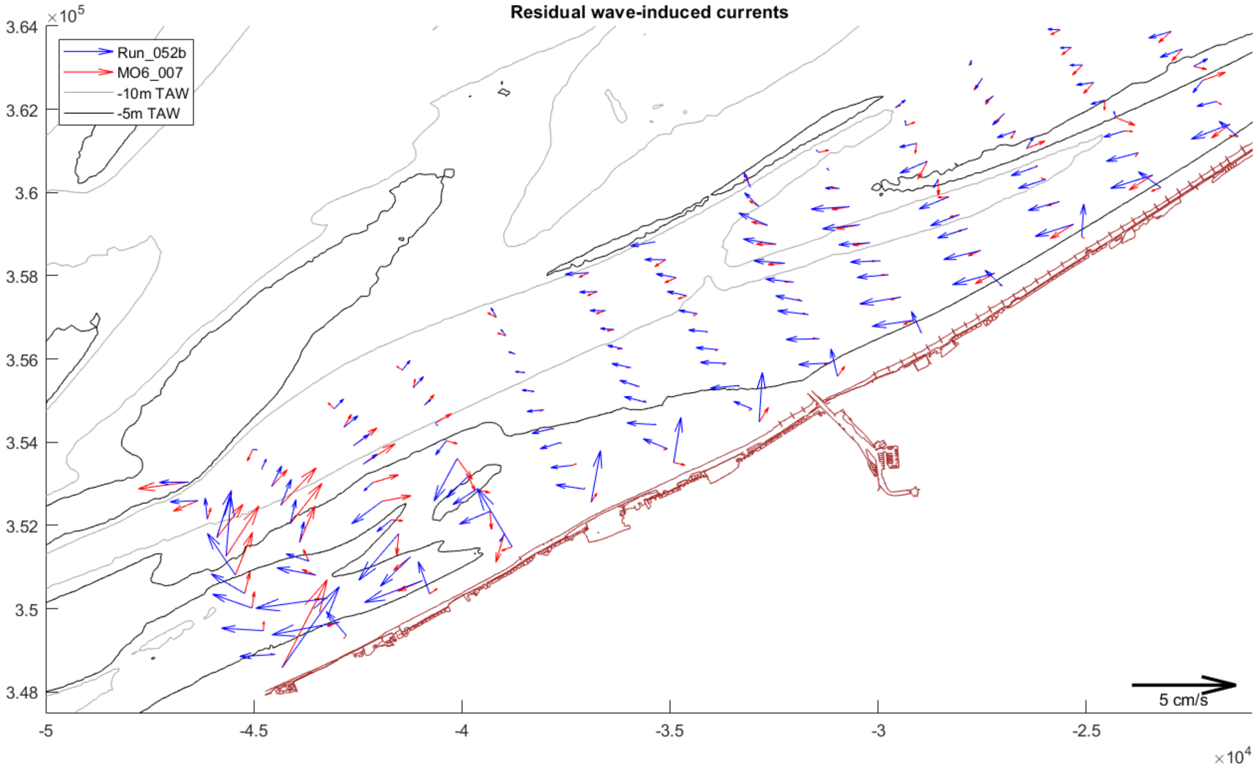

Figure 75 – Comparison of residual currents near Nieuwpoort for simulations with tidal forcing (top) and wave forcing (bottom). Red: Scalis-Coast results; blue: FlemCO results.

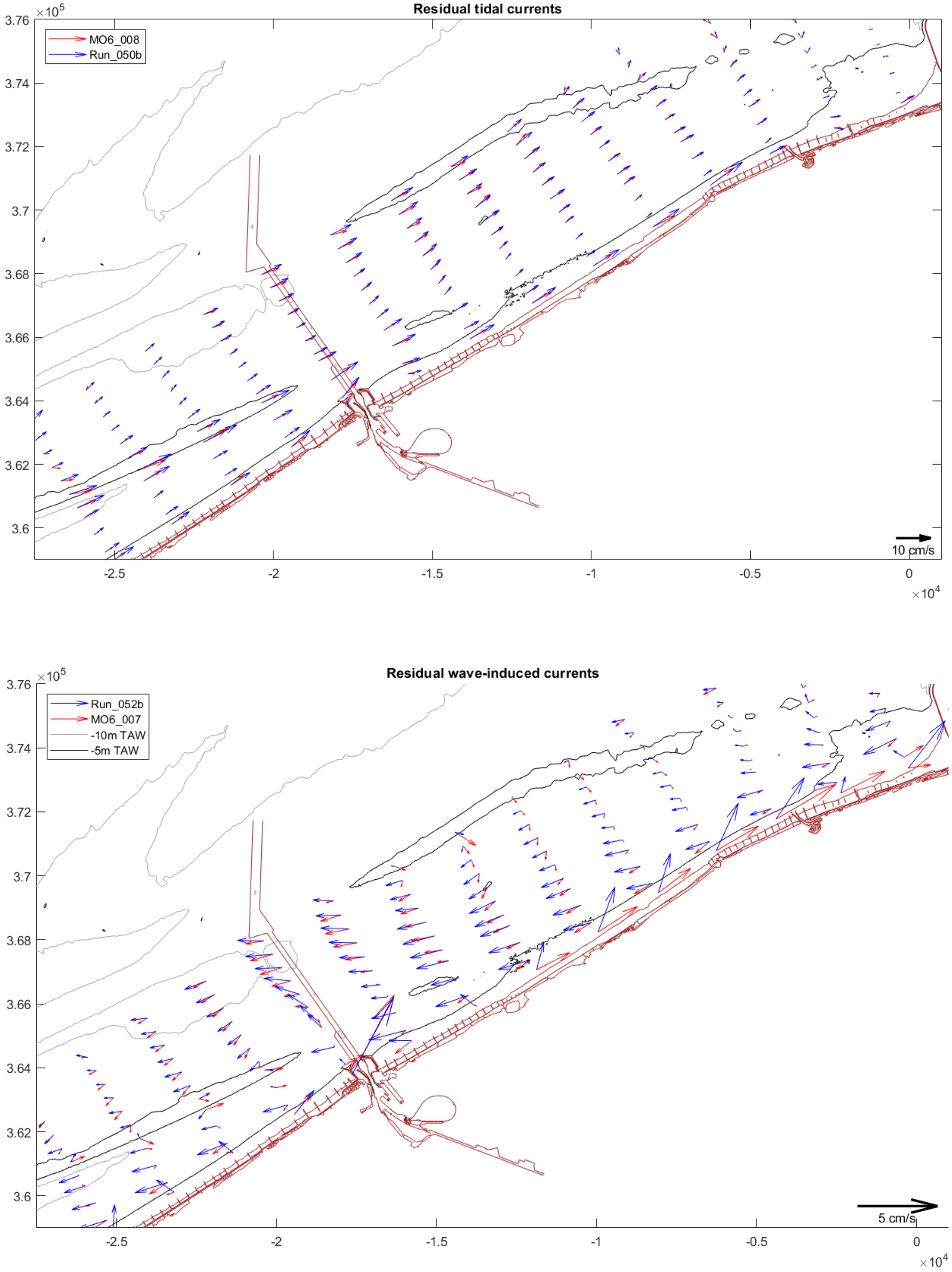

Figure 76 – Comparison of residual currents near Oostende for simulations with tidal forcing (top) and wave forcing (bottom). Red: Scalis-Coast results; blue: FlemCO results.

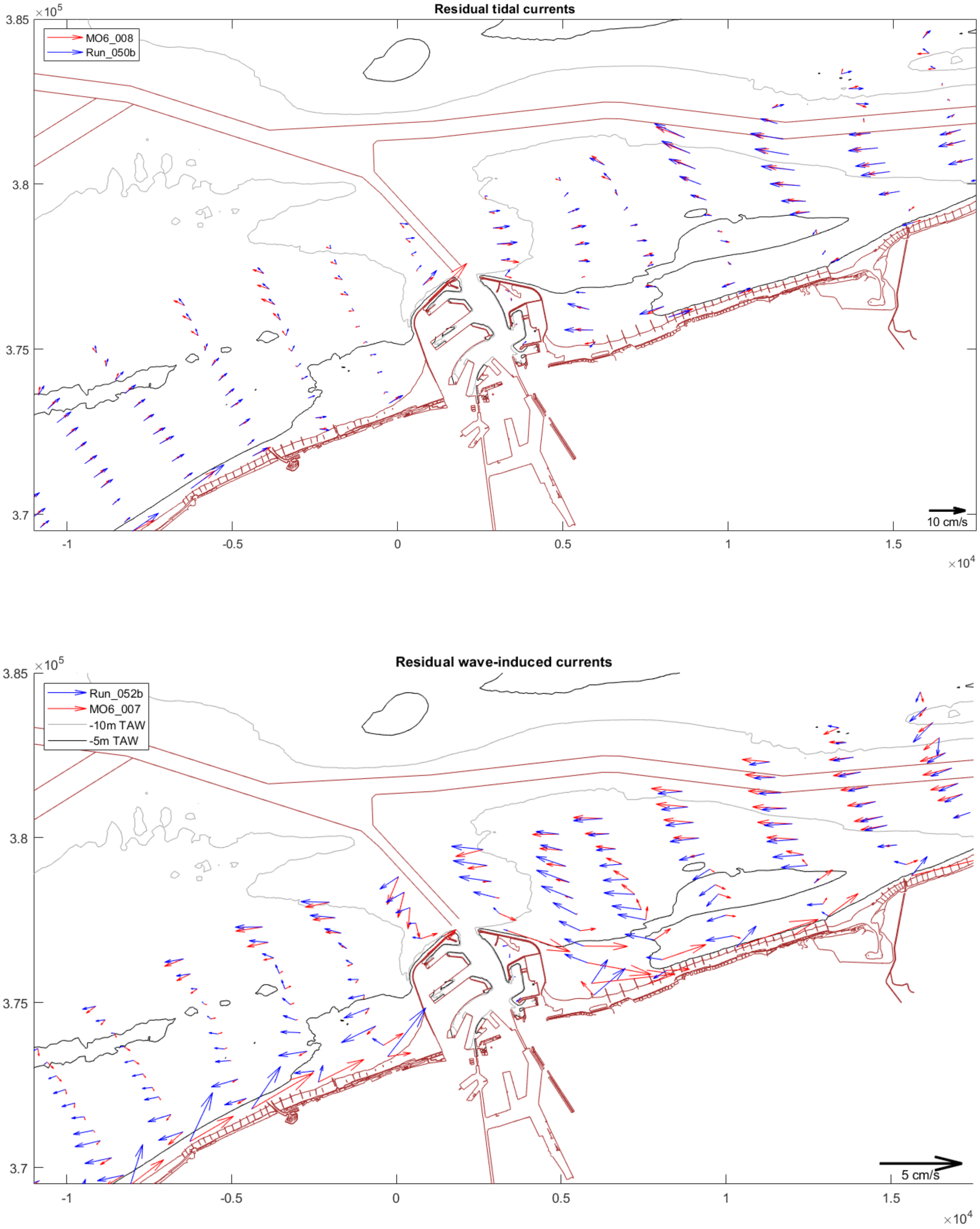
Residual tidal currents

Residual wave-induced currents

Figure 77 – Comparison of residual currents near Zeebrugge for simulations with tidal forcing (top) and wave forcing (bottom). Red: Scalis-Coast results; blue: FlemCO results.

Wave heights and directions

Since the discrepancies in the predicted longshore transport between the Scaldis-Coast and FlemCo models are associated with the effects of wind on the simulated waves in the models (Figure 61), we compared the predicted significant wave heights *Hs* with measured ones for several stations along the Flemish coast (Figure 78). For the wave directions, only a model-to-model comparison was performed due to the lack of sufficient measurements for the simulated period.

The comparison of the predicted with measured wave heights (Figure 79 to Figure 85) shows that – in the simulated period – the Scaldis-Coast model overestimates the *Hs* during high waves coming from the (north-west (see peaks esp. after 7th of May). This can be observed at all buoys, i.e. at Trapegeer buoy (up to 0.5 m too high), Nieuwpoort buoy (up to 0.5 m too high), Wandelaar buoy (up to 0.7 m too high) and at A2 buoy (up to 0.6 m too high).

At Trapegeer buoy and at A2 buoy, also the FlemCo-model overestimates the *Hs* peaks for waves from the (north-)west, although often too a smaller degree/in the case of less peaks. At the same time, the FlemCo-model generally overestimates the smaller wave heights (< 0.6 m), the reason, why the FlemCo-model predicts a higher average *Hs* for several buoys than the Scaldis-Coast model.

The higher *Hs* peaks in Scaldis compared to FlemCo are not restricted to the buoy locations but can be observed at most of the model observation points along the coast, especially at those nearshore. Although, it is not known, which model is more accurate in-between the buoy locations, the observed discrepancy in the predicted *Hs* peaks is a significant difference between both models that probably contributes to the observed higher wave-related sediment transport in the Scaldis-Coast compared to the FlemCo model.

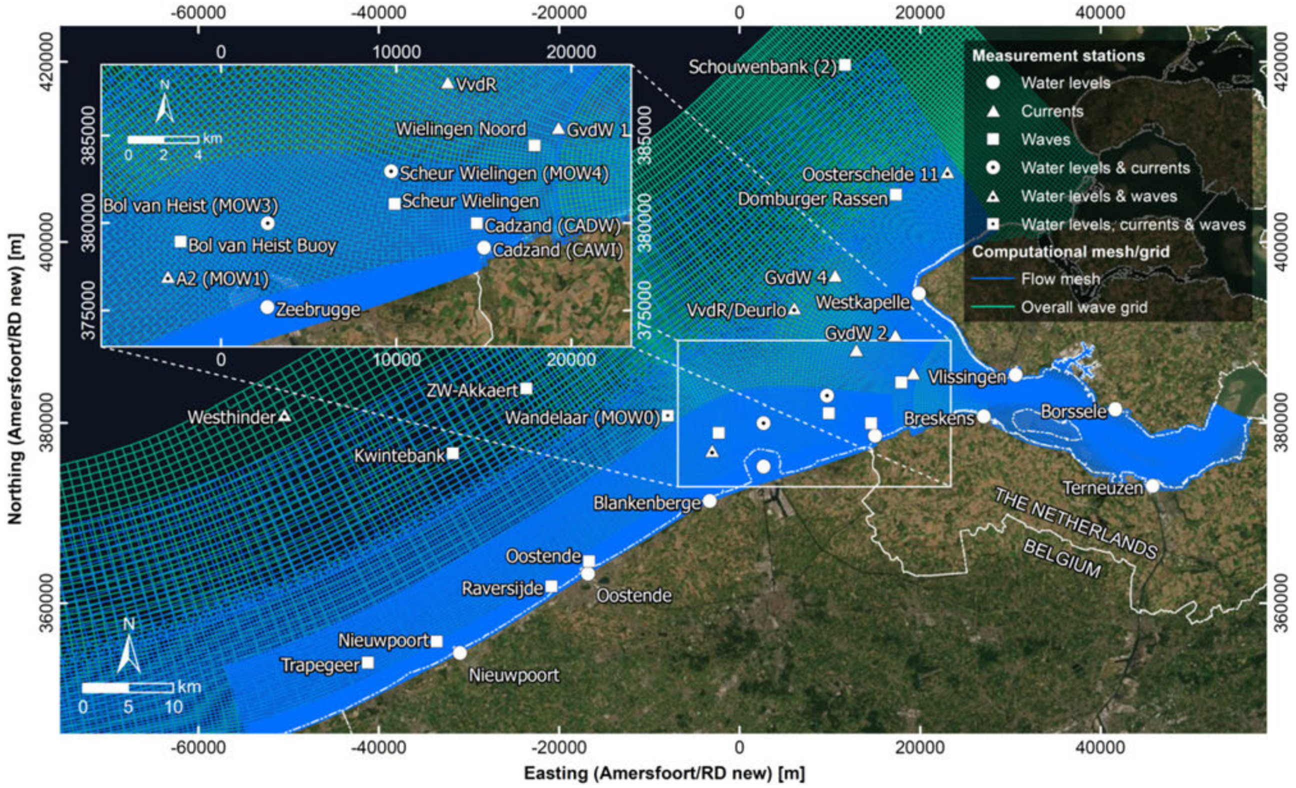

Figure 78 – Location of various wave buoys along the Flemish and Dutch coasts, for some of which the measured significant wave heights Hs have been compared with those predicted by the Scaldis-Coast and FlemCo model based on the period from 14 March to 13 May 2014.

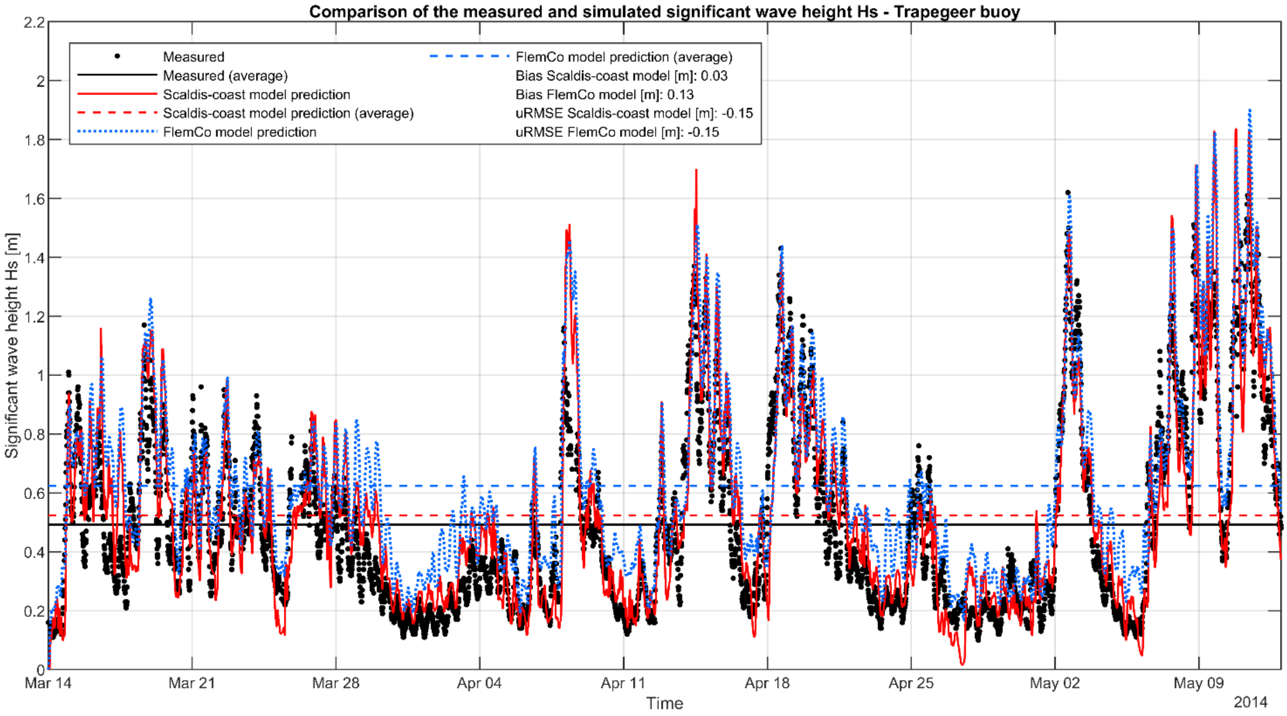

Figure 79 – Comparison of the measured significant wave heights Hs at Trapegeer buoy with those predicted by the Scaldis-Coast (Run MO6_009) and FlemCo (Run 047b) model based on the period from 14 March to 13 May 2014.

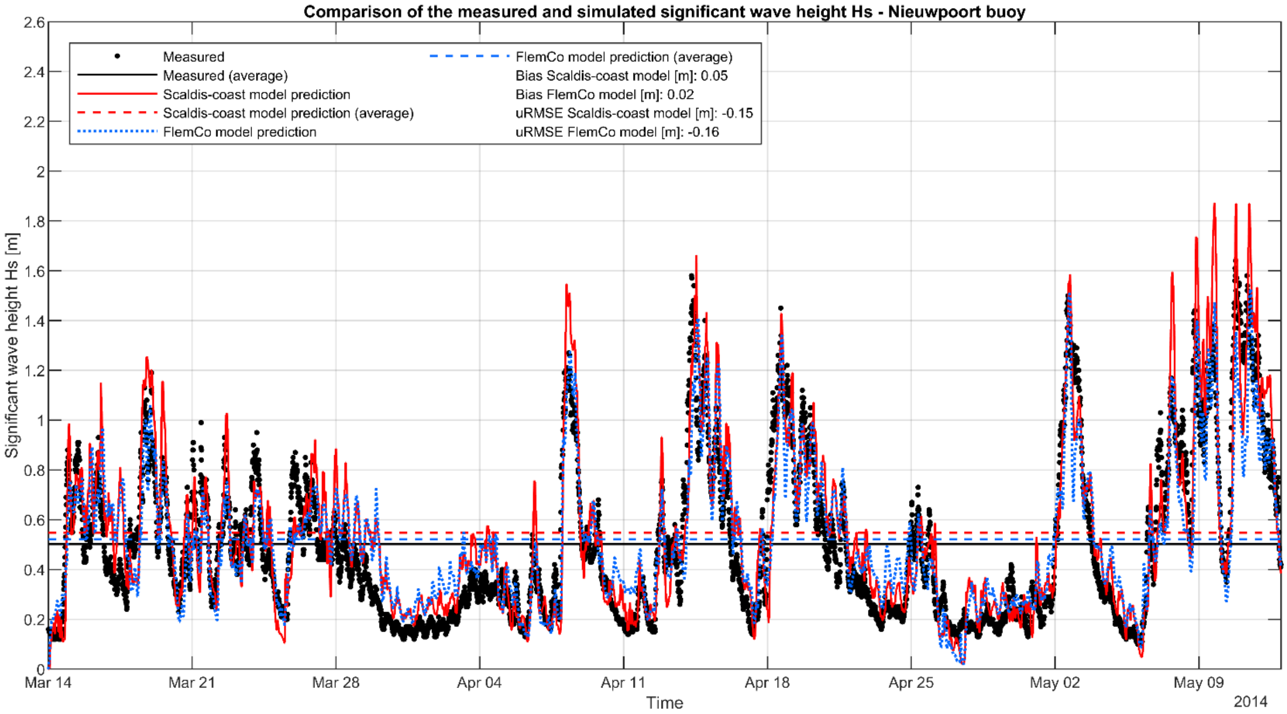

Figure 80 – Comparison of the measured significant wave heights Hs at Nieuwpoort buoy with those predicted by the Scaldis-Coast (Run MO6_009) and FlemCo (Run 047b) model based on the period from 14 March to 13 May 2014.

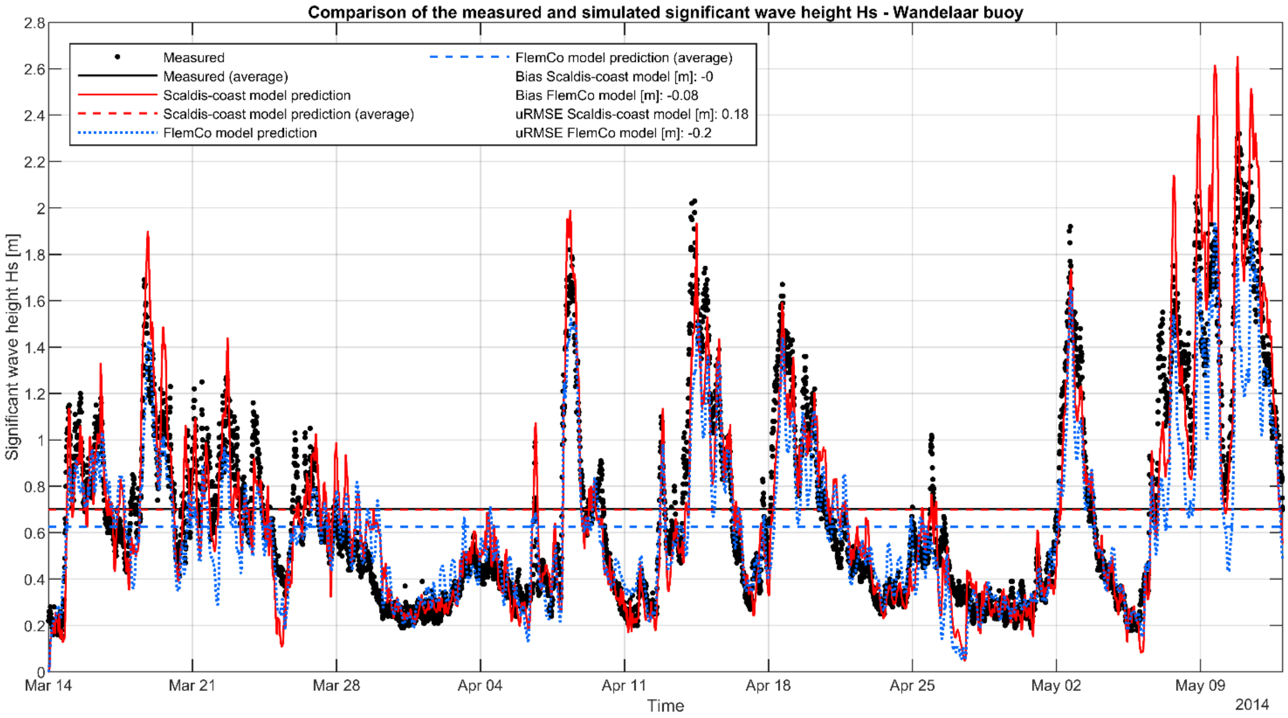

Figure 81 – Comparison of the measured significant wave heights Hs at Wandelaar buoy with those predicted by the Scaldis-Coast (Run MO6_009) and FlemCo (Run 047b) model based on the period from 14 March to 13 May 2014.

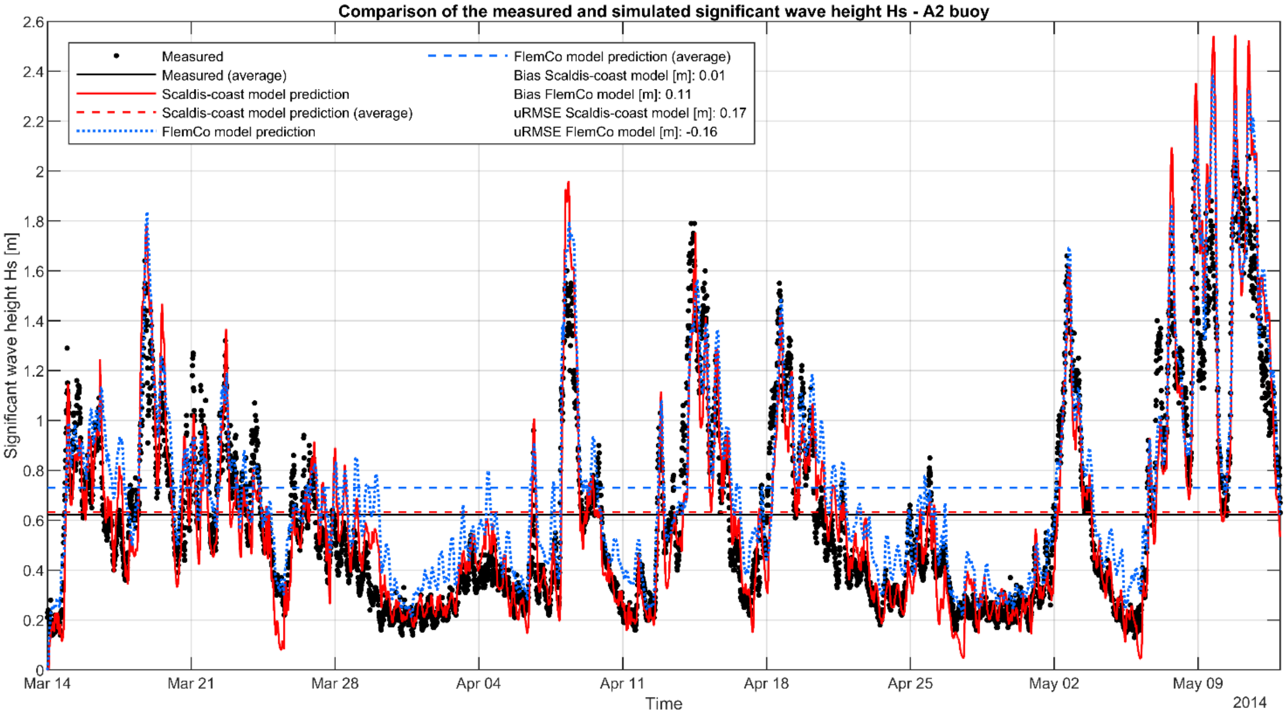

Figure 82 – Comparison of the measured significant wave heights Hs at A2 buoy with those predicted by the Scaldis-Coast (Run MO6_009) and FlemCo (Run 047b) model based on the period from 14 March to 13 May 2014.

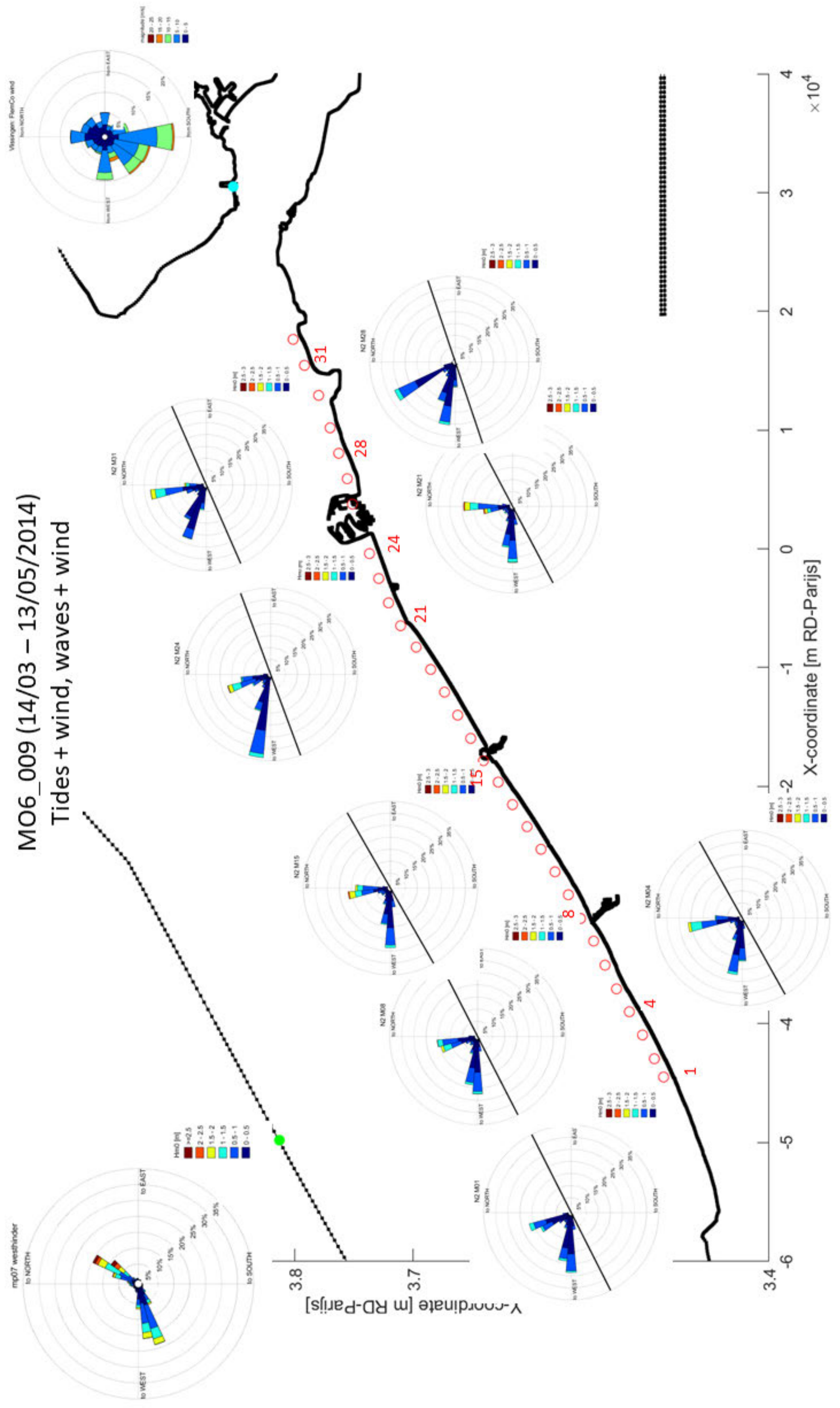

Figure 83 – Wave roses according to Scaldis-Coast model run MO6_009, which is based on realistic wave and wind boundary conditions and the simulation period from 14 March to 13 May 2014.

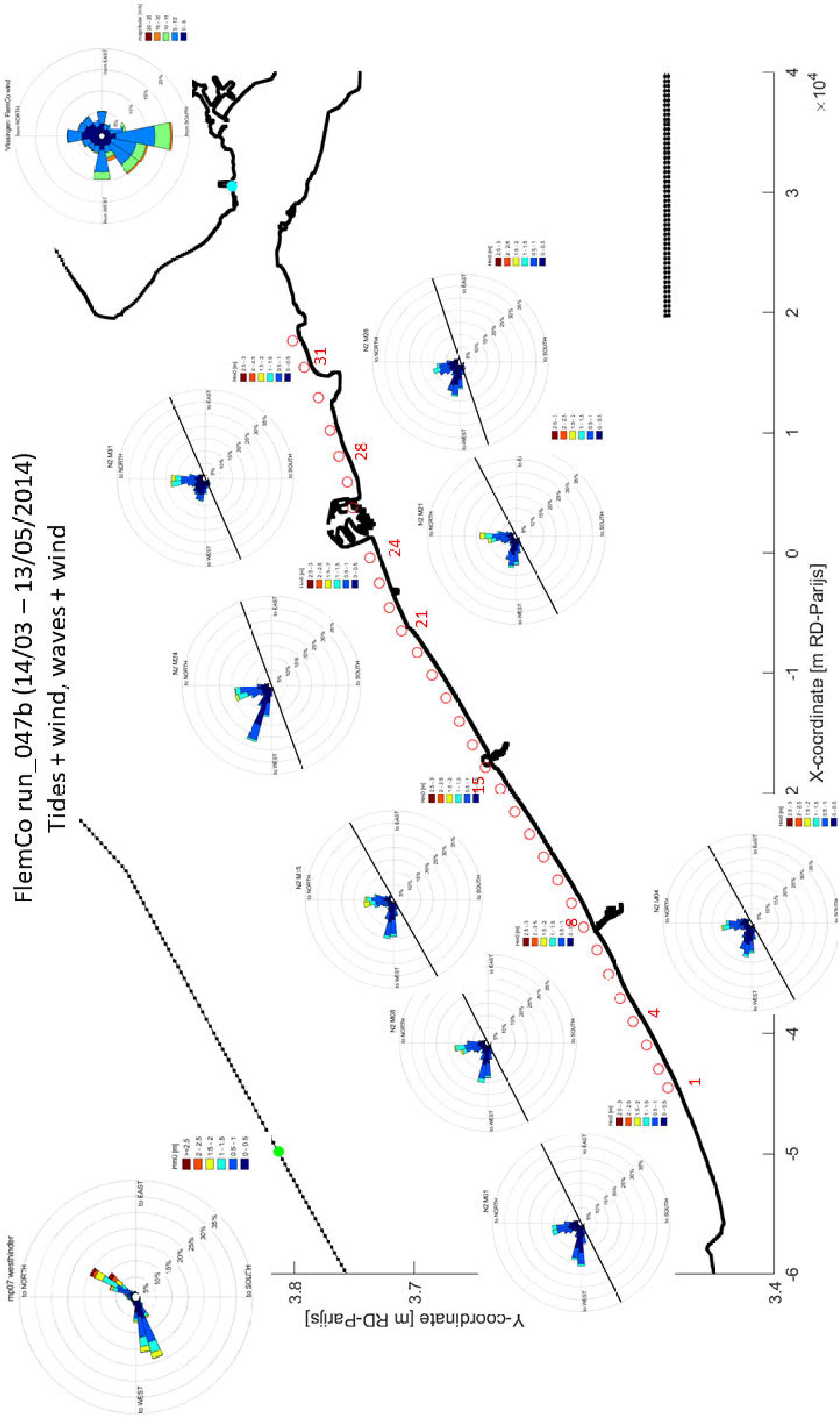

Figure 84 – Wave roses according to FlemCo model run 047b, which is based on realistic wave and wind boundary conditions and the simulation period from 14 March to 13 May 2014.

Figure 83 and Figure 84 show the wave roses for several nearshore locations along the Belgian coast as predicted by the Scaldis-Coast and FlemCo models based on the full model forcing (i.e. tide, waves and wind) and on realistic wave and wind boundary conditions. In line with waves roses based on measurements (e.g. van Eeden *et al.*, 2022), both models predict two dominant wave directions, i.e. the western and the northern sector. Nevertheless, there are two distinct differences between the two models:

- The Scaldis-Coast model predicts higher wave height peaks and by this less wave energy dissipation than the FlemCo model, as was already observed at the H_s measurement locations shown above.
- The Scaldis-Coast model shows less spreading of the wave directions but a more bimodal distribution of the wave directions (waves from the west and north) compared to the FlemCo-model.

The fact that there are higher wave peaks and waves especially from the western sector are more dominant in Scaldis-Coast compared to FlemCo, results in a more distinct wave-induced longshore current in the Scaldis-Coast model, as was observed in Figure 72 to Figure 74, and by this in higher wave-related longshore transports (cf. Figure 63 to Figure 65).

3.2.3 Scaldis-Coast and FlemCo compared; using non-realistic, constant wave and wind boundary conditions

Introduction

The comparison of the predicted longshore sediment transport as well as of the longshore currents and waves between the Scaldis-Coast and FlemCo models showed that it is mainly the discrepancy of the predicted waves and related longshore currents that holds responsible for the differences in the longshore transport between the two models. To unravel the causes for these differences, a closer look was taken at the wave model settings of two models (Table).

Since both the Scaldis-Coast and the FlemCo models use different wave models (Scaldis-Coast: TOMAWAC; FlemCo: D-Wave/SWAN) and were calibrated independently from each other, they use different settings for several wave model parameters. Most relevant with regard to the observed discrepancies of the predicted waves and related longshore currents are different settings applied for the:

- BreakGamma γ_b coefficient (which relates the wave height H_b at breaking to the water depth h_b at the breakpoint: H_b/h_b). In the Scaldis-Coast model, a higher value for γ_b is applied causing waves to break in shallower water than in the FlemCo model.
- BedFricCoef coefficient (bed friction coefficient). The smaller bed friction coefficient in the Scaldis-Coast model leads to less wave dissipation compared to the FlemCo model.
- Groynes at the beaches of the Flemish coast. In the Scaldis-model, groynes are implemented in the model bathymetry and – due to the limited resolution of the computational grid – are smaller in length and height than the actual groynes at the beaches (Figure 85). In the FlemCo model, groynes are not implemented in the model bathymetry but as fixed weirs (i.e. lines) with a specific height. The length of the fixed weirs coincides with the actual length of the groynes at the beaches. The height of the start and end point of the fixed weirs coincides with the corresponding height in the measured bathymetry.

The above-described differences of the applied settings between the two models are altogether in favour for higher wave energy in the nearshore zone in the Scaldis-Coast than in the FlemCo model and therefore may contribute to the observed discrepancy of the predicted waves and related longshore currents in both models.

For a better comparison of both models, we applied the same settings for the BreakGamma γ_b coefficient and the BedFricCoef coefficient in both models according to Table 10 and used the white capping formulation by Komen et al. (1984). Besides, we simplified the wave model forcing of both models by applying non-realistic constant and uniform wave and wind boundary conditions (H_s = 1 m, T_p = 6 s, *Dir* = 285°; windspeed = 8 m/s, wind direction = 285 deg). These wave and wind boundary conditions were chosen in order to generate a distinct eastward orientated wave-induced longshore current and related longshore sediment transport along the Flemish coast in the models. Based on the same simulation period as before, i.e. from 14 March 2017 to 13 May 2017, both models were run with the full model forcing (i.e. tidal forcing together with wave and wind forcing; Scaldis-Coast run MO6_027, FlemCo run 053; Table 10). Besides these two reference runs, we performed an additional FlemCo model run (054), in which we removed the groynes, and analysed the sensitivity with regard to the predicted longshore sediment transport (Table 10).

In the case of the FlemCo model, all simulations were performed based on a maximum flow and wave grid resolution in the nearshore zone (between the coastline and ca. 2 km offshore) of ca. 23 m x 23 m, the latter being comparable to the resolution in the Scaldis-Coast model (up to 20 m at the beaches).

Table 9 – Overview of selected Scaldis-Coast and FlemCo wave model settings

Wave model setting	**Scaldis-Coast**	**FlemCo**
Simulation mode	**Non-stationary**	**Non-stationary**
Time interval	**2 min**	**30 min**
BreakGamma γ_b (depth induced breaking; H_b/h_b)	**0.8 [-]**	**0.73 [-]**
BedFricCoef (bed friction coefficient)	**0.038 [s $m^{-1/3}$]**	**0.067 [s $m^{-1/3}$]**
WhiteCapping formulation	**van der Westhuysen (2007)**	**Komen et al. 1984**
Minimum water depth	**0.0 m**	**0.05 m**
Seaward groyn height above NAP	**ca. 1 m**	**ca. 2 m**
Groyn length	**Length according to contours from 2018 DEM; ca. 100 m shorter than in FlemCo**	**Length according to 2020 satellite imagery**

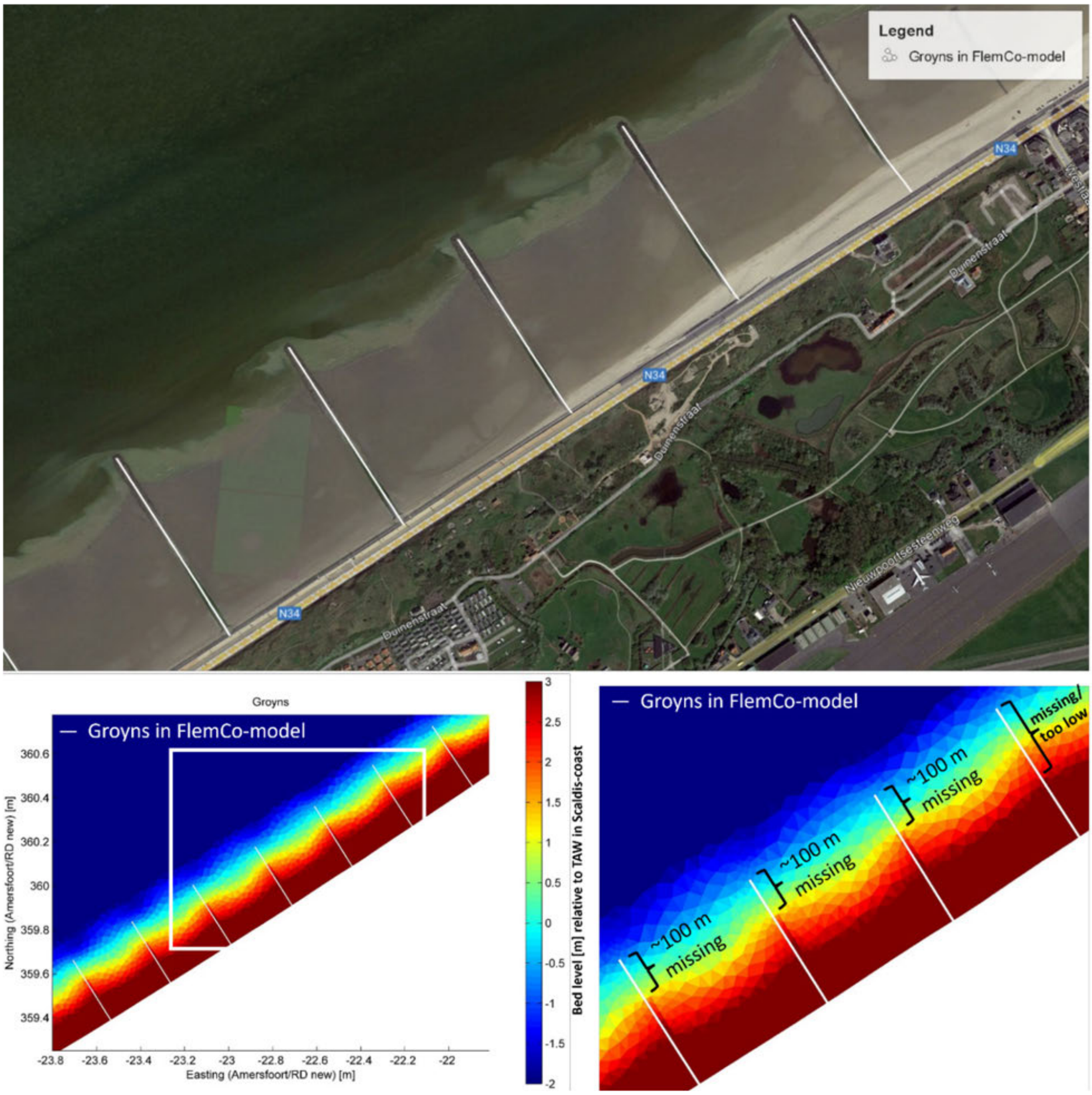

Figure 85 – Comparison of the dimensions of groynes as implemented in the Scaldis-Coast and in the FlemCo models.

Table 10 – Overview of the Scaldis-Coast and FlemCo sensitivity runs based on constant (non realistic) model forcing

Scaldis-Coast Run ID	FlemCo Run ID	Tidal forcing	Wave forcing	Wind forcing	Gamma	BedFricCoef	Groynes
MO6_027	**Run053**	On	On	On	0.5	0.067	Included
-	**Run054**	On	On	On	0.5	0.067	Not included

Longshore sediment transport

As was the case in Section 3.2.2, the longshore sediment transport was determined based on the simulated cumulative suspended and bedload sediment transport in the ca. 750 m nearshore zone (between the beach and approximately the -5 m TAW/-7.33 m NAP contour) of the Belgian coast.

Figure 86 shows that with the same settings for the Break Gamma and the BedFriCoef coefficients and with (constant) wave forcing, the longshore sediment transport clearly better agrees between the Scaldis-Coast and in the FlemCo models than was observed for the realistic wave and wind boundary conditions (cf. Figure 60). Larger discrepancies between both models can only be observed in the western part between Nieuwpoort and Oostende and east of Zeebrugger harbour. When groynes are removed in the FlemCo model, the predicted sediment transport closely agrees with the predictions by the Scaldis-Coast model; only west of ‘t Zwin, the transport remains smaller in FlemCo compared to Scaldis-Coast. This implies that the predicted higher longshore transport in the Scaldis-Coast model based on realistic wave and wind conditions (cf. Section 3.2.2) is – among others – related to the effects of the groynes which are smaller in dimension in the Scaldis-Coast compared to the FlemCo model.

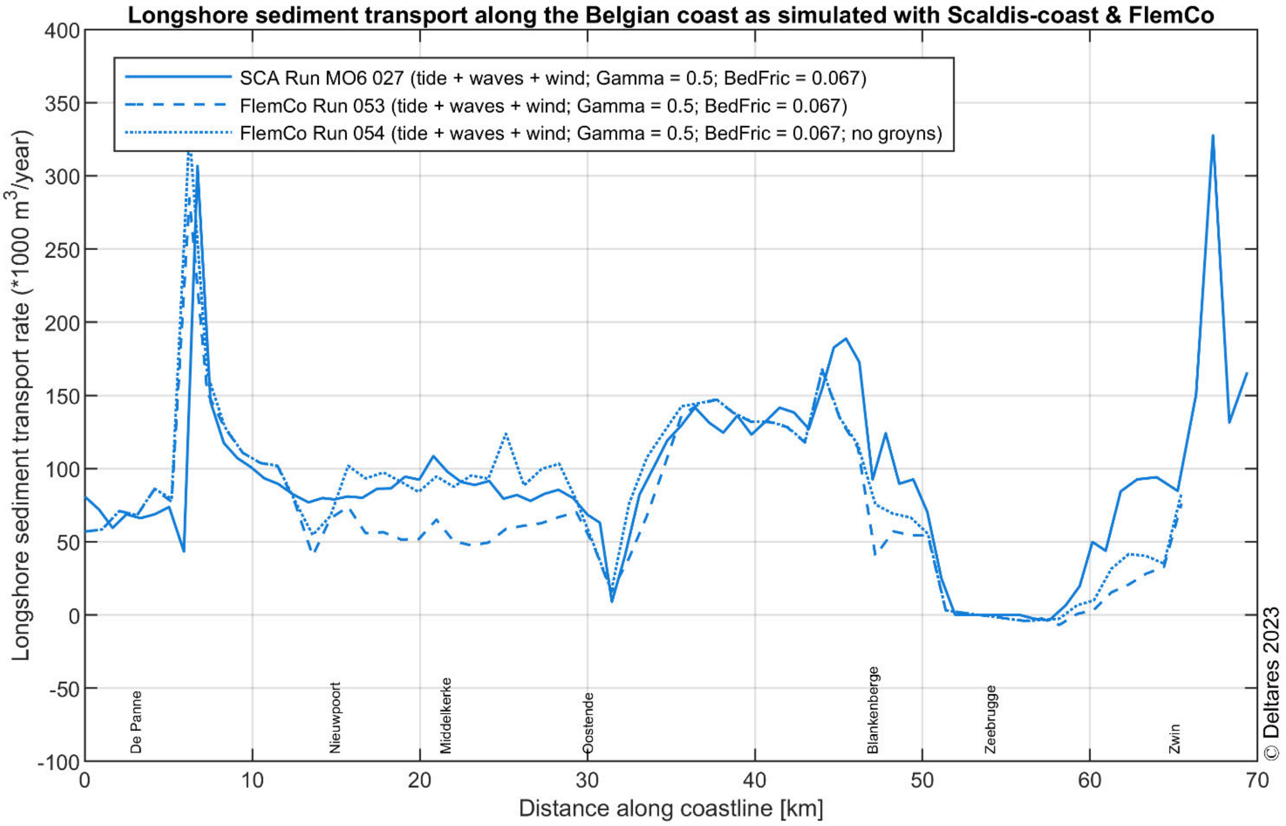

Figure 86 – Sediment longshore transport as simulated with the Scaldis-Coast and FlemCo model with the full model forcing (i.e. tide, waves and wind) based on non-realistic, constant waves and wind conditions.

Wave heights and directions

Figure 87 and Figure 88 show the wave roses for several nearshore locations along the Belgian coast as predicted by the Scaldis-Coast and FlemCo models based on realistic tide and non-realistic, constant wave and wind boundary conditions. As a result of the constant wave and wind direction from 285°N, all wave energy in both models comes from the north-western sector. While the wave roses look very similar in both models at almost all locations, higher waves are predicted by the Scaldis-Coast model in the areas to the east and especially to the west of Zeebrugge harbour. This probably explains why the Scaldis-Coast model predicts higher longshore transports in these two areas than the FlemCo model (cf. Figure 86).

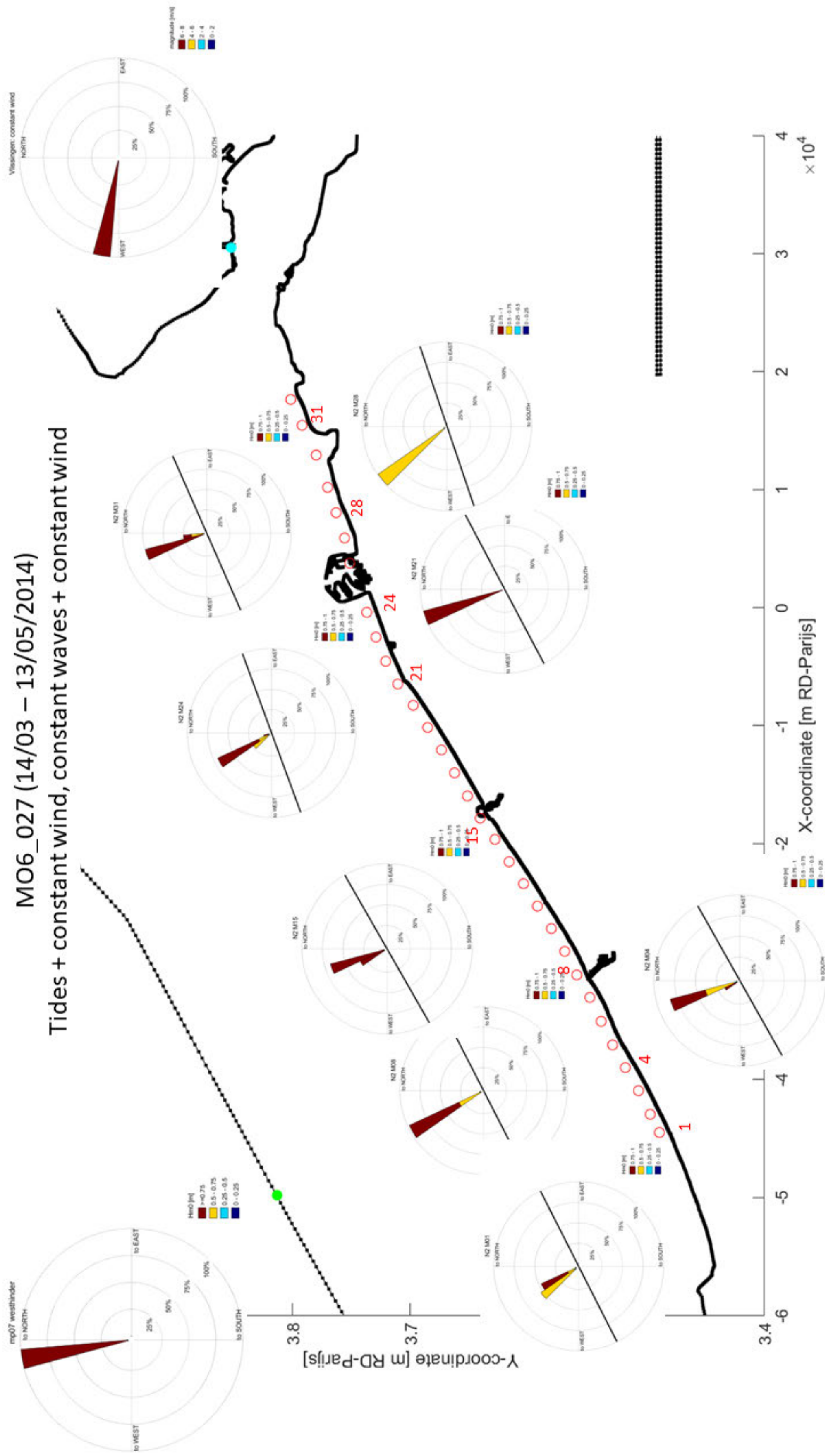

Figure 87 – Wave roses according to Scaldis-Coast model run MO6_009, which is based on constant wave and wind boundary conditions and the simulation period from 14 March to 13 May 2014.

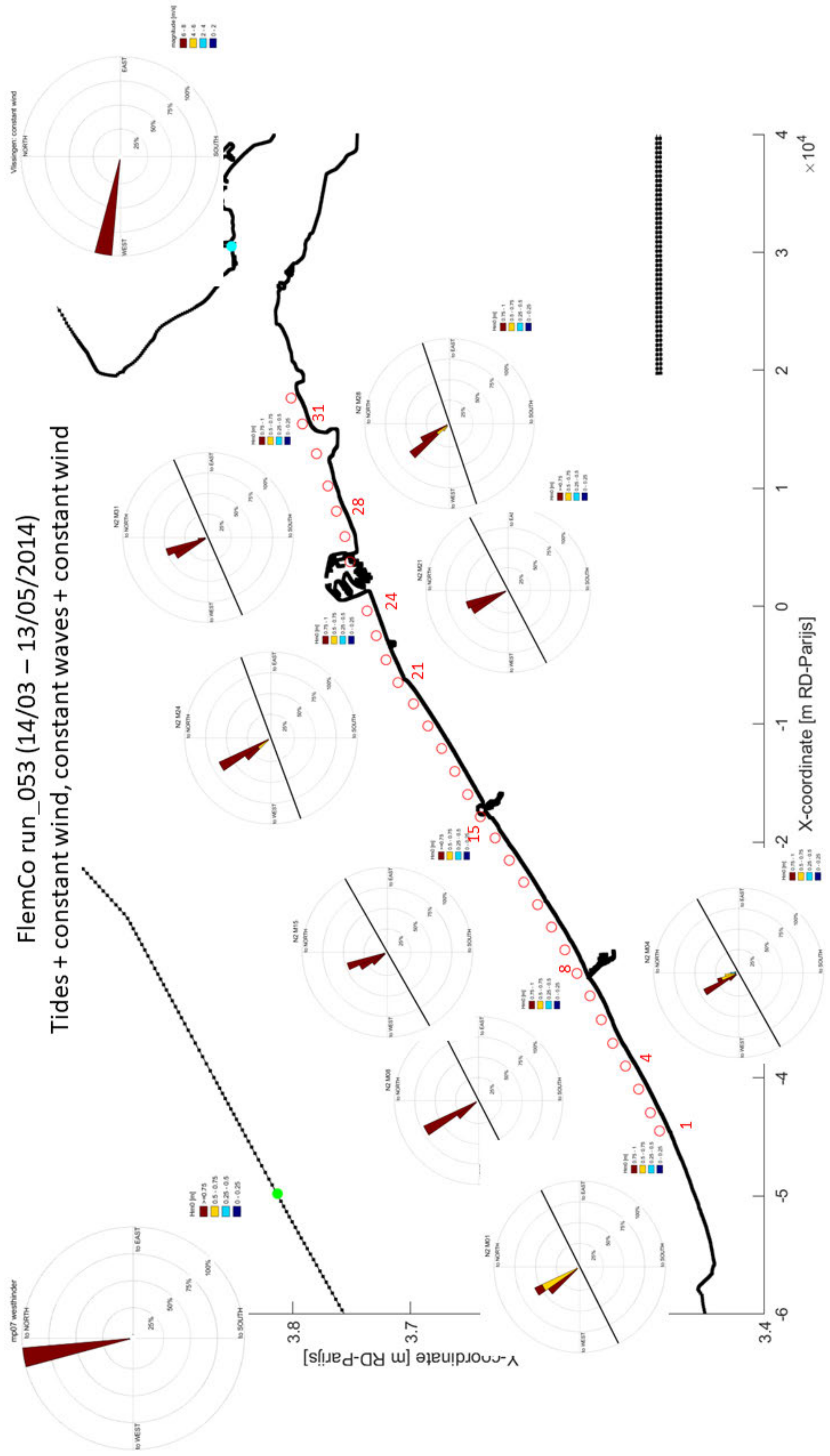

Figure 88 – Wave roses according to FlemCo model run 047b, which is based on constant wave and wind boundary conditions and the simulation period from 14 March to 13 May 2014.

3.2.4 Synthesis of simulation results

The current study showed that even with a similar grid resolution in the nearshore zone, the FlemCo model predicts smaller longshore sediment transport for the Belgian coast than the Scaldis-Coast model. Sensitivity simulation runs performed with the two models based on different forcing combinations (tide, waves and wind) revealed that it is mainly the wave related longshore sediment transport that differs between the two models, while the tide related transports show a closer match. The differences in the wave related longshore transport mainly occur as soon as wind is added to the models, which results in clearly higher wave height peaks and a more dominant northern but especially western wave direction in the Scaldis-Coast model. This leads to a more distinct wave-induced longshore current and by this in a higher wave-related longshore transport in Scaldis-Coast compared to FlemCo. The observed discrepancies of the predicted waves between models is – apart from the different wave models used by Scaldis-Coast and FlemCo (TOMAWAC/SWAN) – related to different settings used in the two wave models, especially the applied bed friction coefficient (lower in Scaldis-Coast) and breaker index (higher in Scaldis-Coast). Moreover, groynes in the Scaldis-Coast model are clearly smaller in dimension as in the FlemCo model, and therefore block the wave-induced longshore current to a smaller degree as compared to the FlemCo model. This and the different applied wave model settings are altogether in favour for higher wave energy/more pronounced wave-induced longshore currents and by this higher longshore transport in the Scaldis-Coast than in the FlemCo model. This finding is supported by the observation that the two models predict very similar longshore sediment transports along the Belgian coast, when i) the same wave model settings, ii) constant wave and wind boundary conditions and iii) no groynes in the FlemCo models are applied.

Regardless of the discrepancy of the predicted absolute longshore sediment transport between the Scaldis-Coast and the FlemCo models, they both indicate dominating wave-induced longshore transport in the first few hundred meters seawards the coastline (breaker zone), followed by dominating tide-induced longshore transport further seawards. While both models suggest a considerable but narrow peak for the wave-induced transport, they show a much wider but flattened peak (numerous hundreds of meters wide) for the tide-induced transport. According to both models, the tide-induced transport is still significant even numerous kilometres offshore.

In order to further calibrate and validate the wave models of the Scaldis-Coast and FlemCo models – especially with regard to the predicted wave directions – we suggest to run both models for a different simulation period for which sufficient nearshore wave direction measurements are available. Once the predicted wave directions are better validated, the models should be applied (potentially in three-dimensional mode) for hindcast simulations aiming at a reproduction of the measured bed level changes at the Belgian coast (e.g. the period 1986–1996). Based on the comparison of the simulated and measured bed level changes, both models can be further calibrated and validated, as is currently the case based on the existing estimates of the longshore sediment transport at the Belgian coast which are associated with uncertainty.

The model simulations with full hydrodynamic forcing do not indicate a residual sediment transport towards the coast over the shoreface connected ridges. It seems these models are not able to capture/parametrize the complex 3D currents in the breaker zone – which are assumed to be responsible for the process of natural feeding of the coast – with their current 2DH (depth averaged) setup. To examine the assumption of natural feeding further, we suggest to apply the models in three-dimensional mode (potentially only for a subdomain) to test if the 3D flow patterns in the breaker zone can be resolved.

3.3 Effect of the gradual deepening of nearshore tidal channels on the beach erosion (WP4)

3.3.1 Introduction

Task 4 of the MOZES-project (WP4) deals with the effects of the observed gradual deepening of nearshore tidal channels along the Belgian coast on beach erosion and on the intensity of beach nourishments required to maintain the coastline. The hypothesis is that a deeper/wider channel causes an increased erosion of the adjacent beaches, which requires larger nourishment volumes.

In the MOZES-project, task 4 is investigated based on the example of the Appelzak channel located off the coast of Knokke-Heist between Zeebrugge harbour and the Dutch border (Figure 41). After the extension of Zeebrugge harbour in the year 1986, a significant deepening of the Appelzak channel has been observed, while the Paardenmarkt ridge (located seaward of the Appelzak) experienced pronounced sedimentation (Figure 89). The morphological development of the Appelzak channel is most probably related to the extension of Zeebrugge harbour and the observed erosion along the harbour breakwaters as well as the sedimentation on the Paardenmarkt ridge (Dujardin *et al.*, 2023). Moreover, intensive beach nourishments and the presence of groynes at Knokke-Heist slow down or even prevent landward migration of the Appelzak channel.

3.3.2 Methodology

Both the Scaldis-Coast and FlemCo models indicate a strong increase of the longshore sediment transport between Zeebrugge harbour and the Belgian-Dutch border (Figure 61). This distinct gradient in longshore transport implies net erosion of the coast and is probably related to the observed deepening of the Appelzak channel. In order to better understand the relevant processes that control the morphological development of the area, we applied the Scaldis-Coast and FlemCo models using different synthetic model bathymetries for the coast between Zeebrugge harbour and the Belgian-Dutch border. Based on these model bathymetries we particularly investigate how the longshore sediment transport changes in the case of a shallower Appelzak channel and a deeper Paardenmarkt ridge (as it was the case in 1986; Figure 89). For this purpose, we created two synthetic model bathymetries based on the 2020 measured bathymetry:

- For the first synthetic model bathymetry, the 2020 measured bathymetry was replaced by the 1986 measured bathymetry inside the 0 m contour polygon (grey dotted polygon in Figure 89) of the bed level differences between 2020 and 1986 in the area of the Appelzak channel (Figure 90).
- For the second synthetic model bathymetry, the 2020 measured bathymetry was replaced by the 1986 measured bathymetry inside the 0 m contour polygon (black dotted polygon in Figure 89) of the bed level differences between 2020 and 1986 in the area of both the Appelzak channel and the Paardenmarkt ridge (Figure 90). Note that north of the Paardenmarkt ridge, there is no continuous contour line that indicates 0 m bed level changes between 2020 and 1986. Here, the polygon therefore follows the area with the smallest observed bed level changes.

For both synthetic model bathymetries, we performed Scaldis-Coast and FlemCo model runs based on (i) tidal and wind forcing, (ii) wave and wind forcing and (iii) tidal, wave and wind forcing (Table). For the wave and wind forcing, the realistic boundary conditions from Section 3.2.2 were used. The simulation results for the two synthetic model bathymetries were then compared with the corresponding simulation results already gained for the 2020 measured bathymetry (Scaldis-Coast runs MO6 008, MO6 007, MO6 009/FlemCo runs 050b, 052b, 047b; Table).

Table 11 – Overview of the Scaldis-Coast and FlemCo runs performed to investigate the impact of the deepening of the Appelzak channel on the longshore sediment transport and on the beach erosion.

Scaldis-Coast Run ID	FlemCo Run ID	Tidal forcing	Wave forcing	Wind forcing	Bathymetry
MO6_008	**050b**	On	Off	On	**2020**
MO6_032	**062**	On	Off	On	**2020 (Appelzak 1986)**
MO6_035	**063**	On	Off	On	**2020 (Appelzak + Paardenmarkt 1986)**
MO6_007	**052b**	Off	On	On	**2020**
MO6_031	**064**	Off	On	On	**2020 (Appelzak 1986)**
MO6_034	**065**	Off	On	On	**2020 (Appelzak + Paardenmarkt 1986)**
MO6_009	**047b**	On	On	On	**2020**
MO6_030	**060**	On	On	On	**2020 (Appelzak 1986)**
MO6_033	**061**	On	On	On	**2020 (Appelzak + Paardenmarkt 1986)**

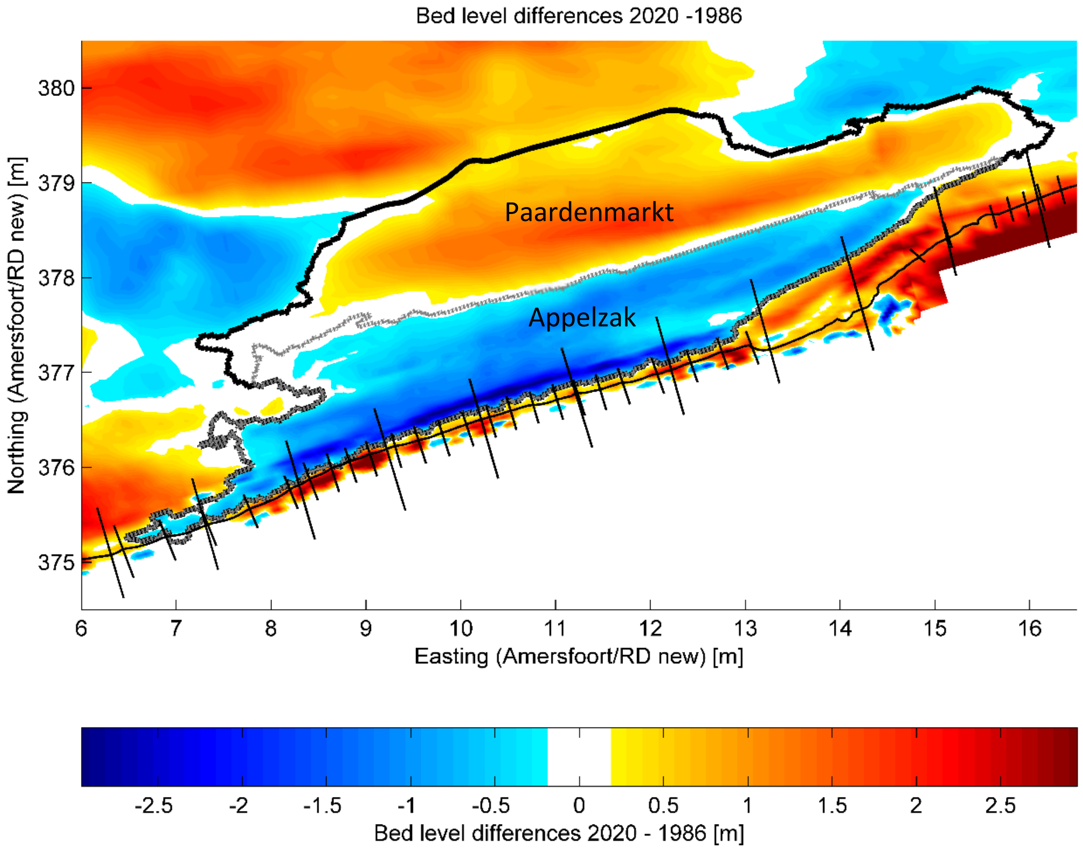

Figure 89 – Differences between the 2020 and the 1986 measured bathymetries in the area between Zeebrugge harbour and Cadzand. The two polygons indicate the 0 m contour lines of the bed level differences for the area of the Appelzak channel (grey dotted polygon) and for the Paardenmarkt bank (black solid polygon).

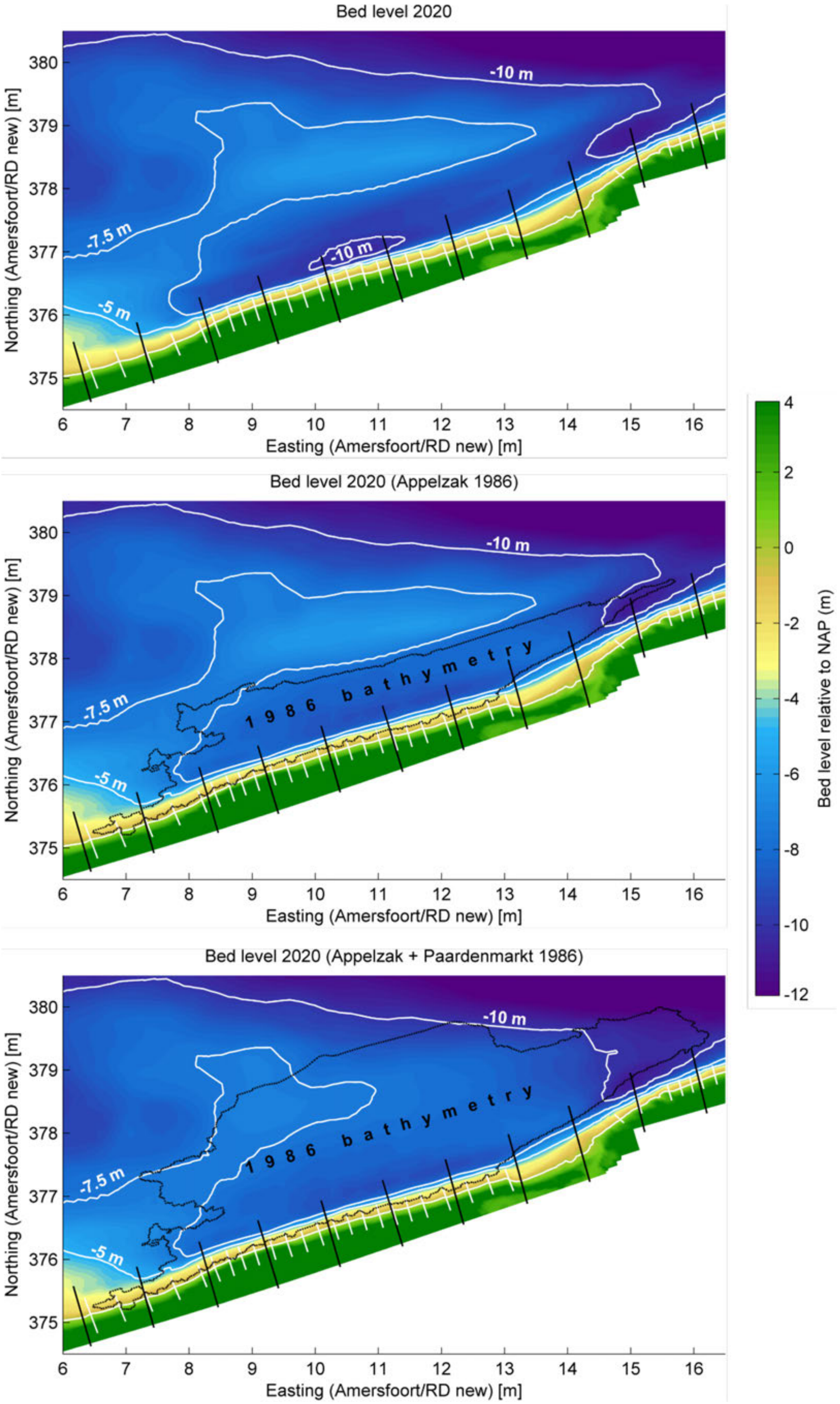

Figure 90 – The three model bathymetries, i.e. the 2020 bathymetry (top), the 2020 bathymetry combined with the 1986 bathymetry in the area of the Appelzak channel (centre) and the 2020 bathymetry combined with the 1986 bathymetry in the area of the Appelzak and Paardenmarkt, as applied in the Scaldis-Coast and the FlemCo models.

3.3.3 Results

As already shown before the wave-induced longshore transport is confined to a narrow band between the coastline and the -5 m TAW isobath: the breaker zone (Figure 91). Figure 92 shows the total residual sediment transport for the reference run of both models. In top view, the differences in yearly residual sediment transport between scenarios cannot be seen very well. Sediment transport vectors remain mostly parallel to the coastline on both the shoreface and in the Appelzak gully; the vectors only differ in length. For the scenario's, the modelled sediment transport vectors change orientation only over the changed bathymetry of the Paardenmarkt: a more shallow Paardemarkt leads to a reorientation of the vectors towards the coast. This change in orientation is more pronounced in the Scaldis-Coast model runs than in FlemCo, while the increase of (tidally driven) transport magnitude in the shallower Appelzak gully is more pronounced in the FlemCo simulations.

Therefore the results for the different scenarios with only wave + wind and with full hydrodynamic forcing will be explained on the basis of two transects: Transect 29 from the sea dike in Knokke-Zoute over the western part of the Appelzak gully and the Paardenmarkt sand ridge into the Wielingen channel, and Transect 30 over the eastern part of the Appelzak gully, in front of the Zwin nature reserve ca. 1 km west of its tidal inlet. In these cross-sectional Figure 93 to Figure 96 Scaldis-Coast results are shown in the top panel and FlemCo results in the bottom panel. The 2020 reference bathymetry is shown as a black line, while the shallower 1986 Appelzak gully and less pronounced 1986 Paardenmarkt ridge are shown in dotted grey. The large shoreface nourishment conducted in 1986 can clearly be seen in these figures, as the lower beach and shoreface are positioned more seawards in 1986 than nowadays. As a result, in front of Knokke-Zoute the peak of the wave-driven residual alongshore sediment transport shifts seawards with the 1986 shoreface in the Scaldis-Coast model. In the FlemCo model the peak in wave-driven residual sediment transport is very small for all scenarios, but the seawards shift can be observed (Figure 93). In front of the Zwin, the three scenarios show almost identical wave-induced residual transport (Figure 95).

The two simulations with synthetic bathymetry (Appelzak 1986 and Appelzak + Paardenmarkt 1986) show almost identical results for the wave-driven residual sediment transport on the shoreface. Therefore we can conclude that the height of the Paardenmarkt sand ridge has little to no influence on the wave climate for these simulations in the models. One might expect that a more pronounced crest of the sand ridge would attenuate some of the wave energy reaching the coast, but probably even nowadays the crest, situated at -3.68 m TAW, is not high enough to have an influence. This is in contrast to the Stroombank (Figure 63) and Trapegeer – Broersbank (Figure 64), where the shallow crests of the sand ridges (-2.88 m TAW, -2.28 m TAW and -1.14 m TAW respectively) are under the effect of wave action.

The bathymetric changes since 1986 do have an influence on the modelled tidally driven, and thus total residual longshore sediment transport. In the western part of the Appelzak the deepening of the channel leads to a decrease in modelled residual sediment transport (Figure 94). The more pronounced crest of the Paardenmarkt leads to an increase of the residual longshore sediment transport. In the eastern part of the Appelzak (Figure 96) these trends are inversed: a deeper channel shows more residual transport, while on the seaward flank of a more pronounced Paardenmarkt the (flood-directed) residual longshore sediment transport decreases and becomes ebb-directed. This behaviour is observed in both models. It is at this moment unclear if this is solely an effect of the shallower crest restricting (tidal) flow over it, or if changes in tidal asymmetry also play a role.

3.3.4 Discussion

Model results show that the yearly residual sediment transport in the west of the Appelzak gully (Knokke-Heist to Knokke-Zoute) is decreasing when the bottom of the gully is deeper. In the eastern part of the Appelzak (Knokke-Zoute to Zwin gully) a deeper gully shows an increase of residual longshore transport (Figure 98).

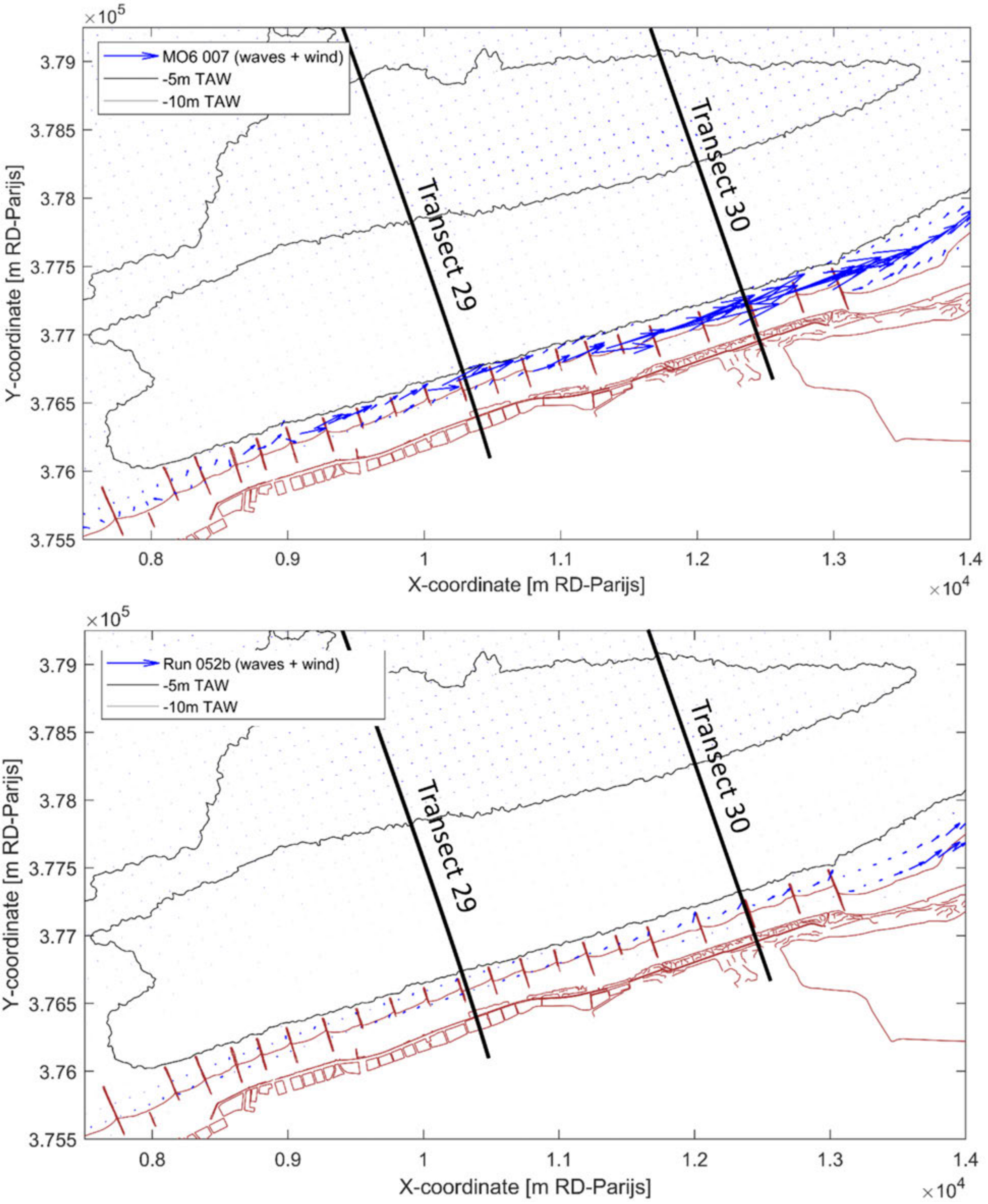

Figure 91 – Wave-induced residual sediment transport according to Scaldis-coast (top) and FlemCo (bottom) for the 2020 bathymetry (reference) in the area of the Appelzak.

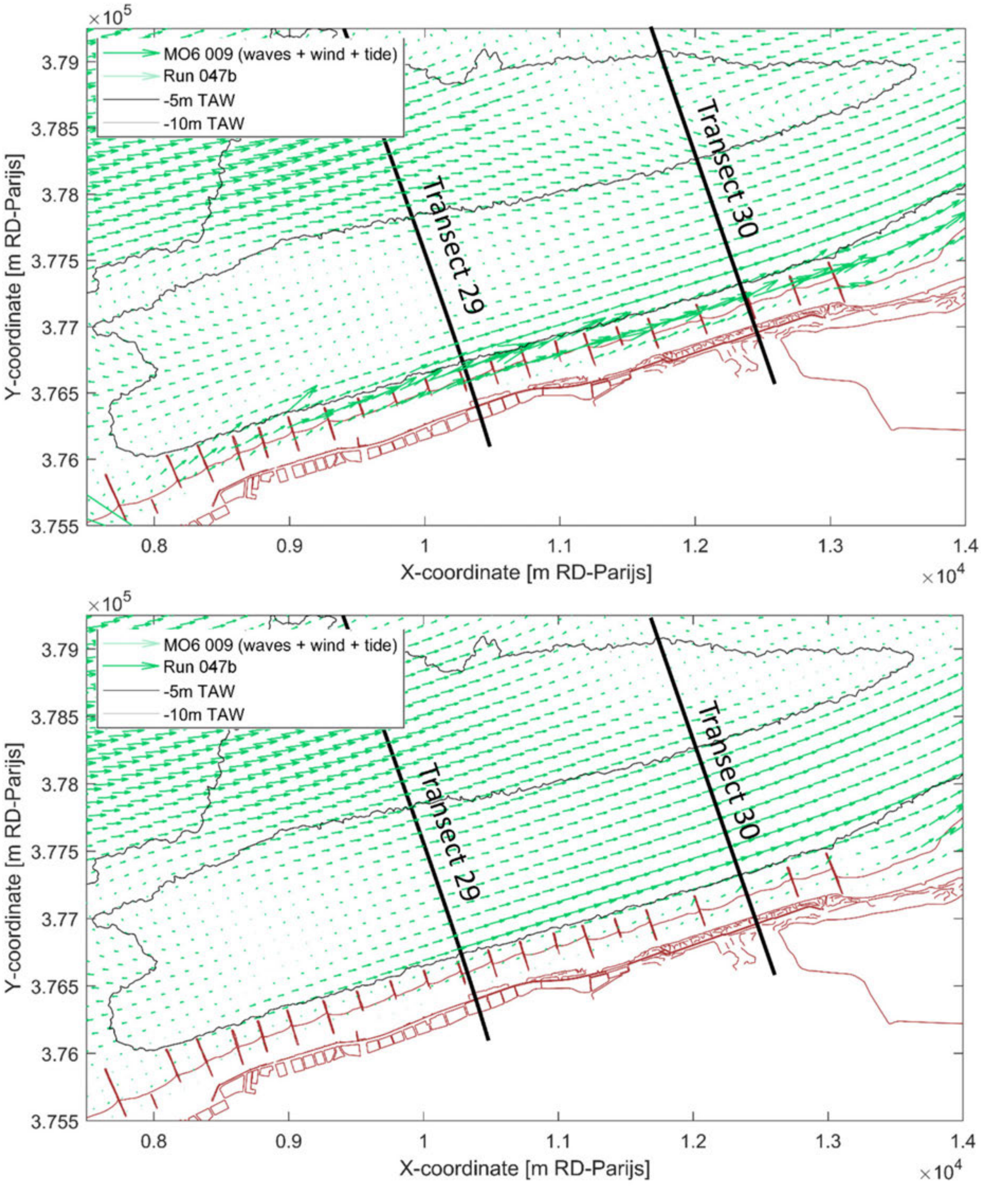

Figure 92 – Total residual sediment transport according to Scaldis-coast (top) and FlemCo (bottom) for the 2020 bathymetry (reference) in the area of the Appelzak

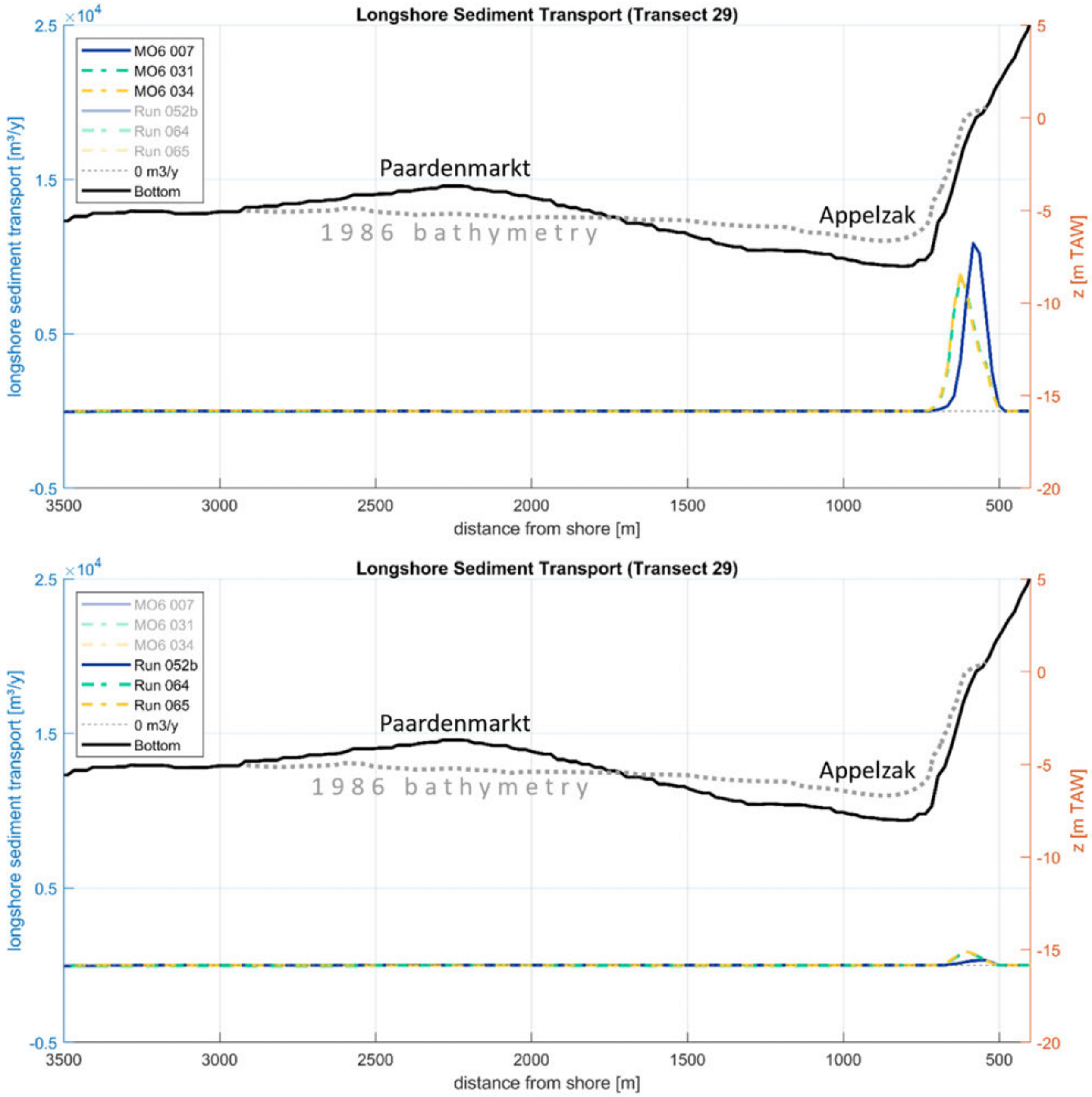

Figure 93 – Cross-shore distribution of the wave-induced residual longshore sediment transport, simulated with the Scaldis-Coast (top) and FlemCo (bottom); transect 29 over the Paardenmarkt sand ridge and Appelzak gully at Knokke-Zoute.

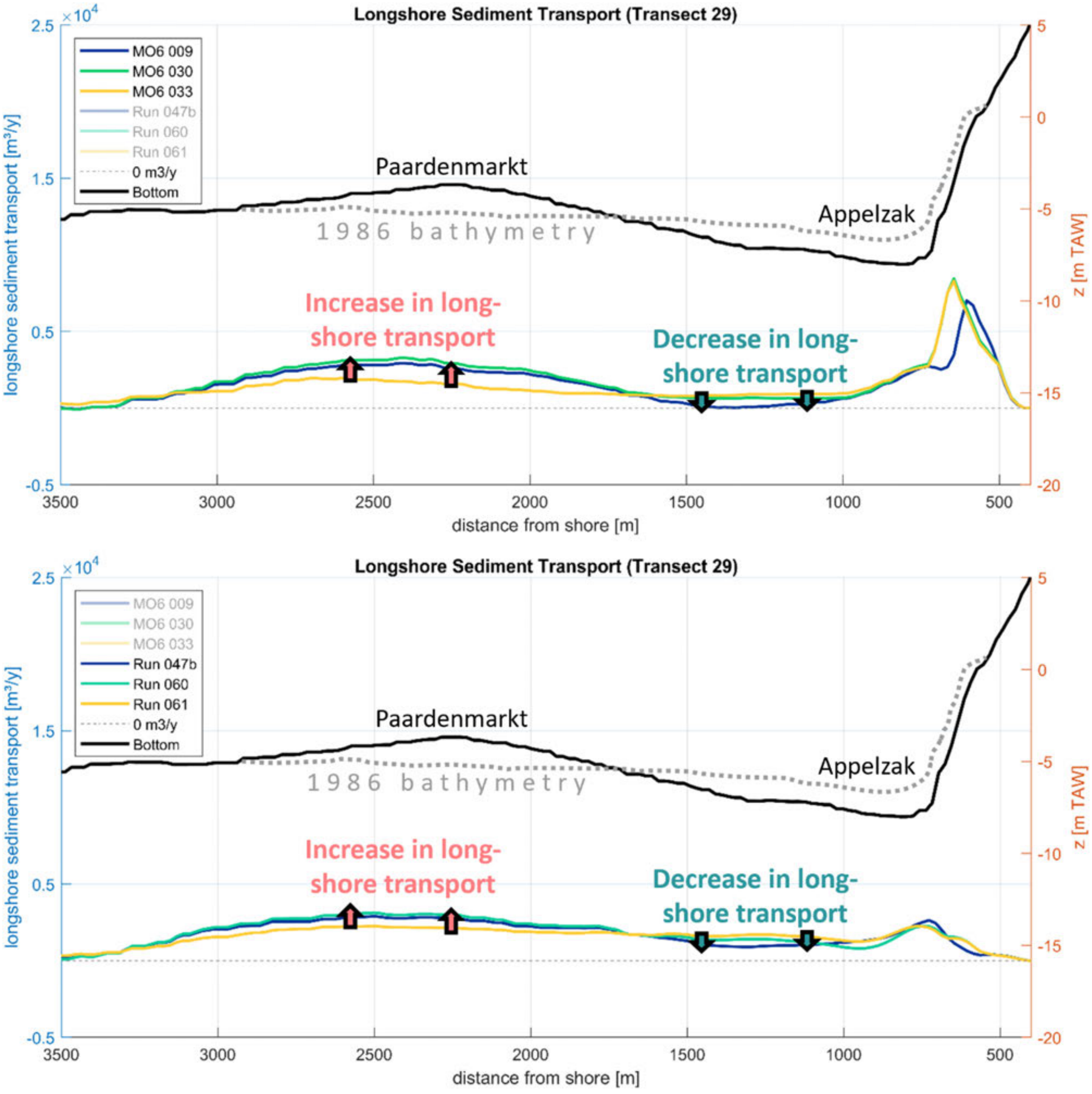

Figure 94 – Cross-shore distribution of the total residual longshore sediment transport, simulated with the Scaldis-Coast (top) and FlemCo (bottom); transect 29 over the Paardenmarkt sand ridge and Appelzak gully at Knokke-Zoute.

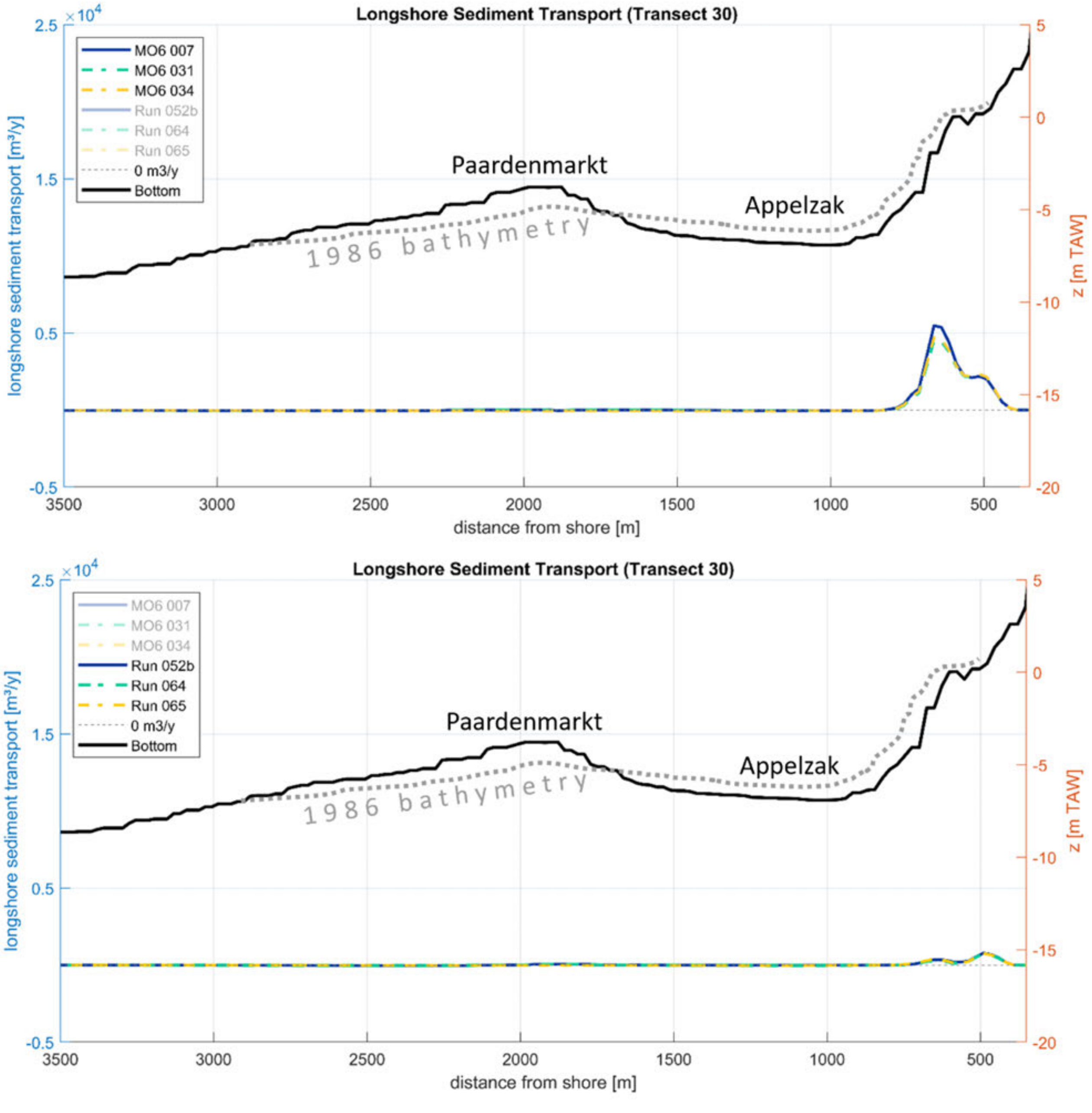

Figure 95 – Cross-shore distribution of the wave-induced residual longshore sediment transport, simulated with the Scaldis-Coast (top) and FlemCo (bottom); transect 30 over the Paardenmarkt sand ridge and Appelzak gully at the Zwin.

From the model results there's no direct evidence that a deeper Appelzak gully or a steeper shoreface leads to more erosion on the beaches of Knokke-Heist. The peak in wave-driven yearly residual sediment transport only shifts landwards/seawards with the location of the beach and shoreface (Figure 93), while the transport vectors generally remain parallel to the coastline (Figure 92). However, alongshore residual transport increases from east to west on this stretch of coast (Figure 97 and Figure 98), which indicates its erosional character from Knokke-Heist to Zwin. But since there's no significant change in the wave-driven alongshore yearly residual sediment transport in the breaker zone (Figure 97), the erosional character of this stretch of coast does not seem to be altered by changes in the nearshore sea bottom (Appelzak and Paardenmarkt).

However, it needs to be stressed that these models are not capable of resolving the 3D cross-shore wave processes; these are parametrized in a depth-averaged way. Especially for the long term predictions of coastal morphology this can be troublesome: e.g. quick erosion under storm conditions and slow rebuilding of the beach profile during calm conditions cannot be simulated with these models. It is expected that on a steeper beach and shoreface, sediment would erode quicker due to slope effects; end up in the Appelzak gully and transported with the tides. This assumption cannot be tested with these 2DH-models, but needs a 3D model that can fully resolve the cross-shore processes.

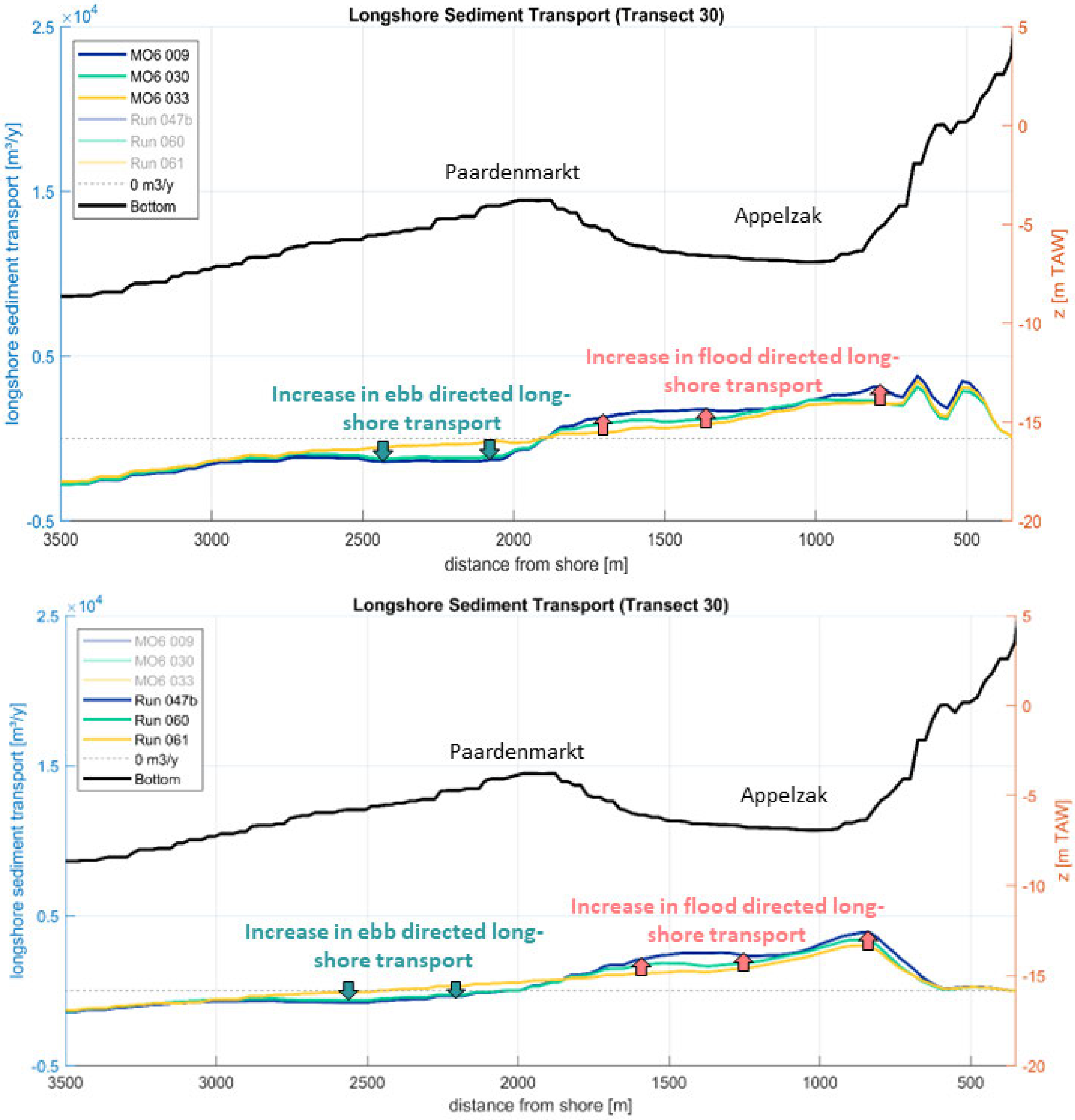

Figure 96 – Cross-shore distribution of the longshore sediment transport simulated with the Scaldis-Coast and FlemCo models; transect 30 over the Paardenmarkt sand ridge and Appelzak gully at the Zwin. Top panel: Scaldis-Coast results; bottom panel: FlemCo results.

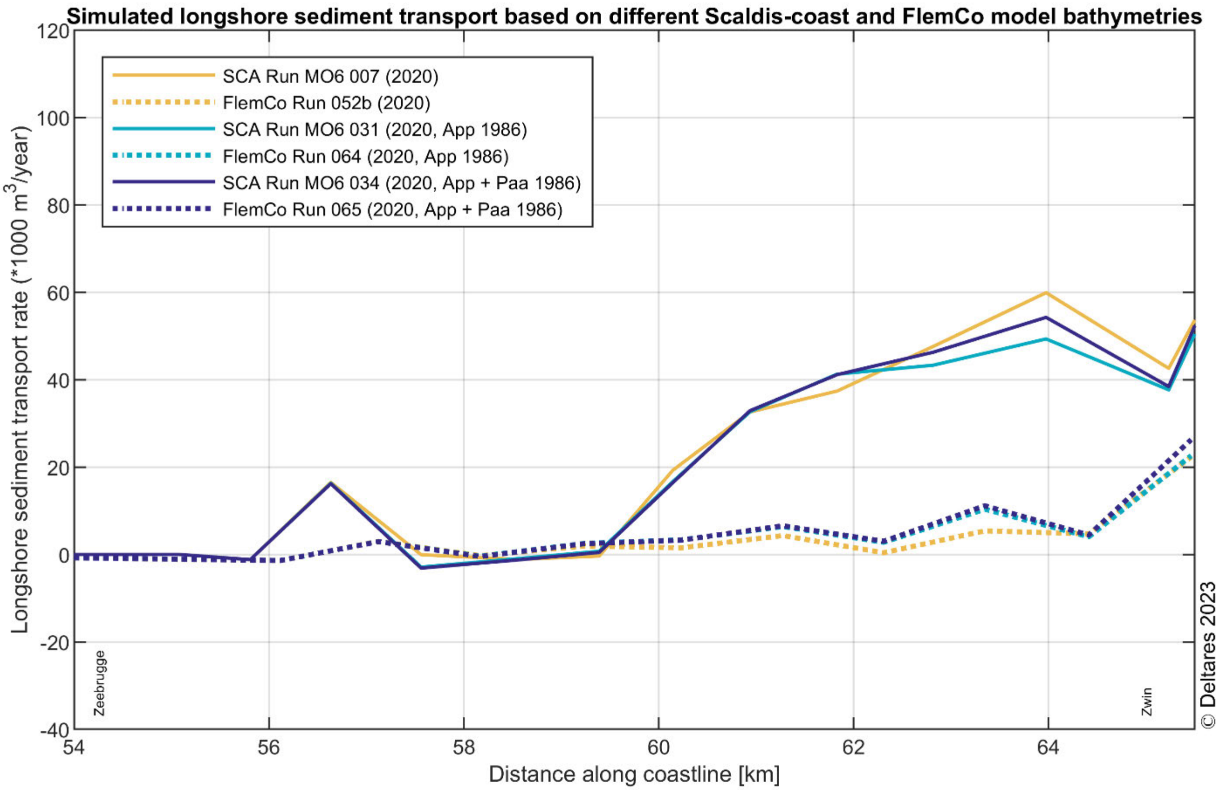

Figure 97 – Sediment longshore transport as simulated with the Scaldis-Coast (full lines) and FlemCo (dashed lines) model with only wave + wind forcing based on realistic 2020 bathymetry and synthetic bathymetries for Appelmarkt and Paardenmarkt 1986.

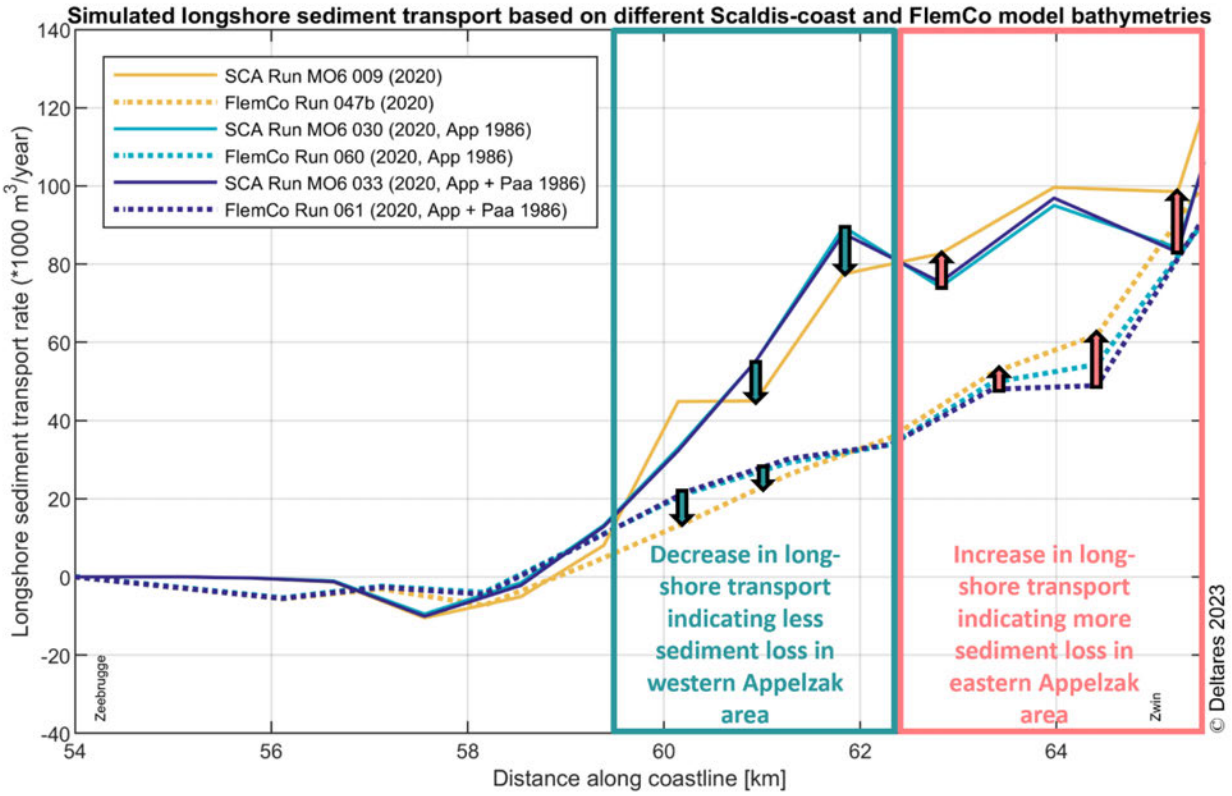

Figure 98 – Sediment longshore transport as simulated with the Scaldis-Coast (full lines) and FlemCo (dashed lines) model with full hydrodynamic forcing based on realistic 2020 bathymetry and synthetic bathymetries for Appelmarkt and Paardenmarkt 1986.

3.4 Calculation of Longshore Sediment Transport

3.4.1 Introduction and definitions[1]

Littoral drift, or **Longshore Sediment Transport (LST)**, is the term generally used for the longshore transport of sediments (mainly sand) along the upper shoreface due to the action of breaking waves and longshore currents. The division of lower and upper shoreface is based on the wave transformation caused by decreasing water depth: on the lower shoreface waves shoal (wave height increases, wave length decreases), while on the upper shoreface waves break. The division between upper and lower shoreface profiles is often marked by an inflexion point, a bar or a terrace, indicating transition of morphodynamics.

The assumption that sand transport in the coastal zone is mainly driven by waves only holds within a zone of limited cross-shore width. In deep water, waves and seabed hardly interact, because wave orbital motion decreases exponentially with depth. The strip along the coast where sand transport is mainly driven by waves is called the active coastal zone. The **closure depth** (or depth of closure, **DoC**) indicates the seaward boundary of the active coastal zone. Wave-induced sand transport has both a longshore and a cross-shore component. The longshore component plays a major role in structural long-term shore accretion or erosion (transport convergence or divergence). The cross-shore component is mainly responsible for large seasonal sand transfers up and down the beach, especially by alternating mild weather and storm weather conditions. This illustrates the temporal component of the active coastal zone concept, with different transport components and processes working on different time scales.

Hallermeier (1978, 1981, 1983) empirically determined the seaward limits of the lower (h_{out}) and upper shoreface (h_{in}):

$$h_{out} \approx 0.013 H_s T_s \sqrt{\frac{g}{d_{50}}} \qquad \text{(Hallermeier, 1981, 1983)}$$

$$h_{in} \approx 2.28 H_{12h/y} - 68.5 \frac{H_{12h/y}^2}{g T_{12h/y}^2} \qquad \text{(Hallermeier, 1978, 1981)}$$

In these equations the outer and inner closure depth are calculated from the significant wave height and according wave period for a certain time interval (e.g. 1 year). For the outer closure depth, the (yearly) average significant wave height and according period would be used, while for the inner closure depth the extreme significant wave height only exceeded 12 hours/year (or 0.137% probability of exceeding during a certain time period) is used in combination with its corresponding wave period. d_{50} represents the medium sediment grainsize in the shoreface profile, and g the gravitational acceleration. The wave conditions for calculating h_{in} should be determined just outside the breaker zone.

While sand transport in the coastal zone is assumed to be mainly driven by waves, other drivers of sediment transport can’t always be ignored. The combined wave- and tide-driven sediment transport on macrotidal beaches can be much larger than sediment transport only by waves (Valiente *et al.*, 2019). In the vicinity of shoreface-connected sand ridges wind (storm) driven currents are believed to be the main driver of sediment transport (Trowbridge, 1995).

The closure depth can also be determined based on morphological or sedimentary features in the shoreface profile: (1) a zone of minimum sand accretion or erosion (minimum variability of the profile in time) or (2) a discontinuity of the shoreface slope or a discontinuity in the shoreface sediment composition. Krauss *et al.* (1998) compared h_{in} and h_{out} derived from 4 years of surveys of shoreface profiles on the United States Atlantic coast (Figure 99) with the results from Hallermeiers equations, and found reasonable agreement.

---

[1] This section is a summary of several articles on shoreface profiles, active coastal zone and closure depth, wave transformation, sand ridges in shelf seas, littoral drift and shoreline modelling, etc. Which can be found on www.coastalwiki.org (Coastal Wiki, 2024).

Barrineau *et al*. (2021) repeated a similar study on a much larger set of transects and found that the morpholocal inner closure depth corresponds well with the Hallermeier formula for wave dominated coastal sections. However, for coastal sections where the energy of tides and waves is of the same order (mixed-energy coasts), the estimates for the morphological closure depth appear to be substantially smaller than the results of the Hallermeier formula. Also an influence of coastal inlets on the DoC was observed. Based on 5 years of profile data, Udo et al. (2020) found that the coefficients in Hallermeiers equation – although providing acceptable estimates – appear to be location dependent, overestimating DoC along the Pacific Ocean side and underestimating DoC along the Sea of Japan side. Birkemeier (1985) compared Hallermeiers formula with 16 months of profile data on the Pacific Ocean and Gulf of Mexico. He concluded that Hallermeier's equation overpredicts the inner closure depth, and proposed a modified version with reduced coefficients:

$$h_{in} \approx 1.75 H_{12h/y} - 57.9 \frac{H_{12h/y}^2}{g T_{12h/y}^2} \text{ (Birkemeier, 1985)}$$

Aragones *et al.* (2018) derived depth of closure estimates by analysing trend changes in the grain size distribution of several coastal profiles of the Mediterranean coast near Valencia. This local grain size minimum coincided with the closure depth derived from the convergence of the profile envelope (Figure 99). However, the depth was substantially smaller than the closure depth predicted by Hallermeier's formula and also smaller than predicted by the formula of Birkemeier.

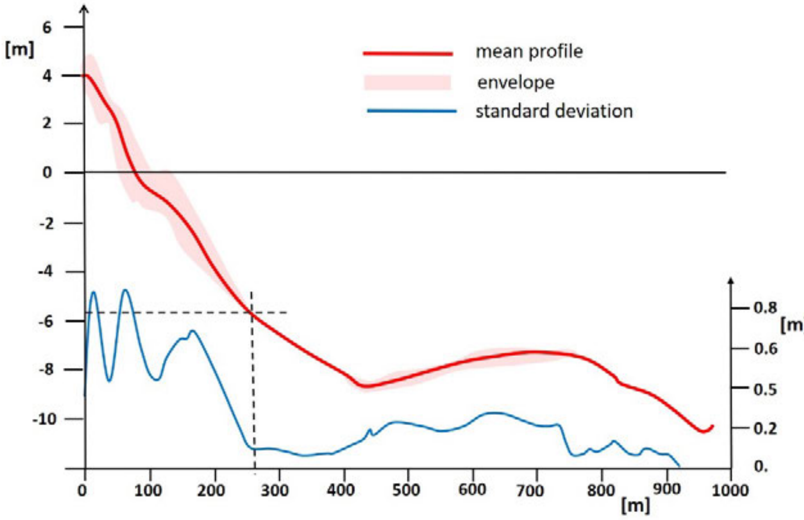

Figure 99 – Mean, envelope and standard deviation of profile survey elevations at the foot of 56th Street, Ocean City, Maryland, from Krauss et al. (1998). The inner depth of closure (h_{in}) is found at ca. 5.5 m depth, at the landwards side of a zone where the shoreline profile changes show a local minimum in standard deviation. The outer depth of closure (h_{out}) is found at ca. 10 m depth, where no elevation change of the profile is observed during the survey period (standard deviation of depth change = 0).

The section above shows that Hallermeier's formula can result in a good estimate of the inner closure depth; although local deviations can be expected, especially for mixed-energy coasts and coastal sections that hold a large variation in shoreface profiles (e.g. shoreface-connected sand ridges). In the section below we want to investigate the applicability of **Hallermeiers inner depth of closure** concept for the Belgian coast and its influence on the calculation of numerically modelled longshore sediment transport.

3.4.2 Inner closure depth along the Belgian coast

Vandebroek *et al*. (2017) computed Hallermeier's inner depth of closure for the whole Belgian coast. Firstly, they defined 9 longshore morphologic coastal cells for which they want to calculate the sediment budget (red polygons in Figure 101). These analysis cells were bound primarily by the harbours; in some cases the distance between the harbour was divided in approximately half, based on a key landmark or a change in coastline orientation. Wave climate data was retrieved from the SWAN model developed by IMDC (2009) for Flanders Hydraulics. This model propagates offshore wave time series (May 1st, 1996 – August 31st, 2005) towards the coast and exports the wave climate for 9 measurement locations (used for calibration/validation) and for more than 300 shallow water output locations along the -5 m TAW depth contour. From these shallow water output locations, Vandebroek *et al*. (2017) used 9 points: one for each coastal municipality, Zeebrugge excluded (Table 12 and Figure 100); to calculate the inner closure depth along the Belgian coast.

Pre-processing of the wave data was needed, since 21% of the time series was missing due to measurement gaps in one or more input wave buoys. Because much of the missing data occurs in winter, these data gaps could not be ignored, as these months are usually stormier and contribute more significantly to the longshore transport rates. For the application of the Hallermeier formula, small gaps (<4 hour duration) were linearly interpolated in time, and $H_{12h/y}$ and corresponding $T_{12h/y}$ were calculated from the resulting time series. Figure 100 (top panel) shows the obtained inner closure depth along the Belgian Coast; the results proved consistent with the offshore boundary selection of -5 m TAW.

Figure 101 shows the contour of the inner closure depth (green) as obtained by Vandebroek *et al.* (2017) in respect to the most offshore gridline in the N2V-model (Nieuwpoort to Vlissingen, Delft3D model) (blue) used by Wang *et al*. (2015) to integrate longshore sediment transport on the shoreface. The inner closure depth contour always lays more offshore than the offshore gridline in the N2V-model, except for the sections between De Haan and Wenduine (eastern half of cell 5) and between Knokke-Heist and Knokke-Zoute (eastern half of cell 8), where both lines show a good agreement. East of Knokke-Zoute the inner depth of closure lies closer to shore than the offshore gridline for integration in the N2V-model. This means that in the N2V-model, the width of the breaker zone might be underestimated for the area west of Knokke-Zoute, and as a result also the longshore sediment transport might be underestimated in the model. East of Knokke-Zoute the area in the N2V-model where the longshore sediment transport is integrated might be too wide, thus overestimating the width of the breaker zone. This means that alongshore sediment transport induced by the tidal currents in the Appelzak will also be integrated, resulting in an overestimation of the littoral drift (longshore sediment transport in the breaker zone).

Kolokythas *et al*. (2023) calculated yearly residual longshore transport in a similar way as Wang *et al*. (2015): by interpolating the Scaldis-Coast unstructured model results on a curvi-linear grid, and then integrating the alongshore component of the residual transport until a certain offshore gridline (Figure 102). The integration polygon for the Scaldis-Coast model extends more offshore than the one used for the N2V-model, and has a somewhat better agreement with the inner depth of closure as obtained by Vandebroek *et al.* (2017). Figure 102 clearly shows how the inner DoC jumps more offshore east of the sfcr Trapegeer-Broersbank-Den Oever, the remains of the sfcr Stroombank and in the wake of the Zeebrugge harbour breakwaters. In between those features, the inner DoC is situated ca. 200 m more shorewards than the integration polygon used for Scaldis-Coast; in the Appelzak tidal gully east of Zeebrugge even 300 m more shorewards. This shows clearly how the location of the inner DoC is influenced by the occurrence of near-shore morphological features like shoreface connected ridges and tidal gullies.

Table 12 – Output locations for the modelled nearshore wave climate used by Vandebroek et al. (2017). Source: IMDC (2009).

Coastal Municipality	Output Location	X	Y	Depth in model [m TAW]
De Panne	5mV_023	470931	5662065	4.9614
Koksijde - Oostduinkerke	5mV_038	473498	5664586	3.6454
Nieuwpoort	5mV_094	479850	5667537	5.5518
Middelkerke - Westende	5mV_121	486455	5671160	4.9527
Oostende	5mV_147	492895	5675867	6.4350
Bredene	5mV_161	495981	5679099	5.2790
De Haan - Wenduine	5mV_188	501611	5681711	5.2120
Blankenberge	5mV_225	508487	5686226	5.1081
Zeebrugge	PvZand_004	511637	5691881	12.9214
Knokke-Heist	5mV_260	519616	5689721	6.0028

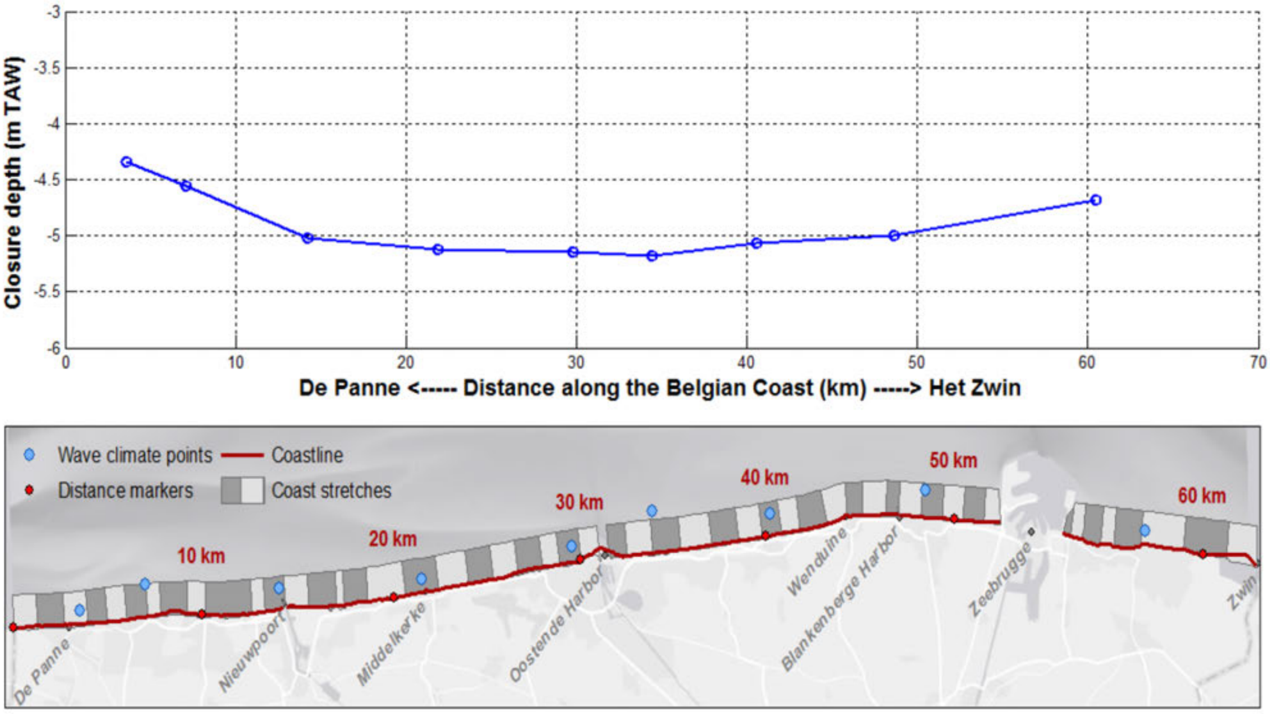

Figure 100 – Closure depth (in m TAW) along the Belgian coast, as calculated with Hallermeier (1981).
Source: Vandebroek et al. (2017).

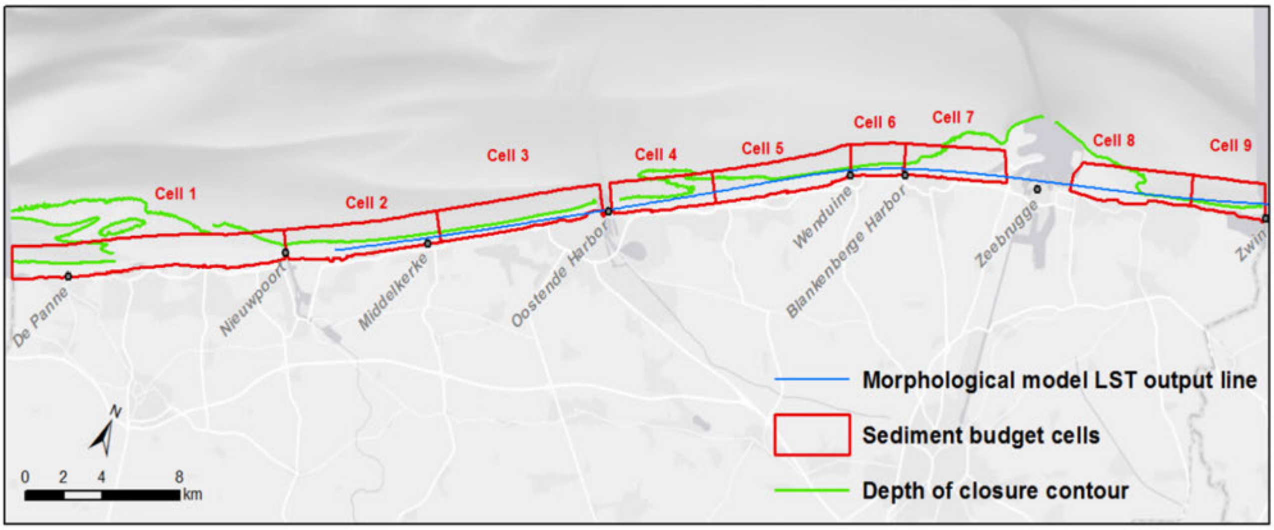

Figure 101 – Inner depth of closure contour (closest contour to shore, shown in green) and output line for modelled longshore sediment transport (blue) as defined in the N2V-model (Wang et al., 2015). Source: Vandebroek et al. (2017).

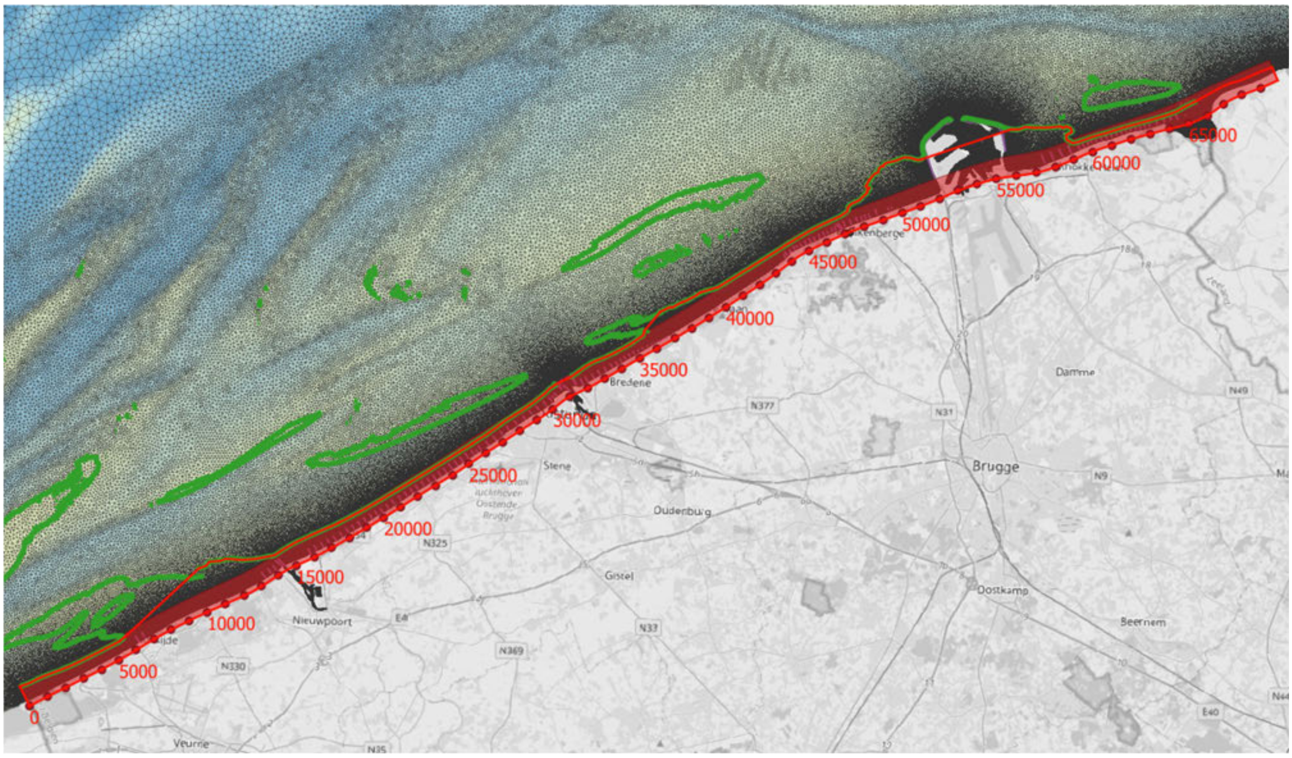

Figure 102 – Inner depth of closure contour derived by Vandebroek et al. (2017) (shown in green, cfr. Figure 101) and integration polygon for modelled longshore sediment transport (red shaded polygon) as used in the Scaldis-Coast model post-processing (Kolokythas et al., 2023). The new suggested integration polygon, based on the inner closure depth concept is shown as a thick red line.

3.4.3 Results

Figure 103 shows the longshore sediment transport (LST) as calculated with the Scaldis-Coast model for both the integration polygon used by Kolokythas *et al.* (2023) and the integration polygon based on the inner depth of closure as defined by Vandebroek *et al*. (2017). The top panel of Figure 103 shows the wave-induced LST. Differences between both integration polygons are only visible around the harbour of Zeebrugge: the larger cross-shore distance for the polygon based on the inner DoC (full line) yields higher transport volumes, and just in front of the western breakwater even some westwards transport. The bottom panel of Figure 103 shows the tide-induced LST. Where the inner DoC is located more offshore than the integration polygon of Kolokythas *et al*. (2023) the computed tide-induced LST becomes higher. This is the case for the area between Koksijde and Nieuwpoort, where the sfcr Broersbank – Den Oever attaches to the coast; between Bredene and De Haan, where the remains of the Stroombank attaches to the coast; and finally the sedimentation area between Blankenberge and the western breakwater of Zeebrugge, and to a minor extent the Baai van Heist east of Zeebrugge.

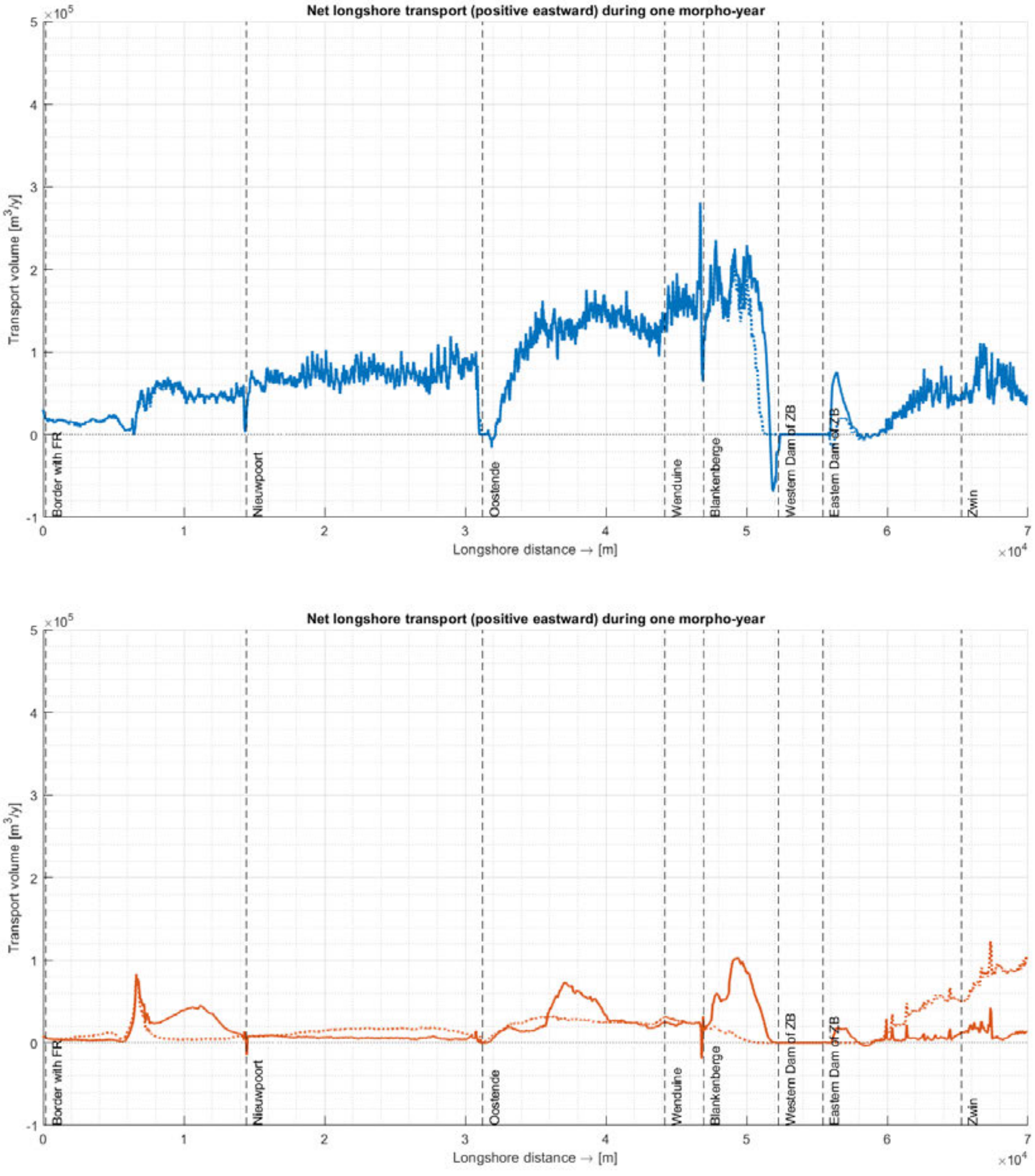

Figure 103 – Longshore Sediment Transport along the Belgian coast. Top panel: wave-induced LST; bottom: tide-induced LST. Dotted line: integration polygon from Kolokythas et al. (2023); full line: integration polygon based on Vandebroek et al. (2017).

Where the inner DoC is located closer to shore than the integration polygon of Kolokythas *et al*. (2023) the computed tide-induced LST becomes lower. This is the case for the Potje gully west of Koksijde, the Kleine Rede gully between Nieuwpoort and Oostende, and especially in the Appelzak gully east of Knokke-Heist.

Figure 104 shows the calculated LST for simulations with wave (blue), tide (red) and full forcing (yellow); full lines represent the results for the integration polygon based on the inner DoC, dotted lines the results for the integration polygon of Kolokythas *et al*. (2023). As to be expected, differences in calculated LST for the run with full forcing occur in exactly the same areas as for the run with only tidal forcing.

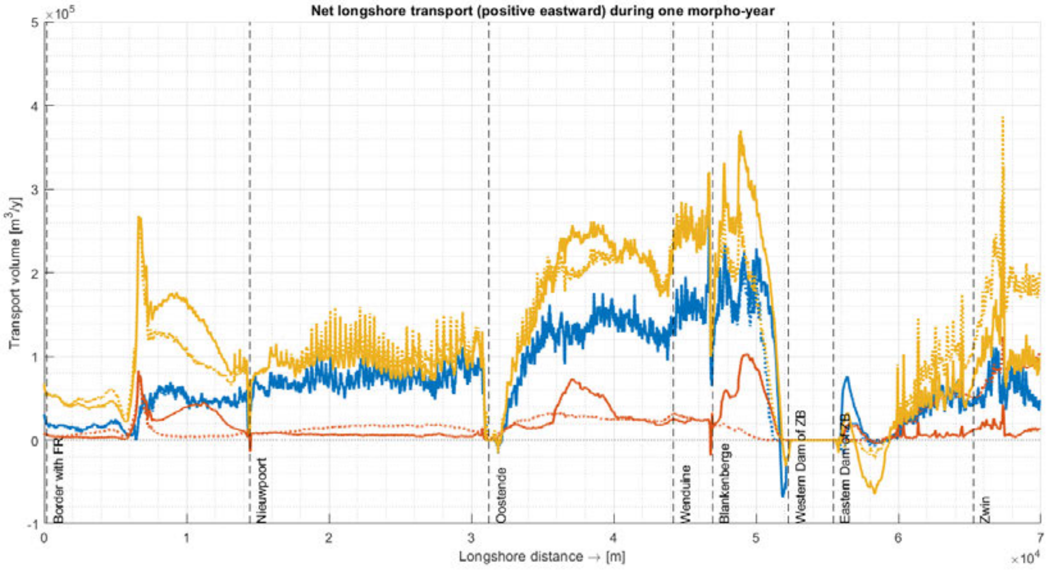

Figure 104 – Longshore Sediment Transport along the Belgian coast. Blue line: wave-induced transport; red line: tide-induced transport; yellow line: full forcing; dotted line: integration polygon from Kolokythas et al. (2023); full line: integration polygon based on Vandebroek et al. (2017).

Figure 105 shows the cross-shore distribution of the calculated LST for simulations with wave (blue), tide (red) and full forcing (yellow). The vertical green and red lines indicate the offshore extent of the interpolation polygons based on the inner DoC as defined by Vandebroek *et al.* (2017) and the one used by Kolokythas *et al.* (2023) respectivily. The transect over Broersbank – Den Oever (Transect 5) shows how a small part of the wave-induced LST is not taken into account when using the integration polygon of Kolokythas *et al.* (2023). For Transect 24, in the shallow zone directly west of the western breakwater of the Zeebrugge harbour, a large part of the wave-induced LST is missed by the integration polygon of Kolokythas *et al.* (2023). At Transect 18, where the remainder of the Stroombank attaches to the coast, both integration polygons will include all wave-induced LST.

Because of its larger offshore extent the integration polygon based on the inner DoC will yield (relatively) higher tide-induced LST for all transects shown in Figure 105. One might argue that, for the wave conditions used for these simulations, the inner DoC is situated too far offshore for these locations with a shallow, mildly sloping shoreface. As mentioned above, where a tidal gully is present in front of the coastline, the integration polygon based on the inner DoC will be closer to shore in respect to one of Kolokythas *et al.* (2023). This is illustrated by Figure 106, showing the cross-shore distribution of the calculated LST in the Kleine Rede (Transect 13), Grote Rede (Transect 21) and Appelzak (Transect 29). For Transect 21 (Grote Rede) both integration polygons seem to be slightly too close to shore, and missing a tiny bit of the wave-induced LST. For Transect 29 (Appelzak) only the integration polygon based on the inner DoC seems to be a tiny bit too close to shore. While the offshore extent of the integration polygon of Kolokythas *et al.* (2023) seems too far offshore for Transect 13 (Kleine Rede) and Transect 29 (Appelzak), and will thus yield (relatively) higher tide-induced LST.

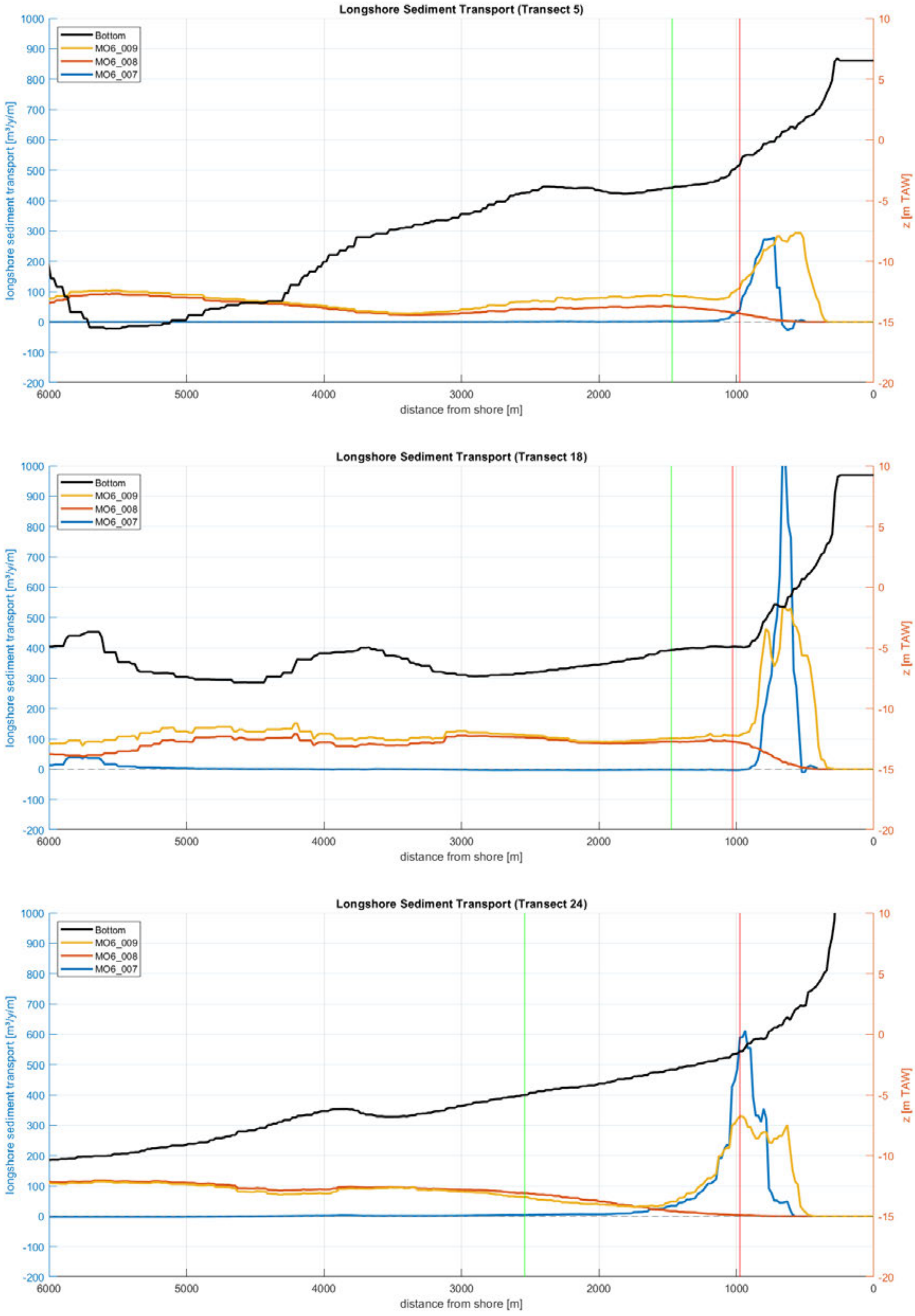

Figure 105 – Cross-shore distribution of the longshore sediment transport as simulated with the Scaldis-Coast model for several transects in shallow zones west of Zeebrugge. Transect 5: Broersbank – Den Oever east of Koksijde; Transect 18: remainder of the Stroombank between Breden and De Haan; Transect 24: shallow zone directly west of Zeebrugge harbour. Green and red vertical lines show the offshore extent of the interpolation polygons based on the inner DoC and the one used by Kolokythas et al. (2023). Blue lines: only wave-induced LST; red lines: only tide-induced LST; yellow lines: full forcing.

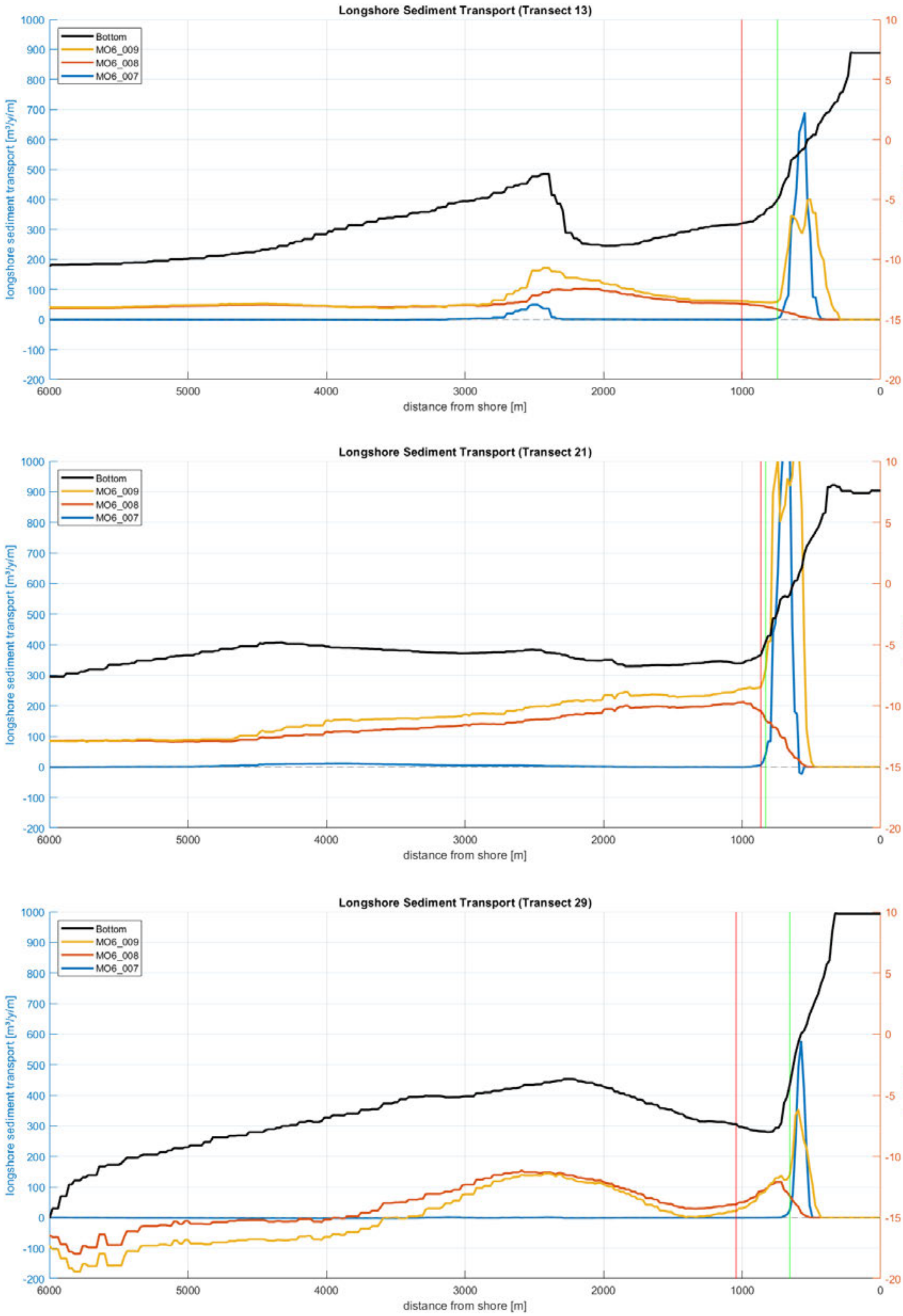

Figure 106 – Cross-shore distribution of the longshore sediment transport as simulated with the Scaldis-Coast model for several transects where a tidal gully is present in front of the coastline. Transect 13: Kleine Rede, near Raversijde; Transect 21: Grote Rede, at Wenduine; Transect 29: Appelzak gully at Knokke-Zoute. Green and red vertical lines show the offshore extent of the interpolation polygons based on the inner DoC and the one used by Kolokythas et al. (2023). Blue lines: only wave-induced LST; red lines: only tide-induced LST; yellow lines: full forcing.

Both the plan views shown from Figure 66 till Figure 71 and the cross-shore profiles shown in Figure 105 and Figure 106 indicate that the modelled wave-induced LST occurs in a narrow strip along the coast: the breaker zone. Tide-induced LST gradually increases from the shoreline till offshore, reaching a maximum outside of the breaker zone. But tidal forces do have an influence on the LST in the breaker zone; not only does the width of the breaker zone increase due to the variation of the water level, also interactions between wave-induced and tidal currents can alter the LST.

Figure 107 shows the distribution of the simulated LST along the Belgian coast, normalised for the summed wave- and tide-induced LST. By definition, the relative wave- and tide-induced LST's are complementary in this graph: the sum of both is always equal to one. But the figure also shows that interaction between wave and tides is non-linear: the combined effect of both is (mostly) larger than one. Both models show a variation of this non-linear behaviour along the coast, although the effect is more important in the Scaldis-Coast model. West of Nieuwpoort the total LST is 1.5 to 3 times bigger than the sum of wave- and tide-induced LST; between Nieuwpoort and Zeebrugge the factor is around 1.25, while between Zeebrugge and the Zwin the factor is around one. For some locations the combined effect of wave and tides might even reduce the total LST. What is causing this alongshore differences has not yet been investigated. Possible influence factors that come to mind are the alongshore variations in beach profile, tidal amplitude, residual (tidal) current or tidal asymmetry, or the amount of wave energy that reaches the coast.

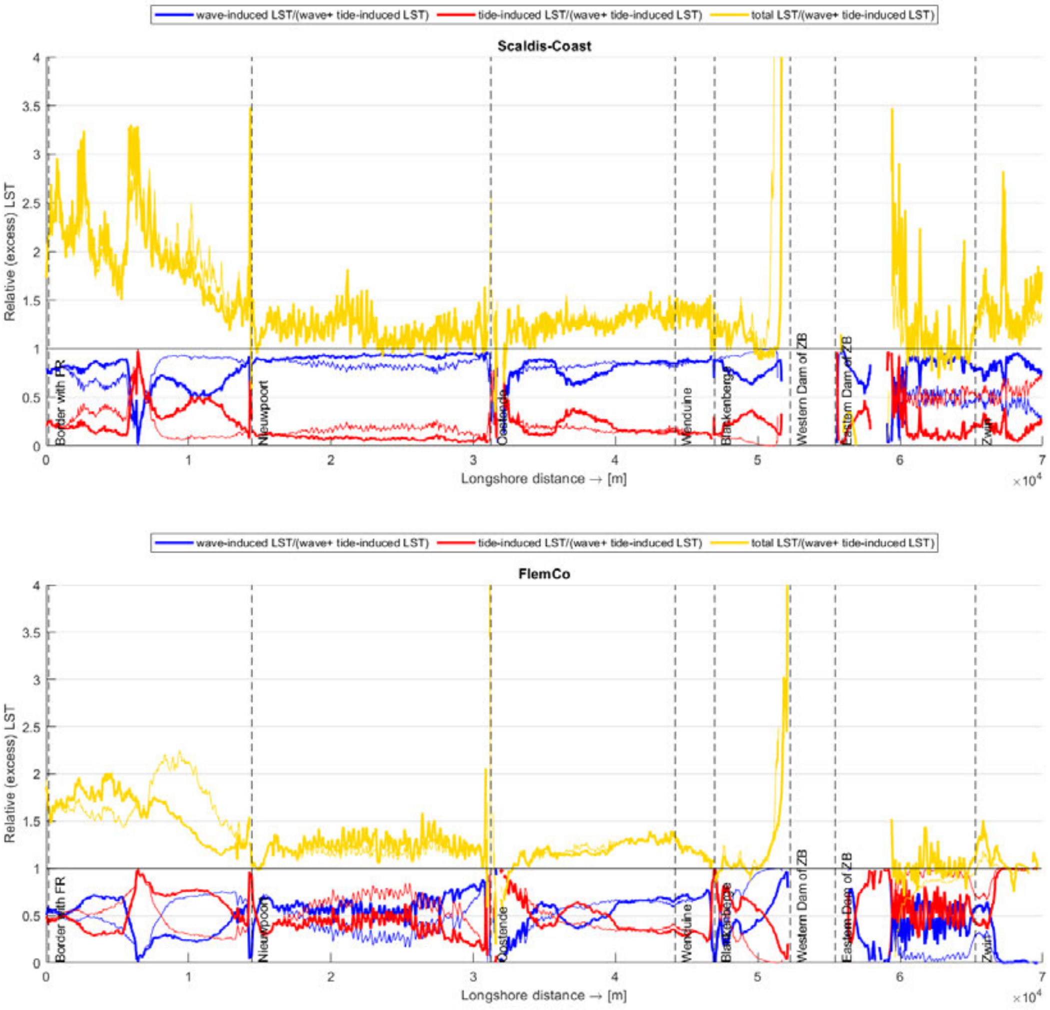

Figure 107 – Simulated Longshore Sediment Transport (LST) normalized for the sum of the wave- and tide-induced LST. Thick lines – integration polygon based on inner DoC as defined by Vandebroek et al. (2017); thin lines – integration polygon based on Kolokythas et al. (2023). Top panel – Scaldis-Coast simulations; bottom panel – FlemCo simulations.

Figure 107 shows once again that the tide-induced LST is relatively more important in the FlemCo model than in Scaldis-Coast. In the Scaldis-Coast model the ratio between wave- and tide-induced LST varies between 90/10 and 80/20. Only where Broersbank – Den Oever attaches to the coast, and other shallow areas like the Baai van Heist, simulated tide-induced LST is relatively more important than wave-induced LST. In the FlemCo model however, the ratio is much closer to 50/50, with large areas where the tide-induced LST is relatively more important than the wave-induced LST. East of Zeebrugge the relative contribution of both driving forces to the total LST is totally different in both models. The FlemCo model barely produces any wave-driven LST in this zone (see Figure 60). When the integration polygon of Kolokythas *et al.* (2023), which includes an important part of the Appelzak tidal gully, is used, the relative contribution of the wave-driven LST is only 5%. When the integration polygon is reduced to the width of the breaker zone, the relative contribution increases to 50%. In the Scaldis-Coast model the relative contributions of wave- and tide-driven LST for the integration polygons are 50/50 and 90/10.

As illustrated above, the strong influence of the integration polygon which was used also shows in the figure. Where the integration polygon from Kolokythas *et al.* (2023) takes into account a part of the tidal gully (Potje, Kleine Rede, Appelzak), the relative importance of the tide-induced LST is higher than for the integration polygon based on the inner DoC (respectively thin and thick lines in the plot). On the other hand, in the shallow areas, where the integration polygon based on the inner DoC is situated more offshore (Broersbank – Den Oever, remainder of Stroombank, accretion areas around Zeebrugge breakwaters) tide-induced LST will be relatively higher than for the one used by Kolokythas *et al.* (2023).

3.4.4 Conclusion

In this section, a sensitivity analysis on the influence of the offshore extent for cross-shore integration of the longshore sediment transport (LST) was carried out. Two approaches were followed to define the offshore extent of the integration polygon:

i. Hallermeiers inner depth of closure as defined by Vandebroek e*t al*. (2017), and
ii. an approximation of the -5 m TAW isobath based on a single gridline from a curvi-linear grid draped along the coastline as defined by Kolokythas *et al.* (2023).

Numerical model simulations were performed with the boundary conditions listed in Table 8. For both integration methods, locations can be found where the offshore extents seems to be either too far from, or too close to the shore, given the used (wave) boundary conditions. The cross-shore extent is considered to be too close to the shore when part of the calculated wave-induced LST falls outside the polygon. However, differences in computed wave-induced LST are negligible. When the offshore extent of the integration polygon is too far offshore, this will yield (relatively) higher tide-induced LST.

One might argue that Hallermeiers inner DoC approach is not fully valid for mixed-energy coasts and areas with a great variation in shoreface profiles, as it is based on the (long term) wave climate and a digital elevation model, but does neglect possible influences of (tidal) currents. The other approach however, is a crude approximation of the active coastal zone by a representation of the -5 m TAW isobath by a curvi-linear gridline. It therefore has a rather arbitrary, constant cross-shore extent. But since differences in calculated wave-induced LST are negligible, both methods can be used as long as results are analysed and compared cautiously. E.g. when analysing the influence of the tides on LST, both methods will yield relatively higher tide-induced LST in different areas. The use of the integration polygon based on the inner DoC as defined by Vandebroek *et al*. (2017) will result in higher tide-induced LST in the shallow areas of shoreface connected sand ridges and sedimentation areas around the breakwaters of Zeebrugge harbour. While the use of the integration polygon as defined by Kolokythas *et al*. (2023) will result in higher tide-induced LST in the coastal sections where a tidal gully is present.

The interaction between wave and tides is non-linear: the combined effect of both driving forces on the calculated LST is (mostly) larger than the sum of the solely wave- and tide-driven LST. Both models show a variation of this non-linear behaviour along the coast, although the effect is more important in the Scaldis-Coast model. West of Nieuwpoort the LST is enhanced the most, while between Knokke and Het Zwin there's no enhancement. What is causing this alongshore differences has not yet been investigated. Possible influence factors could be alongshore variations in beach profile, tidal amplitude, residual (tidal) current or tidal asymmetry, or the amount of wave energy that reaches the coast.

4 Summary and conclusions

4.1 WP1: Data Acquisition and Analysis

In the second year further bathymetric and beach topographic data were digitized in Task 1, Data Acquisition and Analysis: a cover of the inner shelf consisting of a mosaic of surveys in the 1960s, another one for the 1990s, the nearshore survey of Spring 1992, and most of the beach and outer dune topographic mapping of Spring 1992 (complete coast save the section from Nieuwpoort to Oostende). The uncertainty of bathymetric surveys was analysed for the past decades. It appears that even on today's surveys, an vertical uncertainty of ± 0.15 m is to be taken into account in all analyses, regardless of whether they are based on SB or MB surveys. A start was made of providing an overview of bed sediment parameters of the inner shelf and nearshore zone. A first analysis over the last decades of depth contour line shifts confirms the sand retaining quality of groynes. Much sand is trapped at both sides of the outer harbours of Oostende and Zeebrugge. Extensive and sustained beach nourishments have induced a seaward beach expansion, but at the same time the shoreface base is widely eroded. Finally, a case study of morphological bed change was conducted in relation to dredging (BIS) reports for 2014-2016 in Pas van Stroombank. Both geographically and quantitatively, the BIS export rasters of Reduced Volume are in good agreement with the bed changes revealed by repeated bathymetric surveys. From the BIS export rasters available for the case study, no reliable information on dredged sediment type could be obtained, as sediment density appeared to be equal across all time intervals and zones. The BIS parameter "reduced volume" gave good agreement between dredged amounts per time interval and zone, and volumes calculated from successive bathymetric surveys. In the study period and area, yearly dredged volumes ranged from about 100,000 to over 300,000 m^3. Two regimes of sedimentation are active, sometimes simultaneously. One is sandy sedimentation at the western flank of the navigation channel due to trapping of longitudinal bed transport on Stroombank. The other is spatially extensive sedimentation most likely caused by a combination of trapping fine suspended sand and influx of fluid mud. A first estimate from successive profiles of longitudinal bed transport over Stroombank of about 100 m^3/m was obtained. In Kleine Rede, sediment transport derived in an analogous manner was about 4 times higher.

4.2 Numerical modelling

4.2.1 WP2: Shelf-shoreline coupled morphodynamics: idealized model

In WP2 of the MOZES project, the second year focused on two main activities (Activity 1 and 2) aimed at further developing the morphodynamic shelf model and the coupled shelf-shoreline model established in the first year. In the morphodynamic model the shelf bottom changes in time, whereas in the coupled shelf-shoreline model, the shelf bottom is freezed (morphostatic) and the shoreline evolves in time.

In Activity 1, the morphodynamic shelf is further improved by incorporating the Belgian shelf bathymetry and by computing wave propagation on the shelf using the original SWAN model. In Activity 2, the coupled shelf-shoreline model is further refined by 1) using a synthetic ridge with geometry (length, width and orientation) similar to those of the Belgian shelf, 2) implementing a more realistic wave forcing, and by 3) considering tides in shoreline model.

Key achievements in the second year include:

1. Establishment of a realistic wave climate and background topography based on bathymetric data and offshore wave buoy information.
2. Development of a new morphodynamic shelf model capable of simulating self-developing shoreface-connected sand ridges (sfcr) in the presence of (for the first time!) wave-topography feedbacks. The simulated ridges have notable similarities to observed Belgian shelf ridges. Distinctions (alignment with respect to coast, alongshore spacing) were noted, attributed to factors like the absence of tides, simplified wave forcing, and exclusion of sea level rise.
3. Significant improvements to the coupled shelf-shoreline model, reproducing observed shoreline progradation adjacent to the ridge and a steeper bathymetry profile in the breaker zone near the channel. Simulations with this model indicate that the observed onshore movement of sfcr on the Belgian shelf is likely to intensify shoreline retreat near the channels and progradation near the ridge crests.
4. Implementation of a new (analytical) tide model in the shoreline evolution model (Q2Dmorfo), revealing dominance of wave-induced sediment transport in the breaker zone and significant tide-induced transport further offshore. These findings align with results from complex models FlemCo and Scaldis-coast.

4.2.2 WP3: Natural feeding of the beach over shoreface connected ridges

Main focus was to understand differences between simulated longshore sediment transport and sediment pathways over ridges by the Scaldis-Coast and FlemCo models. Compared with the former model, FlemCo simulates smaller alongshore transport and a cross-shore deflection of sediment particles over the shoreface-connected ridges. Many simulations have been carried out using different model configurations and forcings combinations (grid size, only waves, waves + wind, only tide, tide + wind, tide + wind+ wave, simplified forcings, etc.).

Model outcomes indicate that, even when reducing grid resolution in the nearshore zone, the FlemCo model still predicts a smaller longshore sediment transport for the Belgian coast compared to the Scaldis-Coast model. Sensitivity simulation runs, utilizing different forcing combinations (tide, waves, and wind), reveal that the differences between the simulated transports of two model lies in wave-induced longshore sediment transport, while the tide-induced transports are similar. The differences in wave-induced longshore transport emerge when wind is introduced, resulting in higher wave height peaks and more dominant northern and western wave directions in the Scaldis-Coast model. This leads to a more pronounced wave-induced longshore current and, consequently, higher wave-related longshore transport in Scaldis-Coast compared to FlemCo.

Discrepancies in predicted waves result not only from the different wave models (TOMAWAC/SWAN) but also from varying settings, notably the bed friction coefficient (lower in Scaldis-Coast) and breaker index (higher in Scaldis-Coast). Additionally, groynes in the Scaldis-Coast model are smaller, obstructing the wave-induced longshore current to a lesser extent than in the FlemCo model. Collectively, these factors favour higher wave energy, more pronounced wave-induced longshore currents, and consequently, higher longshore transport in the Scaldis-Coast model. These outcomes are further supported by the fact that, when the same wave model settings, constant wave and wind boundary conditions, and no groynes are applied in the FlemCo model, both models predict very similar longshore sediment transports along the Belgian coast.

Despite the differences in the longshore sediment transport that exist between the Scaldis-Coast and FlemCo models, both models highlight the dominance of wave-induced longshore transport within the initial few hundred meters from the coastline (breaker zone). Tide-induced longshore transport becomes dominant further seaward. These results confirm wave-induced transport dominance in the breaker zone and the tide-induced transport further offshore, as was found by the idealized model (WP2). It is shown that tides do have an influence on the (wave-induced) longshore transport in the breaker zone. In cross-shore profiles a broadening (due to the varying water level) of the peak of longshore transport in the breaker zone can be observed when tides are added to the model. Depending on the location along the Belgian coast, the height of this peak can increase, decrease or remain identical, but the net alongshore transport in the breaker zone will almost always increase. Also the non-linear interaction between waves and tides is shown: the computed annual longshore sediment transport for simulations with full hydrodynamic forcing is in general larger than the sum of the purely wave- and tide-driven longshore transport. Both models show a variation of this non-linear behaviour along the coast, although the effect is more important in the Scaldis-Coast model. West of Nieuwpoort the longshore sediment transport is enhanced the most, while between Knokke and Het Zwin there’s no enhancement. What is causing this alongshore differences has not yet been investigated. Possible influence factors could be alongshore variations in beach profile, tidal amplitude, residual (tidal) current or tidal asymmetry, or the amount of wave energy that reaches the coast.

Finally, the model simulations, employing the full hydrodynamic forcing, do not reveal any residual sediment transport towards the beaches. However, no firm conclusion regarding the process of natural feeding is possible from this as these models do not include cross-shore sand transport in a validated way. As these models are 2DH they do not explicitly resolve cross-shore processes. In particular, the complex 3D currents in the breaker zone are expected to be responsible for the process of natural feeding of the coast. To further investigate the hypothesis of natural feeding, a possible way forward is applying the models in three-dimensional mode, possibly limited to a subdomain, to assess their ability to resolve the 3D flow patterns in the breaker zone.

4.2.3 WP4: Linking deepening of nearshore tidal channels to beach erosion

In WP4, the study examined the impacts of the observed deepening of nearshore tidal channels on the neighbouring beach in the Knokke-Heist region. Various scenarios were investigated by decreasing the depth of the Appelzak channel and/or increasing the depth of the Paardenmarkt ridge, reflecting the conditions observed in the year 1986.

The model results do not provide direct evidence linking a deeper Appelzak channel or a steeper shoreface results to increased erosion on the beaches of Knokke-Heist. The peak in wave-driven yearly residual sediment transport shifts landwards or seawards with changes in beach and shoreface location, while transport vectors generally remain parallel to the coastline. Alongshore residual transport increases from east to west along this coast stretch, indicating an erosional character from Knokke-Heist to Zwin. However, since there is no significant change in wave-driven alongshore yearly residual sediment transport in the breaker zone, alterations in the nearshore sea bottom (Appelzak and Paardenmarkt) do not result in changes of the erosional character of this coast stretch in the 2DH models used. As emphasized in WP3, given the absence of 3D cross-shore processes in the Scaldis-Coast and Flemco models, it is crucial to interpret these results with caution.

5 References

Antia, E. E. (1996). Shoreface-connected ridges in German and US Mid-Atlantic Bights: similarities and contrasts. Journal of Coastal Research, 12(1), 141–146.

Aragonés, L.; Ignacio Pagán, J.; López, I.; Serra, J.C. (2018). Depth of closure: New calculation method based on sediment data. Int. J. Sediment Res. 33: 198–207.

Arriaga, J., Rutten, J., Ribas, F., FalquÅLes, A., & Ruessink, G. (2017). Modeling the longterm diffusion and feeding capability of a mega-nourishment. Coastal Engineering, 121, 1 - 13. doi: 10.1016/j.coastaleng.2016.11.011

Bailard, J. A. (1981). An energetics total load sediment transport model for a plane sloping beach. Journal of Geophysical Research, 86 (C11), 10938–10954.

Barrineau, P.; Janmaat, R.; Kana, T. (2021). Empirical depths of closure along the US East coast. Coastal Engineering 170, 104009.

Birkemeier, W. A. (1985). Field data on seaward limit of profile change. Journal of Waterway, Port, Coastal and Ocean Engineering 111(3): 598-602.

Calvete, D., Falqués, A., de Swart, H. E., & Walgreen, M. (2001). Modelling the formation of shoreface-connected sand ridges on storm-dominated inner shelves. Journal of Fluid Mechanics, 441, 169–193. doi: 10.1017/S0022112001004815

Coastal Wiki (2024). https://www.coastalwiki.org/wiki/Main_Page. Consulted on 29/01/2024.

Duane, D. B., Field, M. E., Meisburger, E. P., Swift, D. J., & Williams, S. J. (1972). Linear shoals on the Atlantic inner continental shelf, Florida to Long Island. In: Shelf Sediment Transport: Process and Pattern, 447–498.

Dujardin, A.; Houthuys, R.; Nnafie, A.; Röbke, B.; van der Werf, J.; de Swart, H.E.; Biernaux, V.; De Maerschalck, B.; Dan, S.; Verwaest, T. (2023). MOZES – Research on the Morphological Interaction between the Sea bottom and the Belgian Coastline: Working year 1. Version 4.0. FH Reports, 20_079_1. Flanders Hydraulics: Antwerp

Falqués, A., & Calvete, D. (2005). Large-scale dynamics of sandy coastlines: Diffusivity and instability. Journal of Geophysical Research: Oceans, 110 (C3). doi: 10.1029/2004JC002587

Garnier, R., Calvete, D., Falqués, A., & Caballeria, M. (2006). Generation and nonlinear evolution of shore-oblique/transverse sand bars. Journal of Fluid Mechanics, 567, 327–360. doi: 10.1017/S0022112006002126

Grasmeijer, B.; Röbke, B.R.; van der Werf, J. (2020). The Delft3D-FM Flemish Coast Model. Set-up of sediment transport and morphology and first steps towards calibration and validation. Deltares report, vol. 1210301-001-ZKS-0014. Delft, The Netherlands.

Hallermeier, R. J. (1978). Uses for a calculated limit depth to beach erosion. Proceedings, 16th Coastal Engineering Conference, American Society of Civil Engineers, pp. 1493 - 1512.

Hallermeier, R. J. (1981). A Profile Zonation for Seasonal Sand Beaches from Wave Climate. Coastal Engineering. 4: 253-277.

Hallermeier, R. J. (1983). Sand Transport Limits in Coastal Structure Design. Proceedings, Coastal Structures ’83, American Society of Civil Engineers, pp. 703-716.

Houthuys; R., Vos, G.; Dan, S.; Verwaest, T. (2021). Long-term morphological evolution of the Flemish coast: Holocene, Late Middle Ages to present. Version 1.0. FHR Reports, 14_023_1. Flanders Hydraulics Research: Antwerp

Houthuys, R.; Verwaest, T.; Dan, S. (2022). Morfologische trends aan de Belgische Kust: Evolutie van de Vlaamse kust tot 2019. Versie 3.0. WL Rapporten, 18_142_1. Waterbouwkundig Laboratorium: Antwerpen.

Huthnance, J. M. (1982). On one mechanism forming linear sand banks. Estuarine, Coastal and Shelf Science, 14(1), 79–99.

International Hydrographic Organization (IHO) (2020). Standards for Hydrographic Surveys (S-44 Edition 6.1.0). https://iho.int/uploads/user/pubs/standards/s-44/S-44_Edition_6.1.0.pdf

International Marine & Dredging Consultants (IMDC) (2009). Afstemming Vlaamse en Nederlandse voorspelling golfklimaat op ondiep water; Deelrapport 5: Rapportage jaargemiddeld golfklimaat. Vlaamse Overheid Departement Mobiliteit en Openbare Werken – Afdeling Waterbouwkundig Laboratorium. I/RA/11273/09.091/SDO. (in Dutch)

Kolokythas, G.; Fonias, S.; Wang, L.; De Maerschalck, B.; Vanlede, J. (2023). Modelling Belgian Coastal zone and Scheldt mouth area: Sub report 14: Scaldis-Coast model – Model setup and validation of the morphodynamic model. Version 4.0. FH Reports, 15_068_14. Flanders Hydraulics: Antwerp.

Kraus, N. C.; Harikai, S. (1983). Numerical model of the shoreline change at Oarai Beach Coastal Engineering 7: 1-28.

Longuet-Higgins, M. S. (1970). Longshore currents generated by obliquely incident sea waves: 1. Journal of Geophysical Research (1896-1977), 75 (33), 6778-6789. doi: 10.1029/JC075i033p06778.

Nnafie, A., de Swart, H. E., Falqués, A., & Calvete, D. (2021). Long-term morphodynamics of a coupled shelf-shoreline system forced by waves and tides, a model approach. Journal of Geophysical Research: Earth Surface, 126 (12).

Nnafie, A., de Swart, H. E., Garnier, R., & Calvete, D. (2014). Formation and long-term evolution of shoreface-connected sand ridges: Modeling the effects of sand extraction and sea level rise (Unpublished doctoral dissertation). Utrecht University.

Parker, G., Lanfredi, N. W., & Swift, D. J. P. (1982). Seafloor response to flow in a southern hemisphere sand-ridge field: Argentine inner shelf. Sedimentary Geology, *33*(3), 195–216.

Ribas, F., Falqués, A., de Swart, H. E., Dodd, N., Garnier, R., & Calvete, D. (2015). Understanding coastal morphodynamic patterns from depth-averaged sediment concentration. Reviews of Geophysics, 53. doi: 10.1002/2014RG000457

Röbke, B.R., Gawehn, M. & van der Werf, J. (2018). The morphodynamic Delft3D-Vlaamse Baaien model. Deltares report, vol. 1210301-001-ZKS-0007. Delft, The Netherlands.

Röbke, B.R.; Grasmeijer, B. & van der Werf, J. (2020). The Delft3D-FM Flemish Coast Model. Model set-up and hydrodynamic validation. Deltares report, vol. 1210301-001-ZKS-0009. Delft, The Netherlands.

Roest, B. (2019). Gecombineerde topografie en bathymetrie van de Belgische kust, geïnterpoleerd naar kustdwarse raaien (1997-2019). Katholieke Universiteit Leuven (KUL), Belgium.
https://marineinfo.org/id/dataset/6366

Southgate, H. N. (1989). A nearshore profile model of wave and tidal current interaction. Coastal Engineering, 13 (3), 219-245. doi: 10.1016/0378-3839(89)90050-1. Sedimentary Geology, 33(3), 195–216.

Swift, D. J. P., & Freeland, G. L. (1978). Current lineations and sand waves on the inner shelf, Middle Atlantic Bight of North America. Journal of Sedimentary Research, 48(4), 1257–1266.

Swift, D. J. P., Parker, G., Lanfredi, N. W., Perillo, G., & Figge, K. (1978). Shorefaceconnected sand ridges on American and European shelves: a comparison. Estuarine and Coastal Marine Science, 7(3), 257–273.

Trouw, K. & Houthuys, R. (2024). Seabed morphological study. FPS Economy, Brussels, Development as a wind farm zone of the Princess Elisabeth Zone, Belgian Continental Shelf (under preparation).

Trowbridge, J. H. (1995). A mechanism for the formation and maintenance of shore-oblique sand ridges on storm-dominated shelves. Journal of Geophysical Research, 100(C16), 16071-16086.

Udo, K.; Ranasinghe, R.; Takeda, Y. (2020). An assessment of measured and computed depth of closure around Japan. Sci. Rep. 10, 2987

Valiente, N.C.; Masselink, G.; Scott, T.; Conley, D.; McCarroll, R.J. (2019). Role of waves and tides on depth of closure and potential for headland bypassing. Marine Geology 407: 60–75.

Vandebroek, E.; Dan S.; Vanlede, J.; Verwaest, T.; Mostaert, F. (2017). Sediment Budget for the Belgian Coast: Final report. Version 2.0. FHR Reports, 12_155_1. Flanders Hydraulics Research: Antwerp & Antea Group.

Van de Meene, J. W. H., Boersma, J. R., & Terwindt, J. H. J. (1996). Sedimentary structures of combined flow deposits from the shoreface-connected ridges along the central Dutch coast. Marine Geology, 131(3-4), 151–175.

van Eeden, Frans & Klonaris, Georgios & Verbeurgt, Jeffrey & Wulf, Alain & Troch, Peter. (2022). Sensitivities in Wind Driven Spectral Wave Modelling for the Belgian Coast. Journal of Marine Science and Engineering. 10. 1138. 10.3390/jmse10081138.

Verfaillie, E.; Van Lancker, V.; Van Meirvenne, M. (2006). Multivariate geostatistics for the predictive modelling of the surficial sand distribution in shelf seas. Cont. Shelf Res. 26(19): 2454-2468. https://dx.doi.org/10.1016/j.csr.2006.07.028

Vis-Star, N. C., de Swart, H. E., & Calvete, D. (2008). Patch behaviour and predictability properties of modelled finite-amplitude sand ridges on the inner shelf. Nonlinear Processes in Geophysics, 15, 943-955.

Vittori, G., & Blondeaux, P. (2022). Predicting offshore tidal bedforms using stability methods. Earth-Science Reviews, 235, 104234. doi: 10.1016/j.earscirev.2022.104234

Wang, L., N. Zimmermann, K. Trouw, B. De Maerschalck, R. Delgado, T. Verwaest, F. Mostaert (2015). Scientific support regarding hydrodynamics and sand transport in the coastal zone: Calibration of a Long term morphological model of the Belgian shelf. Version 4.0. WL Rapporten, 12_107. Flanders Hydraulics Research & IMDC: Antwerp, Belgium.

Appendix 1: Bathymetric surveys of Pas van Stroombank

The Flemish Bathymetric Database (TRITON) contains over 800 surveys covering all or part of the Pas van Stroombank and Oostende harbour entrance over the period 2009-2022.

The surveys are grouped and named per survey area, that each are repeated at irregular intervals:

- NNO = Noordelijke Nadering Oostende = passage through Wenduinebank and Grote Rede until 2019, is north of our focus area. May contain interesting data for morphodynamics on Wenduinebank but the number of surveys is limited.
- NAO = Nieuwe Aanloop Oostende = passage through Stroombank, during the construction dredging work in 2009-2012.
- PVS = Pas van Stroombank = passage through Stroombank + stretch to outer harbour dams + passage of Grote Rede channel north of. Name in use since 2013. Mostly SB surveys.
- RO = Rede van Oostende = passage through Stroombank + (sometimes) stretch to outer harbour dams + wider area east and west of the navigation channel. Name was used till 2014. MB surveys.
- OST = haven van Oostende = area enclosed by the harbour dams + often also the area just off the harbour dams. Mostly MB.
- OSTSTR = haven van Oostende en strekdam = area enclosed by the harbour dams + often also the area just off the harbour dams unto the beach. Mostly MB.
- OSTBR = nearshore map sheet Oostende-Bredene; these are the routine nearshore surveys if SB, plus an occasional extra MB survey of part of the shoreface and navigation channel.
- BWO = Bruggen en Wegen Oostende, same as STOST till 2018.
- STOST = stortzone Oostende = (new) disposal site since 2019

From these, a selection was made using the following criteria:

- the dataset should cover the passage of the navigation channel through Stroombank or the area near the outer harbour dams
- no disposal site
- for SB the 210 kHz survey frequency was chosen
- for MB, points gridded on a 1m-grid were chosen

This reduced the available surveys to 177. Figure 108 gives an idea of the coverage of these surveys.

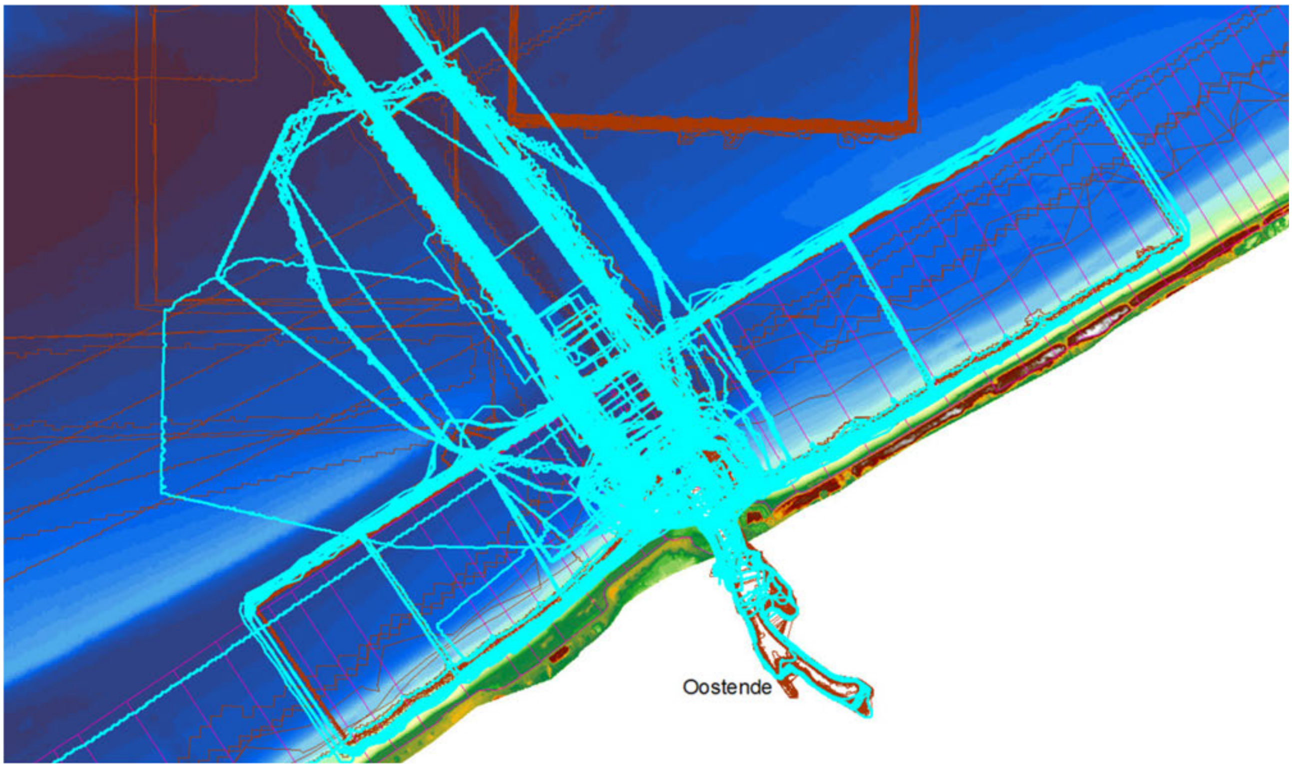

Figure 108 – Survey areas with survey dates between 2009 and 2022, available in the bathymetric database TRITON.

Of these no processing is needed for the nearshore surveys, as they are already available from recent coastal morphology reports.

Given the large number of data, it was decided to align the investigation with ScaldisKust developments. In consultation with its project leader ir. Bart De Maerschalck, it was decided to focus on the period 2009-2017, which contains the construction of the new access channel and the new outer dams around 2009-2010, and the hindcast period 2014-2016 used in the ScaldisKust development. In 2010 a remarkable change in nearshore morphology was noted (Houthuys et al., 2022), also in areas outside the possible morphological influence of Oostende harbour works.

This narrows the number of surveys down to 102. They are listed in Table 13.

Table 13 – Selection of bathymetric surveys requested for the investigation of the morphological information from dredging operation near Oostende.

planam	OBJNAM	CoverageTy
RO	090000_RO_MB_300	CSAR Grid (.csar)
OSTSTR	090115_MKOST_NOS_SB_200	CSAR Point Cloud (.csar)
RO	090200_RO_MB_300	CSAR Grid (.csar)
OSTSTR	090209_MKOST_NOS_SB_200	CSAR Point Cloud (.csar)
OSTSTR	090219_MKOST_NOS_MB_300	CSAR Grid (.csar)
OSTSTR	090302_MKOST_NOS_SB_200	CSAR Point Cloud (.csar)
PVS	090313_NAO_SB_210	CSAR Point Cloud (.csar)
OSTSTR	090414_MKOST_NOS_MB_300	CSAR Grid (.csar)
PVS	090416_NAO_SB_210	CSAR Point Cloud (.csar)
OSTSTR	090428_NAO_MB_300	CSAR Grid (.csar)
OSTSTR	090429_MKOST_NOS_SB_200	CSAR Point Cloud (.csar)
PVS	090500_NAO_SB_210	CSAR Point Cloud (.csar)
OSTSTR	090500_OSTBRE_MB_300	CSAR Grid (.csar)
PVS	090600_NAO_SB_210	CSAR Point Cloud (.csar)
OSTSTR	090800_OST_HAV_SB_210	CSAR Point Cloud (.csar)
PVS	090803_NAO_SB_210	CSAR Point Cloud (.csar)

PVS	090831_NAO_SB_210	CSAR Point Cloud (.csar)
PVS	091000_NAO_SB_210	CSAR Point Cloud (.csar)
RO	091200_RO_MB_300	CSAR Grid (.csar)
OSTSTR	100114_NAO_SB_210	CSAR Point Cloud (.csar)
PVS	100121_NAO_SB_210	CSAR Point Cloud (.csar)
OSTSTR	100205_NAO_MB_300	CSAR Grid (.csar)
OSTSTR	100205_NAO_SB_210	CSAR Point Cloud (.csar)
PVS	100224_NAO_SB_210	CSAR Point Cloud (.csar)
OSTSTR	100225_NAO_SB_210	CSAR Point Cloud (.csar)
OSTSTR	100300_NAO_SB_210	CSAR Point Cloud (.csar)
OSTSTR	100302_NAO_SB_210	CSAR Point Cloud (.csar)
OSTSTR	100316_NAO_MB_300	CSAR Grid (.csar)
PVS	100324_NAO_SB_210	CSAR Point Cloud (.csar)
OSTSTR	100326_NAO_SB_210	CSAR Point Cloud (.csar)
PVS	100400_NAO_SB_210	CSAR Point Cloud (.csar)
OSTSTR	100418_NAO_MB_300	CSAR Grid (.csar)
PVS	100419_NAO_SB_210	CSAR Point Cloud (.csar)
PVS	100428_NAO_SB_210	CSAR Point Cloud (.csar)
RO	100500_RO_MB_300	CSAR Grid (.csar)
OSTSTR	100519_NAO_SB_210	CSAR Point Cloud (.csar)
OSTSTR	100521_NAO_MB_300	CSAR Grid (.csar)
OSTSTR	100600_NAO_SB_210	CSAR Point Cloud (.csar)
OSTSTR	100601_NAO_MB_300	CSAR Grid (.csar)
PVS	100601_NAO_SB_210	CSAR Point Cloud (.csar)
OSTSTR	100618_NAO_MB_300	CSAR Grid (.csar)
PVS	100701_NAO_SB_210	CSAR Point Cloud (.csar)
OSTSTR	100709_OST_STRD_MB_300	CSAR Grid (.csar)
OSTSTR	100811_OST_STRD_MB_240	CSAR Grid (.csar)
PVS	100906_NAO_SB_210	CSAR Point Cloud (.csar)
OSTSTR	100924_OST_STRD_MB_300	CSAR Grid (.csar)
OSTSTR	100927_NAO_SB_210	CSAR Point Cloud (.csar)
PVS	101100_NAO_SB_210	CSAR Point Cloud (.csar)
OSTSTR	101207_OST_STRD_MB_240	CSAR Grid (.csar)
OSTSTR	101228_NAO_MB_300	CSAR Grid (.csar)
OSTSTR	110106_OST_STRD_MB_240	CSAR Grid (.csar)
PVS	110217_NAO_SB_210	CSAR Point Cloud (.csar)
RO	110500_RO_MB_300	CSAR Grid (.csar)
OSTSTR	110627_OST_STRD_MB_240	CSAR Grid (.csar)
RO	110800_RO_MB_300	CSAR Grid (.csar)
OSTSTR	110902_OST_STRD_MB_240	CSAR Grid (.csar)
OSTSTR	110905_OST_STRD_MB_300	CSAR Grid (.csar)
RO	120200_RO_MB_300	CSAR Grid (.csar)
OSTSTR	120210_OST_STRD_MB_240	CSAR Grid (.csar)
OSTSTR	120404_OST_STRD_MB_300	CSAR Grid (.csar)
PVS	120510_PVS_MB_300	CSAR Grid (.csar)
RO	121100_RO_MB_300	CSAR Grid (.csar)
OSTSTR	130322_OST_STRD_MB_300	CSAR Grid (.csar)
PVS	130600_PVS_SB_210	CSAR Point Cloud (.csar)
OSTSTR	130626_OST_STRD_MB_300	CSAR Grid (.csar)
OSTSTR	130700_OST_STRD_MB_300	CSAR Grid (.csar)
PVS	130800_PVS_SB_210	CSAR Point Cloud (.csar)
RO	131000_RO_MB_300	CSAR Grid (.csar)
OSTSTR	131007_OST_STRD_MB_300	CSAR Grid (.csar)
PVS	131024_PVS_SB_210	CSAR Point Cloud (.csar)
PVS	131212_PVS_MB_300	CSAR Grid (.csar)
RO	140200_RO_MB_300	CSAR Grid (.csar)
OSTSTR	140204_OST_STRD_MB_300	CSAR Grid (.csar)
PVS	140402_PVS_SB_210	CSAR Point Cloud (.csar)
PVS	140402_RO_MB_300	CSAR Grid (.csar)
PVS	140416_PVS_SB_210	CSAR Point Cloud (.csar)
PVS	140505_PVS_SB_210	CSAR Point Cloud (.csar)
PVS	140527_PVS_SB_210	CSAR Point Cloud (.csar)
PVS	140626_PVS_SB_210	CSAR Point Cloud (.csar)

OSTSTR	140716_OST_STRD_MB_300	CSAR Grid (.csar)
PVS	140825_PVS_SB_210	CSAR Point Cloud (.csar)
RO	141015_RO_MB_300	CSAR Grid (.csar)
PVS	150107_PVS_MB_300	CSAR Grid (.csar)
PVS	150320_PVS_SB_210	CSAR Point Cloud (.csar)
PVS	150423_PVS_SB_210	CSAR Point Cloud (.csar)
OSTSTR	150630_OST_STRD_MB_300	CSAR Grid (.csar)
RO	150630_RO_MB_300	CSAR Grid (.csar)
PVS	150731_PVS_SB_210	CSAR Point Cloud (.csar)
PVS	150925_PVS_MB_300	CSAR Grid (.csar)
PVS	160122_PVS_SB_210	CSAR Point Cloud (.csar)
OSTSTR	160226_OST_STRD_MB_300	CSAR Grid (.csar)
PVS	160310_PVS_SB_210	CSAR Point Cloud (.csar)
PVS	160509_PVS_SB_210	CSAR Point Cloud (.csar)
PVS	160622_PVS_SB_210	CSAR Point Cloud (.csar)
OSTSTR	160921_OST_STRD_MB_300	CSAR Grid (.csar)
PVS	161004_PVS_SB_210	CSAR Point Cloud (.csar)
PVS	170315_PVS_SB_210	CSAR Point Cloud (.csar)
RO	170414_RO_MB_300	CSAR Grid (.csar)
PVS	170530_PVS_SB_210	CSAR Point Cloud (.csar)
PVS	170831_PVS_SB_210	CSAR Point Cloud (.csar)
OSTSTR	170922_OST_STRD_MB_300	CSAR Grid (.csar)
PVS	171115_PVS_SB_210	CSAR Point Cloud (.csar)

In a first stage, it was decided to focus on the 2014-2016 period, so as to get a feel with the data and to learn how they can be exploited for morphological research. This further reduced the needed dataset to 26 (all those of Table 13 whose OBJNAM begins with 14, 15 or 16 and the first one of 17), 11 of which are MB surveys.

Appendix 2: Analysis results of morphological change and dredged amounts in Pas van Stroombank

This appendix contains the results (maps and volumes) of the Pas van Stroombank case study, presented in section 2.5. The case study looked at the crossing of the navigation channel Pas van Stroombank through Stroombank in the period 2014-2016. 21 bathymetric surveys and 17 BIS export raster sets were evaluated geographically through map representations and quantitatively through volume computations per time interval between the bathymetric surveys of Survey volume difference and BIS dredged volume per zone of interest.

More particularly, for each bathymetric survey interval the following elements are presented:

- a map showing the BIS export raster over the time interval (parameter Reduced Volume)
- a map showing the bathymetry difference over the interval (most recent minus earlier survey)
- a table containing
    1. the volume difference (DV) per analysis zone,
    2. the area of the part of the zone covered jointly by the survey before and after the interval,
    3. the uncertainty of the corresponding volume difference (obtained by multiplying the covered area of the analysis zone by $\sqrt{2} \cdot 0.15$)
    4. the average depth difference over the interval, all (1) to (4) derived from the after minus before bathymetric survey difference map
    5. the volume
    6. type of dredged matter derived from the BIS export rasters.

The legend applies to all figures and tables:

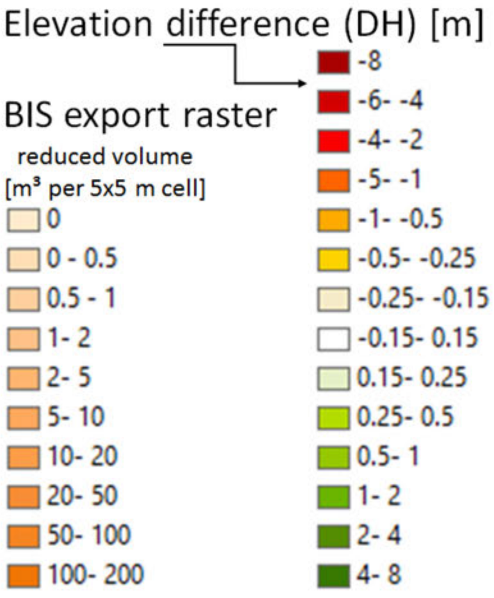

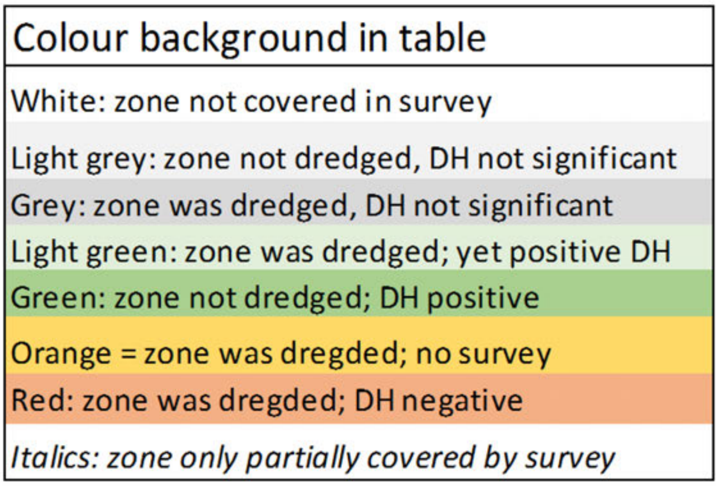
Colour background in table

White: zone not covered in survey

Light grey: zone not dredged, DH not significant

Grey: zone was dredged, DH not significant

Light green: zone was dredged; yet positive DH

Green: zone not dredged; DH positive

Orange = zone was dregded; no survey

Red: zone was dregded; DH negative

Italics: zone only partially covered by survey

The width of the three zones across the navigation channel is 455 m.

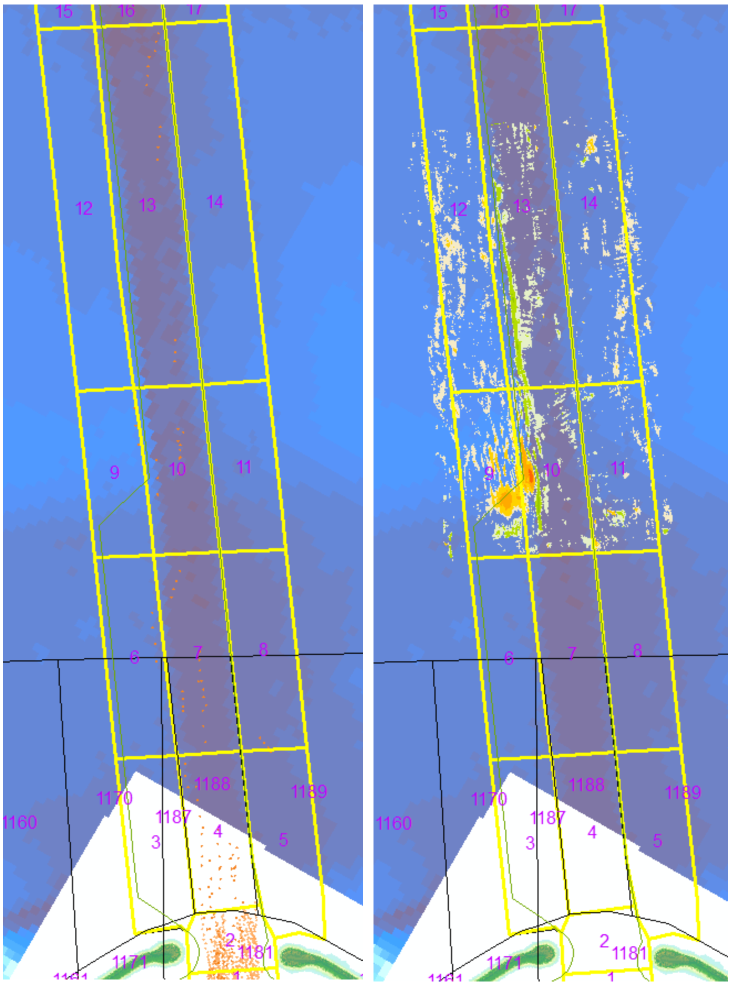

	2/04/2014 - 3/02/2014		
zone	12	13	14
survey DV (m^3)	-8 300	7 300	-6 100
area (m^2)	83 000	108 700	99 600
uncert. DV (m^3)	17 400	22 800	20 900
avg. DH (m)	-0.10	0.07	-0.06
BIS DV (m^3)		900	
sediment		mud	
zone	9	10	11
survey DV (m^3)	-5 500	2 500	-2 400
area (m^2)	56 500	65 100	60 800
uncert. DV (m^3)	11 900	13 700	12 800
avg. DH (m)	-0.10	0.04	-0.04
BIS DV (m^3)	200	700	
sediment	mud	mud	
zone	6	7	8
survey DV (m^3)	0	0	0
area (m^2)	200	700	100
uncert. DV (m^3)	0	100	0
avg. DH (m)	0.00	0.00	0.00
BIS DV (m^3)	200	1 100	200
sediment	mud	mud	mud
zone	3	4	5
survey DV (m^3)			
area (m^2)			
uncert. DV (m^3)			
avg. DH (m)			
BIS DV (m^3)		2 300	100
sediment		mud	mud
zone		2	
survey DV (m^3)			
area (m^2)			
uncert. DV (m^3)			
avg. DH (m)			
BIS DV (m^3)		3 700	
sediment		mud	
zone		1	
survey DV (m^3)			
area (m^2)			
uncert. DV (m^3)			
avg. DH (m)			
BIS DV (m^3)		6 600	
sediment		mud	

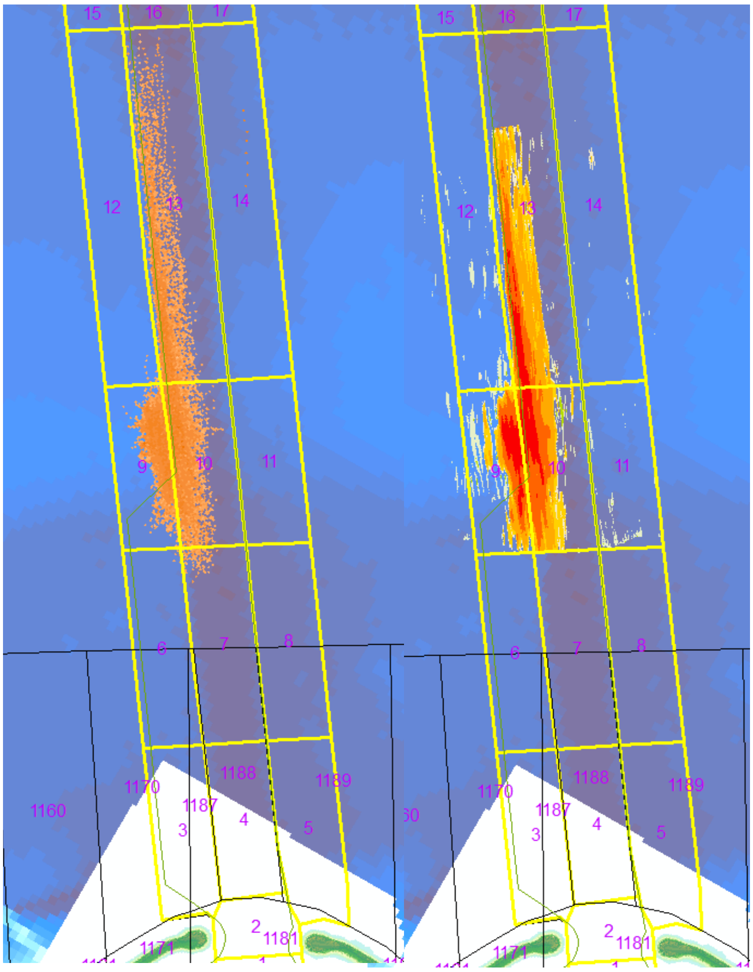

16/04/2014 - 2/04/2014

zone	12	13	14
survey DV (m³)	6 300	-41 100	5 300
area (m²)	83 000	108 700	99 600
uncert. DV (m³)	17 400	22 800	20 900
avg. DH (m)	0.08	-0.38	0.05
BIS DV (m³)	100	31 800	700
sediment	mud	mud	mud
zone	9	10	11
survey DV (m³)	-25 200	-43 000	4 100
area (m²)	56 500	65 100	60 800
uncert. DV (m³)	11 900	13 700	12 800
avg. DH (m)	-0.45	-0.66	0.07
BIS DV (m³)	23 700	35 000	
sediment	mud	mud	
zone	6	7	8
survey DV (m³)	0	0	0
area (m²)	200	700	100
uncert. DV (m³)	0	100	0
avg. DH (m)	0.00	0.00	0.00
BIS DV (m³)	100	1 000	
sediment	mud	mud	
zone	3	4	5
survey DV (m³)			
area (m²)			
uncert. DV (m³)			
avg. DH (m)			
BIS DV (m³)			
sediment			
zone		2	
survey DV (m³)			
area (m²)			
uncert. DV (m³)			
avg. DH (m)			
BIS DV (m³)			
sediment			
zone		1	
survey DV (m³)			
area (m²)			
uncert. DV (m³)			
avg. DH (m)			
BIS DV (m³)			
sediment			

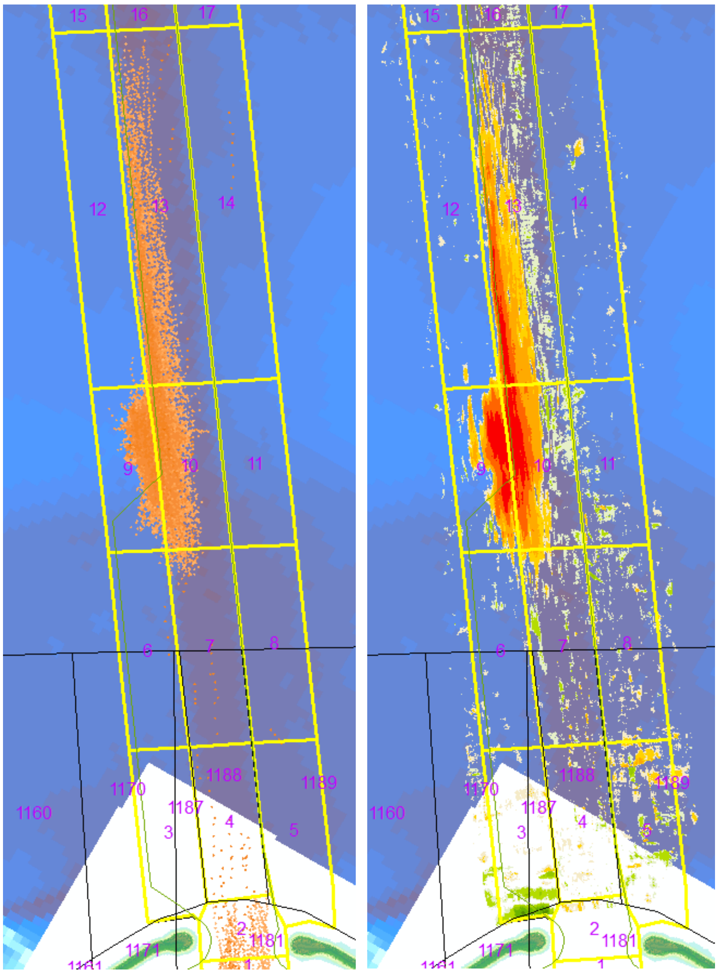

16/04/2014 - 3/02/2014

zone	12	13	14
survey DV (m³)	-3 100	-24 400	-500
area (m²)	115 200	147 800	134 100
uncert. DV (m³)	24 200	31 000	28 200
avg. DH (m)	-0.03	-0.17	0.00
BIS DV (m³)	100	32 700	700
sediment	mud	mud	mud
zone	9	10	11
survey DV (m³)	-28 200	-37 100	2 000
area (m²)	56 500	65 100	63 100
uncert. DV (m³)	11 900	13 700	13 300
avg. DH (m)	-0.50	-0.57	0.03
BIS DV (m³)	23 900	35 700	
sediment	mud	mud	
zone	6	7	8
survey DV (m³)	-3 000	-2 400	-1 500
area (m²)	69 100	76 000	74 600
uncert. DV (m³)	14 500	16 000	15 700
avg. DH (m)	-0.04	-0.03	-0.02
BIS DV (m³)	300	2 100	200
sediment	mud	mud	mud
zone	3	4	5
survey DV (m³)	2 000	-4 500	100
area (m²)	60 900	58 000	56 800
uncert. DV (m³)	12 800	12 200	11 900
avg. DH (m)	0.03	-0.08	0.00
BIS DV (m³)		2 300	100
sediment		mud	mud
zone		2	
survey DV (m³)		*-200*	
area (m²)		*4 900*	
uncert. DV (m³)		*1 000*	
avg. DH (m)		*-0.04*	
BIS DV (m³)		3 700	
sediment		mud	
zone		1	
survey DV (m³)			
area (m²)			
uncert. DV (m³)			
avg. DH (m)			
BIS DV (m³)		6 600	
sediment		mud	

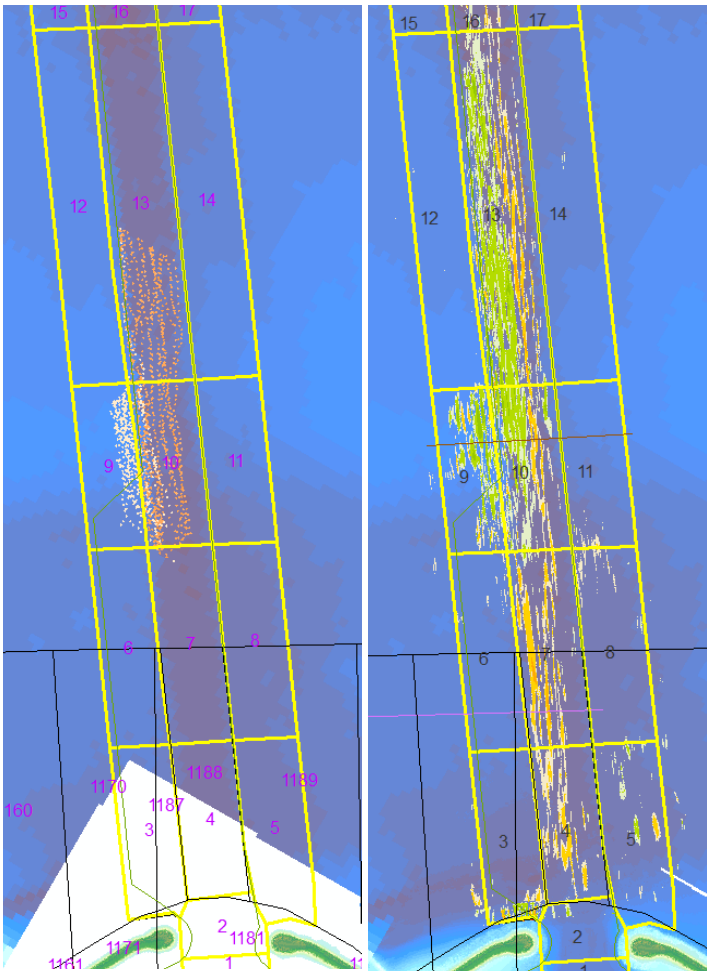

5/05/2014 - 16/04/2014

zone	12	13	14
survey DV (m³)	-300	8 700	100
area (m²)	115 200	147 800	134 100
uncert. DV (m³)	24 200	31 000	28 200
avg. DH (m)	0.00	0.06	0.00
BIS DV (m³)		2 500	
sediment		mud	
zone	9	10	11
survey DV (m³)	2 500	3 400	300
area (m²)	56 500	65 100	63 100
uncert. DV (m³)	11 900	13 700	13 300
avg. DH (m)	0.04	0.05	0.00
BIS DV (m³)	0	2 900	
sediment	mud	mud	
zone	6	7	8
survey DV (m³)	-1 100	-3 900	-700
area (m²)	69 100	76 000	74 600
uncert. DV (m³)	14 500	16 000	15 700
avg. DH (m)	-0.02	-0.05	-0.01
BIS DV (m³)		100	
sediment		mud	
zone	3	4	5
survey DV (m³)	900	-3 100	1 300
area (m²)	61 000	58 000	63 600
uncert. DV (m³)	12 800	12 200	13 400
avg. DH (m)	0.01	-0.05	0.02
BIS DV (m³)			
sediment			
zone		2	
survey DV (m³)		*300*	
area (m²)		*7 100*	
uncert. DV (m³)		*1 500*	
avg. DH (m)		*0.04*	
BIS DV (m³)			
sediment			
zone		1	
survey DV (m³)			
area (m²)			
uncert. DV (m³)			
avg. DH (m)			
BIS DV (m³)			
sediment			

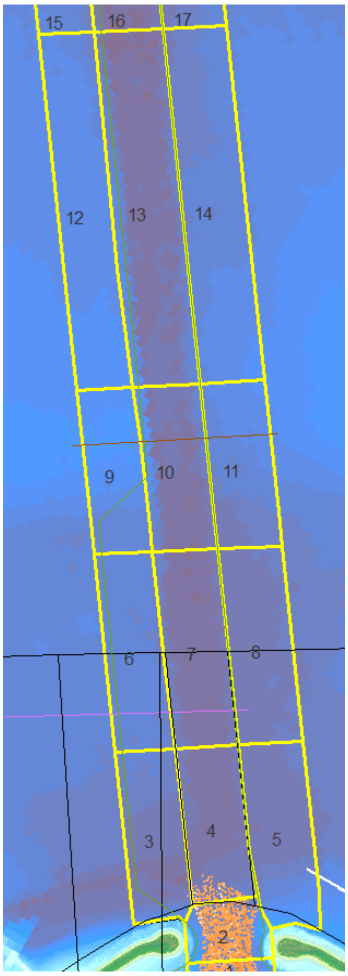

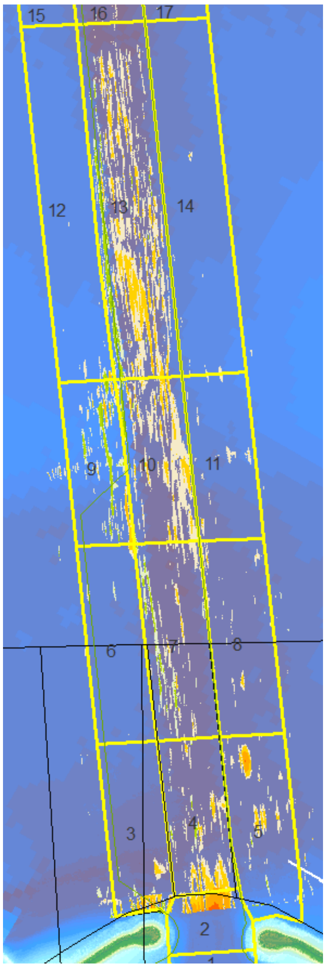

	27/05/2014 - 5/05/2014		
zone	12	13	14
survey DV (m^3)	-1 700	-10 700	-3 100
area (m^2)	115 200	147 800	134 100
uncert. DV (m^3)	24 200	31 000	28 200
avg. DH (m)	-0.01	-0.07	-0.02
BIS DV (m^3)			
sediment			
zone	9	10	11
survey DV (m^3)	400	-6 300	-3 200
area (m^2)	56 500	65 100	63 100
uncert. DV (m^3)	11 900	13 700	13 300
avg. DH (m)	0.01	-0.10	-0.05
BIS DV (m^3)			
sediment			
zone	6	7	8
survey DV (m^3)	-700	-1 600	-2 100
area (m^2)	69 100	76 000	74 600
uncert. DV (m^3)	14 500	16 000	15 700
avg. DH (m)	-0.01	-0.02	-0.03
BIS DV (m^3)			
sediment			
zone	3	4	5
survey DV (m^3)	-2 100	-3 700	-2 500
area (m^2)	61 000	58 000	64 000
uncert. DV (m^3)	12 800	12 200	13 400
avg. DH (m)	-0.03	-0.06	-0.04
BIS DV (m^3)	0	800	
sediment	mud	mud	
zone		2	
survey DV (m^3)		*-3 000*	
area (m^2)		*8 000*	
uncert. DV (m^3)		*1 700*	
avg. DH (m)		*-0.38*	
BIS DV (m^3)		6 300	
sediment		mud	
zone		1	
survey DV (m^3)			
area (m^2)			
uncert. DV (m^3)			
avg. DH (m)			
BIS DV (m^3)		7 700	
sediment		mud	

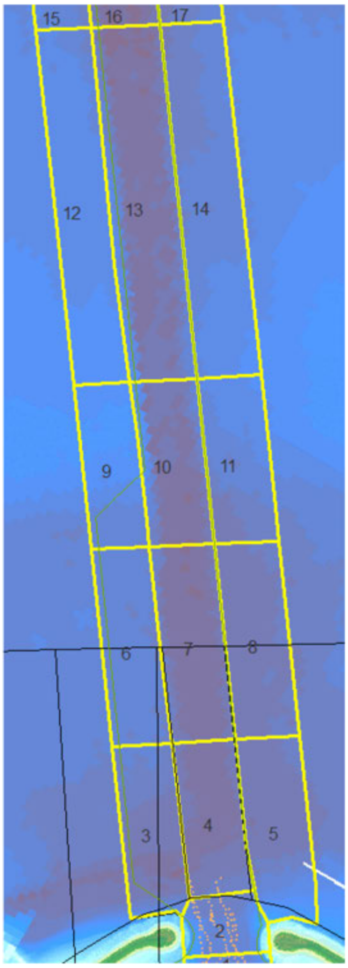

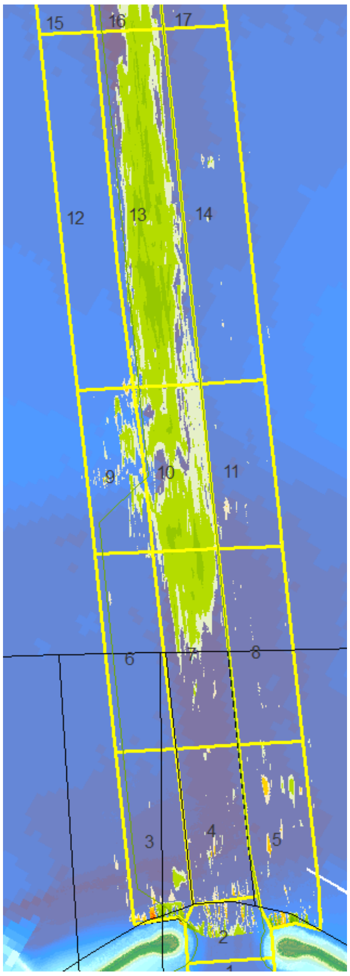

	26/06/2014 - 27/05/2014		
zone	12	13	14
survey DV (m^3)	-2 800	39 300	-1 900
area (m^2)	115 200	147 800	134 100
uncert. DV (m^3)	24 200	31 000	28 200
avg. DH (m)	-0.02	0.27	-0.01
BIS DV (m^3)			
sediment			
zone	9	10	11
survey DV (m^3)	1 400	16 600	-300
area (m^2)	56 500	65 100	63 100
uncert. DV (m^3)	11 900	13 700	13 300
avg. DH (m)	0.02	0.25	0.00
BIS DV (m^3)			
sediment			
zone	6	7	8
survey DV (m^3)	-900	9 200	-800
area (m^2)	69 100	76 000	74 600
uncert. DV (m^3)	14 500	16 000	15 700
avg. DH (m)	-0.01	0.12	-0.01
BIS DV (m^3)			
sediment			
zone	3	4	5
survey DV (m^3)	-600	-800	400
area (m^2)	60 900	58 000	68 100
uncert. DV (m^3)	12 800	12 200	14 300
avg. DH (m)	-0.01	-0.01	0.01
BIS DV (m^3)		0	
sediment		mud	
zone		2	
survey DV (m^3)		*1 200*	
area (m^2)		*15 700*	
uncert. DV (m^3)		*3 300*	
avg. DH (m)		*0.08*	
BIS DV (m^3)		200	
sediment		mud	
zone		1	
survey DV (m^3)			
area (m^2)			
uncert. DV (m^3)			
avg. DH (m)			
BIS DV (m^3)		200	
sediment		mud	

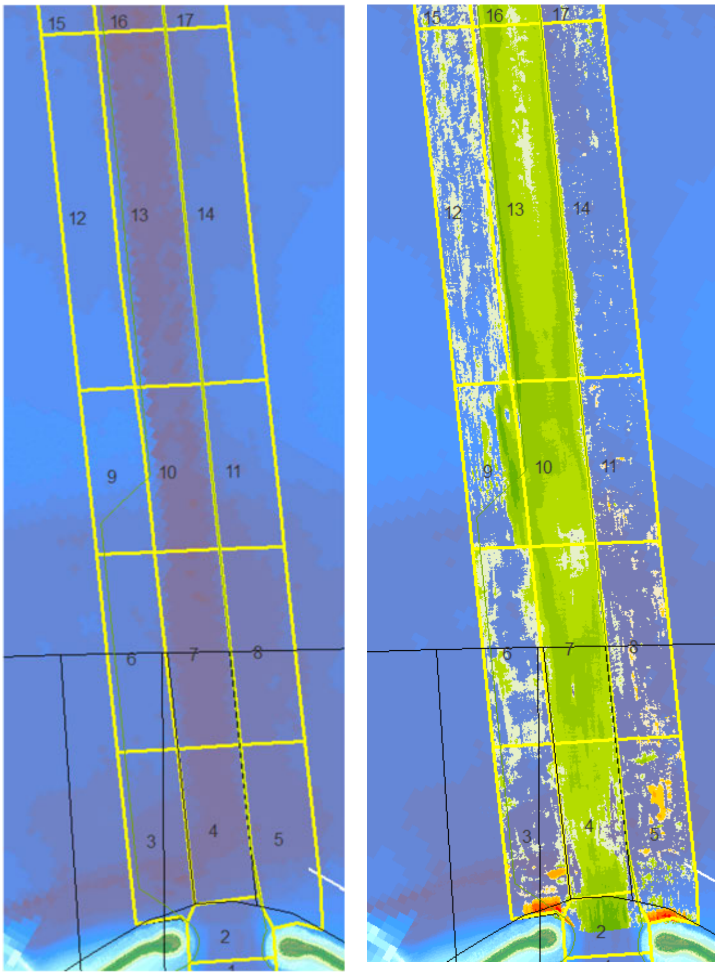

	7/01/2015 - 26/06/2014		
zone	12	13	14
survey DV (m^3)	15 500	65 200	6 000
area (m^2)	114 100	147 800	134 100
uncert. DV (m^3)	24 000	31 000	28 200
avg. DH (m)	0.14	0.44	0.04
BIS DV (m^3)			
sediment			
zone	9	10	11
survey DV (m^3)	16 200	31 500	300
area (m^2)	55 900	65 100	63 100
uncert. DV (m^3)	11 700	13 700	13 300
avg. DH (m)	0.29	0.48	0.00
BIS DV (m^3)			
sediment			
zone	6	7	8
survey DV (m^3)	10 000	35 000	-1 400
area (m^2)	68 200	76 000	74 600
uncert. DV (m^3)	14 300	16 000	15 700
avg. DH (m)	0.15	0.46	-0.02
BIS DV (m^3)			
sediment			
zone	3	4	5
survey DV (m^3)	300	20 200	-1 800
area (m^2)	60 200	58 000	68 100
uncert. DV (m^3)	12 600	12 200	14 300
avg. DH (m)	0.00	0.35	-0.03
BIS DV (m^3)			
sediment			
zone		2	
survey DV (m^3)		*9 500*	
area (m^2)		*15 600*	
uncert. DV (m^3)		*3 300*	
avg. DH (m)		*0.61*	
BIS DV (m^3)			
sediment			
zone		1	
survey DV (m^3)			
area (m^2)			
uncert. DV (m^3)			
avg. DH (m)			
BIS DV (m^3)			
sediment			

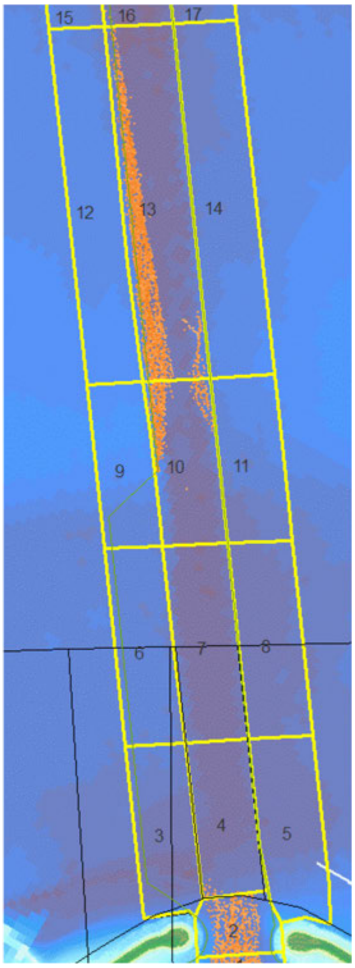

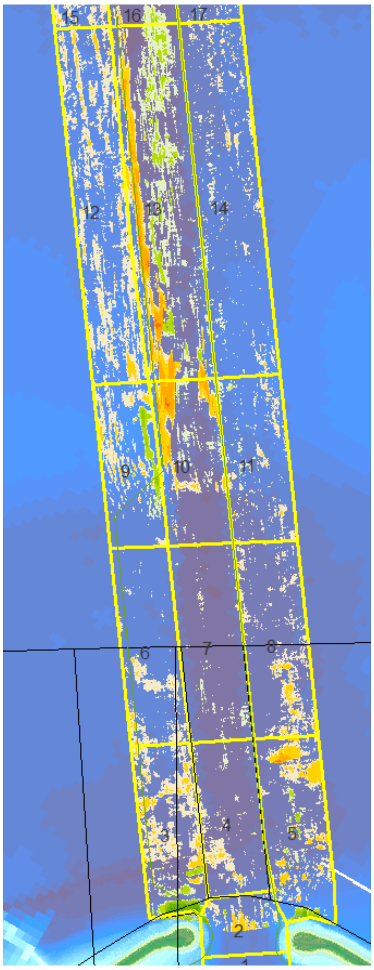

20/03/2015 - 7/01/2015

zone	12	13	14
survey DV (m³)	-15 100	300	-5 600
area (m²)	114 100	147 800	134 100
uncert. DV (m³)	24 000	31 000	28 200
avg. DH (m)	-0.13	0.00	-0.04
BIS DV (m³)		33 400	
sediment		mud	
zone	9	10	11
survey DV (m³)	-1 700	-4 100	-2 100
area (m²)	55 900	65 100	63 100
uncert. DV (m³)	11 700	13 700	13 300
avg. DH (m)	-0.03	-0.06	-0.03
BIS DV (m³)		7 100	
sediment		mud	
zone	6	7	8
survey DV (m³)	-5 500	600	-6 000
area (m²)	68 200	76 000	74 600
uncert. DV (m³)	14 300	16 000	15 700
avg. DH (m)	-0.08	0.01	-0.08
BIS DV (m³)			
sediment			
zone	3	4	5
survey DV (m³)	-3 200	-2 200	-4 300
area (m²)	60 300	58 000	68 100
uncert. DV (m³)	12 700	12 200	14 300
avg. DH (m)	-0.05	-0.04	-0.06
BIS DV (m³)		200	
sediment		mud	
zone		2	
survey DV (m³)		*-700*	
area (m²)		*15 700*	
uncert. DV (m³)		*3 300*	
avg. DH (m)		*-0.04*	
BIS DV (m³)		5 500	
sediment		mud	
zone		1	
survey DV (m³)			
area (m²)			
uncert. DV (m³)			
avg. DH (m)			
BIS DV (m³)		11 900	
sediment		mud	

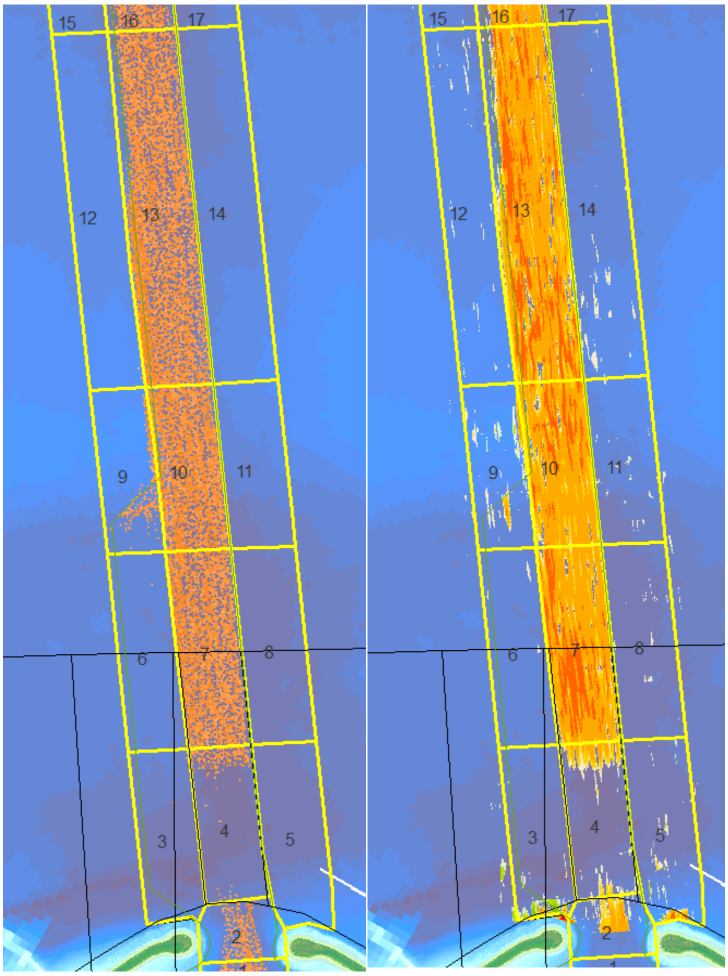

	23/04/2023 - 20/03/2015		
zone	12	13	14
survey DV (m³)	-1 200	-101 900	-5 100
area (m²)	115 200	147 800	134 100
uncert. DV (m³)	24 200	31 000	28 200
avg. DH (m)	-0.01	-0.69	-0.04
BIS DV (m³)	200	94 600	0
sediment	mud	mud	mud
zone	9	10	11
survey DV (m³)	-2 800	-45 900	-2 200
area (m²)	56 500	65 100	63 100
uncert. DV (m³)	11 900	13 700	13 300
avg. DH (m)	-0.05	-0.71	-0.03
BIS DV (m³)	4 300	56 900	
sediment	mud	mud	
zone	6	7	8
survey DV (m³)	-2 500	-57 300	-2 000
area (m²)	69 100	76 000	74 600
uncert. DV (m³)	14 500	16 000	15 700
avg. DH (m)	-0.04	-0.75	-0.03
BIS DV (m³)	100	56 700	0
sediment	mud	mud	mud
zone	3	4	5
survey DV (m³)	500	-3 600	-1 900
area (m²)	61 000	58 000	67 800
uncert. DV (m³)	12 800	12 200	14 200
avg. DH (m)	0.01	-0.06	-0.03
BIS DV (m³)	0	3 700	0
sediment	mud	mud	mud
zone		2	
survey DV (m³)		*-2 900*	
area (m²)		*15 300*	
uncert. DV (m³)		*3 200*	
avg. DH (m)		*-0.19*	
BIS DV (m³)		4 400	
sediment		mud	
zone		1	
survey DV (m³)			
area (m²)			
uncert. DV (m³)			
avg. DH (m)			
BIS DV (m³)		9 900	
sediment		mud	

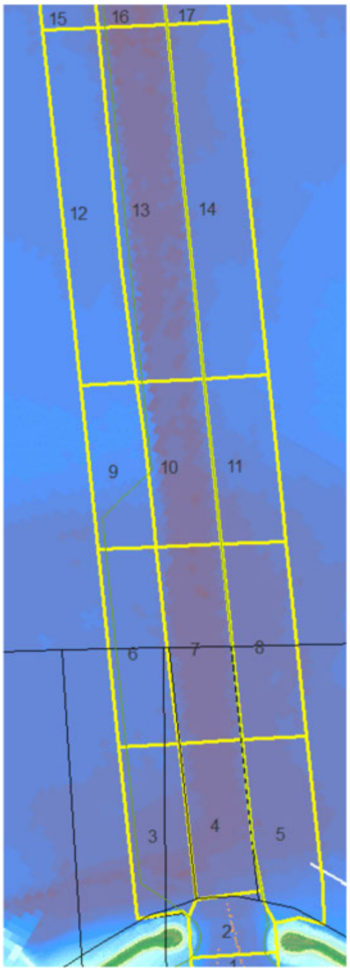

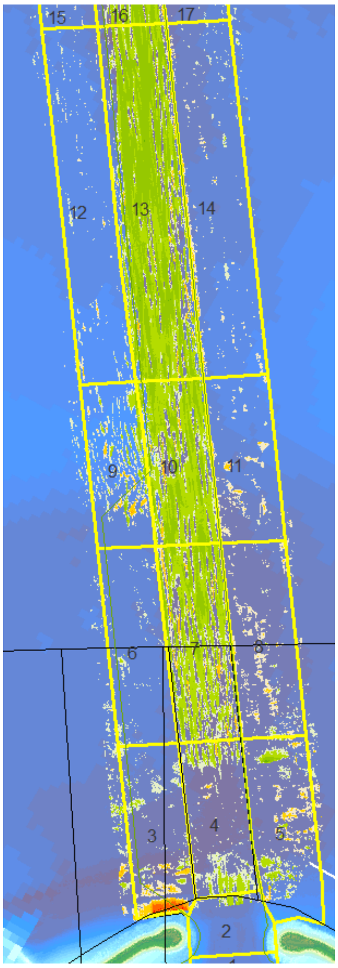

30/06/2015 - 23/04/2023

zone	12	13	14
survey DV (m^3)	1 100	55 200	-1 000
area (m^2)	115 200	147 800	134 100
uncert. DV (m^3)	24 200	31 000	28 200
avg. DH (m)	0.01	0.37	-0.01
BIS DV (m^3)			
sediment			
zone	9	10	11
survey DV (m^3)	2 900	21 800	-2 400
area (m^2)	56 500	65 100	63 100
uncert. DV (m^3)	11 900	13 700	13 300
avg. DH (m)	0.05	0.33	-0.04
BIS DV (m^3)			
sediment			
zone	6	7	8
survey DV (m^3)	3 100	17 500	-3 500
area (m^2)	69 100	76 000	74 600
uncert. DV (m^3)	14 500	16 000	15 700
avg. DH (m)	0.04	0.23	-0.05
BIS DV (m^3)			
sediment			
zone	3	4	5
survey DV (m^3)	-800	3 300	300
area (m^2)	60 900	58 000	56 800
uncert. DV (m^3)	12 800	12 200	11 900
avg. DH (m)	-0.01	0.06	0.01
BIS DV (m^3)			
sediment			
zone		2	
survey DV (m^3)		*600*	
area (m^2)		*4 900*	
uncert. DV (m^3)		*1 000*	
avg. DH (m)		*0.12*	
BIS DV (m^3)		100	
sediment		mud	
zone		1	
survey DV (m^3)			
area (m^2)			
uncert. DV (m^3)			
avg. DH (m)			
BIS DV (m^3)		300	
sediment		mud	

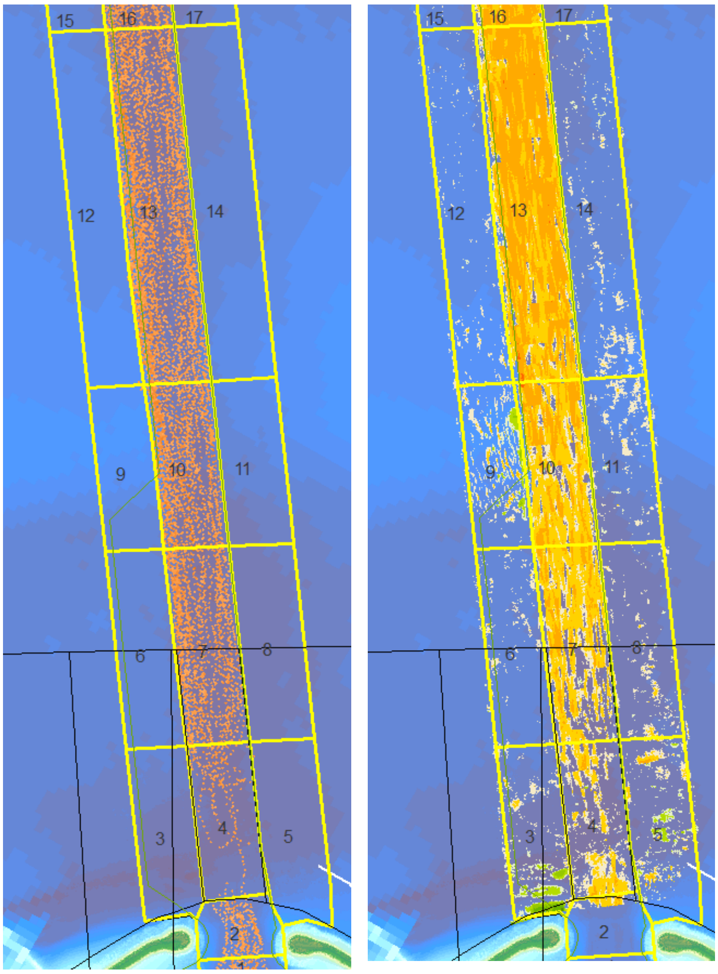

31/07/2015 - 30/06/2015

zone	12	13	14
survey DV (m^3)	-3 600	-74 400	-5 800
area (m^2)	115 200	147 800	134 100
uncert. DV (m^3)	24 200	31 000	28 200
avg. DH (m)	-0.03	-0.50	-0.04
BIS DV (m^3)	100	46 700	0
sediment	mud	mud	mud
zone	9	10	11
survey DV (m^3)	-1 800	-23 000	-3 500
area (m^2)	56 500	65 100	63 100
uncert. DV (m^3)	11 900	13 700	13 300
avg. DH (m)	-0.03	-0.35	-0.06
BIS DV (m^3)	0	21 200	
sediment	mud	mud	
zone	6	7	8
survey DV (m^3)	-4 000	-20 400	-2 600
area (m^2)	69 100	76 000	74 600
uncert. DV (m^3)	14 500	16 000	15 700
avg. DH (m)	-0.06	-0.27	-0.03
BIS DV (m^3)	0	18 400	
sediment	mud	mud	
zone	3	4	5
survey DV (m^3)	700	-7 200	-700
area (m^2)	60 900	58 000	56 800
uncert. DV (m^3)	12 800	12 200	11 900
avg. DH (m)	0.01	-0.12	-0.01
BIS DV (m^3)		2 900	0
sediment		mud	mud
zone		2	
survey DV (m^3)		*-900*	
area (m^2)		*4 900*	
uncert. DV (m^3)		*1 000*	
avg. DH (m)		*-0.18*	
BIS DV (m^3)		2 200	
sediment		mud	
zone		1	
survey DV (m^3)			
area (m^2)			
uncert. DV (m^3)			
avg. DH (m)			
BIS DV (m^3)		5 000	
sediment		mud	

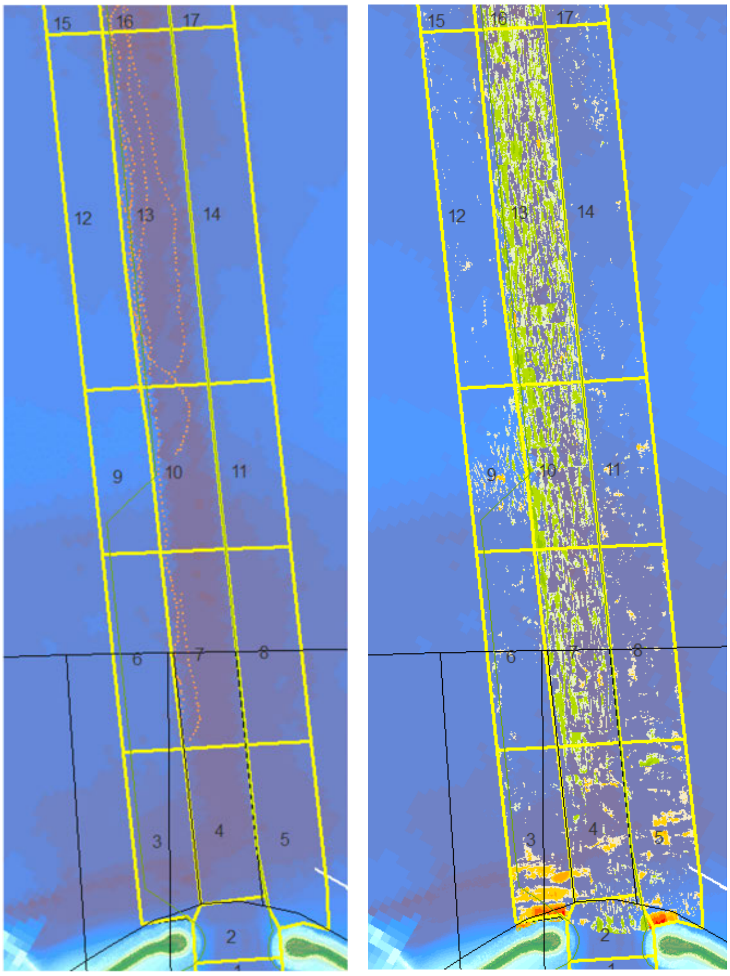

	25/09/2015 - 31/07/2015		
zone	12	13	14
survey DV (m^{3})	-3 400	23 000	-1 800
area (m^{2})	114 000	147 800	134 100
uncert. DV (m^{3})	23 900	31 000	28 200
avg. DH (m)	-0.03	0.16	-0.01
BIS DV (m^{3})	0	3 100	
sediment	mud	mud	
zone	9	10	11
survey DV (m^{3})	300	10 200	-1 600
area (m^{2})	55 800	65 100	63 100
uncert. DV (m^{3})	11 700	13 700	13 300
avg. DH (m)	0.01	0.16	-0.03
BIS DV (m^{3})	0	400	
sediment	mud	mud	
zone	6	7	8
survey DV (m^{3})	-1 200	7 700	-2 500
area (m^{2})	68 200	76 000	74 600
uncert. DV (m^{3})	14 300	16 000	15 700
avg. DH (m)	-0.02	0.10	-0.03
BIS DV (m^{3})		600	
sediment		mud	
zone	3	4	5
survey DV (m^{3})	-6 500	-1 100	-4 300
area (m^{2})	60 300	58 000	67 800
uncert. DV (m^{3})	12 700	12 200	14 200
avg. DH (m)	-0.11	-0.02	-0.06
BIS DV (m^{3})			
sediment			
zone		2	
survey DV (m^{3})		*400*	
area (m^{2})		*15 300*	
uncert. DV (m^{3})		*3 200*	
avg. DH (m)		*0.03*	
BIS DV (m^{3})			
sediment			
zone		1	
survey DV (m^{3})			
area (m^{2})			
uncert. DV (m^{3})			
avg. DH (m)			
BIS DV (m^{3})			
sediment			

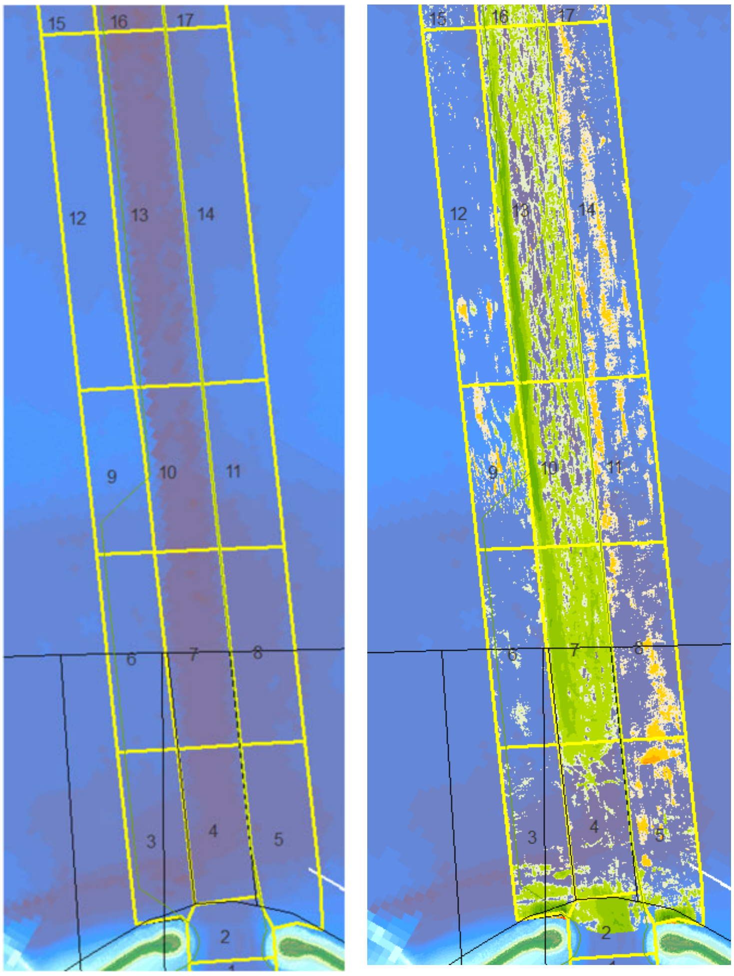

	22/01/2016 - 25/09/2015		
zone	12	13	14
survey DV (m³)	-200	39 900	-13 600
area (m²)	114 100	147 800	134 100
uncert. DV (m³)	24 000	31 000	28 200
avg. DH (m)	0.00	0.27	-0.10
BIS DV (m³)			
sediment			
zone	9	10	11
survey DV (m³)	1 100	20 800	-6 300
area (m²)	55 800	65 100	63 100
uncert. DV (m³)	11 700	13 700	13 300
avg. DH (m)	0.02	0.32	-0.10
BIS DV (m³)			
sediment			
zone	6	7	8
survey DV (m³)	3 600	30 700	-6 800
area (m²)	68 200	76 000	74 600
uncert. DV (m³)	14 300	16 000	15 700
avg. DH (m)	0.05	0.40	-0.09
BIS DV (m³)			
sediment			
zone	3	4	5
survey DV (m³)	7 100	6 000	1 600
area (m²)	60 300	58 000	68 200
uncert. DV (m³)	12 700	12 200	14 300
avg. DH (m)	0.12	0.10	0.02
BIS DV (m³)			
sediment			
zone		2	
survey DV (m³)		*7 400*	
area (m²)		*15 500*	
uncert. DV (m³)		*3 300*	
avg. DH (m)		*0.48*	
BIS DV (m³)			
sediment			
zone		1	
survey DV (m³)			
area (m²)			
uncert. DV (m³)			
avg. DH (m)			
BIS DV (m³)			
sediment			

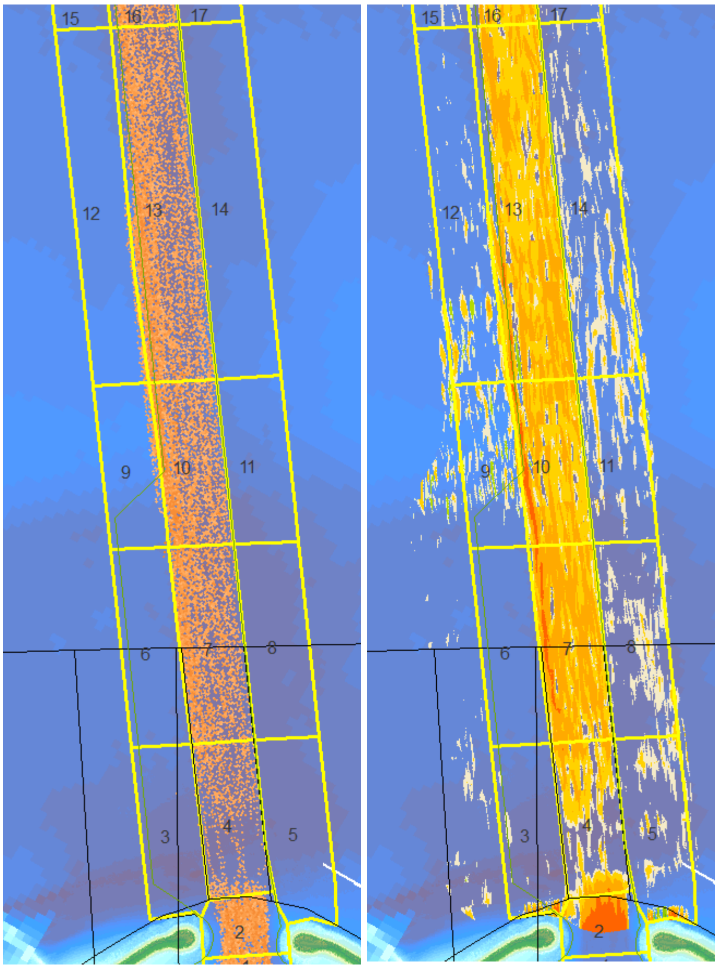

	10/03/2016 - 22/01/2016		
zone	12	13	14
survey DV (m³)	-4 900	-60 700	-15 000
area (m²)	115 200	147 800	134 100
uncert. DV (m³)	24 200	31 000	28 200
avg. DH (m)	-0.04	-0.41	-0.11
BIS DV (m³)	700	38 800	0
sediment	mud	mud	mud
zone	9	10	11
survey DV (m³)	-2 100	-30 400	-6 300
area (m²)	56 500	65 100	63 100
uncert. DV (m³)	11 900	13 700	13 300
avg. DH (m)	-0.04	-0.47	-0.10
BIS DV (m³)	1 100	21 600	0
sediment	mud	mud	mud
zone	6	7	8
survey DV (m³)	-1 800	-40 900	-8 500
area (m²)	69 100	76 000	74 600
uncert. DV (m³)	14 500	16 000	15 700
avg. DH (m)	-0.03	-0.54	-0.11
BIS DV (m³)	200	19 700	0
sediment	mud	mud	mud
zone	3	4	5
survey DV (m³)	-3 900	-14 800	-6 200
area (m²)	61 000	58 000	68 200
uncert. DV (m³)	12 800	12 200	14 300
avg. DH (m)	-0.06	-0.26	-0.09
BIS DV (m³)	0	6 100	
sediment	mud	mud	
zone		2	
survey DV (m³)		*-12 300*	
area (m²)		*15 600*	
uncert. DV (m³)		*3 300*	
avg. DH (m)		*-0.79*	
BIS DV (m³)		10 400	
sediment		mud	
zone		1	
survey DV (m³)			
area (m²)			
uncert. DV (m³)			
avg. DH (m)			
BIS DV (m³)		12 800	
sediment		mud	

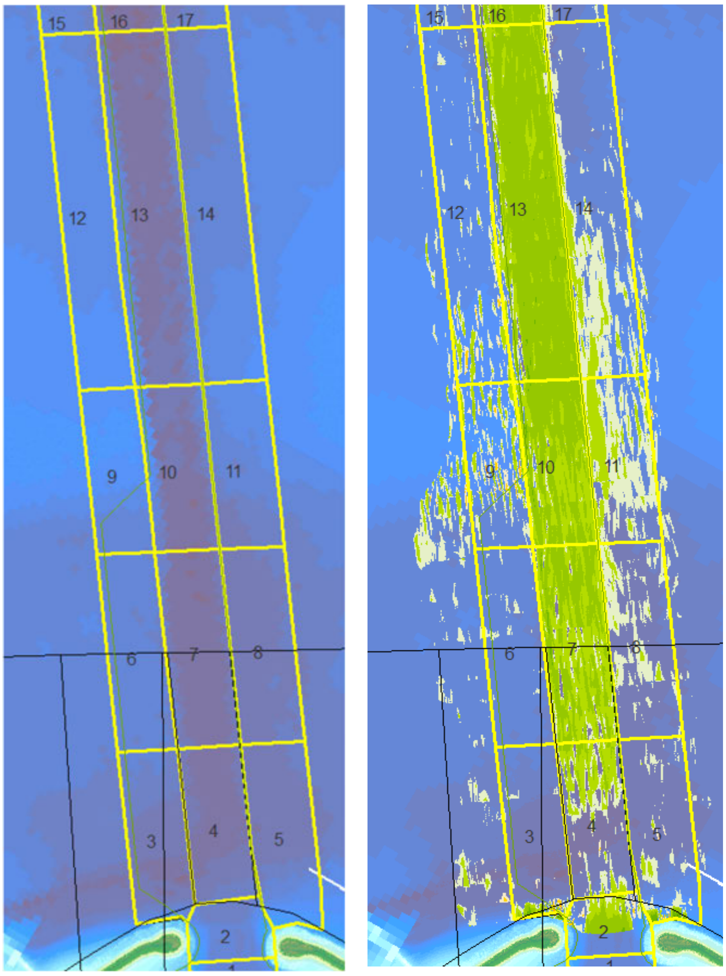

	9/05/2016 - 10/03/2016		
zone	12	13	14
survey DV (m^3)	7 700	84 300	16 300
area (m^2)	115 200	147 800	134 100
uncert. DV (m^3)	24 200	31 000	28 200
avg. DH (m)	0.07	0.57	0.12
BIS DV (m^3)			
sediment			
zone	9	10	11
survey DV (m^3)	5 200	34 800	12 000
area (m^2)	56 500	65 100	63 100
uncert. DV (m^3)	11 900	13 700	13 300
avg. DH (m)	0.09	0.53	0.19
BIS DV (m^3)			
sediment			
zone	6	7	8
survey DV (m^3)	5 200	34 500	8 200
area (m^2)	69 100	76 000	74 600
uncert. DV (m^3)	14 500	16 000	15 700
avg. DH (m)	0.08	0.45	0.11
BIS DV (m^3)			
sediment			
zone	3	4	5
survey DV (m^3)	2 500	9 100	5 800
area (m^2)	61 000	58 000	68 200
uncert. DV (m^3)	12 800	12 200	14 300
avg. DH (m)	0.04	0.16	0.09
BIS DV (m^3)			
sediment			
zone		2	
survey DV (m^3)		*5 300*	
area (m^2)		*16 600*	
uncert. DV (m^3)		*3 500*	
avg. DH (m)		*0.32*	
BIS DV (m^3)			
sediment			
zone		1	
survey DV (m^3)			
area (m^2)			
uncert. DV (m^3)			
avg. DH (m)			
BIS DV (m^3)			
sediment			

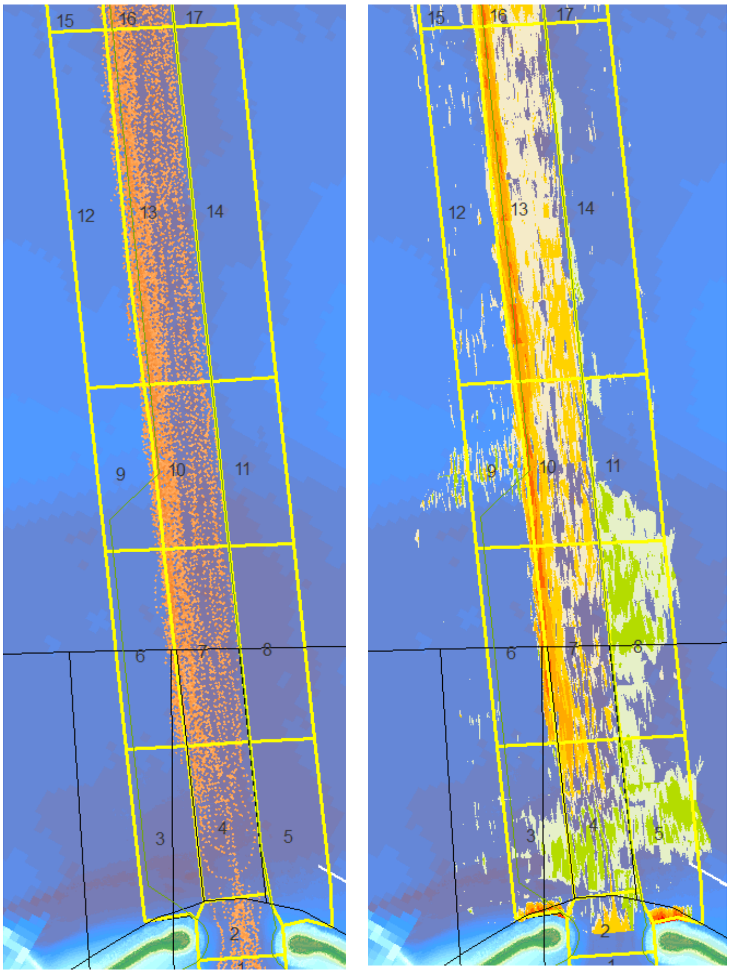

		22/06/2016 - 9/05/2016	
zone	12	13	14
survey DV (m³)	-6 500	-43 400	-1 200
area (m²)	115 200	147 800	134 100
uncert. DV (m³)	24 200	31 000	28 200
avg. DH (m)	-0.06	-0.29	-0.01
BIS DV (m³)	1 000	37 500	
sediment	mud	mud	
zone	9	10	11
survey DV (m³)	-2 000	-19 100	5 400
area (m²)	56 500	65 100	63 100
uncert. DV (m³)	11 900	13 700	13 300
avg. DH (m)	-0.04	-0.29	0.09
BIS DV (m³)	1 900	16 500	0
sediment	mud	mud	mud
zone	6	7	8
survey DV (m³)	-3 300	-19 900	13 300
area (m²)	69 100	76 000	74 600
uncert. DV (m³)	14 500	16 000	15 700
avg. DH (m)	-0.05	-0.26	0.18
BIS DV (m³)	2 400	16 500	
sediment	mud	mud	
zone	3	4	5
survey DV (m³)	4 000	3 300	7 400
area (m²)	61 000	58 000	68 200
uncert. DV (m³)	12 800	12 200	14 300
avg. DH (m)	0.07	0.06	0.11
BIS DV (m³)	100	4 400	0
sediment	mud	mud	mud
zone		2	
survey DV (m³)		*-600*	
area (m²)		*16 800*	
uncert. DV (m³)		*3 500*	
avg. DH (m)		*-0.04*	
BIS DV (m³)		2 100	
sediment		mud	
zone		1	
survey DV (m³)			
area (m²)			
uncert. DV (m³)			
avg. DH (m)			
BIS DV (m³)		3 100	
sediment		mud	

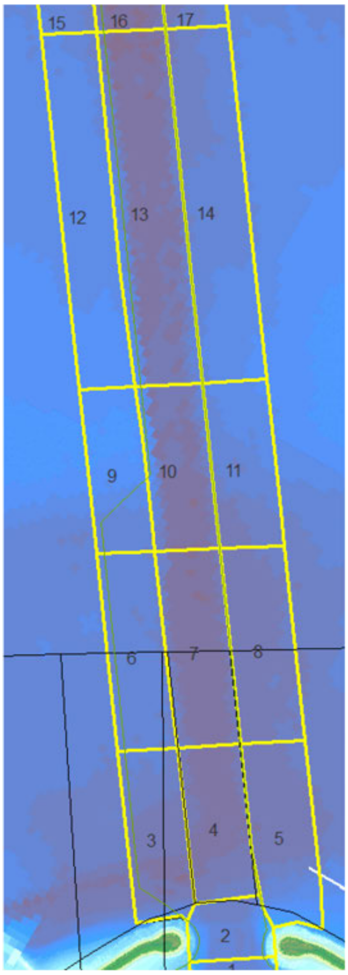

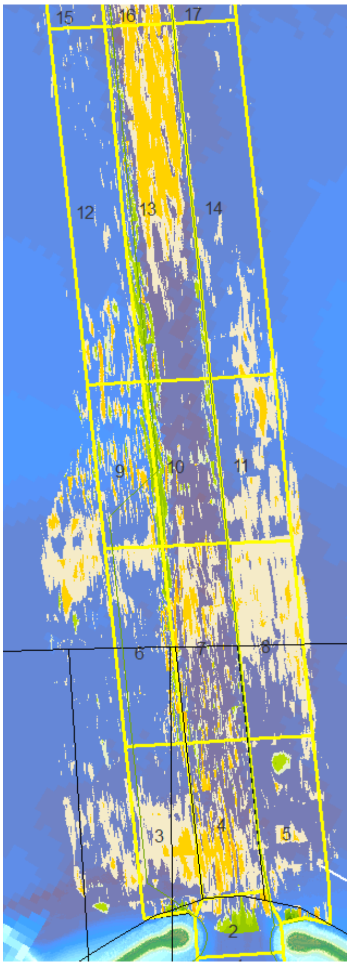

		4/10/2016 - 22/06/2016	
zone	12	13	14
survey DV (m³)	-4 300	-14 600	-10 100
area (m²)	115 200	147 800	134 100
uncert. DV (m³)	24 200	31 000	28 200
avg. DH (m)	-0.04	-0.10	-0.08
BIS DV (m³)			
sediment			
zone	9	10	11
survey DV (m³)	-2 000	4 200	-8 900
area (m²)	56 500	65 100	63 100
uncert. DV (m³)	11 900	13 700	13 300
avg. DH (m)	-0.04	0.06	-0.14
BIS DV (m³)			
sediment			
zone	6	7	8
survey DV (m³)	-3 700	-7 100	-12 600
area (m²)	69 100	76 000	74 600
uncert. DV (m³)	14 500	16 000	15 700
avg. DH (m)	-0.05	-0.09	-0.17
BIS DV (m³)			
sediment			
zone	3	4	5
survey DV (m³)	-7 900	-8 400	-4 200
area (m²)	61 000	58 000	68 200
uncert. DV (m³)	12 800	12 200	14 300
avg. DH (m)	-0.13	-0.14	-0.06
BIS DV (m³)			
sediment			
zone		2	
survey DV (m³)		*1 300*	
area (m²)		*16 300*	
uncert. DV (m³)		*3 400*	
avg. DH (m)		*0.08*	
BIS DV (m³)			
sediment			
zone		1	
survey DV (m³)			
area (m²)			
uncert. DV (m³)			
avg. DH (m)			
BIS DV (m³)			
sediment			

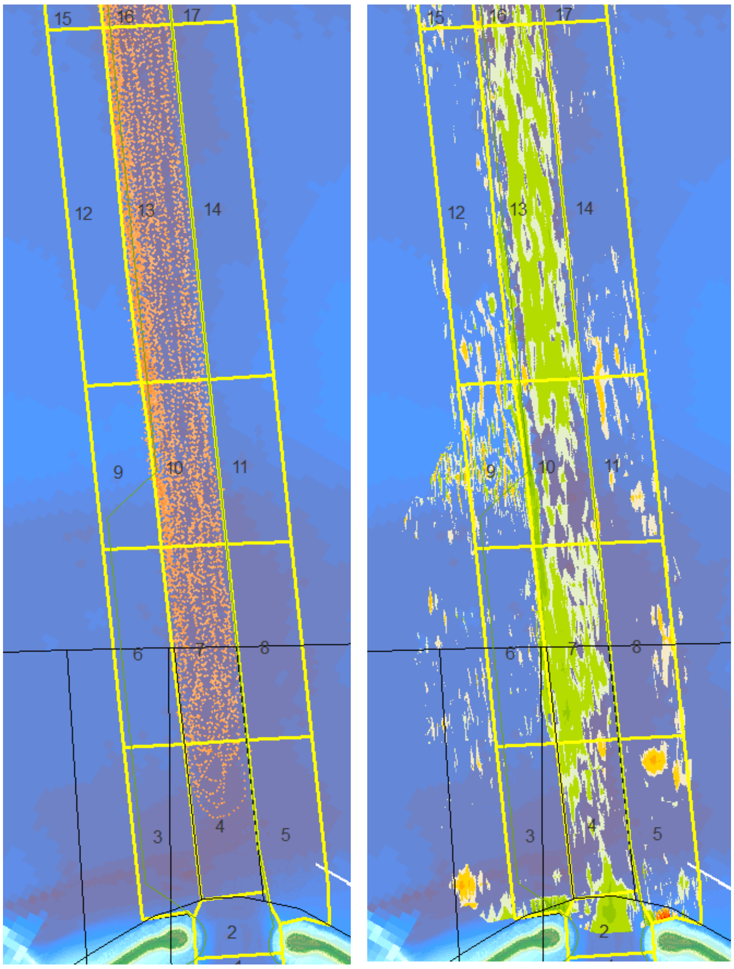

	15/03/2017 - 4/10/2016		
zone	12	13	14
survey DV (m^3)	1 300	28 900	-7 700
area (m^2)	115 200	147 800	134 100
uncert. DV (m^3)	24 200	31 000	28 200
avg. DH (m)	0.01	0.20	-0.06
BIS DV (m^3)	200	18 100	
sediment	mud	mud	
zone	9	10	11
survey DV (m^3)	-400	11 900	-5 000
area (m^2)	56 500	65 100	63 100
uncert. DV (m^3)	11 900	13 700	13 300
avg. DH (m)	-0.01	0.18	-0.08
BIS DV (m^3)	200	9 200	0
sediment	mud	mud	mud
zone	6	7	8
survey DV (m^3)	1 600	18 800	-2 800
area (m^2)	69 100	76 000	74 600
uncert. DV (m^3)	14 500	16 000	15 700
avg. DH (m)	0.02	0.25	-0.04
BIS DV (m^3)	0	7 100	
sediment	mud	mud	
zone	3	4	5
survey DV (m^3)	3 800	6 100	-1 100
area (m^2)	61 000	58 000	68 100
uncert. DV (m^3)	12 800	12 200	14 300
avg. DH (m)	0.06	0.11	-0.02
BIS DV (m^3)		1 200	0
sediment		mud	mud
zone		2	
survey DV (m^3)		*4 300*	
area (m^2)		*16 300*	
uncert. DV (m^3)		*3 400*	
avg. DH (m)		*0.26*	
BIS DV (m^3)			
sediment			
zone		1	
survey DV (m^3)			
area (m^2)			
uncert. DV (m^3)			
avg. DH (m)			
BIS DV (m^3)		🟨	
sediment			

Appendix 3: Development of an idealized coupled shelf-shoreline model

Appendix 3.1: Analytical wave model

The wave-induced longshore velocity $v_w(x)$ is estimated by solving the following equation of motion in the longshore direction, which assumes a balance between divergence of radiation stresses (S_{xx}), and the exchange of momentum due to horizontal turbulent eddies and bottom friction

$$-\frac{\partial S_{xx}}{\partial x}+\frac{\partial}{\partial x}\left[\mu H\frac{\partial v_w}{\partial x}\right]-\frac{2}{\pi}\rho c_f\hat{u}_w v_w=0, \qquad \text{(A1)}$$

$$\frac{\partial S_{xx}}{\partial x}=-\frac{5}{4}\alpha^2\rho(gH)^{3/2}\frac{\partial H}{\partial x}\frac{\sin\theta}{\sqrt{gH}}, \qquad \text{(A2)}$$

$$\mu=N\rho x\sqrt{gH}. \qquad \text{(A3)}$$

Here, μ represents the eddy viscosity coefficient, H is the water depth, ρ is the density, c_f is the friction coefficient, $\hat{u}_w$ is the amplitude of the near-bed wave orbital velocity, α is a breaking index, θ is the wave angle and N is a dimensionless constant.

<u>Without exchange of momentum:</u>

By neglecting the exchange of momentum (second term in Eq. A1), the following expression for the longshore wave velocity (called $v_{w,0}(x)$) can be derived:

$$v_{w,0}(x)=\begin{cases}\frac{5\pi}{8}\frac{\alpha}{c_f}g\frac{\partial H}{\partial x}\frac{\sin\theta_b}{\sqrt{gH_b}}H(x) & H<H_b\\ 0 & H>H_b\end{cases}, \qquad \text{(A4)}$$

In this expression, H_b and θ_b are, respectively, the wave height and wave angle at breaking. Note that, as $\sin\theta/(gH)^{1/2}=\sin\theta_B/(gH_b)^{1/2}$ is constant (Snell's law), and assuming that bottom slope $\partial H/\partial x$ is constant, velocity $v_{w,0}$ is simply proportional to water depth H.

<u>With exchange of momentum:</u>

Let us assume a Dean equilibrium profile representing the bathymetry of the nearshore zone, i.e., $H = sx^{2/3}$, with s a constant. Then, Eq. A1 can be written in the form

$$p\frac{\partial}{\partial x}\left[x^2\frac{\partial v_w}{\partial x}\right]-qx^{1/3}v_w=\begin{cases}-rx^{2/3} & 0<x<x_b,\\ 0 & x_b<x<\infty\end{cases} \qquad \text{(A5)}$$

,

where x_b is the cross-shore location where waves start to break. Furthermore, p, q and r are constants given by

$$
\begin{aligned}
p &= N\rho g^{1/2} s^{3/2}, \\
q &= \frac{2}{\pi}\alpha c_f \rho g^{1/2} s^{1/2}, \\
r &= \frac{5}{6}\alpha^2 \rho g^{3/2} s^{5/2} \frac{\sin\theta_b}{\sqrt{gH_b}}
\end{aligned}
\quad . \tag{A6}
$$

By introducing the following nondimensional variables

$$
\begin{aligned}
X &= \frac{x}{x_b}, \\
V_w &= \frac{v_w}{v_{w,0}(x = x_B)}, \\
v_{w,0}(x = x_B) &= \frac{5\pi}{8}\frac{\alpha}{c_f} gH \frac{\partial H}{\partial x}\frac{\sin\theta_b}{\sqrt{gH_b}} = \frac{5\pi}{12}\frac{\alpha}{c_f} g s x_b^{2/3} s x_b^{-1/3} \frac{\sin\theta_b}{\sqrt{gH_b}} = \\
&\frac{5\pi}{12}\frac{\alpha}{c_f} g s^2 x_b^{1/3} \frac{\sin\theta_b}{\sqrt{gH_b}},
\end{aligned}
\tag{A7}
$$

Eq. A5 becomes

$$
P\frac{\partial}{\partial X}\left[X^2 \frac{\partial V_w}{\partial X}\right] - X^{1/3} V_w = \begin{cases} -X^{2/3} & 0 < X < 1, \\ 0 & 1 < X < \infty, \end{cases} \tag{A8}
$$

$$
P = \frac{\pi s N}{2\alpha c_f x_b^{1/3}} \quad . \tag{A9}
$$

This differential equation cannot be solved analytically. To find an approximate solution, the X^2 in the first term on the left-hand-side is approximated by $X^{7/3}$, which yields the following general solution:

$$
\begin{aligned}
V_w &= \begin{cases} \overbrace{C_2 X^{p_1}}^{\text{homogenous solution}} + \overbrace{C_1 X^{1/3}}^{\text{particular solution}} & 0 < X < 1, \\ C_3 X^{p_2} & 1 < X < \infty. \end{cases} \\
p_1 &= -\frac{2}{3} + \sqrt{\frac{4}{9} + \frac{1}{P}}, \\
p_2 &= -\frac{2}{3} - \sqrt{\frac{4}{9} + \frac{1}{P}}, \\
C_1 &= \frac{1}{1 - \frac{5}{9}P},
\end{aligned}
\tag{A10}
$$

By imposing that V_w and $\partial V_w/\partial x$ are continuous at $X = 1$, following expressions for C_2 and C_3 are deduced

$$
\begin{aligned}
C_2 &= \frac{p_2 - \frac{1}{3}}{p_1 - p_2} C_1 \quad , \\
C_3 &= \frac{p_1 - \frac{1}{3}}{p_1 - p_2} C_1,
\end{aligned}
\tag{A11}
$$

Note that the Equation A10 is derived based on the assumption of a Dean equilibrium profile, representing the bathymetry of the nearshore zone. The bathymetry profile of Equation 1 is a more appropriate choice, which will be considered in future research.

Appendix 3.2: Analytical tide model

To account for tides in the nearshore, an expression for the tidal velocity (v_t) is derived from the momentum equation, thereby assuming a balance between inertia, alongshore gradient in the water level and bottom friction:

$$\frac{\partial v_t}{\partial t} = -gs - \frac{\tau_{b,y}}{\rho H}. \qquad \text{(A12)}$$

Here, $s = \partial\zeta/\partial y$ is the longshore gradient in surface elevation ζ and $\tau_{b,y}$ is the bed shear stress, which is linearly approximated as $\tau_{b,y} = \rho\, r\, v_t$, with r a constant friction factor. Note that tidal velocity v_t is assumed to depend only on x and time t. Longshore gradient s is assumed to consist of two oscillating components with the frequency of M_2 (with angular frequency σ) and M_4 tide (angular frequency is 2σ):

$$s = -s_2 \exp[i(\sigma t)] - s_4 \exp[i(2\sigma t + \theta_4)], \qquad \text{(A13)}$$

where θ_4 is a phase difference between M_2 and M_4 signals in the alongshore gradient in the tidal water level. Hence, Eq. (A12) becomes

$$\frac{\partial v_t}{\partial t} + \frac{r v_t}{H} = g s_2 \exp[i(\sigma t)] + g s_4 \exp[i(2\sigma t + \theta_4)]. \qquad \text{(A14)}$$

The complex solution of this equation reads

$$v(x,t) = \hat{v}_2(x) \exp[i(\sigma t + \phi_2)] + \hat{v}_4(x) \exp[i(2\sigma t + \phi_4)]. \qquad \text{(A15)}$$

The real part is

$$v_t(x,t) = \hat{v}_2(x) \cos[\sigma t + \phi_2)] + \hat{v}_4(x) \cos(2\sigma t + \phi_4 + \theta_4)], \qquad \text{(A16)}$$

where the amplitudes and phases of the tidal current are given by

$$\begin{aligned}
\hat{v}_2(x) &= \frac{g s_2 H}{\sqrt{\sigma^2 H^2 + r^2}}, \\
\phi_2(x) &= \arctan\left[\frac{r}{\sigma H}\right], \\
\hat{v}_4(x) &= \frac{g s_4 H}{\sqrt{4\sigma^2 H^2 + r^2}}, \\
\phi_4(x) &= \arctan\left[\frac{r}{2\sigma H}\right].
\end{aligned} \qquad \text{(A17)}$$

Table 14 – Parameters wave and tide model.

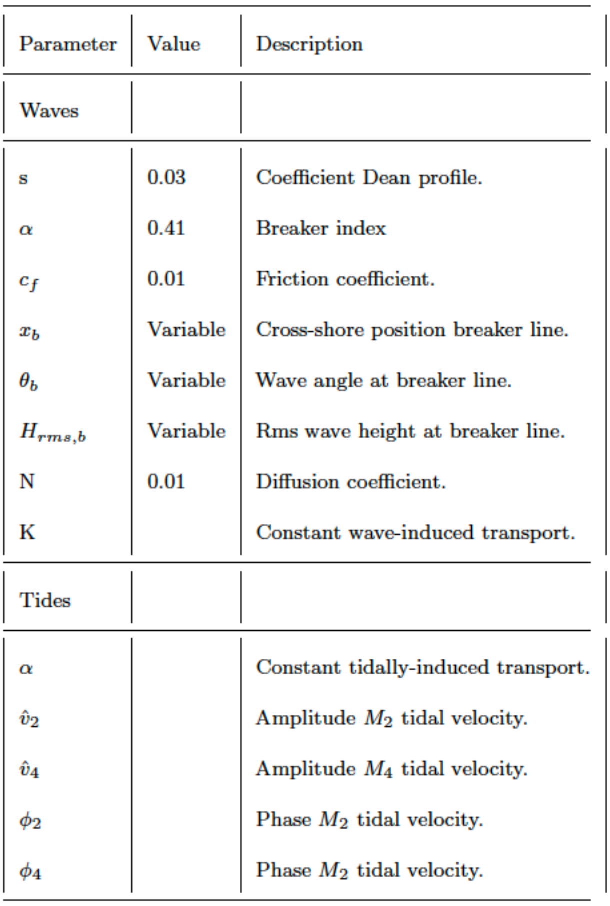

Parameter	Value	Description
Waves		
s	0.03	Coefficient Dean profile.
α	0.41	Breaker index
c_f	0.01	Friction coefficient.
x_b	Variable	Cross-shore position breaker line.
θ_b	Variable	Wave angle at breaker line.
$H_{rms,b}$	Variable	Rms wave height at breaker line.
N	0.01	Diffusion coefficient.
K		Constant wave-induced transport.
Tides		
α		Constant tidally-induced transport.
$\hat{v}_2$		Amplitude M_2 tidal velocity.
$\hat{v}_4$		Amplitude M_4 tidal velocity.
ϕ_2		Phase M_2 tidal velocity.
ϕ_4		Phase M_2 tidal velocity.

Table 15 – Overview of the physical and numerical parameters of the coupled shelf-shoreline model.

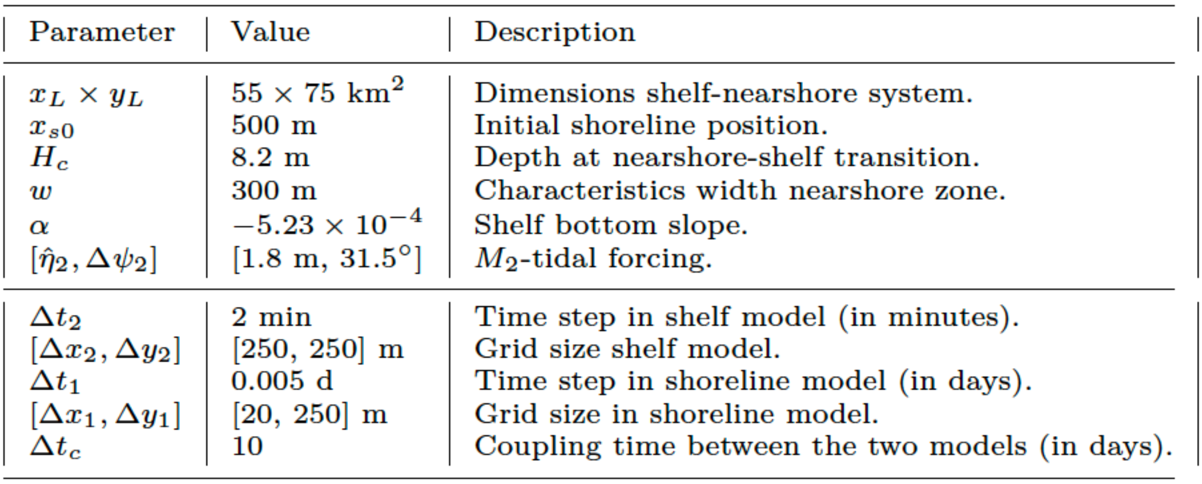

Parameter	Value	Description
$x_L \times y_L$	55×75 km^2	Dimensions shelf-nearshore system.
x_{s0}	500 m	Initial shoreline position.
H_c	8.2 m	Depth at nearshore-shelf transition.
w	300 m	Characteristics width nearshore zone.
α	-5.23×10^{-4}	Shelf bottom slope.
$[\hat{\eta}_2, \Delta\psi_2]$	[1.8 m, 31.5°]	M_2-tidal forcing.
Δt_2	2 min	Time step in shelf model (in minutes).
$[\Delta x_2, \Delta y_2]$	[250, 250] m	Grid size shelf model.
Δt_1	0.005 d	Time step in shoreline model (in days).
$[\Delta x_1, \Delta y_1]$	[20, 250] m	Grid size in shoreline model.
Δt_c	10	Coupling time between the two models (in days).

Appendix 4: FlemCo and Scaldis-Coast parameter settings

Table 16 – Overview of selected model parameter settings and essential features of the FM-FlemCo model and comparison with the Telemac Scaldis-Coast model (Wang et al., 2021; Kolokythas et al., 2020 & 2021).

Model feature	FM-FlemCo	Telemac Scaldis-Coast
Software	Delft3D Flexible Mesh/SWAN	openTELEMAC-suite v7p2_cookie
Solver	Finite Volumes on a staggered grid, solving shallow water equations	Finite Element method, solving Saint-Venant equations (uni-directional shallow water equations) making use of generalized wave equation
Flow model domain	see Figure 36 in Dujardin *et al.,* 2023	see Figure 41 in Dujardin *et al.,* 2023
Wave model domain	see Figure 37 in Dujardin *et al.,* 2023	see Figure 43 in Dujardin *et al.*, 2023
Grid resolution nearshore	ca. 45 m x 45 m/23 m x 23 m	ca. 20 m
Bathymetry	Same as Scaldis-Coast coast but converted to NAP	see Figure 44 and Table 11 in in Dujardin *et al.*, 2023
Computational approach	Two-dimensional (2DH)	Two-dimensional (2DH)
Origin of flow forcing	Derived from Simona DCSMv6-ZUNOv4 model (Zijl, 2013 & 2014) for the year 2014	Derived from Simona DCSMv6-ZUNOv4 model (Zijl, 2013 & 2014) for the year 2014
Type of flow forcing	Water level boundary conditions (sea) and discharge (Western Scheldt)	Water level boundary conditions (sea); discharge (Western Scheldt) is possible, but not applied in the morphodynamic runs
Tidal forcing	Representative morphological period: 14-03-2014 to 13-05-2014	Representative morphological tide of 24 hours and 50 minutes: #137 25/05/2014 17:20 – 26/05/2014 08:10
Wind forcing	Time series measured at Westhinder buoy (2014)	Time series measured at Westhinder buoy (2014)
Wave forcing	Time series measured at Westhinder buoy (2014)	Time series measured at Westhinder buoy (representative morphological year 30/11/2015 – 29/11/2016)
Coupling interval flow-wave	30 min	30 min
Wave computational mode	Non-stationary (time step: 30 min)	Non-stationary (time step: 30 min)

Secondary flow	Switched on	Switched off
Salinity	Switched off	Switched off
Maximum time step	30 s	10 s
Horizontal eddy viscosity	1 $m^2\ s^{-1}$ (uniform)	1 $m^2\ s^{-1}$ (uniform)
Horizontal eddy diffusivity	1 $m^2\ s^{-1}$ (uniform)	1 $m^2\ s^{-1}$ (uniform)
Bottom roughness	Manning's n = 0.02 [s $m^{-1/3}$] (uniform)	Manning's n = 0.022 [s $m^{-1/3}$] (uniform at sea), varying in Western Scheldt (Figure 45 in Dujardin *et al.*, 2023)
Threshold depth wet/dry cells	0.1 m	0.0 m
Morphological simulation period	1 year by using a morphological scale factor of 6 (6 x 2 months = 1 year)	10 years by using a morphological scale factor of 10 (10 x 1 year = 10 years)
Type of morphological model	Morphostatic (only sediment transport, no morphodynamics)	Morphodynamic (sediment transport + bed update + dredging & dumping)
Considered sediment fraction	200 µm	2 fractions: 200 µm and 500 µm The ratio of the fractions is calculated to mimic a corresponding sediment transport rate as the local observed grain size would
Initial sediment thickness	20 m (uniform), i.e. unlimited in a 1 year simulation	unlimited (10,000 m), except for sediment on top of groyns
Sediment transp. formulation	Bijker (1971)	Bijker (1968)
Current-related suspended and bedload transport factors (Sus, Bed)	1 [-]	1 [-]
Wave-related suspended and bedload transport factors (SusW, BedW)	0.5 [-]	0.5 [-]
Calibration coefficient b for shallow water (only Bijker 1971)	5 [-]	2 [-] (no distinction between shallow and deep water in default SISYPHE)
Calibration coefficient b for deep water (only Bijker 1971)	2 [-]	
Settling velocity (only Bijker 1971)	0.02 [m s^{-1}]	computed explicitly according to grain size

Appendix 5: Tidal asymmetry

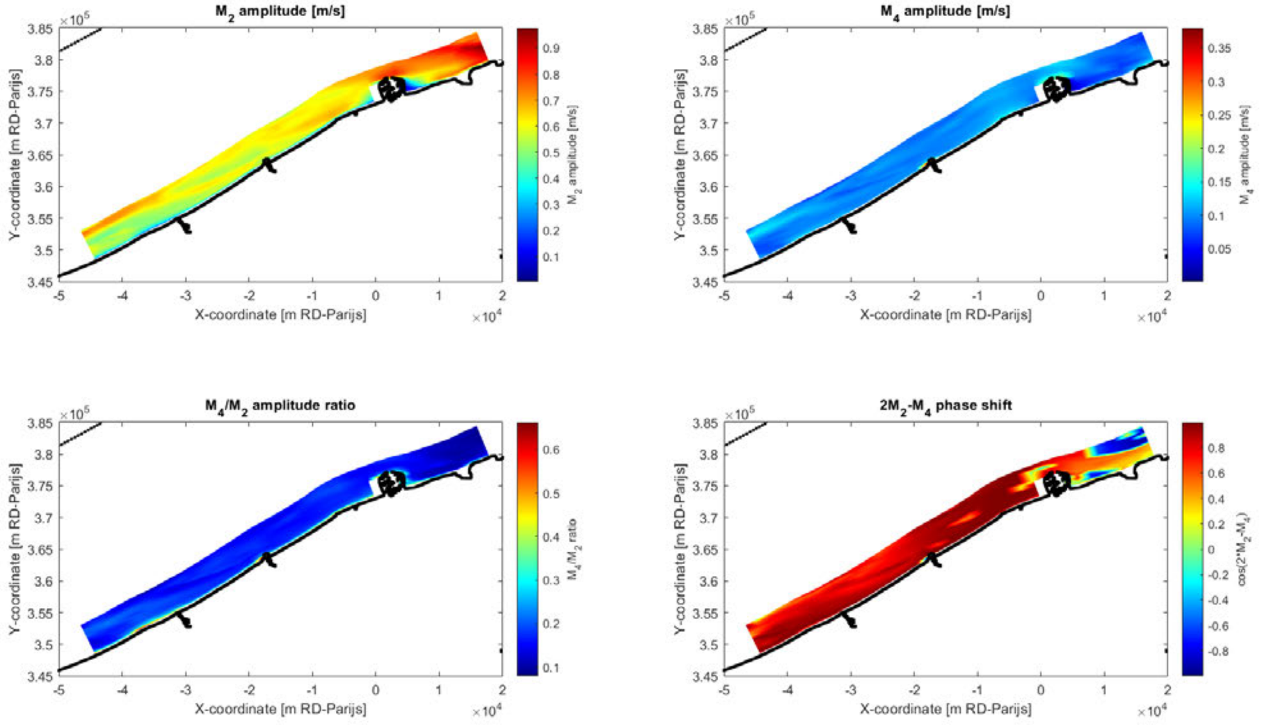

Figure 109 – Harmonic M2 and M4 components of the alongshore currents as computed by Scaldis-Coast.

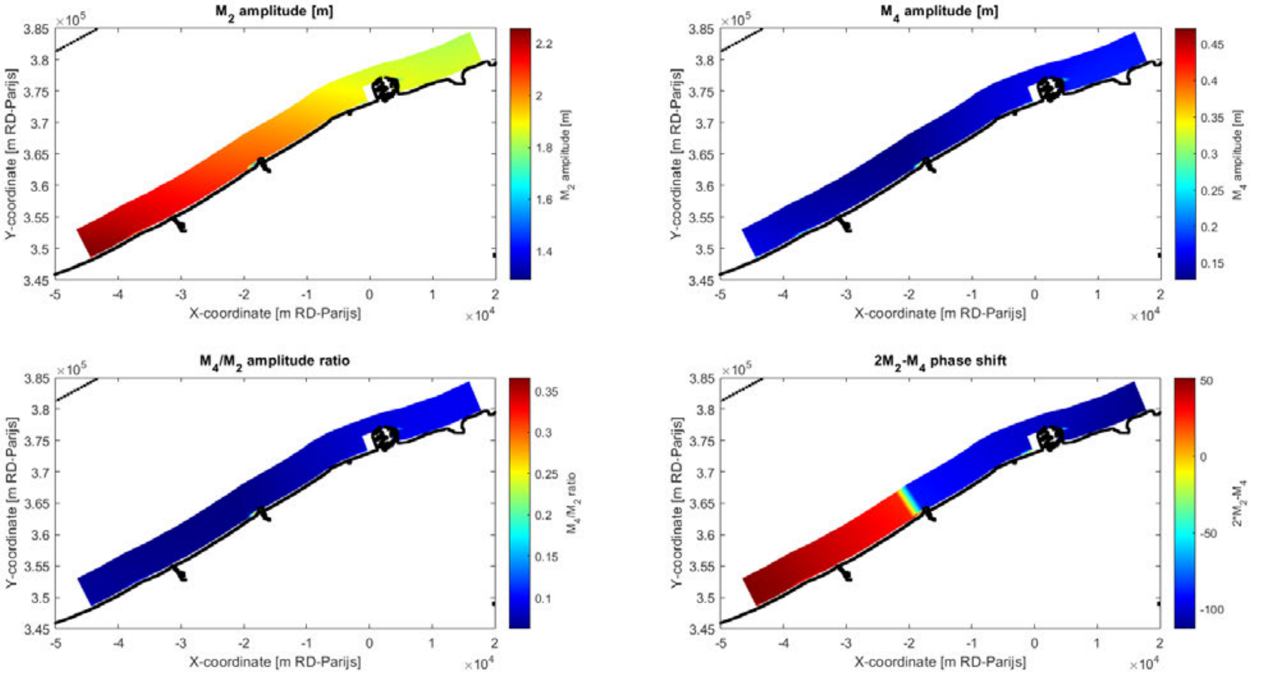

Figure 110 – Harmonic M2 and M4 components of the water levels as computed by Scaldis-Coast.

DEPARTMENT **MOBILITY & PUBLIC WORKS**
Flanders hydraulics

Berchemlei 115, 2140 Antwerp
T +32 (0)3 224 60 35
F +32 (0)3 224 60 36
flanders.hydraulics@vlaanderen.be
www.flandershydraulics.be